Integrated micro-system for real time cell bio-chemical assessment

Dacian Emilian Roman

A Thesis

In the Department

of

Mechanical and Industrial Engineering

Presented in Partial Fulfillment of the Requirements

For the Degree of Doctor of Philosophy at

Concordia University

Montreal, Quebec, Canada

November 2012

CONCORDIA UNIVERSITY

SCHOOL OF GRADUATE STUDIES

This is to certify that the thesis prepared

By: **Dacian Emilian Roman**

Entitled: **Integrated micro-system for real time cell bio-chemical assessment**

and submitted in partial fulfillment of the requirements for the degree of

DOCTOR OF PHILOSOPHY (Mechanical Engineering)

complies with the regulations of the University and meets the accepted standards with respect to originality and quality.

Signed by the final examining committee:

_____ Chair
Dr. P. Grogono

_____ External Examiner
Dr. R. Landry

_____ External to Program
Dr. R. Zmeureanu

_____ Examiner
Dr. R. Sedaghati

_____ Examiner
Dr. W.F. Xie

_____ Thesis Supervisor
Dr. I. Stiharu

Approved by _____
            Dr. A. Dolatabadi, Graduate Program Director

December 19, 2012   _____
            Dr. Robin A.L. Drew, Dean
            Faculty of Engineering and Computer Science

Abstract

Integrated micro-system for real time cell bio-chemical assessment

Dacian Emilian Roman

Miniaturized lab-on-a-chips and micro Total Analysis Systems (µTAS) have already penetrated the area of molecular diagnostics and brought the promise of a shift of paradigm in the way that medical professions will be conducted. Large spectrums of applications have been reported in the area of diagnosis and prognostics, regarding both qualitative and quantitative identification of targeted bio-entities. The advance of Micro Electro Mechanical Systems (MEMS) and microfluidic technologies opened a major challenge for a large number of researchers, industrial health and bio companies to invest their time and budget into the avenue of Point of Care (POC) health instruments or devices that help in the early detection of cancer cells within the human blood, via circulating malignant cells.

A large project that addresses the design of a point of care (POC) prototype in the area of bio-MEMS is presently ongoing in our laboratories. This device will enable the early detection of specific malignant species from a blood sample and integrates subprojects regarding the separation of malignant species from the blood sample, the characterization of these particles and the precise identification of the detected species. The detection method is based on the interaction between a microstructure, in this case a cantilever beam, and the reacting large organic molecules.

The aim of the present work is the detection part and represents the effort of the candidate to confirm theoretically and experimentally a series of pre-existing experimental results

performed within the research group. The detection experiments take in consideration both the specific deflection obtained by means of direct measuring and the optical variation of the capillary angle during the interaction at micro-level between a pair antibody-antigen. The option of performing the assessment on an in-plane configuration rather than the out-of-plane method is also taken in consideration.

The results of this work can help benefiting both care-givers and patients if implemented in a clinical diagnostic device, contributing to an early detection of a malignant condition and the follow-up during the specialized treatment, implicitly reduced costs and improved quality of life.

Acknowledgments

In the first place I would like to express my gratitude to my supervisor, Dr. Ion Stiharu for his judicious and professional guidance, support and inspiration throughout my entire PhD work.

I address also my special thanks to the people whom strongly helped and assisted me during the entire project, namely Arash Firoozrai, Anas Alazzam and Vahé Nerguizian. Special thanks to Dr. Emilia Antecka, Dr. Ala-Eddin Al Moustafa, Dr. Amber Yasmeen and Dr.Matei Mireuta for their biology related advices during the biological experiments. For technical support I thank Jeetender Aamritsar, Davut Erdem, George Floarea, Shahrzad Nouri, Alfin Leo Amalorpasamy, Amin Changizi and Etienne Mfoumou for their help and encouragement as colleagues and partners in both experimental and analytical work.

For moral support, I am thankful, first of all, to my mother, Maria Brezniceanu and my father, Emil Roman for their love, kindness and support.

I want to thank God for blessing me with such wonderful people!

Table of Contents

List of Acronyms

μm	Micrometer
μRNA	Micro ribonucleic acid
μTAS	Micro total analysis systems
2D	Two Dimensional
3D	Three Dimensional
Å	Angstrom (unit of length)
Ab	Antibody
Ag	Antigen
Al	Aluminum
Ansys	Commercial multiphysics software
ATM	Atomic Force Microscopy
atm	Unit of atmospheric pressure
BioMEMS	Biological Micro Electro Mechanical Systems
BRCA1	Human caretaker gene
CFTOOL	Curve Fitting Toolbox
CMOS	Complementary metal–oxide–semiconductor
Cr	Chromium
CTC	Circulating tumor cells
DEP	Dielectrophoresys

DNA	Deoxyribonucleic acid
EDTA	Ethylene Diamino Tetraacetic Acid
ELISA	enzyme-linked immunosorbent assay
EpCAM	Type of expressing epithelial protein
ESO	Evolutionary structural optimization
FDA	Food and Drug Administration
FEM	Finite Element Model
GDP	Gross Domestic Product
GPa	GigaPascal
HyperWorks	Commercial multiphysics software
IBM	International Business Machines Corporation
IgG	Immunoglobulin
ImageJ	Graphic Goftware
kHz	kiloHerz
LMS	Least-Mean Squared
m	Meter
MATLAB	Mathematical software
MEMS	Micro Electro Mechanical Systems
MHz	Mega Herz
min	Minute
mm	Millimetre

MPa	Mega Pascal
mW	miliwatt
N	Newton
nDEP	Negative Dielectrophoreis
nM	Nano Molar
nm	Nanometer
^{o}C	Degree Celsius
Pa	Pascal
PCR	Polymerase Chain Reaction
pDEP	Positive Dielectrophresis
PDMS	PolyDiMethyl Siloxane
pH	Measure of the acidity or basicity of an aqueous solution
POC	Point of Care
PSA	Prostate SpecificAntigen
PSD	Position Sensitive Detector
PSI	Phase Shifting Interferometry
PVDF	Polyvinylidene Fluoride
Rb	Retinoblastoma proteins
RBC	Red Blood Cells
RNA	Ribonucleic acid
RT-PCR	Real Time Polymerase Chain Reaction

s	second
SFM	Scanning Force Microscopy
Si_3N_4	Silicon Nitride
SIMP	Solid Isotropic Material with Penalization
SiO_2	Silicon Dioxide
SU-8	Epoxy based photoresist
TSGs	Tumor Suppressor Genes
USD	United States Dollar
VSI	Vertical Shifting Interferometry

List of Symbols

ρ	Specific mass density of the beam material
χ	Mass of the cantilever beam
ξ	Damping coefficient
Q	Quality factor
ω_{n0}	Frequency in the undamped case
ω	Resonance frequency of a cantilever beam
A_{CS}	Area of the circular segment
α	Angle
γ_L	Surface tension
γ	Surface tension
Θ	Contact angle
ε	Elastic surface strain
c_{SV}	position of the center of the arc
L_{ARC}	Length of the arc
A_{CS}	Area of the circular segment
c_{LP}	Position of the center of the area
V_{CS}	Volume of determined by the circular segment area

c_{CS}	Position of the centroid of the volume
z	Deflection function
z_{max}	Maximum deflection
F	Capillary force of attraction
Ω	Reference domain
F_{DEP}	Dielectrophoretic force
E	Electric field
ε_m	Absolute permittivity of the surrounding medium
ε_0	Permittivity of the vacuum
ε_r	Dielectric constant of the medium
$\boldsymbol{E}$	Electric field vector
φ	Electric potential
$\bar{x}$	Normalized value of the coordinate x
$\bar{y}$	Normalized value of the coordinate y
k_i	Constant
k_e	Constant
$F_e\left(\bar{x}_e\right)$	Force
$G_{e\bar{y}_e\bar{y}_e}$	Force
c_1	Coefficient

C_n	Coefficient
φ_{max}	Maximum value of the electric potential
$N(n)$	Norm
$\bar{E}$	Electric field vector
$\nabla \left| \bar{E} \right|^2$	Gradient of the intensity of the electric field
E_x	Differentiation with respect to x (y)
$\mathrm{Re}\left[CM \right]$	The real part of the Claussius-Mossoti factor
φ_1	Partial potential function
φ_2	Partial potential function
γ_h	Horizontal component of the surface tension
γ_v	Vertical component of the surface tension
A	Cross-section aria of the beam
a	Diameter of the circle
A_i	Constant
B_i	Axial stiffness
B_i	Constant
Ci	Constant
D	Total bending stiffness of the beam
D_i	Constant
E^*	Apparent Young's modulus

$E_{1,2}$	Young's modulus of elasticity of each layer of material
E_c	Complex Young's modulus of elasticity of the beam
$E_{ijkl}(x)$	Stiffness tensor
f	Frequency
$F(x)$	Function of x
F_1	Tensile force
F_2	Compressive force
g	Gravitational acceleration
$G(y)$	Function of y
H	Distance between plates
$h_{1,2,3}$	Thickness of the corresponding layer
I	Second moment of area
I_i	Second moment of inertia of the i-th layer
L	Length of the beam
L	Length of the channel
l	Length of the electrodes
L_1	Distance between the fixed end and the circumference of the droplet
L_{2Di}	Distance between the free end and the circumference of the droplet
m	Number of terms considered

$M(x)$	Bending moment
m^*	Effective mass of the cantilever beam
$M_{1,2,3,4,5}$	Bending moments
Ma	Marangoni number
m_b	Mass of the beam
n	The position of the neutral axis
n	Number of terms considered
P	Laplace pressure
$P_{1,2}$	Axial load
q	Driving load
R	Radius of curvature
t	Total thickness of the beam
T	Electrode thickness
T_f	Final temperature
t_i	Thickness of layer i
T_i	Initial temperature
V	Volume of the dro
V_0	Electric potential of the electrode
w	Width of the beam
x,y,z	Cartesian coordinate
Z	Deflection

α	Heavy chain (epitope)
$\alpha_{1,2}$	Coefficients of thermal expansion of each layer
γ	Heavy chain (epitope)
γ	Surface tension
δ	Heavy chain (epitope)
$\Delta\sigma$	Surface stress variation
ε	Heavy chain (epitope)
η	Viscosity of the liquid mixture
κ	Light chain(epitope)
κ^{-1}	Capillary length
λ	Light chain (epitope)
μ	Heavy chain (epitope)
v	Poisson's ratio
ρ	Density
ρ	Electric charge density
σ_{zi}	Normal stress

List of Biological Terms

92.1   Human uveal melanoma cell line;

Ab   Antibody;

Ag   Antigen;

D-PBS   Dulbecco's Phosphate Buffered Saline;

EDTA   Ethylene Diamine Tetraacetic Acid widely used in biological

                applications;

FBS   Fetal Bovine Serum rich of proteins and used in cell culturing

                were cells can grow and divide;

Ficoll   Synthetic branched co-polymer of sucrose and epichlorhydrin.

                The solution has high viscosity and low osmotic pressure. Often

                used for preparing density gradients for cell separations;

Hela   Oldest and most commonly used human cervical cancer cell line

MDA231   Breast cancer cells line;

OCM   Human uveal melanoma cell line;

PBS   Phosphate Buffered Saline a buffer solution used in biological

                applications;

PC3   Cell line originally derived from advanced androgen

                independent bone metastasis/metastasized prostate cancer;

RPMI 1640   Cells media used to culture cells was developed at Roswell Park

Memorial Institute (RPMI);

Trypsin   Trypsin is a pancreatic serine protease used to detach adherent

cells from the cell culture dish wall during the process of

harvesting cells to re-suspend them in media;

List of Figures

xxi

xxii

List of Tables

Chapter 1:   Introduction

1.1 Introduction

Malignant conditions, along with the cardiovascular diseases, are the main responsible for premature death in today's world. Cancer associated costs from both traumatic and economic perspective, exceed tens of billions of dollars while the prognosis regarding the number of deaths and debilitating effects is gloom. The causes of these conditions are multiple and not always well understood. The aging of population, the increase of pollutants, the levels of psychological stress, viruses or genetic mutations are just few of the complex sources of this devastating ailment.

Early diagnostics of the malignant condition has been proved as an effective method of saving patients life, of increase in post-treatment quality of life and, in general, of decrease in the cost associated with the management of the disease. Circulating tumor cells are signaling entities in the after treatment prognostics for several oncological conditions, especially in prostate, melanoma, breast and colorectal cancers [1]. Consequently, the demand for accurate, portable and affordable diagnostics units increases and the emergent technologies in the area of micro fabrication represent a hope in satisfying this need in the near future. The goal is to manufacture medical devices for the generalist office, capable of early diagnostics and personalized treatment for a large array of medical condition.

The main qualities of these devices are their precision, safety, affordability and manoeuvrability. The success of several commercial products in the area of pathogen detection

and early diagnostics build hope for future optimization in the desired direction with a more affordable financial cost. The main challenge for these instruments is the fact that they involve highly interdisciplinary research teams and also the existence of a strong pressure from a legal perspective in terms of erroneous medical diagnostics, the false positive or false negative verdicts. In order to minimize the influence of the erroneous data, usually multiple measurements of the same parameter are performed. However, the low costs of minute quantities of analytes and the mature technologies in the area of micro-fabrication tend to act in the direction of reduction of the cost associated with the essay and the exploitation of the instruments.

1.2 Objectives

At the present moment, it is known that primary tumors release circulating cancer tumor cells (CTCs) which travel through the blood stream and install on other organs on which they metastases, making the condition to progress. Separation and characterization of such cells represents the aim of the program. This entire project addresses the design of a BioMEMS prototype that will enable to perform early detection of specific malignant cells from a blood sample. The present project, as part of the program, deals with the characterization of the cells through the interaction between a mini-structure and a bio-molecular reaction.

The entire program consists of three subprojects. The first two subprojects involve the development of non-destructive devices used to separate and differentiate rare cells from the blood of the patient. During these two stages, the cells manipulated and studied in a non-destructive manner are not affected from a biological point of view. In this project, however the

2

membrane of the cells is disrupted because of the biochemical reaction between an antigen and its specific antibody. An artistic representation of the desired virtual device is presented Figure 1.1. The upper and lower blue layers represent the microfluidic parts where the specimens are processed, with all the necessary intermediate steps: preprocessing, lysing, and mixing with the desired reagents and droplet generation. The green layer represents the detection subcomponent and it is related to the present work.
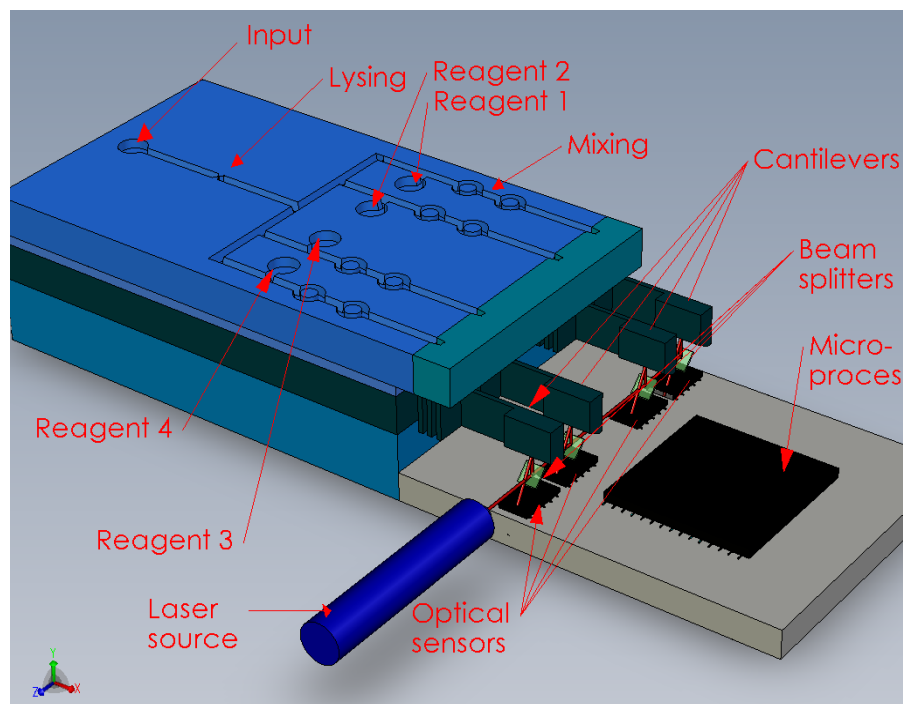
Figure 1.1 Virtual view of the biochip.

The present project deals with characterization of the cells during on the interaction between a mini-structure with the phenomena generated by bio-molecular reaction between an antigen and its complementary antibody [2]. It refers to the detection part only and it illustrates the theoretical and experimental procedures necessary to be performed in order to detect certain

type of circulating tumor cells from a blood sample. The detection sensor consists of a cantilever beam that signals thorough the optical lever method the specific deflection sequence of the structure, that will be called signature.

The deflection of the beam is due to the complexes phenomena that take place on its surface during the interaction of the investigated sample with a specific antibody. The complex biochemical reaction generates a variation in the surface stress due to the droplet mixture placed on its surface. Further, the overlapped effects of evaporation, surface tension, surface stress, weight of the droplet and of the structure itself, plus the thermal phenomena associated both with the evaporation and the reaction will generate a signature of the deflections of the cantilever beam that is very specific for each antigen-antibody pair. The deflection of the beam is sensed using the optical lever method where a laser beam is reflected from the cantilever surface on an optical charge-coupled device (CCD) sensor. The data generated by the measurements is subsequently compared to known deflection pattern of the specific antigen-antibody pair. Figure 1.2 shows all these steps and their interdependencies in a flowchart format.

The objective of the thesis is to investigate the intricate physical, chemical and biological phenomena taking place on the surface of the beam from both the qualitative and quantitative point of view. The mechanical structure is optimized to enhance the sensitivity of the sensor. The evaporation is studied through the variation of the contact angle during a biochemical reaction. The study of the centering of the cells is performed numerically, analytically and experimentally to insure the quality of the sample analysed on the sensor.
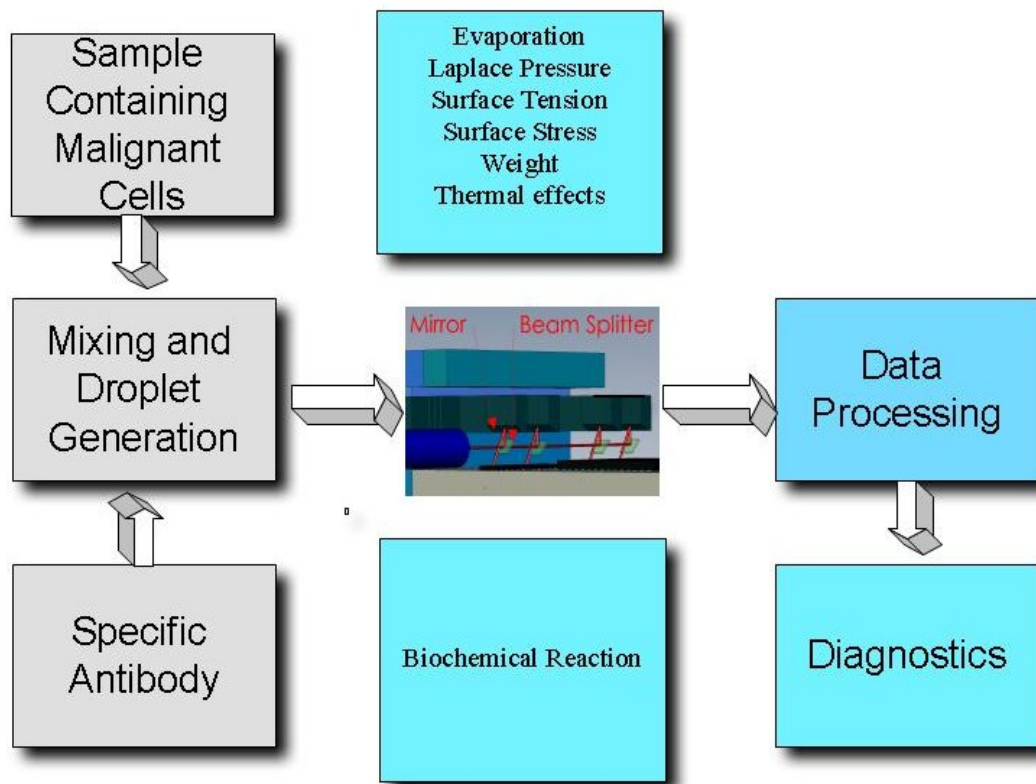
Figure 1.2 Block diagram representing the cantilever-based diagnostics system.

1.3 Originality of the work

There are already applications that detect the presence of oncological species from blood samples through the deflection of a cantilever based sensor, both in prototype stage or commercially available products [3-6]. The novelty of the method studied in this work consists in examining the manner in which the binding of the antibody to its matching antigen occurs. The projects described in the open literature have used a beam coated either with the antigen or the antibody [7-10]. The sensors are inserted in a fluid medium and the mechanical structures interacts with the complementary chemical component, i.e. if the beam is coated with the

5

antigen, it will interact with antibody from the sample or vice versa and the added mass is quantified [11-13].

In the author's knowledge the work of Stiharu and all [2] is the first reported application where the two components are mixed prior to the deposition of the cantilever beam. This approach takes advantage of the fact that the desired biochemical reaction is very slow from a kinetically point of view. Another gain consists in the fact that the deflection takes place in a gaseous environment, so it is not influenced by the viscosity of the surrounding medium, detail that conduce to an increase in the sensitivity of the measurement due to the absence of the drag forces. The drawback is the evaporation phenomena that can influence the signature through the mass loss of the droplet.

1.4   Thesis outline

Chapter 1 presents a short introduction in the subject associated with the focus of the present thesis, its objectives and the originality of the work.

Chapter 2 presents the literature review related to the lab-on-a-chip devices and biosensors. It illustrates the main research direction for the lab-on-a-chip devices available today both in the prototyping stage of or as final products. Their main principle of operation is briefly explained and their characteristics compared and analysed.

Chapter 3 is an introduction in the medical theory behind the cancer diagnostics techniques used in the BioMEMS systems, insisting on the aspects regarding the circulating tumor cells and

the antigen-antibody reactions. It presents both the standard methods followed by physicians when dealing with the disease and reviews the main literature concerning the circulating tumor cells and the antibody-antigen reaction.

Chapter 4 addresses the theoretical aspects regarding to the deflection of the cantilever-based sensor, and a parametric study of its most important feature is discussed. The behaviour of the cantilever beam under the action of various loads is investigated analytically and the results are validated numerically. A novel in-plane sensor is suggested. The process of topological optimization of the proposed in-plane structure is performed and its results discussed.

Chapter 5 presents all the representative tests performed during the experimental phase of the present work. The initial experiments together with their validation through direct measuring were performed and a novel method of assessment of the biochemical reactions is proposed. The evaporation process is also analysed in an attempt to identify and control its most important parameters.

Chapter 6 discusses a method of centering of the droplets containing the cancer cells. The variation of electric potential, electric field and dielectrophoretic force in the cross section of the channel are examined both numerically and analytically. An experiment on polyester beads is performed in order to validate the theoretical findings.

Chapter 7 presents the conclusions that arose from the present work and several direction of future studies than could be considered in order to improve the quality of the measurements and optimize the final proposed micro device.

Chapter 2:   Literature review

2.1 Introduction

Miniaturized lab-on-a-chips and micro Total Analysis Systems (μTAS) have already penetrated the area of molecular diagnostics and brought the promise of a shift of paradigm in the way that medical professions is expected to evolve and be conducted. Large varieties of application have been reported in the area of diagnosis and prognostics, regarding both qualitative and quantitative identification of targeted bio-entities [6, 14-17]. There have also been notable adaptation of these technologies in the areas of pharmacology (drug discovery [18, 19], synthesis , inoculation [20]) and patient follow-up[5, 9, 21, 22]. All the above applications converge towards the implementation of point of care devices for the everyday medical procedures performed in the generalist office, instruments that will open new avenues in terms of precision, personalization, prevention and treatment of specific diseases, with a much lower cost compared to the traditional laboratory methods [23].

The golden standard of identification of specific bio-molecules signalled by living cells is still the interaction between antibodies and their complementary antigens. In this work a number of cell lines of UVEAL melanoma, breast, prostate and colorectal cancer were closely observed by taking in consideration both the bio-chemical reactions and the mechanical interaction at micro-level generated by the mixture antibody-antigen. The generated phenomena are optically examined through their effect on the miniaturized polyvinylidene fluoride (PVDF) cantilever

beams using a focused laser beam and an optical position sensor. The signatures are obtained as time dependent for specific volumes and concentrations of the targeted cell lines and compared with the ones generated in the presence of their specific antibodies. A detection system for specific malignant species is experimentally validated and further steps in miniaturization proposed.

2.2 Biochips

Biological Micro Electro Mechanical Systems (BioMEMS) are part of an area of study where engineering and biology intersects. The main applications of such devices are in the manipulation, processing and analysis of biological and chemical specimens, diagnostics of medical conditions and in the discovery of new drugs and/or their methods of delivery. In order to attain the fore mentioned goals a vast array of materials, manufacturing technologies and biological protocols are employed. These approaches have already matured for the individual specific medical or engineering niches but they still present challenges when scaling down or on chip integration is attempted. Nevertheless, the emphasis placed on this kind of devices leads to larger integration of methods and tasks, and already commercial available products are emerging on the market [23, 24] .

The integration of the BioMEMS chip level generated the development of complex devices known as Lab-on-a-chip. Manz and his coworkers introduced in 1990 the term of Micro Total Analysis System (µTAS) but this concept can designate also units that target a multitude of chemical species, not always biological, for example the environmental detection of harmful

9

chemical compounds [25]. Micro Total Analysis System (µTAS) can address tasks concerning analysis (micro total analysis system), medical screening (point of care systems) and chemical synthesis (microreactions).

From the point of view of the diagnostics applications the advances in micro fabrication lead towards two distinct directions of development [26]. The first tendency is to multiply the amount of testing that can be done in parallel, allowing the identification of a large range of variables in the same time (multiplexing) [27]. The multi-array DNA diagnosis chips are just one examples of such procedures [11]. Array of cantilevers can determine the presence of the absence of several biomarkers, reducing considerably the diagnostics time and diminishing the errors associated with the specific tests [28]. The use of high density arrays of micro-reaction wells in drug discovery evolved from the standard 96-well format to micro-plates counting up to 20 000 wells [29]. With volumes starting at 125 microliters and ending at 50 nanoliters [30], the increasing number of testing points allows more assays to take place in concomitantly. For example, a 1536-well plate can assays up to 1500 different compounds [31].

From the point of view of the biological component tested, there are many applications involving microarrays such as protein or peptide microarrays, DNA and µRNA microarrays, tissue microarrays, cellular or transfection microarray and anti-bodies microarrays [32, 33]. The use of multiplexing technologies is very important in profiling entire genomes of different species or between individual [34]. However, the large amount of data generated by the multiplexed procedures requires a lot of calculating resources both from the hardware and software point of view [35].
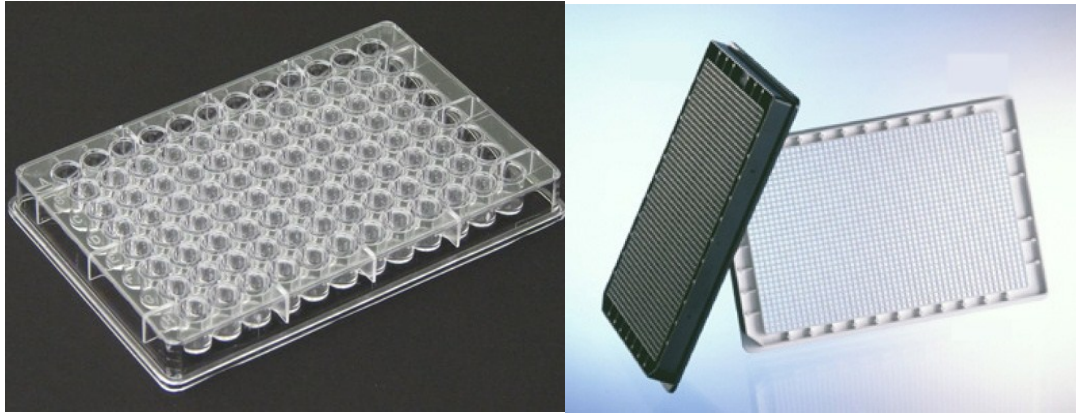
a)   b)

Figure 2.1 Miniaturization of microplates: a) standard 96-well plate, b) CELLSTAR® 1536W

Microplate, HiBase.

A second direction of development of the lab-on-a-chip devices looks into the miniaturization of specific laboratory tasks with the intent of the sample analysis optimization. This type of research brought to the development of micro and nano units on which, due to miniaturization, complete analysis can be performed with results similar or superior to the ones from the traditional laboratory facilities. Several examples of commercial available microchips with applications in the area of pathogen detection emerged on the market [23, 36, 37].

When referring to the term Lab-on-a-chip the following explanation is beneficial in clarifying its functions. Initially the trend was to integrate components that will improve the performance of the investigative instruments [25] but the advantages introduced by miniaturisation dictated the tendency to scale down the components [33]. Consequently, the lab-

on-a-chip systems started to integrate several miniaturized components able to perform a number of laboratory procedures such as [38]:

- acquisition of the sample, generally using microfluidics and electronics components,

- preparation of the sample: separation of undesired species, pre-concentration and dilution. It is made possible by using microfluidic mixers, electro kinetic and dielectrophoretic separation schemes,

- processing: mixing with specific reagents, and if necessary, a period of incubation for the initialisation of the biochemical reaction.
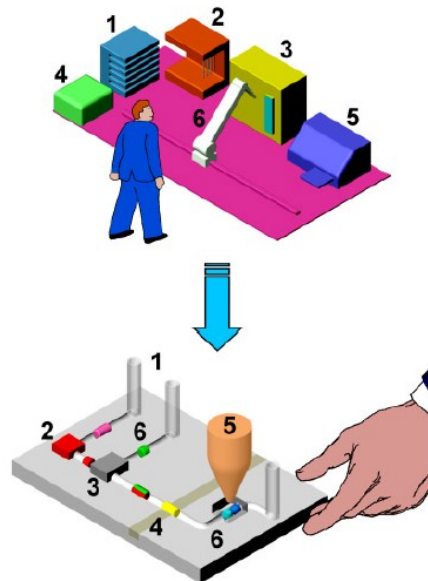
Figure 4. A comparison between the laboratory tasks performed at macro and micro scale: 1) acquisition of the sample, 2) preparation, 3) processing, 4)post-processing, 5)analysis, 6) interconnections. (Reproduced with permission from [38])

12

- post-processing preparation: may include separation of the undesired components/ precipitation products . microfluidics and separation schemes.

- analysis: recording and processing of the signal generated by the transducer

- interconnections:

The above tasks are implemented and integrated on the biochips by using micro devices and micro-constituents especially from the field of microfluidics. The most used components are represented by microfluidic channels, micromixers, pumps (peristaltic, electro osmotic or electrokinetics), microfluidic and dielectrophoretic separators, sensorics for monitoring and electronics for control and analysis [39, 40].

As illustrated in the definition, one has to understand the term of lab on a chip not as an attempt to design a complete miniaturized laboratory having all its components scaled down and the entire task solved under the microscope. Many of the core processes are still performed with the help of some laboratory instruments. The major highlight of a lab-on-a-chip device is the fact that the main part of the analysis is performed in a miniaturized manner with micro components [38]. This concept can be illustrated by the cancer detection techniques using a cantilever-type senor where the presence of the malignant species is signaled by the change in deflection or a shift in natural frequency [41]. The semiautomatic procedure presents a significant advantage compared with the approach that uses the skills of qualified laboratory personnel, a methodology that is both expensive and prone to inherent errors. However, in order to notice the change in the desired parameters of the micro-sensors, there are still laboratory components involved, doing

adjacent signal processing and analysis. In other words, the core components of the measuring technique are the one miniaturized but the miniaturization does not refer necessarily all its constituents.

The total error free miniaturization of laboratory diagnostics tasks is still a vision for the moment. However several commercial applications are able to minimize the erroneous verdicts and perform precise diagnosis with great sensitivity and sensibility. In the following paragraphs the main parameters of two such applications are presented for illustrative purposes.

The test device that was built by IBM and Coris Bio Concept is able to identify a number of 16 bacterial and viral infections and also a number of cancer markers [42, 43]. All the mentioned tasks require a sample of only seven picoliters. The core of this point of care (POC) device is a silicon based cantilever beam coated with a layer of polymers that helps with the attachment of a layer of proteins used to signal the presence of the condition. The external sensor of the beam displacement is a CCD type of optical sensors. To maintain the low cost of the device, the electronics is separated by the portion of the chip where the biochemical reaction takes place. This separation allows the use of different necessary reagents for the preparation of the sample prior the specific biochemical reaction and also to change the demanded biomarker capable to signal the presence of the specific condition.

In 2007 Nature published the work of a research group from the Massachusetts General Hospital Cancer Center that reported the detection of circulating tumor cells (CTCs) with a sensitivity of 99,1% [44]. What is more remarkable was the fact that from a group of healthy

volunteers, using the same chip no cancer cells were detected, i.e. the chip has a specificity of 100%.

2.2.1 Advantages and challenges

The miniaturized systems have many advantages from the point of view of integration, speed, safety, and the cost of the process. The main benefit of the lab on a chip technology is the reduced amount of reagents implied both from the sample and reagent point of view and also the scaling up of the number of samples included in the same amount of space. While the traditional plate miniaturization methodology requires additional instrumentation to monitor or to control the parameters of the sample, the lab-on-a-chip approach tries to integrate all these components into a much smaller, portable instrument.

The cost of the components involved is reduced by the use of the miniaturization techniques. These manufacturing methods matured in the last two decades so the generated products can be used with confidence. The low cost of materials used in these processes combined with the cost of batch silicon micromachining or plastic microfluidic structures and the well-known theory regarding the cantilever beams is considered to be the main reason of the extensive use of this type of sensing in the laboratory and industrial monitoring applications.

Another important advantage is in the evolution of parameters because of the miniaturization. The flow in the micro channels at this scale is laminar. This characteristic allows the use of the same microchannel for the transport of several layers of liquid in parallel. Because of the small dimensions both mixing and separation of suspensions can be done through

15

diffusion methods easily achievable at this small scale by controlling the length of the micro channel. A complete mixing can be achieved in less than one minute over a length of micro channel of 100 micrometers [45]. Separation of blood components from plasma can be achieved due to the laminar flow and difference in the particle density [18]. Low power consumption of these devices compared to their macro counterparts is also a non-negligible advantage.

While the miniaturization has many advantages, it brings also new challenges regarding the transport, mixing and evaporation of the small amounts of samples. New methods of manipulation involving electro wetting on dielectric techniques proved that manipulation of minutes volumes can be performed successfully [46].

Chapter 3:   Overview on cancer research

3.1 Introduction

Cancer research is one of the main areas in which the development of biosensors is focused, mainly because an early diagnostic of such illness improves drastically the patient's prognostics of survival. Another rationale is attributable to the fact that currently the oncologic diagnosis is totally dependent on the human operator, a factor that both raises the cost of the existing procedures and pays its toll through the inevitable errors involved [47]. In both developing and developed countries, cancer represents the second main cause of premature death [48], the first cause being associated with cardiovascular conditions. However, the costs involved in the oncological area are higher than the one associated with the heart diseases [4]. In 2010 the number of cancer related deaths in United States exceeded half of million people [49] . Excluding the unquantifiable human tragedy involved, the global cost of cancer associated with diagnosis, treatment, post-treatment follow-up and premature death was evaluated in 2008 at 895 billion USD, figure that represent about 1.5% of the Gross Domestic Product (GDP) of the entire world [48]. The promise of μTAS devices in being extremely precise, versatile and low cost (as a result of the batch fabrication technologies and the small quantities of analytes involved) brings a perspective where the micro fabricated devices combined with genomic, proteomic, epigenetic profiling, and predictive biomarkers will be accountable for a revolutionary breakthrough in the oncologic field [4, 5, 47, 50].The literature [47, 51-54] in oncology emphasizes the importance of early detection of the disease as the primordial factor in the survival of the patient and an important component of the quality of life following the treatment.

At the present time a patient most often discovers the existence of cancer either after the symptoms are already present, this is when tumors are already grown or accidentally, during the annual check-up or during other investigation with the purpose of discovering/monitoring of another medical condition. The classic approach in the cancer diagnosis involves invasive techniques where bio-samples collected from tumors - biopsies - are prepared using staining techniques and subsequently morphologically analyzed under the microscope [47]. Similar optical inspection methods are used when biological fluids are investigated in search for malignant markers. All these aforementioned procedures are expensive (involve high-cost analytes and highly qualified personnel), time consuming and, last but not least, prone to errors [51].

The normal sequence of clinic events, that most likely will take place in the detection and treatment sequence are: collection of tissue specimen, pathology followed by the treatment for the present stage of the disease (chemotherapy, radiation therapy and/or surgery) and an evaluation of the effects and side effects of the treatment (Figure 3.1) [47]. If the results do not have the accepted degree of success (the tumour is still present, a metastasis appears) another round of therapeutic measures will be performed. The degree of success is presently measured not by considering the total elimination of the disease but by the rate of survival within a period of five years following the initial treatment. The foreseen improved approach involves the existence of a pharmaco-genomic profile of the patient and inexpensive real-time, point-of-care, specialized monitoring of the desired biological parameters combined with a permanent adjustments of the treatment.

18
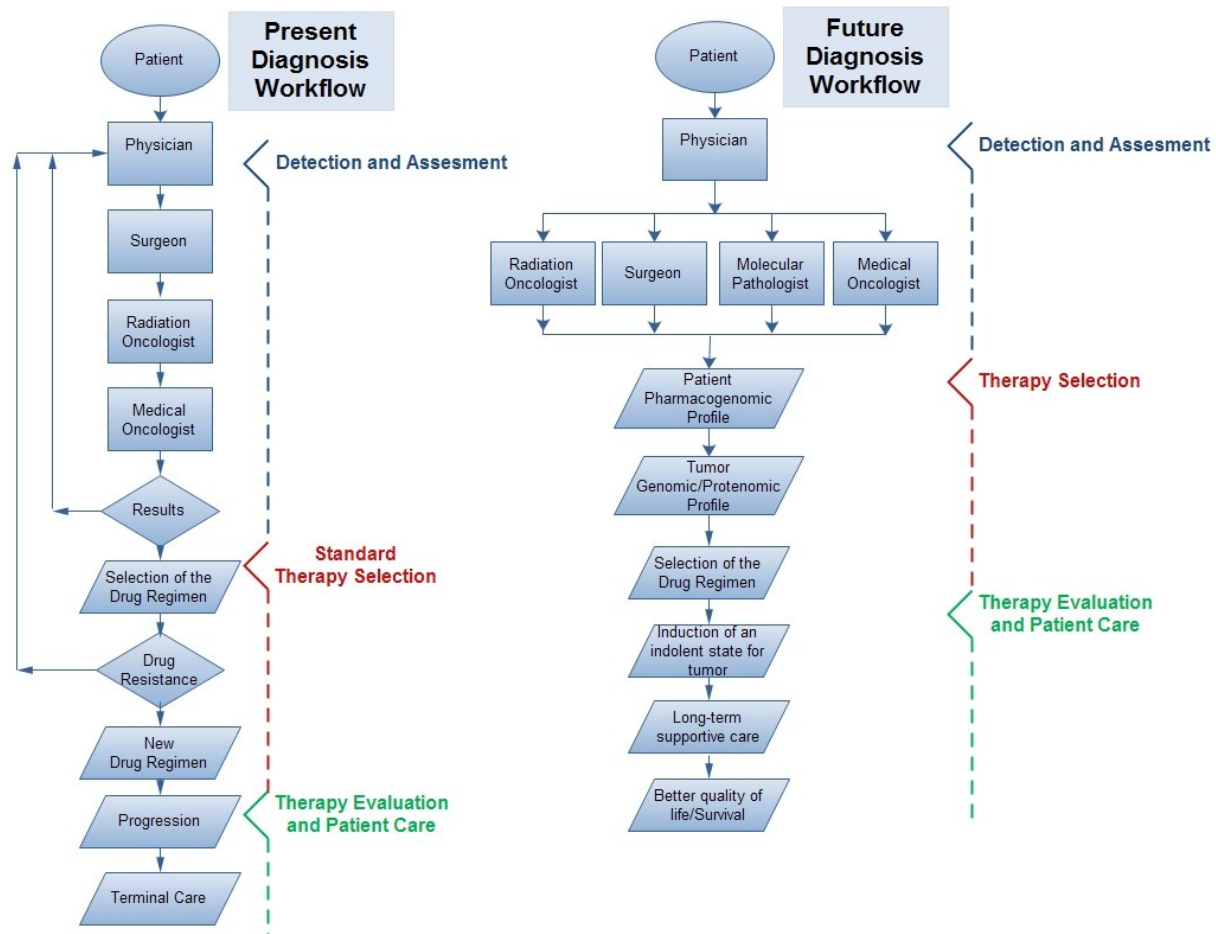
Figure 3.1 Present and future in the diagnostics, treatment and monitoring of the oncological patients. (adapted after [47])

3.2 Circulating tumor cells

In a nutshell cancer can be defined as "abnormal and uncontrolled cell growth due to an accumulation of specific genetic and epigenetic defects" provoked by environmentally and hereditary causes [53]. The cells start a growth that is no longer regulated by the normal mechanisms existent in a healthy organism and accumulating as tumor masses. The tumors are no longer regulated by homeostatic procedures that are present in healthy cells and become resistant to the defense mechanisms of the body. In time, these types of cells continue to migrate within the body and metastasize in other organs. In this stage the condition not more treatable [55].

Two types of mechanism are known as responsible for the formation of tumors[56] [57]:

-the activation of the oncogenes, caused by mutation in normal genes due to the external or internal factors, lead to abnormal growth levels and deregulation of cell growth. The most investigated oncogenes as cancer biomarkers are the growth factor receptors [53].

-the inactivation of the tumor suppressor genes (TSGs) is responsible for obstruction or even cancelation of the cell division mechanism. The most examined TSGs for cancer are retinoblastoma proteins (Rb) [58] that is an important regulator of cell division and BRCA1 which is a repair enzyme [59].

The circulating tumor cells originate in both primary and metastatic tumors but only a small subset of them have stem cells like characteristics and can initiate tumor nuclei in healthy tissues. The investigation of the number and the molecular composition of these type of cells is a research area that promises to generate "clinical information on prognosis, therapy choice, and effectiveness" of drugs, and generates attention from both development of cancer biomarker point of view and new drugs discovery [60].

From the BioMEMS point of view this field of study well established. United States Food and Drug Administration (FDA) approved CellSearch device as an instrument of monitoring the stage of metastatic advance for the patients affected by breast, prostate, lung and colorectal cancers. In this specific instrument the CTCs are separated from blood, fixed on magnetic beads and counted. The number of CTCs gives valuable information regarding the effectiveness of the treatment or the advance of the disease [61].

From the CellSearch point of view, a "true" CTC is defined as "a nucleated circulating cell larger than 4 um, expressing epithelial proteins EpCAM and cytokeratins 8, 18, and/or 19, while being negative for the leukocyte-specific antigen CD45". The number of such cells is, however, reduced in blood (hundreds per milliliter). On the other hand various investigations proved that CTCs are heterogeneous in composition for different types of cancers and not always obey the restrictive definition given above. There are variations from the molecular point of view even between different patients [53]. Nevertheless, the complete characterization of the CTCs can give important information to specialists regarding their source as the primary or metastatic lesion, the impact of the

therapeutic strategy involved and hold promises to replace the existing traumatizing cancer investigation methods involving the biopsy of the scrutinized organ [62].

3.3 Antigen-antibody biochemical reaction

In order to attempt an explanation of the intricate mechanism of the antigen-antibody biochemical reaction, one should define what an antigen and an antibody is. From a biochemical point of view, structurally the antigens are proteins, polysaccharides or even entire cells [63]. An antigen can be exogenous, endogenouos or an autoantigen and it is identified by a set of specialised cells (lymphocytes) as threatening for the organism and generates a response from the immune system. Exogenous refers to an antigen that was inoculated in the body from exterior, endogenous to an antigen created from normal cells that suffered mutations either because of bacterial and viral infection or because of a metabolic transformations, and autoantigen refers to proteins that are targeted by the immune system due to abnormalities in the immune tolerance of the organism. From a structural point of view the antigens are biological polymers, each of them possessing surface features called epitopes that are used potentially by antibodies to establish interactions.

Figure 3.2 illustrates schematically the components of an antibody unit. An antibody unit consists of four polypeptidic chains: two identical heavy chains (the five-segment component in Figure 3.2) that are linked together by at least one sulphidic bonds and two light chains (two-segment component) [64]. The illustrated dark components are variable in

sequence and represent the antigen-biding sites or the paratopes (corresponding to the antigen's epitope). The heavy chains number varies for each animal species and for humans have been detected a number of five, i.e. γ, α, δ, ε and μ. The light chains, two in number, λ and κ, are composed of two regions: one variable in sequence (the dark region) and one constant for each type of light chain (the light region). These five types of heavy chains ,together with the two types of light chains, will determine the major classes of antibodies (immunoglobulins). The IgG immunoglobulin, for example, consists of two light chains and two γ heavy chains. Minor differences in the constant regions of the γ components will generate a subsequent classification as IgG1, IgG2, IgG3 and IgG4[65]. These units further can form polymer-like structures with intricate shapes.

Structurally, an antibody is an Y-shaped protein and exists either as a soluble component secreted by plasma cells or attached on the surface of a B cell (a component of white blood cells).
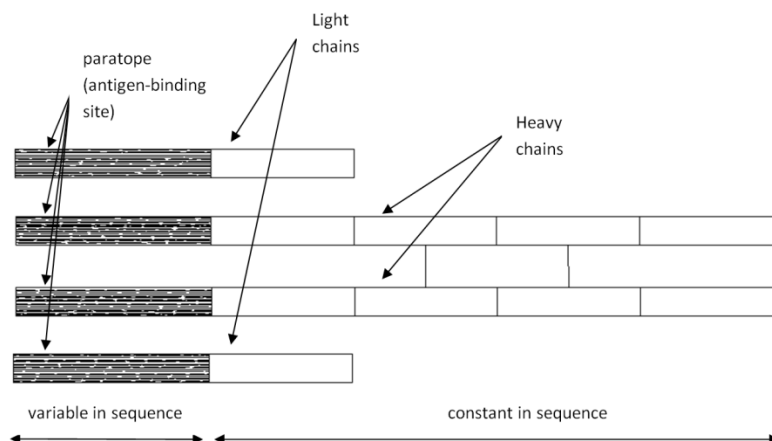
Figure 3.2 The antibody unit [65].

23

The general antigen-antibody reaction takes place when an antigen (Ag), through its epitope, attaches to an antibody (Ab) paratope, and it is symbolically represented by the following reversible chemical reaction:
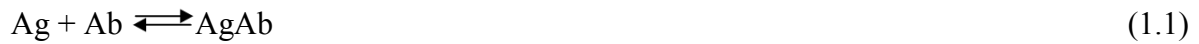
$$Ag + Ab \rightleftharpoons AgAb \qquad (1.1)$$

Further we can calculate from the law of mass action:

$$K = \frac{[AgAb]}{[Ag][Ab]} \qquad (1.2)$$

where K represents the equilibrium constant, [AgAb] is the concentration of the complex antigen-antibody, [Ag] and [Ab] are the concentration of the two reactants in mol per volume.

The reversibility of the reaction is generated by the nature of the weak non-covalent forces that are involved in the process. These forces are [65]:

a) weak electrostatic interactions;

b) van der Waals forces;

c) hydrophobic interactions;

d) hydrogen bondings.

In an antibody-antigen interaction, it is impossible to predict which of the aforementioned interaction will be dominant. However, the chemical configuration of the

24

components can greatly influence the condition of the reaction (for example, pH influences the electrostatic interactions, while the presence of a large number of hydrogen bondings will demand lower temperatures).

Antigens

Antibodies
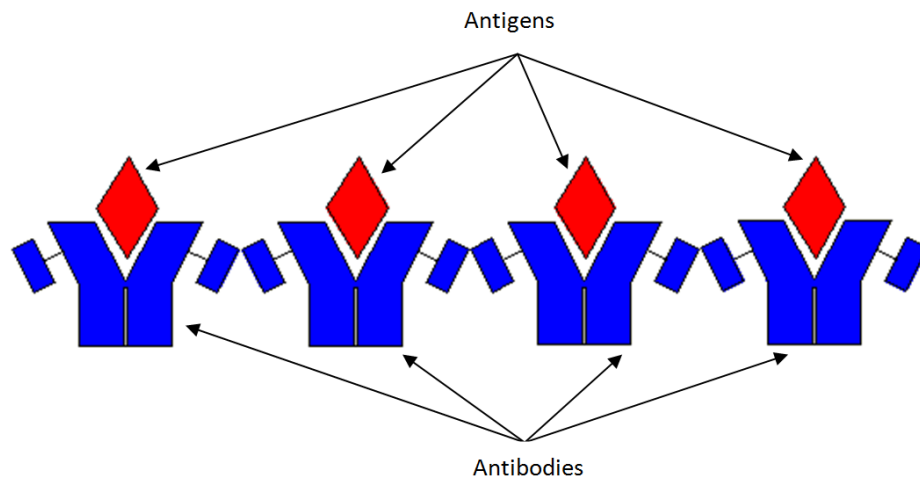
Figure 3.3 Antigen-antibody reaction.

3.4 Cancer diagnostics

The immunoassays and the immunosensors [3, 47, 54, 62, 66-69] use the selectivity of an antibody to specifically bind to the specific antigen from a mixture of complex biological substances (Figure 3.3).

The existing techniques, such as the enzyme-linked immunosorbent assay (ELISA) and all its variants (sandwiched, reverse, indirect, etc.). are very accurate in the detection of the targeted biomarkers [70]. Still, there are drawbacks coming from the fact that for low cytokine concentrations, the ELISA procedure cost increases exponentially and many

biological species cannot be detected under a specific threshold,(1:1 000 000), situation specific to the early stages of the disease [53]. Few such threshold values are given in Table 3-1.

Table 3-1 Normal level for basic tumour markers (adapted after [47])

Tumour marker	Thresholds
NSE	12.5 mg/l
PSA	4 µg/l
hCG	5 IU/l
CEA	3 µg/l
CA125	35 kU/l
CA50	14-~20 kU/l
CA242	20 kU/l

The antibody detection generally employs either a sandwich or a competitive method [67]. In a sandwich scheme, an initial antibody adheres to the surface of the sensor (generally a cantilever beam) and interacts with the targeted antigen. The interaction can be sensed in the presence of an additional labelled antibody. These labels can be different enzymes, specific radioisotopes or fluorescence generating molecules (fluorophores) [12]. In the case of the competitive method the same principle of immobilising the antibody is used, but compared to the previous technique the labelled antigen that will "compete" in occupying the paratopes of the immoglobulin. The advantages of the sandwich method are

its high specificity and sensitivity, due to the employment of two specific antibodies. However, because of the same reason, the incubation time increases compared with the competitive method [3].

Genomics and proteomics (PCR, RT-PCR, DNA sequencing, Western and Southern blotting) constitute an improvement of the previous diagnostics protocols and are able to generate multi-markers profiles with the additional advantage of eliminating the need for invasive procedures. The use of these methods improved the understanding of the genetic and environmental factors causing the malignant condition. The drawback comes from the increased cost derived from the complexity of the generated information and the demand of complex databases and equipment for its storage and manipulation.

The precise determination of the existence or the absence of a specific tumour and its stage of development requires, in general, the qualitative and quantitative determination not of a single but of several markers. In Table 3-2, few of the associated tumour markers of the most frequently encountered types of cancer are presented.

The most promising method is the protocol that uses protein based biomarkers instead of the genetic sequencing. Lab-on-a-chip systems were built with the idea to simplify the entire diagnostics procedure applying a real-time multi-marker testing device. A lab-on-a-chip device, or more general, a μTAS, consists of a number of subsystems in which the sample containing the markers is deposited on the sensing element(s) that usually contains a predetermined concentration and volume of antibodies, mono- or polyclonal.

27

Table 3-2 Cancer and tumour associated markers (adapted after [47])

Type of cancer	Marker
Prostate cancer	F-PSA, PSA, PAP
Breast cancer	CA15-3, CA125, CEA
Lung cancer	CEA, CA19-9, SCC, CYFRA21-1, NSE
Colorectal and pancreatic cancer	CEA, CA19-9, CA24-2
Gastric carcinoma	CA72-4, CEA, CA19-9
Epithelial ovarian tumours	CA125,AFP, hCG, CEA

Polyclonal antibodies are the most common molecular species used in the cancer detecting MEMS devices. [9, 21] Using molecular techniques, they can be precisely manufactured for all the investigated biological species, having the advantage of being more affordable from a financial point of view, compared to the monoclonal antibodies. On the other hand, a drawback of the polyclonal antibodies is the fact that they present a lower specificity compared to the monoclonal ones. The antigen-antibody pair is also used as an interactive unit capable of generating the deflection of a micro cantilever and, implicitly, causing a qualitative reaction in a biological sensor. [12]

The biochemical reaction antigen-antibody by itself has specific exo/endothermic effects and is affected by the antigen-antibody ratio, the physical form of the antigen (if the antigen has particulate characteristics or it is a soluble one), the avidity (the overall strength

of binding of an antigen with its multiple antigenic determinants to multiple antibodies sites) and the affinity of the reaction (the strength of the reaction between a single antigenic determinant and a single combining site of the antibody) [71].

There are also several physical factors influencing the quality of the reaction, such as the thermal optimum (when the mixture antigen-antibody will generate the strongest reaction, usually between 4-37° C depending on the reacting pair), the level of pH (generally between 5.5 and 8.5 with an optimum between 6.5-7.5), the ionic strength of the medium (the incubation period is between 30-60 minutes but when the ionic strength has been decreased the time is reduced to 5-15 minutes) and mixing efficiency [63, 64, 69].

From the chemical point of view a strong influence comes from the binding kinetics [72], the reaction order, the limitations in diffusion [73] and the highly non-specific bindings events [74].

The exact phenomena taking place on the surface of sensing element are the subject of some polemic discussion [7, 12, 75-77]. The complex equilibrium between the antigen containing solution and the adherent layer of antibody, the ions present, the conformational changes of the organic molecules plus the additional physical phenomena (temperature, pH, ionic strength and mixing efficiency) concur to make the factors and incidences responsible for these changes not fully elucidated [78-81]. Nonetheless, the effects of these complex interactions are extremely specific and their sensitivity and specificity were extensively used in tumor detection in laboratories in the last 40 years.

Chapter 4:   Cantilever beam sensing: theoretical aspects

Cantilever beams are the most common mechanical structures used as miniaturized sensing devices. In cancer detection they are mainly employed as transducers. Their deflection is sensed by events of mechanical, electrical, electrochemical, optical, calorimetrical and magnetic [7, 9, 82-88] nature. When the cantilever beams are used to detect a change in mass as a result of the binding between an antigen and its complementary antibody often an optical device is employed in order to record the generated effect. [2, 89-91]

The present work investigates the way in which the signature of the deflection of the cantilever sensor takes place due to the specific antigen-antibody biochemical reaction on its surface. This study builds upon the experience generated by previous experiments that investigated the signature of several peptides and enzymes [2, 85, 86]. The sensing of the cantilever deflection for several types of cancer using optical lever method is compared to the signature generated in the absence of the specific antigen and the physical phenomena responsible for the deflection pattern are segregated.

In the following subchapters, a review of the present state-of-art in the area of the cantilever biosensor, followed by an in-depth look at the various theoretical aspects regarding the deflection of the cantilever due to the various aspects related to the deposition of a droplet containing the complex antigen-antibody on its surface. It has to be mentioned

that, for the moment, not all these aspects are fully understood and future theoretical and experimental developments may change the way these complex phenomena are regarded.

4.1   State of the art in cantilever sensing

Micro cantilevers are widely used as sensors in the lab-on-a-chip applications due to their simplicity and versatility. They can operate submerged in fluids, in vacuum or in gases and their deflection can sense changes manifested either in the surrounding environment or on their surface [12]. In our work, the experimental setup was isolated by the air turbulence with lateral panels and the deflection of the aluminum-coated PVDF (Polyvinylidene Fluoride) cantilevers was sensed through optical means by recording the signal generated by the deflected laser beam on the surface of a CCD optical sensor.

Generally speaking, a cantilever beam "senses" the biological target by extracting it from a sample on its surface while it signals this capture by specific changes in its mechanical properties. In order to identify the biological component mainly two methods of sensing are applied: labeled sensing and label-free sensing. The first procedure uses biochemical and chemical species such as fluorescent markers, particular enzymes, nanoparticle and selected radioactive species to label the desired proteins from the specimen.[92, 93]. On the surface of the cantilever a class of receptors that have specific binding affinities for the labeled components are deposited.

This labeled detection scheme has strong signals for the detected molecules, in other words, the detection limit is improved, but also brings a set of challenges. The presence of

31

the unattached labels in the sample disturbs the recognition process. The label can affect the chemical activity of the protein and can decrease the detection lower limit. Moreover, the detection technique that uses labels increases the time and the cost of the process.

These disadvantages stimulated the search for systems capable to increase the limit of detection by using label-free schemes. In a label-free process the biological receptors are also fixed on the surface of the beam but the targeted molecules from the sample are not chemical altered as in the previous case. Using a micro- or nano- cantilever-type sensor the sensitivity of methods using labeling techniques can be reached and even overcome. Masses of attograms were being able to be detected and the sensitivity reached concentration of few nM [93].

The coating with a particular layer of biomolecules on the beam surface is the most important component of a biosensor, granting it the capability of sensing. These types of biosensors derive from the assay methods used in the biochemical laboratories. If an antibody is the detection target, the beam will be coated with its specific antigen or the other way around if a particular antigen is the object of the investigation. The layer on the surface of beam can be composed of specific oligonucleotides that chemically complement the investigated ones [94]. In the case of the nucleic acids, single-stranded DNA is coated on the beam and takes advantage of the hybridization process that will occur when its complementary strand of DNA is present in the investigated specimen [10, 93].

The layer of the receptor biomolecule should be anchored on the surface of the beam in such a way that should not be easily removed and, in the same time, allowing it to preserve its targeted function, i.e. the ability to interact with the aimed molecular species. The deposited film should be uniform and thin in order not alter too much the mechanical characteristics of the beam and to enable its regeneration [28]. The robustness in the presence of temperature changes or pH variation is another quality of an ideal layer.

These goals are achieved by improving the characteristics of the beam surface. For this purpose, the most used method is to evaporate or sputter noble metals on the substrate. Alkane chains molecules in conjunctions with thiols (Figure 4.1) generate well-arranged monolayers on a gold substrate [28, 95]. On silicon, the silanes molecules are used for the same purpose [28, 96]. For particular materials the functionalization is not necessary if the desired antibody adsorbs naturally on it, like in the case of SiO2 that covers naturally the surface of the Si fabricated cantilevers [93].

Other techniques of linking specific receptors on a substrate are polymer grafting [97] by spin coating or dip coating, and sol-gel method [98] when a porous surface is aimed. Inkjet micro-nozzles can also be used. For example, the Nano eNabler device[37], deposits small droplets on the entire area of the cantilever until the entire surface is covered .
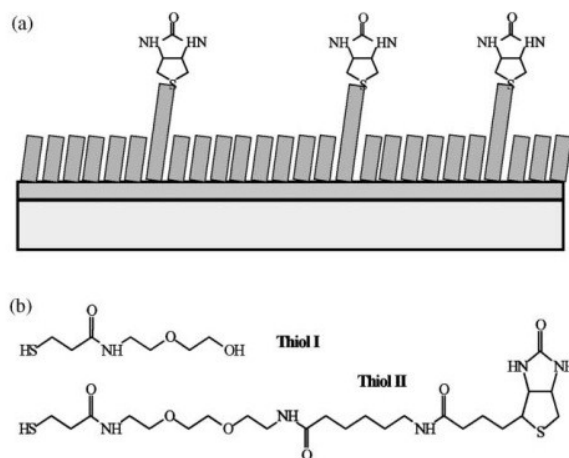
Figure 4.1 a) Si$_3$N$_4$ cantilever beam coated with a combination of two types of thiols (represented as rectangular fins perpendicular on the beam surface) and b) The chemical structures of the short molecule of Thiol I and the long molecule of Thiol II. (Reproduced with permission from[28])

The regular cantilever sensors are fabricated from semiconductors, polymers, piezoelectric materials and metal oxides in a large range of dimensions and shapes. The semiconductor materials generally used are silicons (both crystalline and poly). They take advantage of the microelectronic fabrication processes and can be batch manufactured, therefore lowering the fabrication cost. SU-8's lower modulus of elasticity qualifies it as a good candidate for static measurement methods of detection [7]. The small Young's modulus however makes it impractical for the dynamic methods of detection where stiff and small structures are desired for a better sensitivity. This reason generally disqualifies polymers as materials for dynamic detectors but makes them suitable for static quantification. Piezoelectric materials are used in the dynamic methods: the large

34

length/thickness values cantilevers are employed mostly when the load acts close to the free end of the cantilever, while the small values for surface stress biochemical sensing [99].

The bending of the cantilever beam is detected through several methods that use mainly optical and electrical principles. They can be implemented locally in the structure of the biosensor or, for prototyping, specialised measurement instruments available in the laboratories can be used.

The most used method of optical detection is the optical lever technique (Figure 4.2). In this scheme, the spot generated by a laser diode is reflected from the moving tip of the beam on the surface of a position sensitive photodetector (PSD), such as a CMOS/CCD sensor. The reflective properties of the beam are enhanced by coating a metal, usually gold, on its surface. The recorded signal is proportional with the slope of the beam and the distance between the reflective surface and the sensor. For calibration, the laser spot has to be precisely aligned and the dimensions between the composing elements completely characterized.
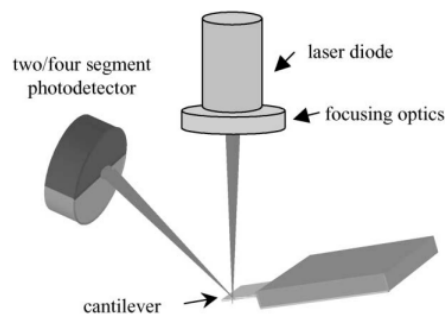
Figure 4.2 Optical lever method of detection. (Reproduced with permission from [28])

The main disadvantage of this method that makes it difficult to use in liquid environments is related to the analytes adhering on the surface of the beam a phenomenon that generates changes its optical properties.

The interferometry principle of detection uses the interference between a laser beam reflected by the surface of the cantilever and a reference spot. This method yields exact values for the deflection with sensitivities in the range of an angstrom [28] [100].

The electric detection schemes consider the beam as a plate of a locally built capacitor. Any change in the position of the beam modifies the capacitance and through signal processing, measures indirectly the displacement of the cantilever. This technique cannot be performed however in a conductive liquid environment.

The most promising measurement method lays in the use of piezoelectrical materials for cantilever beams type sensors. A cantilever built from piezoresistive materials changes its electrical conductivity when strained. The displacement is measured by quantifying this resistivity change through the use of a Wheatstone bridge. To avoid the limited use in liquids, passive resistors can be built within the structure of the sensor [101] .

4.1.1 Principles of operation

There are three main principle of operation that uses cantilever structures to identify the adsorption of the biomolecule of interest on the surface of the deposited receptor:

- dynamic methods use the shift in frequency or the modification of the force contact due to the absorbed molecules;

-calorimetric methods benefit from the deflection generated by the different coefficients of thermal expansion of a bimetallic beam that appears when the adsorption is accompanied by exothermic or endothermic processes;

-static methods take advantage of the variation of surface stress on the side of the beam where the biological species are linked.

In the following subchapters, the theory behind the dynamic, calorimetric and static methods will be shortly introduces to create a better understanding of the motivation behind the thesis work.

4.1.1.1 **Dynamic methods**

In this mode of operation, the beam is excited at a frequency that is close to its resonance one. For the geometry and the materials of the sensors used in this type of detection, the resonance frequency of the structure can be in the kilo or Megahertz range. By affecting the mechanical properties of the beam, the resonance frequency shifts, and this change can be related to the mass change by using the theory of mechanical vibrations.

Considering an Euler-Bernoulli cantilever, the governing equation of motion can be described as:

$$E^* I \frac{\partial^4 y(x,t)}{\partial x^4} + (\rho A + \chi) \frac{\partial^2 y(x,t)}{\partial t^2} + \xi \frac{\partial y(x,t)}{\partial t} = q(x,t) \tag{4-1}$$

where E^* represents the apparent Young's modulus ($E^* = \frac{E}{1-v^2}$), I - the second moment of area of the rectangular cantilever beam, ($I = \int_0^w \int_{-t/2}^{t/2} z^2 dz dy = \frac{1}{12} wh^3$), ρ - the specific mass density of the beam material, A - the cross-section area ($A=wt$, w is the width of the beam while h is its thickness, χ - mass of the cantilever beam, ξ - the damping coefficient and q is the driving load (in our case $q=0$).
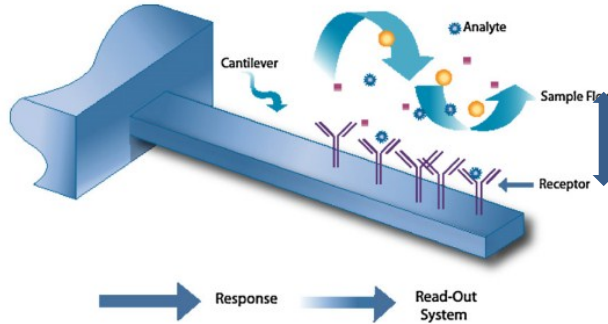
Figure 4.3. The resonant mode principle. (Reproduced with permission[102])

For a rectangular cantilever beam the spring constant can be calculated using the formula $K = \frac{Ewh^3}{4l_0^3}$ and its resonance frequency f is approximated by $f = \frac{1}{2\pi}\sqrt{\frac{K}{m^*}}$, where

38

$m*$ is the effective mass of the cantilever beam that is related to the mass of the beam m_b by the relation $m* = n \cdot m_b = m_i + 0.243m_b$ (n depends on the geometry of the beam and m_i represents the mass of the droplet before its impact with the beam). According to the above theory, a cantilever sensor with reduce spring constant but large aspect ratio is preferred when surface stress modifications are addressed while for mass detection a thick and short beam is more suitable.

Both the spring constant of the beam and the effective mass are altered during the chemical reaction that takes place in droplet containing the mixture of cells and their corresponding marker further complicating the attempt to generate an analytical model of the process. The concomitant evaporation reduces $m*$ with a quantity proportional to the evaporation rate α.

Another important parameter for the dynamic behaviour is the quality factor Q defined by the relation:

$$Q = \frac{\omega(\rho A + \chi)}{\xi} \tag{4-2}$$

Then resonance frequency of a cantilever beam ω can be expressed as a function of its resonance frequency in the undamped case ω_{n0} and its quality factor Q :

$$\omega_n = \omega_{n0} \left(1 + \frac{1}{4Q^2}\right)^{-\frac{1}{2}}$$

$$n = 0, 1, 2, ...$$

(4-3)

According to the equation (4-1) and (4-2), the viscosity of the surrounding environment has significant influence reducing both the resonance frequency and the quality factor. For this reason the cantilevers operating in a gaseous environment are more sensitive. In order to overcome this challenge and increase the sensitivity of the sensor an interesting solution is to manufacture a microfluidic channel inside the beam and to circulate the liquid sample through it[103] .

In terms of sensitivity, these type of sensors are reported to be able to detect quantities as small as the mass of a single cell ($\approx 10^{-15}$g) [28, 104]. For biological detection have applications ranging from single cell detection [105] to carcino-embryonic antigens [106] and viruses [107] . An important review of this mode of operation presenting a large range of application and their sensitivities is presented by Johnson et al [102].

4.1.1.2 Static deflection methods

Due to the difference between the surface stresses generated on the top and the bottom surfaces, a cantilever bends. The bending magnitude depends on the intensity of the chemical or physical alteration of the surfaces. If both the surfaces of the beam are exposed

to the same agents the difference in surface stress will be the same and the deflection will be zero. However if the one side of the beam is functionalized with a receptor layer a differential surface stress change will be produced.
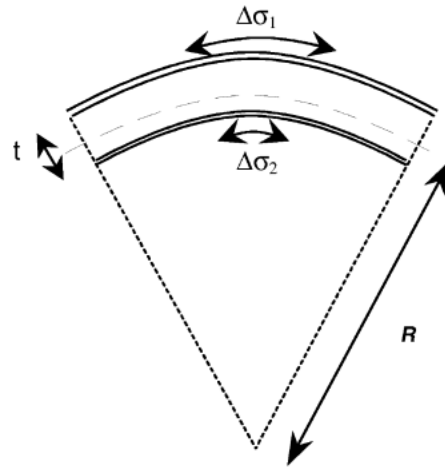
Figure 4.4 The principle of detecting surface stress variations.(Reproduced with permission from [28])

The bending of the cantilever beam due to surface stress is proportional to the difference between the value of surface stress $\Delta\sigma_1$ on the upper side of the cantilever and value of surface stress $\Delta\sigma_2$, acting on the lower face of the beam. When dealing with a tensile compressive surface stress the bending of the beam will be toward the stressed surface. According to Stoney's formula, the beam will bend generating a radius of curvature R that equals to:

$$\frac{1}{R} = 6\frac{1-\nu}{E_c t^2}\left(\Delta\sigma_1 - \Delta\sigma_2\right)$$
(4-4)

41

Here E_c represents the complex Young's modulus of elasticity of the beam, v is the Poisson's ratio and t denotes the thickness of the structure. The deflection Z due to this magnitude of surface stress in the case of a cantilever beam with rectangular cross-section and length L will be [108]:

$$Z \approx \frac{3L^2 (1-v)}{tE_c} \left(\Delta\sigma_1 - \Delta\sigma_2 \right)$$
(4-5)

For biochemical reaction the generated surface stress is in the range of only few mN/m [28]. For example when an antigen-antibody binding takes place on one side of the beam the magnitude of the surface stress is 1-6 mN/m [109]. A special attention should be paid to the pH of the sample and the concentration of the analyte because both these factors are found to influence the magnitude of the surface stress [82, 110]. The change in surface stress that occurs during an antigen-antibody reaction was studied by Wu et al [68]. There are numerous applications using the static deflection to detect DNA sequences [11], prostate specific antigen from purified blood[68] or changes in conformation of proteins [28, 111]. The sensitivity of the static sensing varies depending on the targeted property and varies from 100 pM [81] when DNA oligonucleotide are investigated to 10 pg/ml when the targeted biomolecules are proteins [8].

4.1.1.3 **Bimetallic deflection based detectors**

The thermal effects are very significant when the material of the beam consists of two or more layers of different materials. The bending of a bimetallic beam actuator or

42

thermostat under uniform heating was studied by many authors [112, 113] and the analytical model is well established. Different coefficients of expansions of the materials yield linear expansion with different ratios in the presence of temperature variations. This unequal deformation of different materials induces the bending of a cantilever beam, upwards (when the layer of material having a lower coefficient of expansion is on top) or downwards such as illustrated in the figure 4.4:
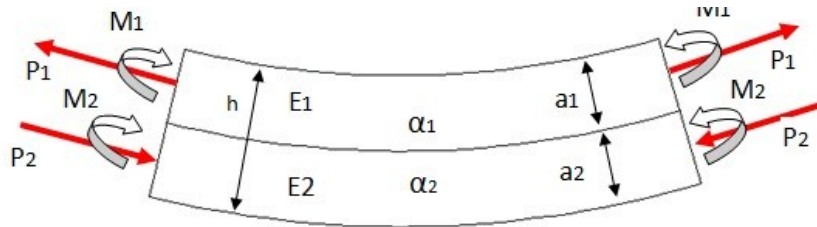
Figure 4.5 Bi-layered cantilever uniformly heated illustrating the thickness of each layer (a1, a2; a1+a2=h), the efforts involved (the axial loads P1, P2 and the bending moments M1,M2), the coefficients of thermal expansion for each layer(α1,α2) and the Young modulus of each material (E1,E2). (adapted after [44])

In the following calculations the bellow hypotheses are assumed:

-the differences between the coefficients of expansions of the two metallic layers remains constant during the heating phase;

-the width of the beam is very small compared to its length;

-there is no friction in the supports;

Let us consider a beam consisting of two strips of different metals welded, joined or bonded together. The coefficients of thermal expansion of the two materials are designated by α_1 and α_2. Uniformly heating the beam from the initial temperature T_i to the final temperature T_f the beam will deflect due a difference in the linear expansion of the metals. If the above layer has a larger coefficient of thermal expansion the beam will deflect downwards. The above layer undertakes a tensile force F_1 and a bending moment M_1. At the same time, the inferior layer experiences the compressive load F_2 and bending moment M_2.

Assuming that the cross-section of the beam, initially plane and perpendicular on its own axis, preserves its geometric properties during bending, and no external forces act on the beam we can consider that the following equalities take place [113]:

$$k = \frac{1}{r} = \frac{6w^2 E_1 E_2 h_1 h_2 (h_1 + h_2)(\alpha_2 - \alpha_1)(T_1 - T_0)}{(wE_1 h_1^2)^2 + (wE_2 h_2^2)^2 + 2w^2 E_1 E_2 h_1 h_2 (2h_1^2 + 3h_1 h_2 + 2h_2^2)} \tag{4-6}$$

where k is the inverse of the radius of curvature $k = \frac{1}{r}$.

The tip deflection of a bimetallic cantilever can be now calculated, for small deflections using the following formula [113, 114]:

$$d = \frac{kL^2}{2}$$
(4-7)

The tip deflection of a bimetallic cantilever can be now calculated, for small deflections using the following formula [113, 114]:

The above solution is valid only when heating is homogenous. If the heating occurs only locally, i.e. on the portion of the beam where the chemical reaction occurs this solution is not valid because the above equations lose their continuous characteristics. Moreover, an analytical solution may be difficult to achieve and numerical methods are the preferred choice for the evaluation of the deflection of the beam.

A bimetallic cantilever beam is sensitive to temperature changes of up to 10^{-5} K [115]. There are applications involving a bimorph structure varying from the monitoring of thermal gradients during chemical reaction in the presence of catalyst to photo-thermal spectroscopy with a time resolution lower than a millisecond [28].

4.2 Theoretical aspects

The quasi-static deflection of the cantilever beam, in contact with the droplet of liquid containing the precise mixture of cancer cells and their specific markers, is generated by intricate physical and biochemical phenomena. The most important biochemical and physical factors influencing the bending of the cantilever sensor are:

-   the biochemical reaction between the cancer cells and their markers,

45

- the evaporation of the droplet,

- the influence of the thermal gradient: due to the chemical reaction, the laser spot and the endothermic effects taking place due to evaporation,

- the change in surface stress,

- the normal and transversal components of the surface tension of the mixture,

- the pressure (Laplace) inside the droplet,

- the weight of the droplets and the own weight of the cantilever.

When the biochemical reaction initiates, some of the aforementioned specific parameters of the liquid mixture become time dependent and the evaporation of the liquid initiates. Consequently, the variation of the above quantities becomes even more evident. The evaporation is an endothermic process while the chemical reaction can be either endothermic or exothermic. From this point of view, the thermal effects are also of influencing significantly the accurate characterization of the deformation of the beam. A droplet with a diameter less than 40 μm has a weight is considered to be insignificant compared to the ones generated by the capillary phenomena i.e. a deflection of few nano meters and forces of nano Newtons. [116, 117]. The deflection of the microstructure owing to the weight of the containing drop of liquid, gains importance because, in this case, the droplet has a diameter larger than 200 μm.

In the following subchapters the influence on the deflection of the cantilever beam of each of the fore mentioned loads will be analysed.

4.2.1 **Dynamic loading**

When the free falling droplet of liquid reaches the surface of the cantilever beam, part of its mass is lost due to the splashing, and the remaining part spreads on the surface of the beam. Obeying the principle of minimal energy, the droplet assumes a spherical shape [118]. The energy generates a very short ($\tau_s = \frac{\rho V^{\frac{2}{3}}}{\eta} \approx 1ms$ for 8µl H_2O droplets[116]) damped vibration of the drop having the characteristic frequency $f_d = \sqrt{\gamma/\rho V} \approx 50kHz$ where V represents the volume of the droplet while ρ are the density, γ the surface tension and η the viscosity of the liquid mixture [116]. Immediately after the droplet is added on the surface of the beam, the transferred momentum generates a short vibration of the cantilever. The damping of the cantilever element generated by both internal (material and geometrical features) and external causes (due to the beam support and air drag) brings fast the mechanical structure at rest[118, 119] .

Even if the droplet vibration can generate in cantilever other mode shapes, its general influence on the signature of the malignant species is considered to be negligible due to the length of the biochemical reaction (≈1200 seconds). However, to avoid the aforementioned splashing, the droplets were deposited on the surface with a pipette. For the foreseen miniaturization of the device other methods of droplet detection are suggested such as capillary absorption or electro-wetting on dielectric droplet manipulators (EWOD) [46].

4.2.2 **Bending of the cantilever beam due to thermal effects**
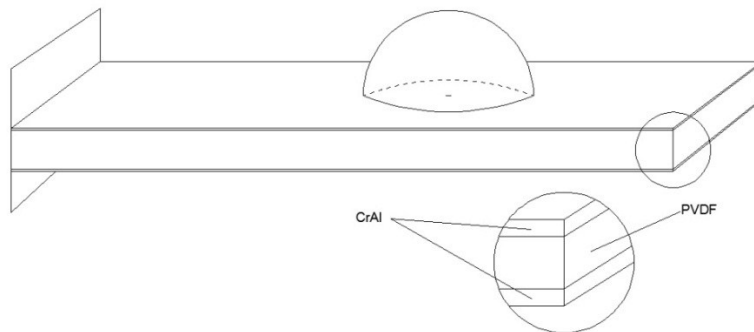
Figure 4.6 PVDF cantilever beam coated with Cr-Al-thin film alloy (max. 2% Cr).

The difference of temperature between the upper and lower layers is due to the following factors:

-biochemical reaction: the temperature can increase or decrease, depending of the exothermic or endothermic character of the chemical combination;

-evaporation: the process is endothermic, and it takes place during the entire interval of observation. According to Chandra et all [120] the cooling of the substrate is enhanced when the contact angle decreases. At the same time, a decrease of the contact angle from 90° to 20° produces an increase of 50% in their evaporation time. These observations have a direct application in the amplification of the extinguishing capabilities of water by dissolving in it a wetting agents that reduce its surface tension [120, 121].

-laser heating: the power of the laser excites locally the upper metallic layer of the beam increasing the temperature. However the load exerted during measurements where a laser diode is involved is small. As an example, a 7mW laser generates an equivalent load in the range of 1.6 10^{-11} N [122] so it will be considered negligible due to the comparatively reduced time of our experiments (10-20 minutes) and the presence of radiative dissipation (the laser diode used in SFM heats with 3-4 K per hour the small closed sample chamber in the absence of cooling) [123].

In our case, the cantilever beams are made of polyvinylidene difluoride (*PVDF)*, a thermoplastic fluorpolymer, and are coated on both sides with a layer of Cr-Al alloy with a thicknes of about 150 nanometers. The Cr-Al coating enhances the stiffness of the beam but its main purposes are to minimize the deflection due to the variation in the temperature and to improve the reflective properties of the surface.

The presence of a three-layer beam represents a factor of safety for bending only when both sides are heated uniformly. The evaporative cooling will have small effects on the bending of the beam because it determines variations of temperatures of less than a degree Kelvin[124].

The other aforementioned thermal effects will produce however, a temperature gradient that may cause variations in surface tension if the heat transfer process is considered from a transient point of view. A variable surface tension causes stress modification, buoyancy flow and weak Marangoni effects inside the droplet [124]. The

Marangoni effects generate flow inside a droplet and are responsible for the ring-like deposits created by the droplets of impure water. This flow (Figure 4.7) moves the fluid from the extremity of the droplet towards the center and the other way around and it is characterized by the Marangoni number *Ma*. Marangoni flow is significant in alkanes but is weak on pure or contaminated water [125].
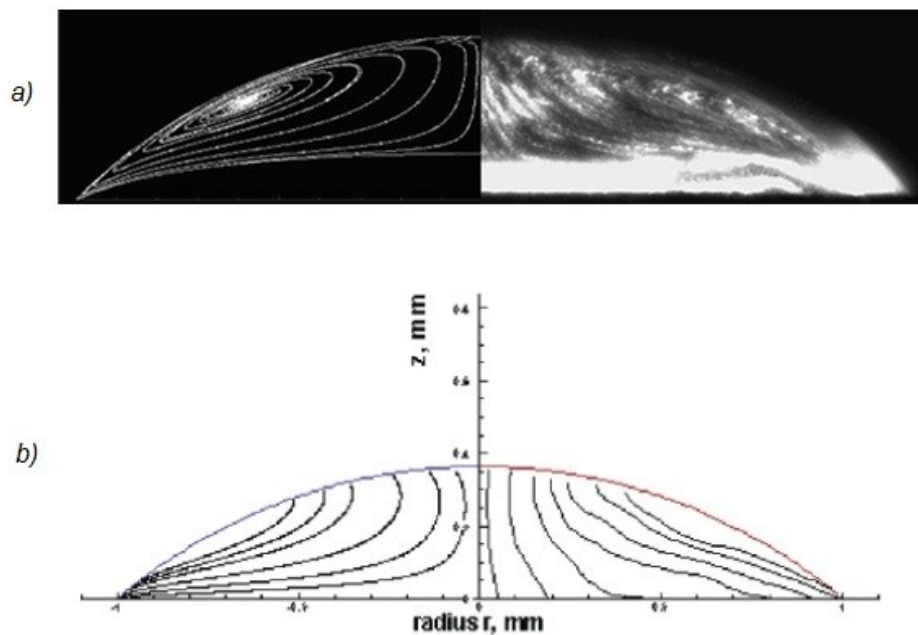
Figure 4.7. Marangoni effects in a a) drying octane droplet *Ma*= 45 800 and b) water *Ma*=8 (Reprinted with permission after [125]).

The above effects can influence both the biochemical reaction and its signature by altering the physical mixing of the two species of analytes, the diffusion effects and the thermal optimum of the reaction.

The characterization of a specific biochemical reaction lasts in average 600 seconds and the transient regime follows a very intricate pattern where heat is generated by the reaction whose kinetics in the case of the Ag-Ab is not completely understood, adsorbed because of the evaporation($T_{endo} \approx 0.56$ K) [124] and dissipated through radiative and conductive mechanisms. The effects of this pattern are non-quantifiable from a theoretical point of view but they are experimentally measurable through the recorded signature of the beam.

In order to evaluate the thermal effects due to the above factors a steady state analysis of the beam is performed using the Hyperworks commercial software. The geometry and the materials of the structure chosen for the simulation are similar to the parameters of the cantilever used in the experiments. A cantilever beam with the length of L = 2500 microns, the width of w = 800 microns and the thickness of 25 microns is considered in a three-layered configuration. The materials of the layers are aluminum and PVDF sandwiched in the sequence Al-PVDF-Al. The thickness of the aluminum layers is 150 nanometers while the PVDF layer is 24.7 microns. The droplet with a diameter of 0.6 mm is deposited at a distance of 1500 microns of the fixed end of the cantilever as shown in the Figure 4.8.

The numerical simulation is performed under hypothesis that the the gradient of temperature is constant (steady-state conditions). The ambient temperature is taken 20°C and the temperature under the droplet 30°C (a value that combines the effects of the exothermic reaction, laser heating and evaporation cooling between 5 and 10 ^{o}C larger than

the room temperature). The mesh of the model consists of 48 246 nodes and 40 711 elements.
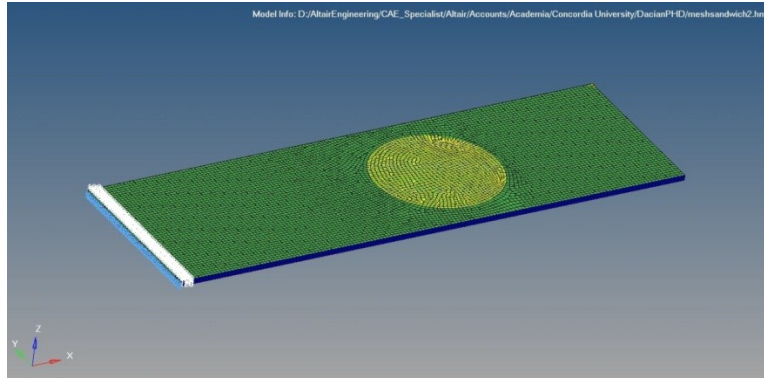
a) Droplet placement;
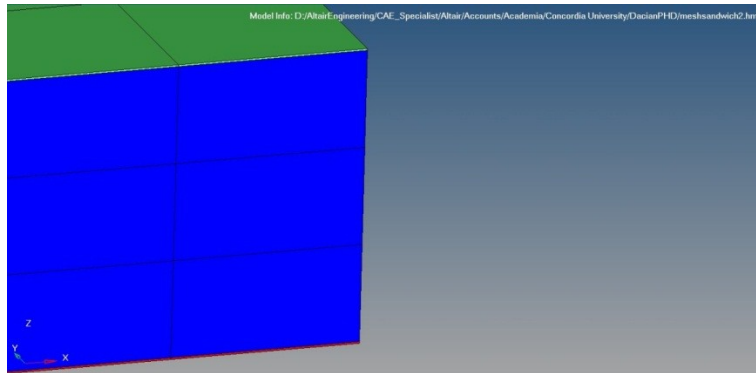
b) Configuration of the layers;

Figure 4.8 The model used in the simulation of the thermal effects on the displacement of the cantilever: a) droplet placement and b) configuration of the layers (in blue the PVDF layer and in green the Aluminum layer).

The deflection of the cantilever reaches a maximum of 13.8 nanometres at the free end of the beam as illustrated in the Figure 4.9. The numerical analysis confirms the fact that the temperature gradient is not responsible for the magnitude of the deflection of the beam recorded in the experiments (tenths of microns) and other factors should be taken in consideration i.e. the loads applied on the beam : Laplace pressure, surface tension, surface stress, line tension and the weight of the droplet.
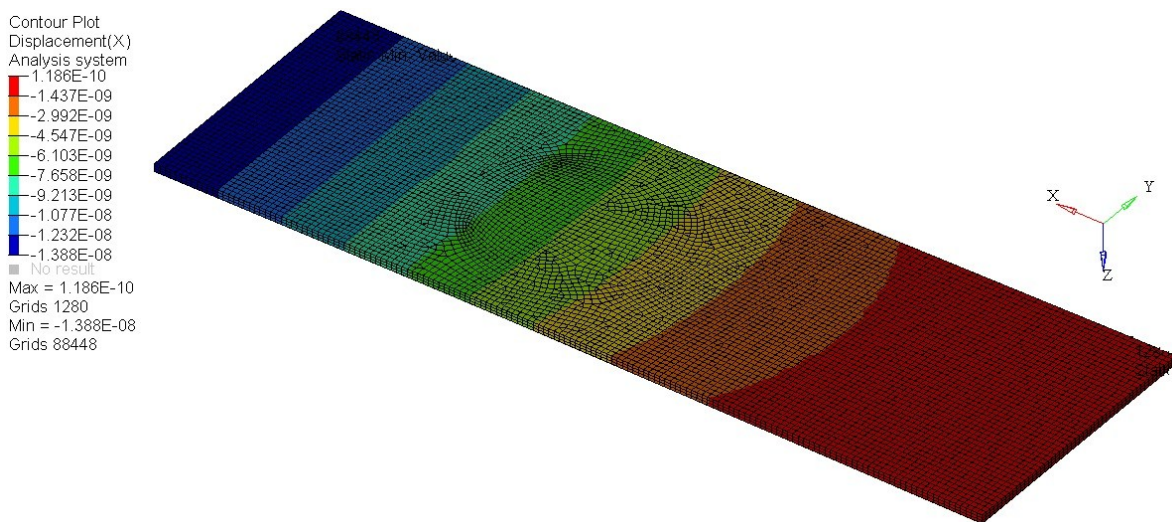
Figure 4.9 The displacement of the three-layered cantilever beam due to the thermal effects.

4.2.3 **Calculation of the stiffness of a multilayer cantilever beam**

Most of the cantilever beams used in biosensing applications have multilayered material. The main reason for this is the need to support layer for the surface

functionalization with the different bio-recognition agents mentioned above. These kinds of composite structures also provide, from the mechanical point of view, improved stiffness and thermal stability.

The purpose of this subchapter is to calculate the equivalent stiffness of the multilayered beam used for experiments in the present work. In a first step the position of the neutral axis is investigated. Subsequently the equivalent stiffness for both bending and axial loading is determined. The formula presented can be adapted for beams having n layers of different thicknesses.
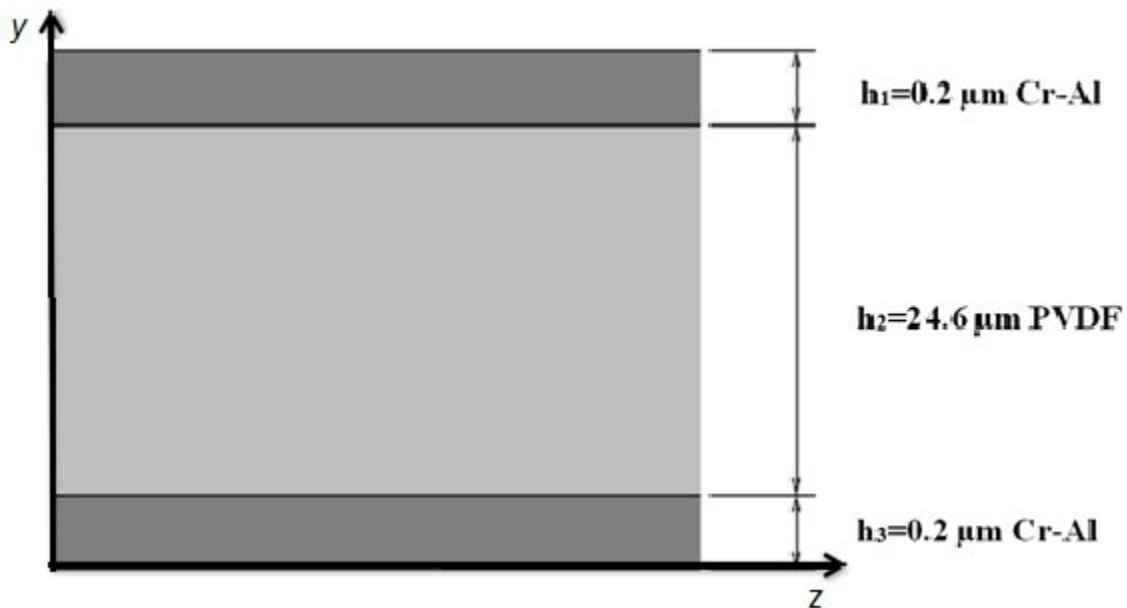
Figure 4.10 A sandwiched composite beam.

The main assumptions used in calculating the properties of a sandwiched beam are the following [126]:

- the strained beam will maintain the cross sections of each composing layer plane and perpendicular to the neutral axis of the beam;

-between the neighboring layers there is no slip;

-Poisson's ratio of the layers has the same value;

-the normal stresses and strains acting in the plane of each layer are negligible;

-the longitudinal strains are distributed linearly along the length of the beam;

4.2.3.1 **Position of the neutral axis for a symmetric three layered beam**

Given a sandwiched cantilever beam (Figure 4.10), having the thickness of the three layers h_1, h_2 respectively h_3, and the Young's modulus E_1, E_2, and E_3, it is required to calculate the position of the neutral axis, i.e. the layer of the beam that remains neither stressed nor compressed during the bending of the structure. According to Bareisis [126, 127] , for a beam having i layers of thickness h_i , and presenting symmetry about y axis, the position of the neutral axis can be calculated using the formula:

$$y_{Ax} = \frac{\sum_{i=1}^{n} B_i h_i + 2 \sum_{i=2}^{n} \left(B_i \sum_{j=1}^{i-1} h_j \right)}{2 \sum_{i=1}^{n} B_i} \tag{4-8}$$

Here $B_i = E_i A_i$ represents the axial stiffness of the layer i for tension and compression.

The total equivalent axial stiffness of the beam will be calculated by adding the individual components:

$$B = \sum_{i=1}^{n} B_i = \sum_{i=1}^{n} E_i A_i \tag{4-9}$$

In the above formula $A_i = wh_i$ represents the aria of the cross-section of each individual layer, w being the width of the cantilever.

For a three layered beam the position of the neutral axis is given by the following equation is:

$$y_{Ax} = \frac{\sum_{i=1}^{3} B_i h_i + 2 \sum_{i=2}^{3} \left(B_i \sum_{j=1}^{i-1} h_j \right)}{2 \sum_{i=1}^{3} B_i} = \frac{B_1 h_1 + B_2 h_2 + B_3 h_3 + 2 \left[B_2 h_1 + B_3 \left(h_1 + h_2 \right) \right]}{2 \left(B_1 + B_2 + B_3 \right)} \tag{4-10}$$

Substituting E_{CrAl} = 69 GPa and E_{PVDF}=3.1 MPa into the equation (4-10), as expected for a symmetrical beam , it is found that the neutral axes passes through the center of the cross section, at y_{Ax}=12.5 μm . The calculated equivalent axial stiffness is B=22.12 N.

4.2.3.2 Bending stiffness calculation for a three layered beam

The total bending stiffness of the beam D is calculated by adding the bending stiffness contribution of each layer [128]:

$$D = \sum_{i=1}^{n} E_i I_i \qquad\qquad (4\text{-}11)$$

Here I_i represents the second moment of inertia of the i-th layer and, for a rectangular cross section, has the following expression [126]:

$$I_i = \frac{w h_i^3}{12} + w h_i y_i^2 \qquad\qquad (4\text{-}12)$$

where y_i represents the distance between the middle of the i-th layer and the neutral axis y_n. Its expression is:

$$y_i^2 = y_n - \frac{h_i}{2} - \sum_{m=1}^{i-1} h_m \qquad\qquad (4\text{-}13)$$

Substituting the parameters of the beam used in our experiments in equations (4.15.) - (4.17) we find the equivalent stiffness D =3.42 •10^{-9} Nm.

4.2.3.3 **Normal stresses**

For each layer the following relation holds[126, 128]:

$$\sigma_i^2 = \frac{y}{\rho} E_i$$

(4-14)

Here $\frac{y}{\rho}$ represents the strain of the i-layer, y the distance to the neutral axis and E_i is the modulus of elasticity.

The normal stresses σ_{zi} in a multiple layers beam will be, at any point, given by the formula:

$$\sigma_{zi} = \frac{My}{D} E_{zi}$$

(4-15)

Calculating the normal stress of the $i+1$ layer and dividing by the normal stress of the i layer proves that the stress changes abruptly (Figure 4.11) from one layer to the other and this step change is proportional with the ratio between the Young's modulus of elasticity of neighboring layers:

$$\sigma_{zi+1} = \sigma_{zi} \frac{E_{zi+1}}{E_{zi}}$$

(4-16)

A temperature variation can modify theoretically the value of the modulus of elasticity in such a way that the situation presented in the Figure 4.1 c) can occur even in the case of $E_1 > E_2$ for materials of the layers with the Young modulus strongly varying with the temperature. If only one surface is heated or cooled, the normal stress distribution is

58

illustrated in d) to f). The extreme case g) requires a uniform temperature increase or decrease of the surrounding medium and it is noticeable the fact that the distribution of the normal stresses is identical to a beam manufactured from a single material.

These distributions of normal stresses are purely theoretical, however they can appear in cases when the Young's modulus of elasticity of the multilayered beam are close in magnitude and their variation with the temperature is unequal.
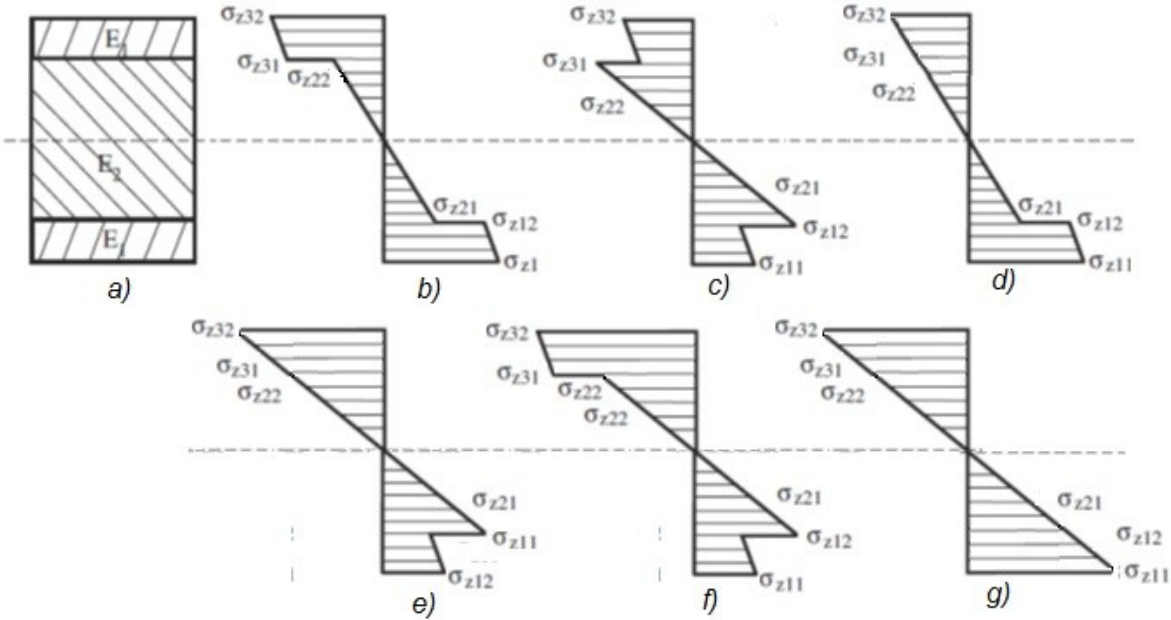
Figure 4.11 a)Cross-section view a three-layer beam, b) Normal stresses distribution for $E_1 > E_2$, c) Normal stresses distribution for $E_1 < E_2$, d)-g) The variation of normal stresses with the temperature.(adapted with permission after[126]).

59

The coordinate system considered for the following calculations has its origin at the fixed edge of the beam as shown in Figure 4.12. For the cantilever beam, all the mechanical constrains will be considered, in different way than the ideal state provided in the literature [116, 129, 130] where the reaction and the moment at the free end of the cantilever where neglected. However the following theoretical approach brings some simplifications in calculating the deflection of the beam mainly by considering the shape of the droplet as a hemisphere and neglecting loads that generate an insignificant deflection.
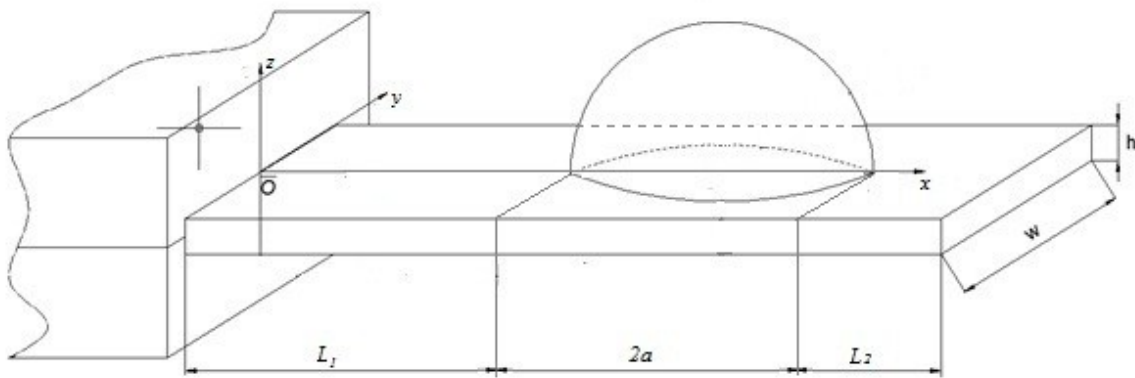
Figure 4.12 The cantilever beam with its coordinate system.

4.2.4 The effect of the surface stress

When crystal growth or surface reconstruction are the monitored parameters the value of surface stresses for macroscopic cantilever beams has an order of several N/m [28]. For biochemical reaction the generated surface stress has an order of magnitude from

only few mN/m [28, 131] to 0.9N/m in the case of formation of a layer of thiol-modified

DNA on a gold coated cantilever [131].

Stoney's formula is valid in the case of a layer of liquid that covers the entire

surface of the beam. If only the contact area is taken in consideration, the bending moment

at the position x (for $L_1 < x \le L_1 + 2a$) has the expression:

$$M_1 = -\Delta\sigma A_{CS} \frac{h}{2} = -\Delta\sigma h \frac{a^2}{4}[2\alpha - \sin(2\alpha)] \tag{4-17}$$

where:

$A_{CS} = \dfrac{a^2}{2}[2\alpha - \sin(2\alpha)]$ represents the area of the circular segment for $L_1 < x \le L_1 + 2a$;

$\alpha = \arccos\left(\dfrac{L_1 + a - x}{2}\right)$ and h represents the total thickness of the beam.

The minus sign appears in the right-hand side because the surface stress decreases

in liquid phase [28] . For this reason the moment induced by the surface stress is tensile and

the beam bends away from the droplet [116] .

The deflection equation of the cantilever beam is:

$$M(x) = EI\frac{d^2 y_1}{dx^2} = D\frac{d^2 y_1}{dx^2} \tag{4-18}$$

The above calculated moment is compensated by the elastic response of the beam, so the following equation holds for $L_1 < x \le L_1 + 2a$:

$$D\frac{d^2 y_1}{dx^2} = -\Delta\sigma h \frac{a^2}{4}\left[2\alpha - \sin(2\alpha)\right] \qquad (4\text{-}19)$$

An analytical solution for the slope and the deflection of the cantilever beam is given by Bonaccurso et all [116]. Bonaccurso shows that in the case of a water droplet evaporating on a cantilever beam the deflection due to the surface stress is insignificant compared to the case when the entire surface of the beam is immersed in the liquid [132]. The existing theoretical models dealing with the action of the surface stress do not take in consideration the presence of different biochemical species in the droplet nor the variation the surface stress during the biochemical reaction. For the duration of the biochemical reaction the chemical components interact with each other. The existing chemical bonds are broken and new intermolecular bonds are created. This is not a simple phenomenon of adsorption, like the one exploited in the most of the BIOMEMS applications presented in the subchapter 4.1.1. The value of $\Delta\sigma$ can become highly variable and cannot be direct measured but evaluated through the response of the structure they are acting on.

The main forces responsible for the deflection of the cantilever beam are the surface tension (mainly its vertical component), the Laplace pressure and the weight of the droplet [133]. The bending moment determined by these components is calculated in the following

subchapters and, using the principle of superposition, their effect is evaluated and compared to the results obtained numerically. The surface stress does not have a major influence of the total deflection however it influences the value of the slope of the tip of the beam [116].

4.2.5 Deflection of the beam due to the surface tension
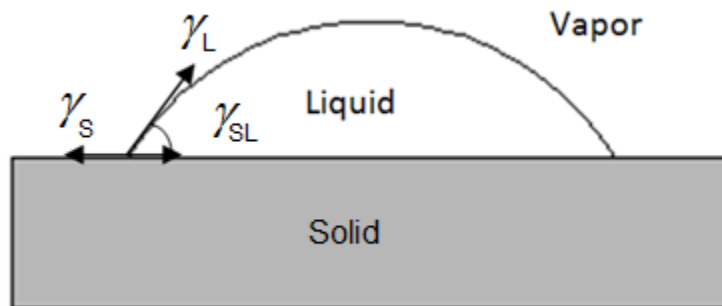
Figure 4.13 Surface tension components.

When the drop of mixture is in equilibrium (no evaporation) on a "perfectly smooth, homogenous and rigid solid surface"[134, 135] of a rigid cantilever beam and the weight of the droplet is neglected, Young's equations holds (γ_L , γ_S and γ_{SL} are the surface tensions that act on the three phase contact line, θ being the contact angle) [136]:

$$\gamma_S - \gamma_{SL} = \gamma_L \cos \Theta \tag{4-20}$$

Surface tension γ_L (will be denoted from now on γ for simplification) acting at liquid-gas contact line has two components: one vertical γ_v and one horizontal γ_h.

Consequently these two components will generate two different loads: a vertical upward force $\gamma_v = \gamma \sin\Theta$ and an horizontal force $\gamma_h = \gamma \cos\Theta$ that can be tensile or compressive, depending on the magnitude of contact angle of the droplet placed on the surface. In other words, the direction of the in plane force depends on the hydrophilic or hydrophobic properties of the surface. In our case the contact angle θ is smaller than 90° so we will consider a compressing effect of the horizontal surface tension.

4.2.5.1 **The effect of the horizontal component of the surface tension**

The horizontal component of the surface tension is parallel with the surface of the beam. On the upper layer its effect can be compressive if the contact angle is acute (hydrophilic surface) or tensile for an obtuse contact angle (hydrophobic surface). The moment generated by this component of the surface tension will be then positive for a contact angle smaller than $\theta<90^o$ and negative for $\theta>90^o$.

The horizontal component of the surface tension is expressed as :

$$\gamma_v = \gamma \cos\Theta \tag{4-21}$$

Similar to the effect of the surface stress, the moment M_2 generated by the horizontal component of the surface tension at the position x (for $L_1 < x \leq L_1 + 2a$) has the expression:

$$M_2 = \gamma_H A_{CS} \frac{h}{2} = \gamma h \frac{a^2}{4} \cos\theta [2\alpha - \sin(2\alpha)] \qquad (4\text{-}22)$$

In this case the moment is compressive due to the orientation of the horizontal component of the surface stress. Its effect increases when the contact angle reaches small values due to the presence of $\cos\theta$ in its expression. The analytical expression is similar to the relation of the surface stress if - $\Delta\sigma$ is replaced by $\gamma\cos\theta$.

Surface stress $\Delta\sigma$ and surface tension γ are related by the Suttleworth formula [28, 137]:

$$\Delta\sigma = \gamma + \frac{\partial\gamma}{\partial\varepsilon} \qquad (4\text{-}23)$$

where ε is the elastic surface strain.

For liquids the second term becomes zero [28]. As a result of this observation the influence of the surface stress can be considered canceled by the horizontal component of the surface tension due to axial symmetry [116]. However, when dealing with suspensions of proteins like antibodies and antigens, complex mechanisms can be involved related to the interactions between the proteins, changes in the hydrophobic or hydrophilic character of the substrate, building of precipitates and liquid ion adsorption. These factors can influence both surface stress and surface tension magnitudes but their mechanisms and the magnitude of their effect is still not elucidated. As mentioned before, these phenomena cannot be assessed theoretically but the experiments prove the presence of these non-

elucidated phenomena and their atypical influence on the slope of the beam in a clockwise or counter clockwise direction.

4.2.5.2 **The effect of the vertical component of the surface tension**

The surface tension acts as a force per unit length along the contact line between the sessile droplet. The magnitude of its vertical component γ_v is given by the equation:

$$\gamma_v = \gamma \sin\theta \tag{4-24}$$
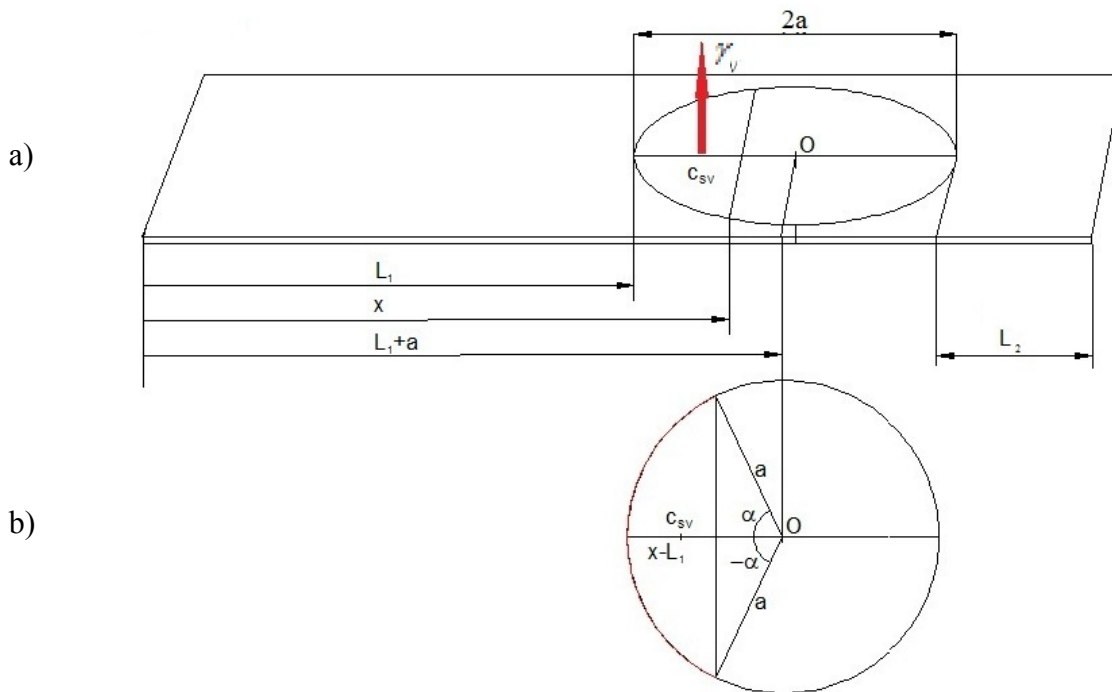
Figure 4.14 The effect of the vertical component of the surface tension: a) Three dimensional view of the droplet on the cantilever. b) Top respectively side view of the droplet on the cantilever.

Three regions of interest can be identified along the length of the beam: the first region where $x \leq L_1$, the second one where $L_1 < x \leq L_1 + 2a$ and the third, where $x \leq L_1 + 2a + L_2$.

Along the first region, the bending moment is due to only the presence of the reactive force and moment generated in the console by the action of the vertical component of the surface tension.
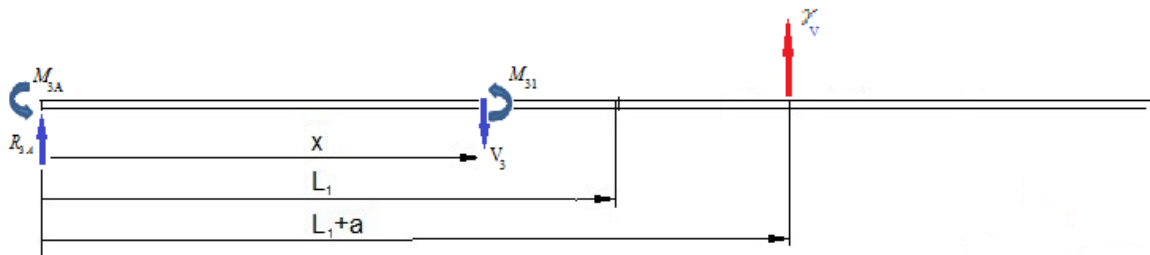
Figure 4.15 The effect of the vertical component of the surface tension: reactions and bending moment in region 1.

The reaction and the moment at the fixed end are:

$$R_{3A} = -2\pi a \gamma_V$$
$$M_{3A} = -(L_1 + a)2\pi a \gamma_V$$

(4-25)

The bending moment generated when $x \leq L_1$ is :

$$M_{31} = -(L_1 + a)2\pi a \gamma_V + R_{3A} x$$

(4-26)

Along the second region $L_1 < x \leq L_1 + 2a$ illustrated in Figure 4.14 b) we have the moment:

$$M_{32} = -M_{3A} + R_{3A}x - L_{ARC}\gamma_V \left(L_1 + a - c_{SV}\right)$$ (4-27)

where:

$L_{ARC} = 2a\alpha$ and $\alpha = \arccos\left(\dfrac{L_1 + a - x}{2}\right)$ is given in radians;

$c_{SV} = L_1 + a - \dfrac{a\sin\alpha}{\alpha}$ is the position of the center of the arc with respect to the origin of the coordinate system.

Along the third region $L_1 + 2a \leq x < L_1 + 2a + L_2$, as illustrated in Figure 4.14 a) the moment $M_{33} = 0$.

The analytical expression of the total slope and total deflection for both vertical component of the surface tension and Laplace pressure are found in literature [138]. For a contact angle varying between $90^o - 0^o$ (theoretically, for an initial hemispherical droplet), the vertical component of the surface tension can decrease from 0.069 N/m to 0 N/m (for RPMI). For a hemispherical droplet with the radius of 0.3 mm the length of circumference of the droplet is 1.88 mm and the resultant of the vertical component of the surface tension can reach a value as high as $0.129 \cdot 10^{-3}$ N.

4.2.6 **Laplace pressure effects**

In a study published in 1805, Laplace identified the existence of a significant pressure in the interior of the bubbles and droplets [136]. This important discovery allows

explaining capillary adhesion and the large forces present in the capillary bridges. The Laplace pressure is larger if the diameter decreases, as illustrated in Table 4.1. For a sessile droplet on the surface of a cantilever beam, the influence of this pressure generated on the substrate will be evaluated as follows.

Table 4-1 Laplace pressure for RPMI -1640.

Radius of the RPMI droplet (m)	Pressure (N/m^2)	Pressure (atm)
500 x 10^{-6}	288	284 x 10^{-5}
10 x 10^{-6}	1.44 x 10^4	142 x 10^{-3}
1x10^{-6}	14.4 x 10^4	1.42
0.3x10^{-6}	48 x 10^4	4.73

In the performed experiments the droplets has a diameter of about one millimeter. If we consider the surface tension of the RPMI-1640 solution to be very close to the surface tension of the water (γ=69 mN/m) [139] the value of the Laplace pressure inside the droplet reaches 458 Pa. We consider that adding the cells as a suspension in the RPMI medium does not modify significantly the value of its surface tension, however further investigations should be considered from this point of view.

The Laplace pressure can be calculated with the following relation:

$$P = \frac{2\gamma}{a} \tag{4-28}$$

where a is the radius of the curvature of the droplet [116, 124, 133].

The Young- Laplace pressure determines a moment onto the cantilever beam that will generate the bending of the structure. The magnitude of this bending will be evaluated in the following paragraphs. The same regions of interest as in the case of the vertical component of the surface tension are chosen. These regions are illustrated in the Figure 4.16 and Figure 4.17.
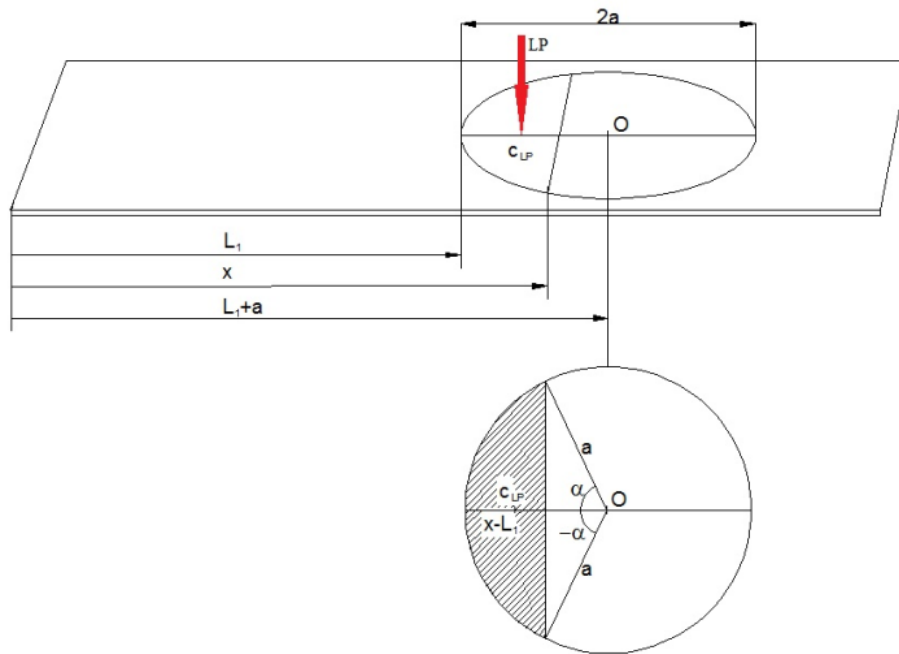
Figure 4.16 The effect of the Laplace pressure a) Three dimensional view of the droplet on the cantilever. b) Top view of the droplet on the cantilever.
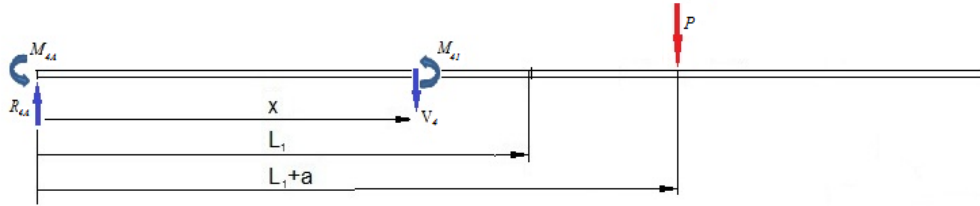
Figure 4.17 The effect of the Laplace pressure: reactions and bending moment in the first region of interest.

Along the first region, the bending moment is due to only the presence of the reactive force and moment generated in the console by the action of the Laplace pressure. The reaction and the moment at the fixed end are in this case Figure 4.17:

$$R_{4A} = \pi a^2 P$$
$$M_{4A} = (L_1 + a)\pi a^2 P$$

(4-29)

The bending moment for the domain $x \leq L_1$ is :

$$M_{41} = -M_{4A} + R_{4A}x = -(L_1 + a)2\pi a \gamma_V + \pi a^2 P x$$

(4-30)

Along the second region $L_1 < x \leq L_1 + 2a$ illustrated in Figure 4.14 b) the bending moment is:

$$M_{42} = -M_{4A} + R_{4A}x - A_{SC}P(L_1 + a - c_{LP})$$

(4-31)

where:

$$A_{CS} = \frac{a^2}{2}(2\alpha - \sin 2\alpha) \text{ and } \alpha = \arccos\left(\frac{L_1 + a - x}{2}\right) \text{ in radians;}$$

$$c_{LP} = L_1 + a - \frac{4a\sin^3\alpha}{3(2\alpha - \sin 2\alpha)}$$ is the position of the center of the area with respect to the

origin of the coordinate system.

Along the third region of interest with $L_1 + 2a \leq x < L_1 + 2a + L_2$, the moment $M_{43} = 0$.

4.2.7 **Deflection of the beam owing to the action of gravitation**

The cantilever beam deflects under the action of the gravity under the influence of the weight of the droplet that can no longer be ignored at the macroscopic scale and due to the weight of the structure itself. As follows each of these actions will be detailed.

4.2.7.1 **The weight of the droplet**

In literature when dealing AFM cantilevers the droplet weight is not taken in consideration because the effect of a droplet with a diameter inferior to 40 μm is represented by a deflection of only few nanometres [140]. However the present experiments deal with a droplet having a diameter of 800 μm so the influence of the weight is taken in consideration. At these dimensions the droplet can still be represented by a hemisphere, since the diameter of the liquid droplet is three times smaller than the capillary length of water ($\kappa^{-1} = (\gamma/\rho g)^{\frac{1}{2}} = 2.7$ mm).

In order to determine the deflection of the beam the same regions of the cantilever are studied as in the previous cases. These intervals of interest together with the loads on the cantilever are shown in Figure 4.18 and Figure 4.19.
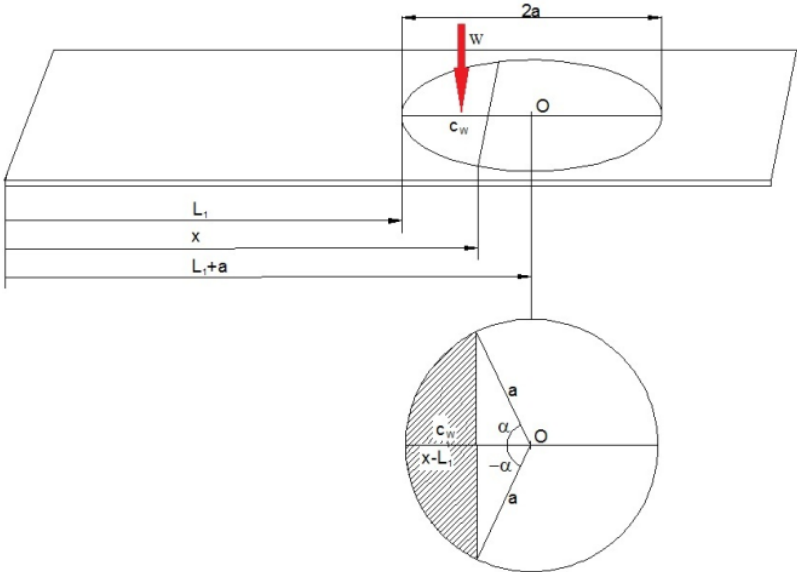
Figure 4.18 The effect of the weight of the droplet: a) Three dimensional view of the droplet on the cantilever. b) Top view of the droplet on the cantilever.
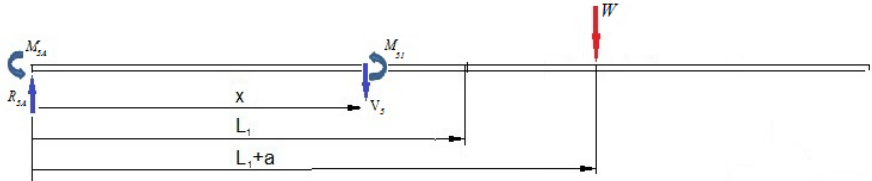
Figure 4.19 The effect of the weight of the droplet: reactions and bending moment in the first region of interest.

73

Along the first region, the bending moment is due to only the presence of the reactive force and moment generated in the console by the action of the weight of the droplet. The reaction and the moment at the fixed end are in this case:

$$R_{5A} = \frac{4\pi a^3}{6} \rho g$$
$$M_{5A} = (L_1 + a) \frac{4\pi a^3}{6} \rho g$$

(4-32)

where ρ represents the density of the antigen-antibody mixture and g is the standard gravity.

The bending moment for the domain $x \leq L_1$ is :

$$M_{51} = -M_{5A} + R_{5A}x = -(L_1 + a)\frac{4\pi a^3}{6} \rho g + \frac{4\pi a^3}{6} \rho g x$$

(4-33)

Taking in consideration the second region $L_1 < x \leq L_1 + 2a$, the bending moment is:

$$M_{52} = -M_{5A} + R_{5A}x - V_{CS}\rho g (L_1 + a - c_{CS})$$

(4-34)

where:

$$V_{CS} = \frac{1}{6}\pi (x - L_1)^2 (3a^2 + L_1 - x);$$

$$c_{CS} = L_1 + a - \frac{3(2a + L_1 - x)^2}{4(3a + L_1 - x)}$$ is the position of the centroid of the volume of the cap of a

sphere with respect to the origin of the coordinate system.

Along the third region of interest with $L_1 + 2a \leq x < L_1 + 2a + L_2$ again the moment is

$M_{53} = 0$. The above expressions are similar to the ones of the Laplace pressure if we

replace the product PA by G [138].

4.2.7.2 **The deflection due to the own weight of the cantilever**

The own weight of the cantilever beam generally is taken in consideration in the case of large macroscopic structures and it is a well-documented and well-studied phenomenon. The structure of buildings or the designs of machines are just two of the evident domains that consider the phenomenon.

In the case in discussion, if we maintain the assumptions of linear elasticity, inextensible cross section and negligible Poisson's ratio and shear deformation, the following observations can be made:

-the uniformly distributed force representing the gravity will be denoted with $q = \rho g t w$, where ρ represents the density of the beam, g the gravitational acceleration, t, the thickness of the cantilever beam and w its width;
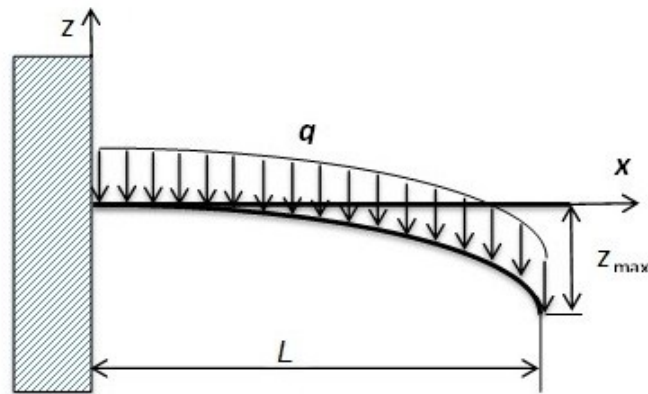
Figure 4.20 Cantilever beam deflection under the influence of its own weight.

- the deflection function at any section in terms of x will be [141] :

$$z = \frac{qx^2}{24D}\left(x^2 + 6L^2 - 4Lx\right)$$

(4-35)

According to formula (4-35) the maximum deflection z_{max} will be:

$$z_{max} = \frac{qL^4}{8D}$$

(4-36)

For the beam used in the presented experiments, having the aforementioned parameters the maximum deflection due to its own weight will be around 0.5 microns which is almost seven times lower than the deflection due to the weight of the droplet.. Compared to the deflection caused by the other parameters, the influence own weight of the beam will be neglected in the following calculations.
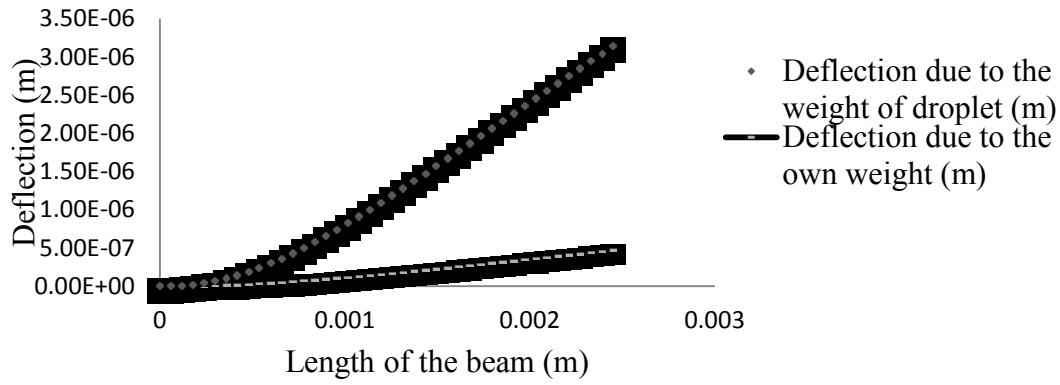
Figure 4.21 Deflection of the beam due to the gravity

In order to find the displacement over the entire span of the beam due to vertical component of the surface tension, Laplace pressure and the weight of the droplet the method of superposition is used.

The moments corresponding to the three regions of interest are the following:

- on the first interval, when $x \leq L_1$ the total moment is according to the equations (4-26), (4-30) and (4-33):

$$
\begin{aligned}
M_1 &= -M_{3A} + R_{3A}x - M_{4A} + R_{4A}x - M_{5A} + R_{5A}x = \\
&= x\left(R_{3A} + R_{4A} + R_{5A}\right) - \left(M_{3A} + M_{4A} + M_{5A}\right)
\end{aligned}
\tag{4-37}
$$

-on the second interval, with $L_1 < x \le L_1 + 2a$, according to the equations (4-27), (4-31) and (4-34) the total bending moment is:

$$
\begin{aligned}
M_2 &= -M_{3A} + R_{3A}x - L_{ARC}\gamma_V\left(L_1 + a - c_{SV}\right) - \\
&\quad -M_{4A} + R_{4A}x - A_{SC}P\left(L_1 + a - c_{LP}\right) - \\
&\quad -M_{5A} + R_{5A}x - V_{CS}\rho g\left(L_1 + a - c_{CS}\right) \\
&= x\left(R_{3A} + R_{4A} + R_{5A}\right) - \left(M_{3A} + M_{4A} + M_{5A}\right) - \\
&\quad -L_{ARC}\gamma_V\left(L_1 + a - c_{SV}\right) - A_{SC}P\left(L_1 + a - c_{LP}\right) - \\
&\quad -V_{CS}\rho g\left(L_1 + a - c_{CS}\right)
\end{aligned}
\tag{4-38}
$$

-on the second interval the bending moment is $M_3 = 0$

According to the equation (4-18), the following equation holds:

$$
\begin{aligned}
M_3(x) &= D\frac{d^2 z_3}{dx^2} \\
M_4(x) &= D\frac{d^2 z_4}{dx^2} \\
M_5(x) &= D\frac{d^2 z_5}{dx^2}
\end{aligned}
\tag{4-39}
$$

Integrating the equation (4-39) twice and using the boundary conditions (4-40) the deflection function is determined and it is illustrated in :

$$x = 0 \qquad z_3 = 0 \qquad \frac{dz_3}{dx} = 0$$

$$x = L_1 \qquad z_3 = z_4 \qquad \frac{dz_3}{dx} = \frac{dz_4}{dx} \qquad\qquad (4\text{-}40)$$

$$x = L_1 + 2a \quad z_4 = z_5 \qquad \frac{dz_4}{dx} = \frac{dz_5}{dx}$$
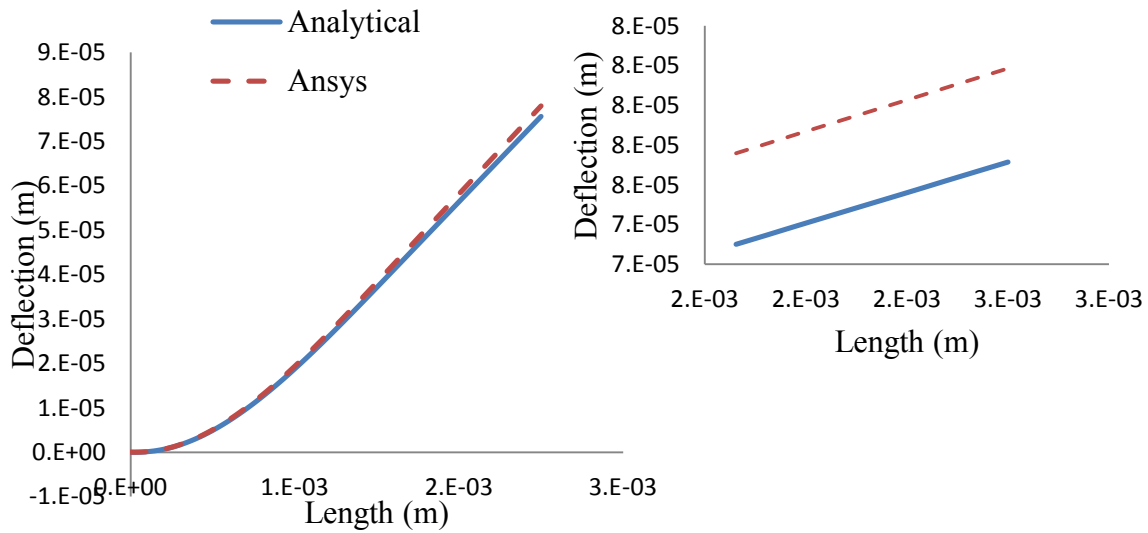
Figure 4.22 Deflection of the beam: analytical and numerical solution.

Ansys numerical simulation of a beam with parameters similar to those used for the study of the influence of the thermal effects on the displacement of the beam (same materials, three layers Al-PVDF-Al, L=2.5 mm, w=0.8 mm, h=25 μm, the droplet positioned at the distance of 1.5 mm from the fixed end of the beam and having a diameter of d=0.6 mm) shows a difference between of deflection calculated analytically and the one generated numerically (Figure 4.22) of only 12 microns (75.6 microns determined analytically versus 77.9 microns numerically with a ratio of 0.97).
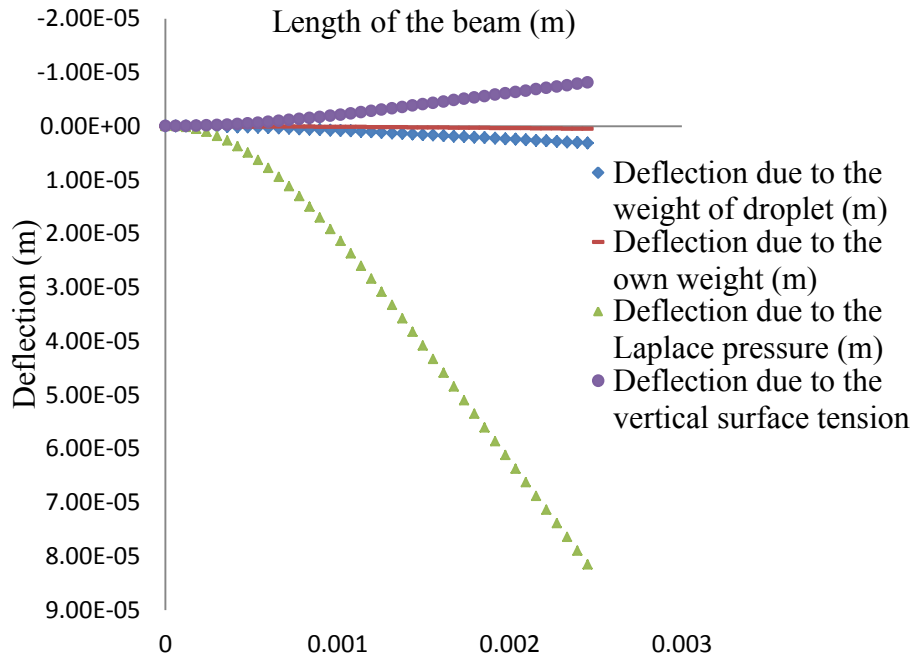
Figure 4.23 Deflection of the beam under the action of a droplet: major loads.

An evaluation of all the major loads acting on the cantilever beam confirm the fact that the Laplace pressure and the vertical component of the surface tension are the most important vertical acting forces that manifest due to the presence of a droplet on a cantilever beam. They hold the main responsibility for the total deflection of the beam. To illustrate this fact, a sandwiched beam consisting of three layers Al-PVDF-Al beam with the dimensions L x w x t of 2.5 x 0.8 x 0.025 mm is studied and a droplet having a radius of 0.3 mm is placed at 1.5 mm from the fixed end. A contact angle of 86$^\text{o}$ was considered in the calculation of the fore mentioned components. The results illustrated in Figure 4.23 show that, from the all vertical acting forces, the Laplace pressure has the major influence on the downward deflection of the beam (82 microns), while the upward deflection is

80

determined by the vertical component of the surface tension (10 microns). The action of the gravity is the lowest (3.5 microns)..

The numerical analysis of the combined effects of the surface stress and the horizontal component of the surface tension is performed using the same beam parameters, but this time the load consists of the difference $\Delta\sigma - \gamma\cos\theta = 0.05$ N/m (considered large) at a contact angle of 86° (Figure 4.24). The result obtained (z=40 nm) confirms the hypothesis that the deflection due to these combined effects is much smaller compared to the other effects presented above and can be neglected in the calculation of the total deflection. However, the same figures demonstrate their influence on the slope of the tip of the beam.

From the numerical simulation it is noticeable the fact that the beam presents a concave upward deflection in the x-y plane. The upward deflection of the tip of the beam explains the upward part of the signature of the biochemical reaction that was found experimentally. This displacement is very important to be determined analytically but unfortunately, the variation of the surface stress is not quantifiable theoretically and the variation of the horizontal component of the surface tension decreases in a known manner when pure liquids evaporate, but during a biochemical reaction can also vary in an unknown fashion. This behaviour can influence also drastically the optical detection system especially in the case of the miniaturisation. If the laser spot is not positioned precisely on the axis of symmetry of the cantilever, the beam twists and the reflected beam might not reach the detection sensor.

81
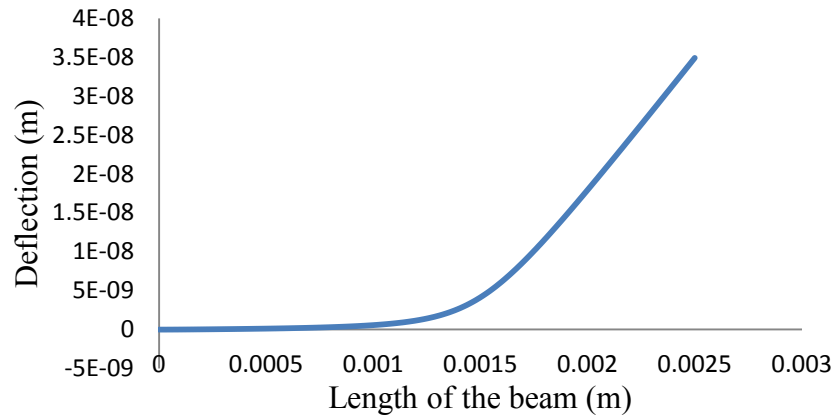
Figure 4.24 a) Deflection on z direction;
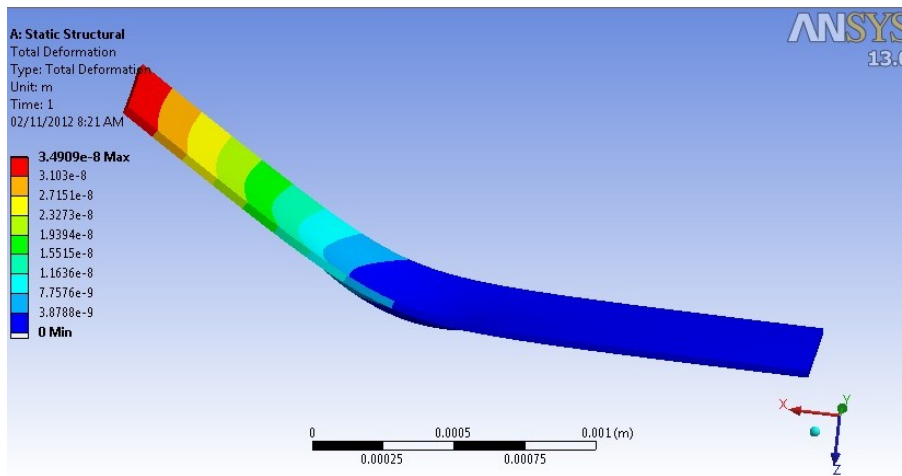
b) Total deformation;

Figure 4.24 Displacement of the beam due to the combined influences of the horizontal component of the surface tension and the surface stress of 0.05 N/m: a) the deflection on z direction, b) total deformation.

Another observation can be made regarding the steep upward deflection of the beam in the x-z plane of the tip of the cantilever. The sudden increase or decrease of the

combined surface stress and horizontal surface tension can amplify this behaviour and deflect the laser spot upward even if the beam presents a descending trend.

4.3 Parametric study

In order to optimize the sensitivity of the cantilever sensor a parametric study on the geometrical characteristics of the beam is performed and the optimal position of the droplet on the surface of the beam is analysed.

In the first numerical investigation, the length of the cantilever beam is varied as follows: 2500 mm, 3000 mm, 3500 mm, 4000 mm. 5000 mm, 6000 mm and 7000 mm, while all the other parameters of the beam are maintained constant (a sandwiched beam consisting of three layers Al-PVDF-Al beam with the dimensions w x t of 2.5 x 0.8 x 0.025 mm is considered and a droplet having a radius of 0.3 mm placed at 1 mm from the free end).

As expected, the increase in the length of the beam gives a larger deflection at the free end of the cantilever. A length of 7 mm or more will lead to an unwanted phenomenon, i.e. the beam is no longer in the domain of small deflection. The domain of large deflections is prone to instabilities and should be avoidable especially in a sensor where a robust behaviour is needed.
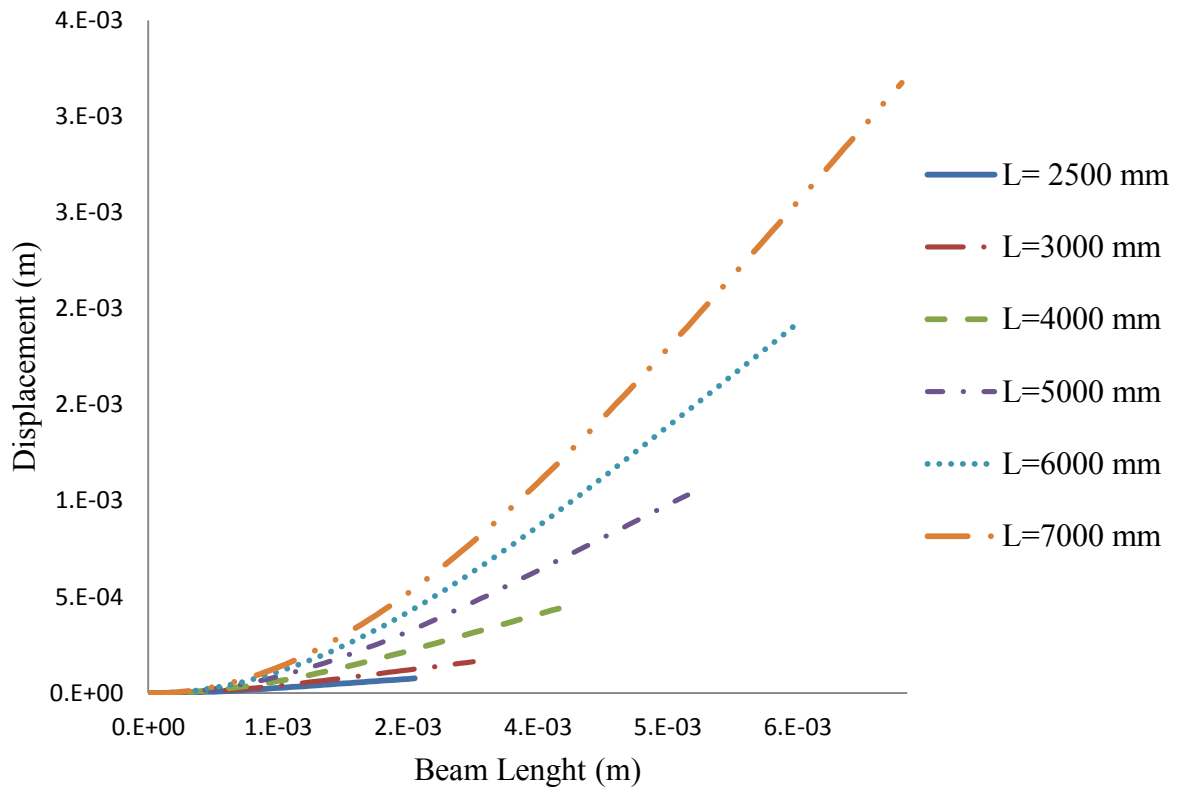
Figure 4.25 Parametric study of the length of the beam.

The second parametric study investigates the variation of the ratio length over thickness (L/t) for the beam. As expected, a decrease in thickness will generate a larger deflection of the cantilever beam. Maintaining a length of 2500 microns, the large deflection domain is reached for a thickness of 1.5 microns (when the ratio L/t = 1667).
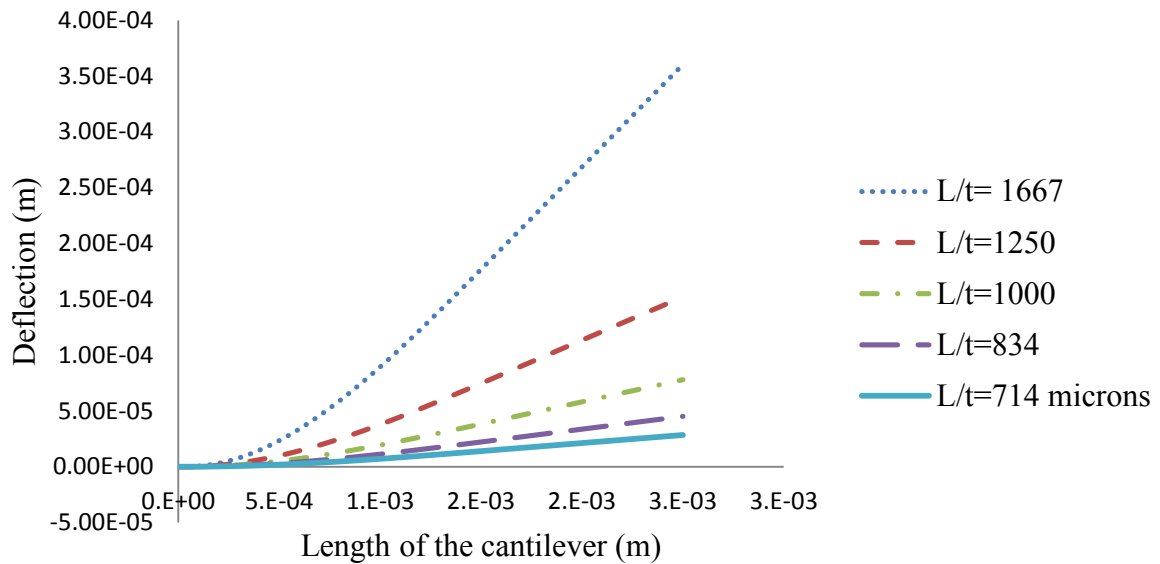
Figure 4.26 Parametric study: L/t ratio.

The ratio length over width is the subject of the third parametrical study of the beam. The length of the beam is maintained constant at 2500 microns while the width is varied between 625 and 1250 microns. As expected, a larger ratio gives a better sensitivity for the cantilever sensor (Figure 4.27). However, a special attention should be given in this case in order to avoid the reach of the edge of the beam by the droplet. In this case new capillary phenomena can occur and the signature of the deflection is altered. This fact will be illustrated in the chapter dealing with the experimental work.
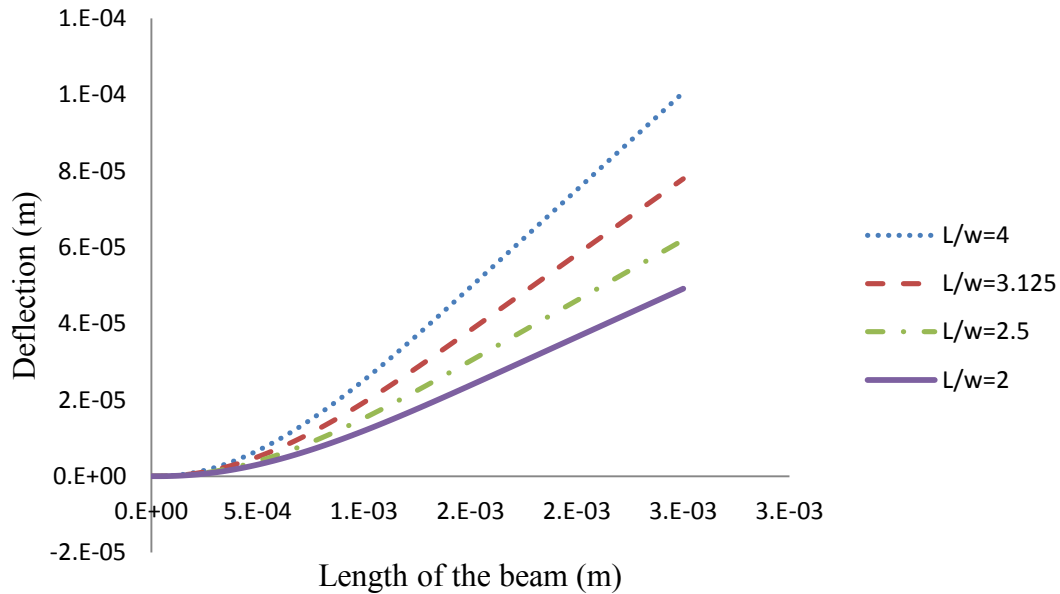
Figure 4.27 Parametric study: length / width ratio.

The maximum deflection of the beam is obtained when the droplet is placed as close as possible to the tip of the cantilever. There is a constrain imposed by the optical detection system (Figure 4.2) that requires a free space in the same position, because of the necessity of the laser beam to reach the beam and further to be reflected towards the position sensing device (PSD).

If the droplet is placed eccentrically from the horizontal axis of symmetry of the beam ce, a rotation about this axis can occur, fact that influence negatively the accuracy of the signature of the biochemical reaction.

In the following study the same finite element model is used as in the previous calculation : a sandwiched beam consisting of three layers Al-PVDF-Al beam with the

dimensions L x w x t of 2.5 x 0.8 x 0.025 mm, and a droplet having a radius of 0.3 mm placed at 1 mm from the free end. The off-center distance between of the center of the droplet and the middle of the beam Figure 4.28 takes the following values: 0 mm (the reference), 0.02 mm, 0.04 mm, 0.06 mm and 0.08 mm.
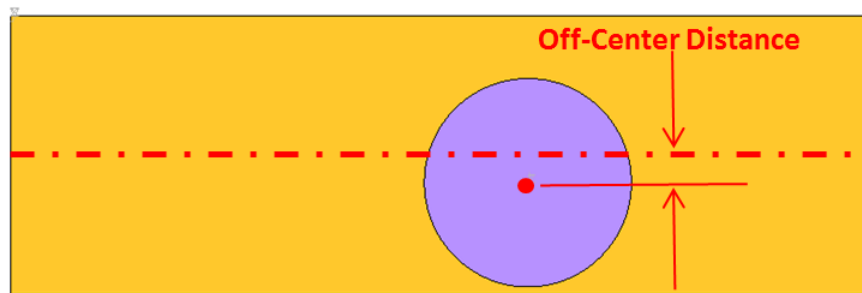
Figure 4.28 Off-center droplet study: schematics of the problem.

As expected, the angle of rotation of the beam increases is direct proportional with the increase of the off-center distance. To build the plots shown in Figure 4.28, at the cross section of the tip of the beam, the displacement of three nodes was observed: one at the lower corner of the cross section, one in the center and one in the upper left corner.
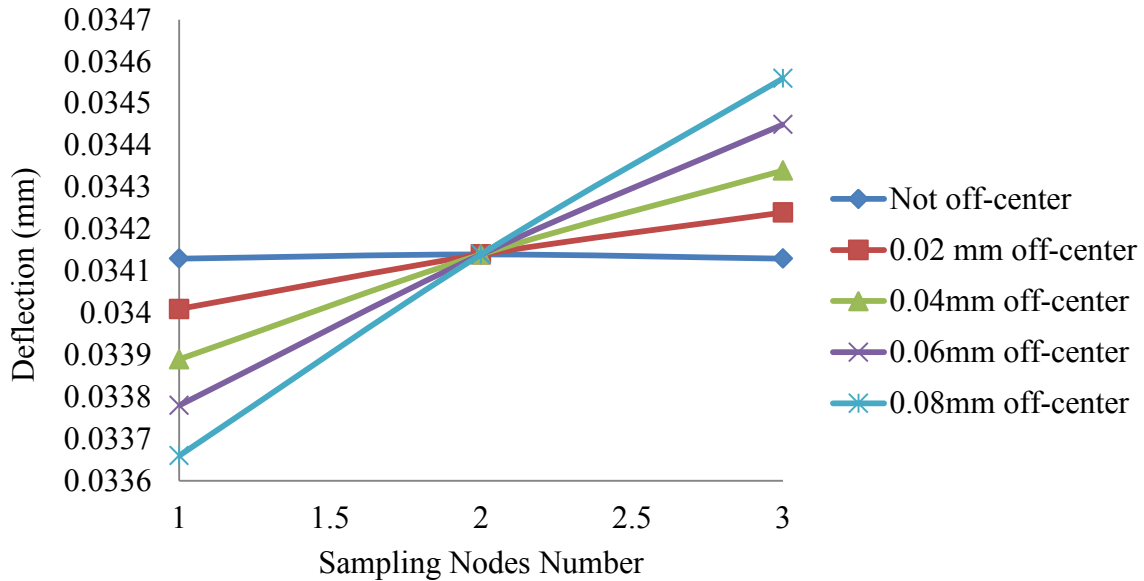
Figure 4.29. Beam rotation due to eccentric loading.

4.4 In-plane motion sensor

In general a micro fabricated product is considered to have 2.5 dimensions. Its main features and components are in a two-dimensional plane while its aspect ratio (width/depth) high values. The term out-of plane cantilever sensor refers here to a cantilever beam type of sensors whose direction of displacement does not take place in the principal plane but in the direction of the depth of the structure as opposed to an in-plane cantilever type of sensor. In general, a sensor operating out of plane has more sensitive parameters that makes it difficult to exploit and more susceptible to malfunctions. An artistic representation of the fore mentioned type of sensors is illustrated bellow.
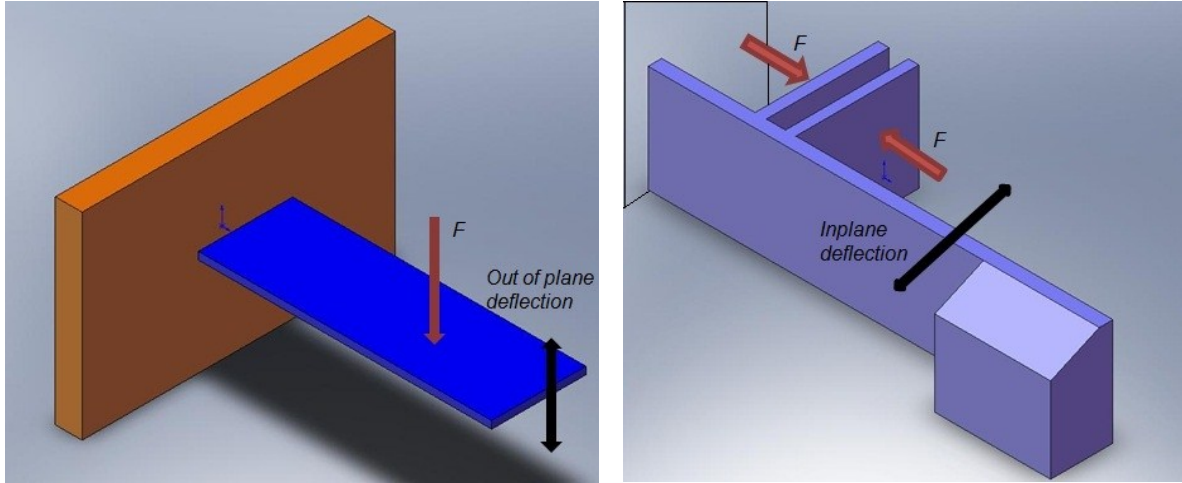
a)   b)

Figure 4.30 Out of plane a) and in-plane and types of deflection.

A very challenging task for the optimum performance of the cantilever sensor is represented by the deposition of the droplet on the surface of the cantilever beam. In general this task is executed using a droplet generator system that quantifies the volume of the liquid using different types of mechanical, acoustical, microfluidics or electrics techniques [142-145]. The generated droplet is released from a certain height [116, 133] and collapses on the desired surface. Even if this impact is minimized, several undesired effects accompany the process. The most important one is represented by the fact that part of the liquid is lost during the impact liquid solid. In a biological sensor this situation can have devastating effects especially when the concentration of cells in the sample is reduced. The vibration generated by the dynamic load can also disturb for short time the equilibrium of the structure [116]. The integration of such a system is a sensible process due to tasks of

alignment and fine tuning needed when its macro and micro components are combined. In general, a sensor operating out of plane has more sensitive parameters that makes it difficult to exploit and more susceptible to malfunctions.

An in-plane micro sensor can be implemented in the structure of the microsystem during the same step of fabrication of other subcomponents of the microsystem. As an example, the deep reactive ion etching technique (DRIE) [146] used in micro fabrication can create both microfluidic and micromechanical structures in the same step, with depths of more than 400 microns [147]. Due to this fact the integration of microsystem is easier achieved.

The main advantage of the proposed in-plane sensor comes from the fact that the quantity of the biological sample is not altered. The droplet reaches its designated area not by dynamical impact but through capillary action. The in-plane sensor can be placed in the vicinity of a microchannel that will deliver the desired amount through a microfluidics valve [148, 149].

The study of capillary phenomena represents a subject of attention and continuous improvement during the last two centuries [150]. The main areas of interests are represented by the analytical formulation of the capillary forces [151, 152] generated between various surfaces, the mathematical expression of the shape of the capillary surfaces and the application of the capillarity in biology, medicine, industry, etc.

A simplified version of the capillary force of attraction generated by a fixed volume of the liquid between two plates manufactured from the same material and with the same surface quality (identical capillary angle θ) is given by the following expression:

$$F_{capillary} = \pi R^2 \frac{2\gamma \cos \theta}{H}$$

(4-41)

where R represents the area of the curvature of the capillary bridge between the plates and , γ is the surface tension of the liquid and H represents the distance between the plates.
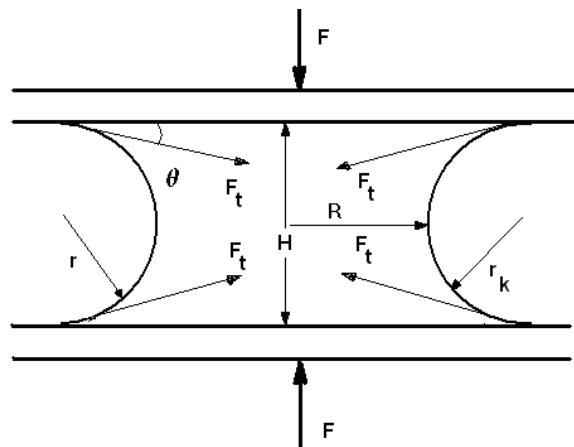
Figure 4.31 Attractive force in capillary bridges.

The attractive capillary forces are responsible, in an in-plane sensor, for its deflection. They will create in the supporting beam a couple that will generate a proportional deflection. As an illustrative example [136], the magnitude of the capillary attractive force exerted between two plates at a distance of H= 5 micrometers of one another by a volume of 40 microliters of water, that creates a radius of curvature of 0.05 m, with a surface tension

91

γ=0.072 N/m and a theoretical capillary angle of θ = 0 has a value of about 10 N. The effect of the attractive force is also complemented by a Laplace pressure in thee drop of 0.3 atmospheres. The scale of these forces cancels the influence of the weight of the droplet in an in-plane sensor and makes it a good candidate as a bio detecting device. In calculations the volume of liquid in a liquid bridge is approximated by the expression $V = \pi R^2 H$ however more detailed formulas are presented in the literature [151-153].

The proposed biosensor will be able to deal with exact volumes of liquids through a precise design of the length, height and the distance between the two fins illustrated in Figure 4.30 b). A reduced volume of the biological sample demanded by the sensor will allow an increasing number of assays but, in the same time, will reduce the magnitude of the attractive force F. In order to overcome this challenge, one can choose to modify the hydrophobicity of the surface or to topologically optimize the structure. In general the DRIE method generates a rough surface [146] that is by default hydrophobic. A further alteration of the quality of the surface is not, however a viable option because the deposition techniques are hindered, in general, by the presence of deep feature in micro fabricated structures [154].

4.4.1 **Topology optimization of the in-plane sensor**

The optimization process is considered to be one of the most difficult tasks encountered in mechanical engineering due to the complexity and the large volume of calculations involved [155]. Topology optimization helps a designer to implement

concepts that allow the best use of material within the given design space in such a way that the such that the objectives demanded from the mechanical structure (stiffness, natural frequency) are maximized or minimized, as a function of the constraints given by the considered set of boundary conditions and loads. The following paragraphs will present briefly several techniques that were created during the past decades in order to achieve this task.

The most applied method of topology optimisation is the density method. In this approach to the density ρ of the material is assigned a value between zero and one. A density of zero suggests the absence of the material while a density of one implies its presence. A value of 0.7 for example can be understood as 30% of the material from the given volume is subtracted. With this assumption the objective function is minimized using a gradient based algorithm [156] (the objective function depends of the demands of the problem, for example a certain load acts on the structure that should not bend more than a certain value). Applying this principle to a finite element approach, the initial structure is divided in a certain number of elements and to each of them is assigned an initial constant density. With this assumption, the optimization algorithm will have to consider only one variable per element, its density. The result will have elements with either the value zero or the value one, eliminating all the intermediate values for manufacturing reasons. This process of elimination is known as introduction of penalties. The density method that uses penalties in solving the topology optimization problem is called the Solid Isotropic Microstructure with Penalization (SIMP) method.

Before eliminating the intermediate elements, the following relation holds:

$$E = \rho E^0 \tag{4-42}$$

where E represents the elasticity tensor.

After the introduction of the penalty p, the relation (4-42) is no longer linear and, and, over a given domain Ω, it transforms into the following expression:

$$E = \rho^p E^0 \tag{4-43}$$

which is equivalent to the following relation:

$$K = \rho^p K^0 \tag{4-44}$$

where K is the stiffness tensor (the compliance is the inverse of the stiffness).

The objective of the optimization process is reduced to the problem of constraining the mass while the compliance is minimized [156]:

$$\min C(\rho) = F^T u(\rho)$$
$$s.t. \begin{cases} \rho^T a = V \\ \rho_{min} \le \rho_e \le \rho_{max}, e = 1..n \end{cases} \tag{4-45}$$

where ρ is the density vector, a is the element areas vector, V is the working volume, $u(\rho)$ are the displacement and F is the function that describes the physical and geometrical characteristics of the particular optimized structure.

Another approach is represented by the method of homogenization [155, 157-159] that uses a material model in which voids are implemented artificially and the topology optimization algorithm uses an optimal criteria to detect the optimal porosity of the material, and, depending on the constrains, produces improved structures from both topological and structural point of view. The drawback of this technique is the fact that the results are difficult to implement due to the existence of voids with small features that cannot or are very hard to be reproduced. A variant of this method that tries to overcome the disadvantages of the original one introduces the idea of solid isotropic material with penalization (SIMP) in which to each element of the discretized domain is assigned as a design variable an intermediate density that is equal to the density of the original material raised at a certain power [155, 160, 161] . The main challenge of this approach is represented by the complexity and instabilities generated by its computational algorithm.

Another approach to topological optimization is represented by the evolutionary structural optimization (ESO) and is dedicated to the shape optimization in mechanical structures mainly for constrains based on the stress, stiffness and frequencies [155, 162]. In principle, this algorithm assesses the contribution of the interrogated element to the general loads applied on the structure and decides if its existence is justified or not in the optimal design domain.   A review in detail of the presented methods can be found in Wang and all [155].

In a case of the in-plane cantilever beam sensor, the main constrain is considered to be the function that models the displacement of the beam: this function is to be maximized but in the same time the integrity of the structure has to be maintained.

The material distribution technique for topology design consists in reformulating the problem as a sizing problem for the density variable ρ on a fixed domain. Practically this means that the following steps are performed, in an iterative scheme:

a) Build the initial design having the material homogenous distributed;

b) Calculate the resulting displacement and constrains (using the FEM);

c) Compute the compliance of the given design and compare it to previous results: if only insignificant improvement is observed then stop if the optimum condition is satisfied; otherwise continue;

d) Update the calculation of the density variable;

e) Continue with step a) or stop [163]

The presented steps are exemplified by taking in consideration the topological optimization of the in-plane detection sensor using the commercial available solver OptiStruct that uses SIMP method for the topology optimisation problems.

The parameters of the beam are the following: length of the beam is 5000 microns, its width (height) is 75 microns, and its thickness 30 microns. Other parameters are the length of the fins 200 microns, the thickness of the fins is 25 microns and the gap between them 50 microns. The distance between the position of the center of the gap and the fixed

end is 100 microns. The material of the structure is considered to be silicon. A force of one Newton was applied in the center of the gap that generated a deflection of the free end of 1.73 microns.

The first step of the optimization process consisted in the assignment to the structure of a global domain of existence with the width of 500 microns and the length of 5000 microns in which the initial structure is completed included. The interval of variation is automatically assigned when a reduction of volume of the design space is desired.
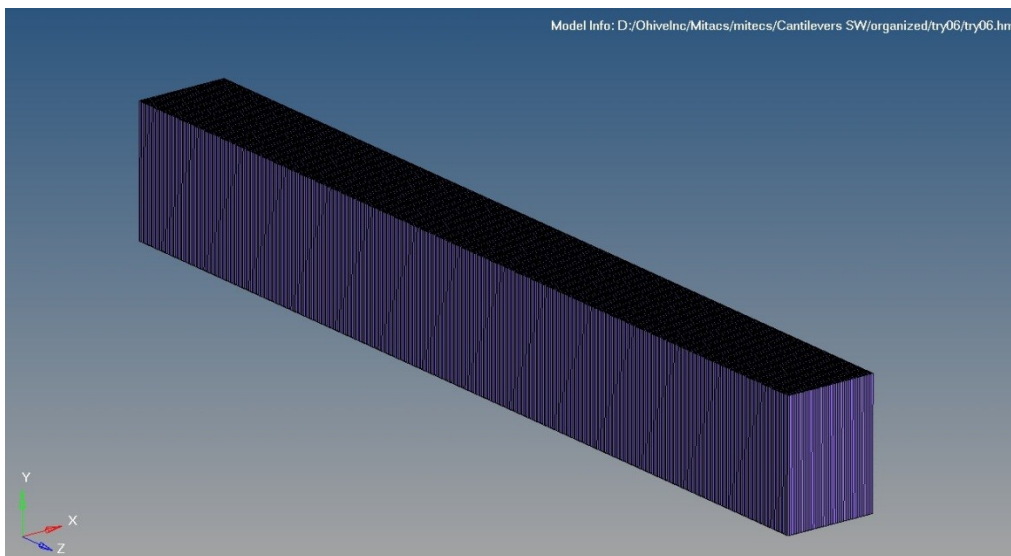
Figure 4.32 The design space assigned to the model.

This domain was discretized with 4000 shell elements, having the height of maximum 0.7 microns. The model of the sensor included the boundary conditions at the fixed end and a standard couple of one Nm placed at a distance of 100 microns of the fixed end. This distance was chosen in order to allow space for the foreseen coupling with droplet

generating microfluidics subcomponents. The initial displacement of the beam under the action of the chosen load onto the structure was given by in the finite element (FEM) solver as 1.73 microns.

The thickness of the shell elements was set at 700 microns. The variable of the algorithm, the density of the element, is initially assigned to 0.6 and can take values between 0 and 1. The constraint chosen was the displacement of a nod at the tip of the cantilever that determines the objective function. Further, a supplementary constraint is set, constraint given by the manufacturing process. For example, in our case, the microfabrication technology demanded that no geometric feature should go less than five micrometers.

In each optimization step, the algorithm implemented by the software reads the displacement given by the FEM solver. The responses of the FEM solver are:

- the displacement of the node placed at the tip of the beam in the x direction;

- the compliance of the structure determined by the result of the multiplication between the density variable and the thickness of the shell element .

The algorithm choses one of these two responses to be a further constraint for the general objective of maximization of the deflection and when the displacement reaches a maximum, the final density of each element is recorded.
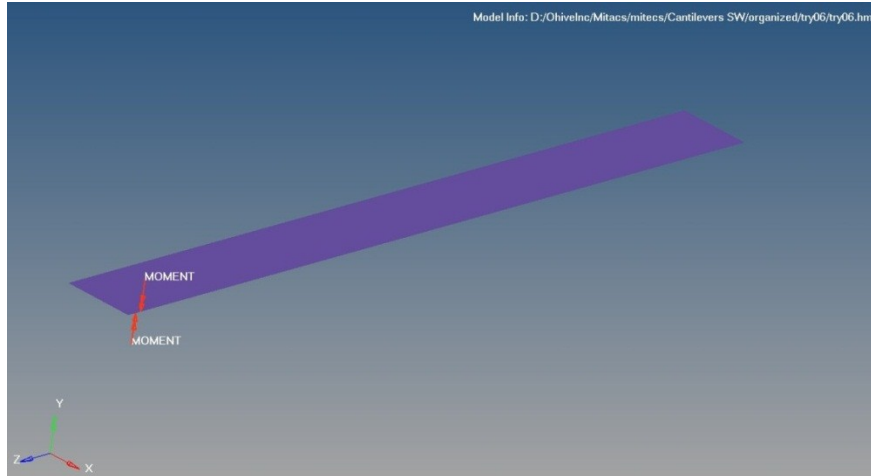
Figure 4.33 Constrains of the optimization process: moments.
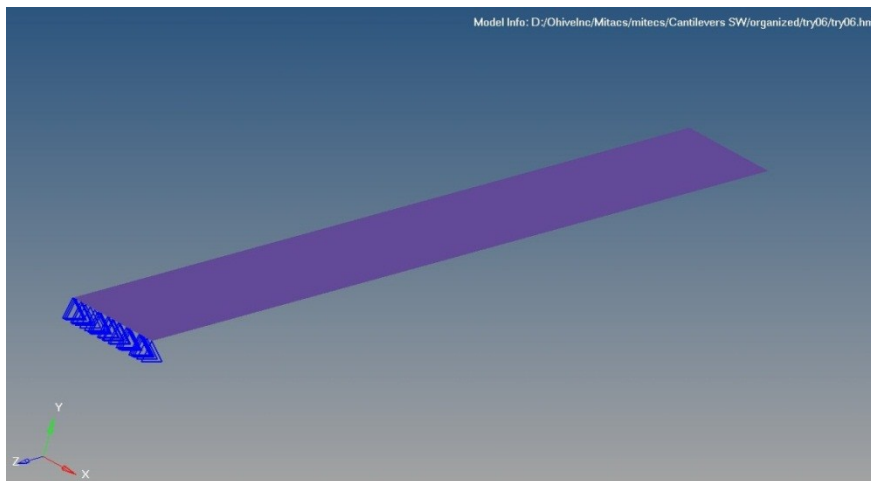
Figure 4.34 Constrains of the optimization process: fixed end.
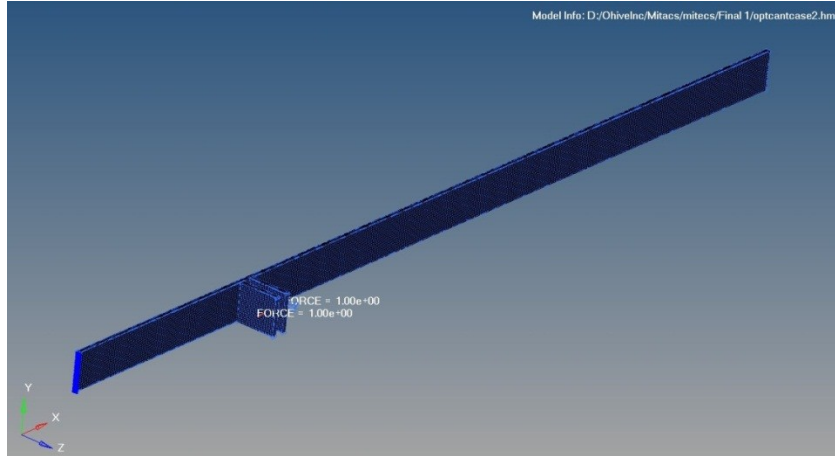
Figure 4.35 The initial design of the in-plane sensor.

The optimization algorithm choses the presence or the absence of each element by evaluating its density. Illustrations of these steps are presented in the figures Figure 4.36-Figure 4.43. In these figures the lower densities are illustrated with darker colors.
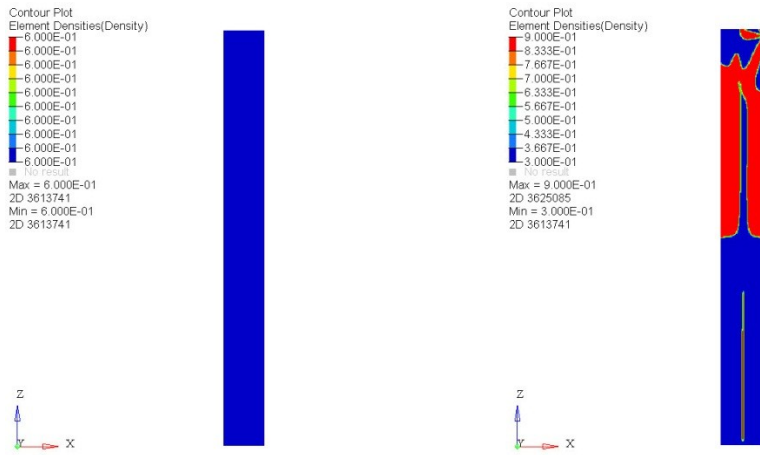
Figure 4.36 Optimization steps 1 and 2.
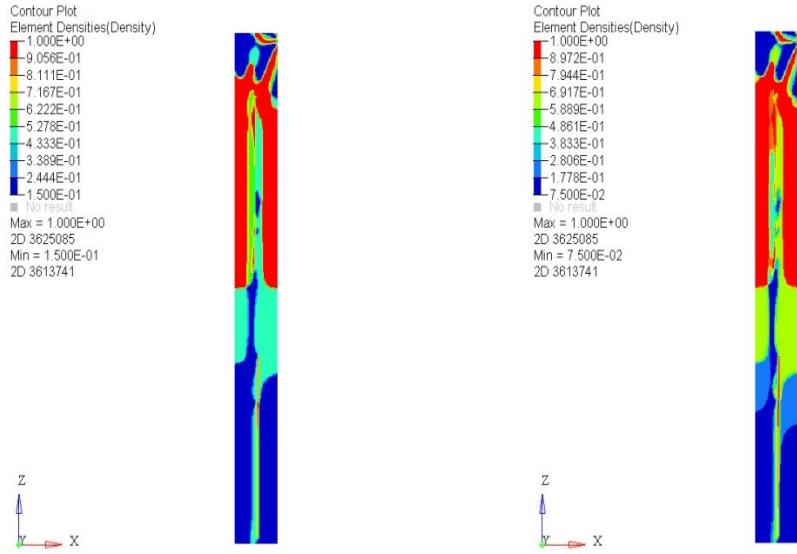
Figure 4.37 Optimization steps 3 and 4.
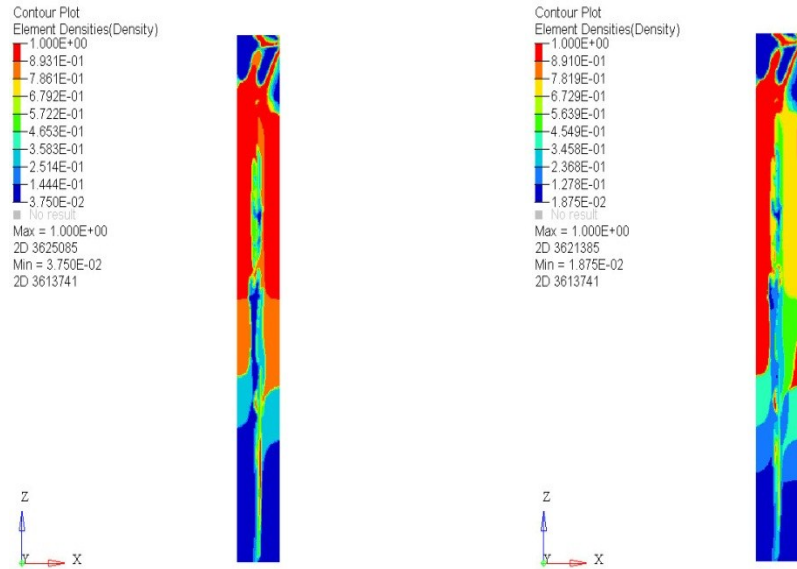
Figure 4.38 Optimization steps 5 and 6.

101
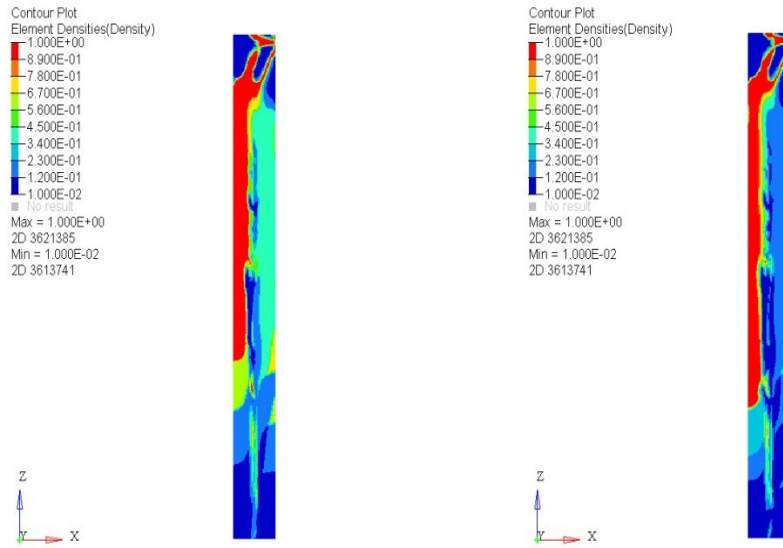
Figure 4.39 Optimization steps 7 and 8.
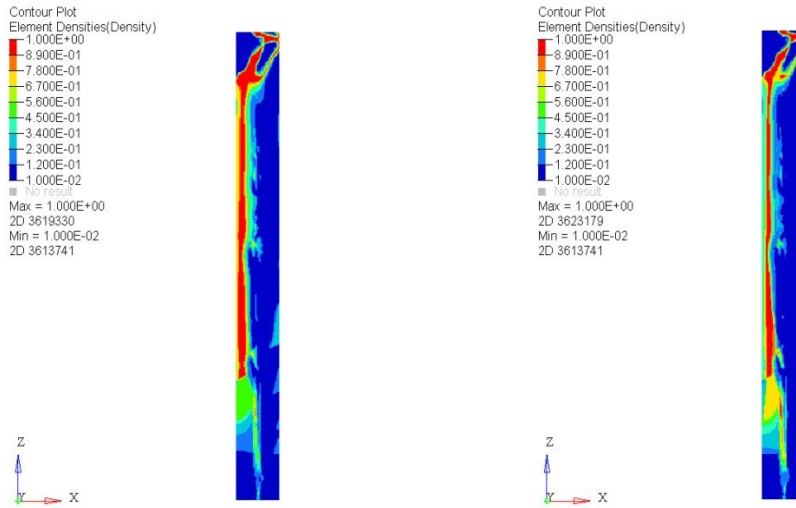
Figure 4.40 Optimization steps 9 and 10.

Contour Plot
Element Densities(Density)
1.000E+00
8.900E-01
7.800E-01
6.700E-01
5.600E-01
4.500E-01
3.400E-01
2.300E-01
1.200E-01
1.000E-02
No result
Max = 1.000E+00
2D 3617131
Min = 1.000E-02
2D 3613741

Contour Plot
Element Densities(Density)
1.000E+00
8.900E-01
7.800E-01
6.700E-01
5.600E-01
4.500E-01
3.400E-01
2.300E-01
1.200E-01
1.000E-02
No result
Max = 1.000E+00
2D 3617077
Min = 1.000E-02
2D 3613741
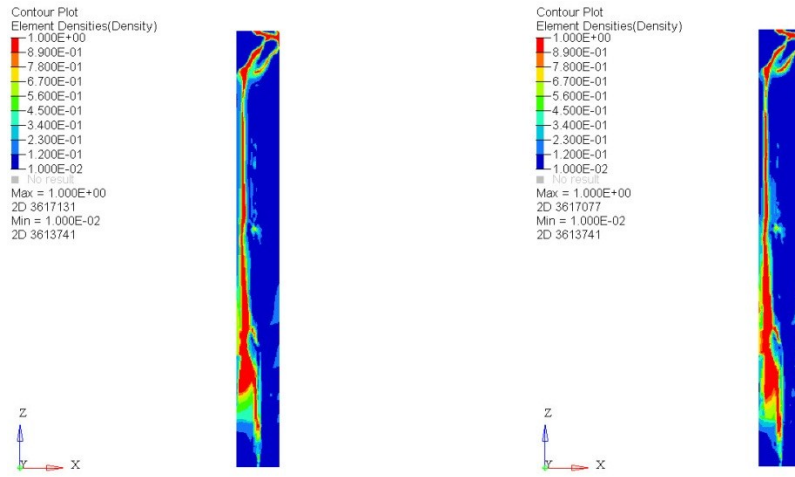
Figure 4.41 Optimization steps 11 and 12.

Contour Plot
Element Densities(Density)
1.000E+00
8.900E-01
7.800E-01
6.700E-01
5.600E-01
4.500E-01
3.400E-01
2.300E-01
1.200E-01
1.000E-02
No result
Max = 1.000E+00
2D 3616475
Min = 1.000E-02
2D 3613741

Contour Plot
Element Densities(Density)
1.000E+00
8.900E-01
7.800E-01
6.700E-01
5.600E-01
4.500E-01
3.400E-01
2.300E-01
1.200E-01
1.000E-02
No result
Max = 1.000E+00
2D 3618676
Min = 1.000E-02
2D 3613741
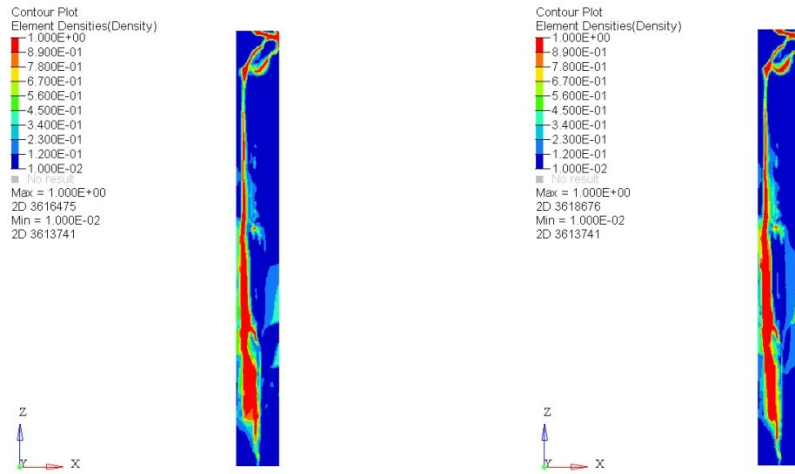
Figure 4.42 Optimization steps 13 and 14.

103
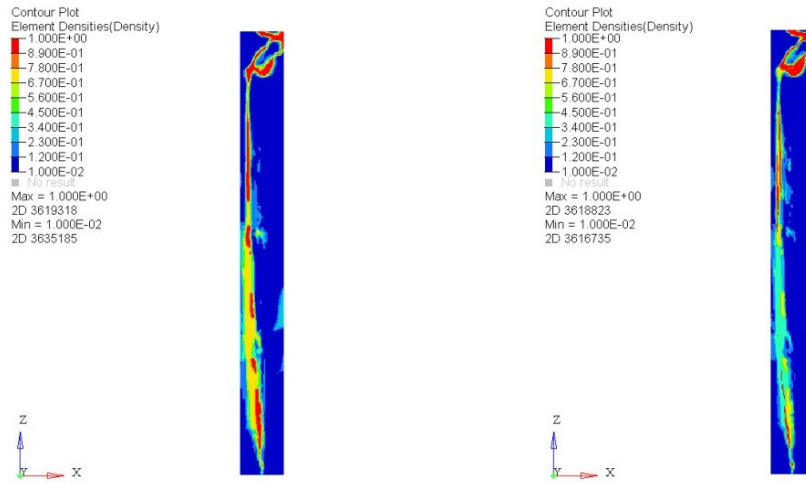
Figure 4.43 Optimization steps 15 and 16.

The suggestion given by the optimization process is a structure with the minimum thickness possible and the existence of a gap in the structure of the analysed element. According to this recommendation, a cantilever beam is designed like in Figure 4.45. Its deflection is analysed with the FEM solver and compared to the deflection of the beam before the optimization (Figure 4.44). The deflection of the optimized structure is 57.16 micrometers, which is 30 times larger than the initial one.

The process of optimization allowed a great improvement of the sensitivity of the structure that makes an in-plane sensor with a similar design a good competitor for the classical out of plane cantilever beam.
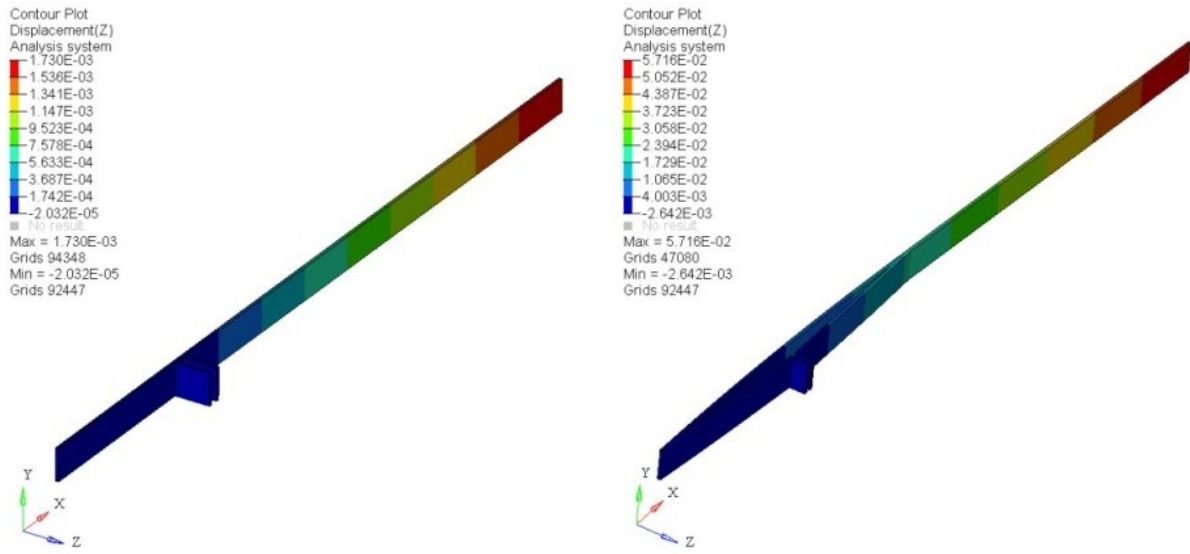
Figure 4.44 The initial and the final structure deflection for a load of 1 N.
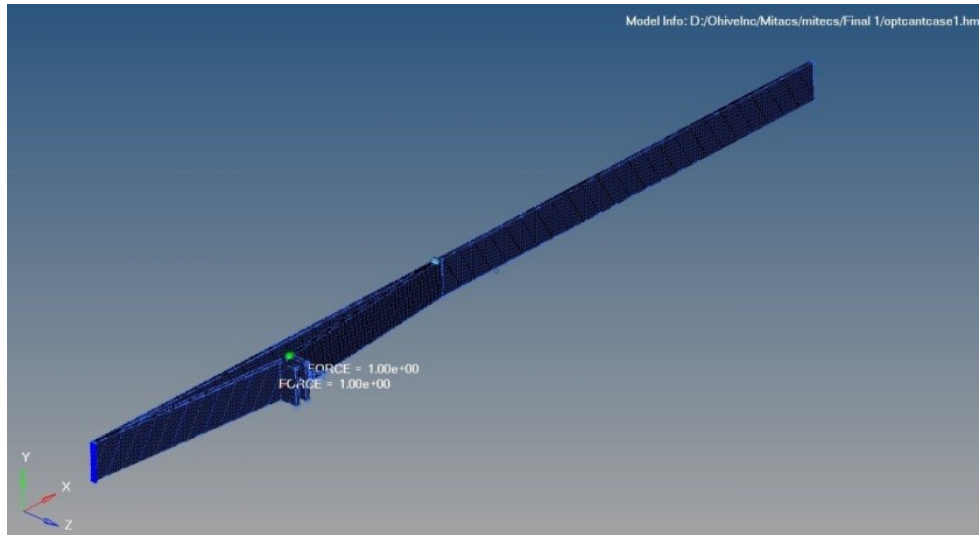
Figure 4.45 The optimized design of the in-plane sensor.

4.5 Conclusions and summary

A literature review of the cantilever as biosensor was performed and the principles of operation that uses the beam as biosensors were identified and compared with the biosensors of the present work. Each of these principles was analysed, underlying its advantages and disadvantages. The loads responsible for the pattern recorded during the biochemical reaction on the cantilever beam were identified and their effect quantified.

The theoretical and numerical studies prove that the present cantilever sensor, moving either in-plane or out of plane, can be used successfully to identify the biochemical reaction between an antigen and its complementary antibody.

The most important parameters influencing the sensitivity of the detection were demonstrated to be the material and the geometry of the beam. The parametric studies illustrate that the position of the specimen on the beam, the ratios length/width and the ratio length/thickness are all influencing the sensitivity of the sensor. The exo/endo thermal effects proved to not influence in a decisive manner the deflection of the sensor due to the three layered symmetrical configuration.

The decisive loads in determining the magnitude of the deflection of the beam are the Laplace pressure, the vertical component of surface tension and the weight of the droplet. However, considering the orientation of the region between the droplet and the free end of the beam (the slope of the beam), the influence of the surface stress and horizontal component of the surface tension cannot be neglected.

Chapter 5: Experimental work

5.1 Introduction

The experimental effort was concentrated on finding a fast method for the molecular diagnostics of several malignant species that can be performed automatically in a point-of-care device that does not require the presence of qualified operators to manipulated the samples and evaluate the results. All the ayatems existent on the market highlighted in the state-of-the-art chapter are based on the biological protocols already existent in the diagnosis laboratories. These methods, in general, scale down the volume of reactant and, following the biological protocols for oncological detection, signal the antigen-antibody binding by sensing modifications either in surface stress or in the added mass.

In a first phase of the experimental work the bending of a cantilever beam generated by a droplet of a mixture of antibody antigens was analyzed. Several types of cancer and their representative cell lines were used during these tests. The results were centralized and the questions that rose were examined during the later set of experiments.

In a second phase the parameters of study were altered in order to establish their influence on the phenomenon. Different combinations of biomolecules were used in order to establish what parameters are influencing most the recorded signature. In order to confirm the result the deflection was observed directly by the means of interferometry instruments.
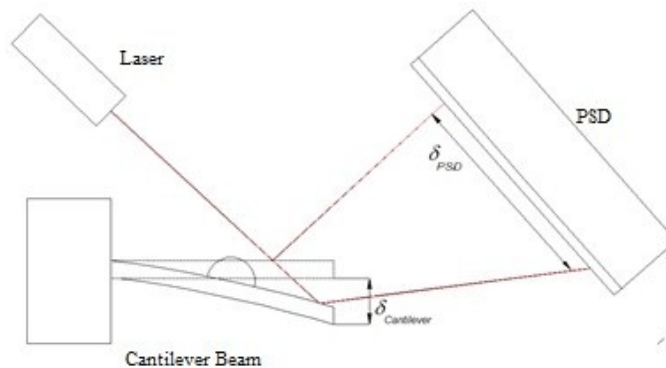
Figure 5.1 Optical lever principle.

In the last stage, an experimental study on the variation of the contact angle during the evaporation/ biochemical reaction of the droplet was performed in an attempt to identify the way in which the contact angle is affected by these phenomena. The evolution of the contact angle was scrutinized for a reduced number of biomolecules and their biochemical conjugates.

5.2 Detection of the malignant cells

The oncological diagnostic procedures either immuno-cytochemistry, immuno-histochemistry, immuno-precipitation protocols, or ELISA, and the western blots techniques have in common the phase of preparation of the reagents. This step consists in their dilution to a certain required concentration. All the reagents used in the present work followed the immuno-precipitation preparation protocol for all the types of malignant cells. The experimental studies were performed in the laboratory of oncological studies at

Rosalind and Morris Goodman Cancer Research Centre McGill University in Montreal and in the BioMEMS laboratory of Concordia University form Montreal.

In all the experiments the cantilever beams were cut manually from a PVDF-coated material at the same dimensions. The thickness of the material is 25 micrometers, the length of the beam 2500 micrometers and the width of 800 micrometers. The presence of small geometrical variations from the desired size, due to the operator or instrumental errors, it has to be mentioned

The experimental setup shown in Figure 5.2 consists of the following items:
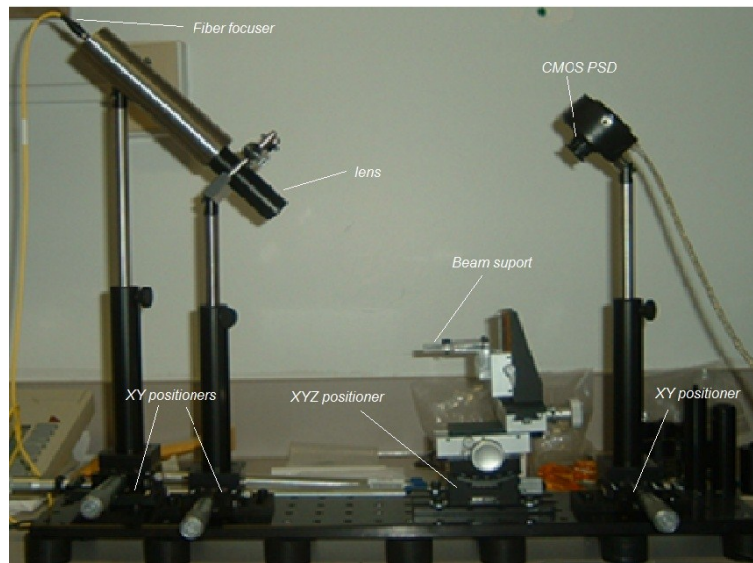
Figure 5.2 The experimental setup for the detection tests.

- pigtail style fiber optic laser diode source having a wavelength of 635 nm wavelength and a power of 2 mW output from OZOptics;

- non-contact style SM fiber focuser (12mm OD) for 635nm with an FC receptacle from OZOptics;

- f=18 spheric lens that generates a spot with a diameter of 50 microns at a working distance of 233millimeters from OZOptics;

- optical aluminum breadboard 12"x12"x12" from Thorlabs. ;

- X-Y (1/2") and X-Y-Z (1") positioners from Thorlabs..;

- X-Y (1/2") and(1") positioners from New Port;

- Spot-O 13 PSC CMOS detector having a reading size of 6.47 x 4.83 mm.

The setup was protected from the air flow Plexiglas enclosure. The temperature in the laboratory room was maintained approximately constant at 22°C. The humidity variation was not recorded during these experiments. The liquid was deposited on the surface of the beam with an electronic pipettor able to manipulate volumes in the range 0.2 – 10 µl. For every measurement a fine tuning of the XY and XYZ positioners was performed in order to have clear reading with the Spot-On Windows software that came auxiliary to the USB CMOS sensor. These adjustments are a major source of errors when one tries to translate the absolute deflection of the beam from the total distance travelled by the reflected laser beam to the sensor. For this reason the term displacement in the following discussions means the distance traveled by the laser spot on the surface of CMOS sensor, not the absolute deflection/rotation of the tip of the cantilever beam. It can be

specified that a positive movement of the spot on the surface of the sensor translates into a downward deflection of the beam.

A first step in the experimental work was to establish the optimum sampling rate for the reading of the PSD. The initial reading of 1 sample/s was hindered by a large amount of parasitic signal, factor that complicated the reading and the interpretation of the data. The working sampling rate for the signal was establish at 0.05 samples /s (one sample each 20 seconds) that gave virtually the same deflection pattern as the previous, but recorded less noise due to the environmental perturbations due to the air drafts, thermal and humidity variations and/or accidental mechanical events.
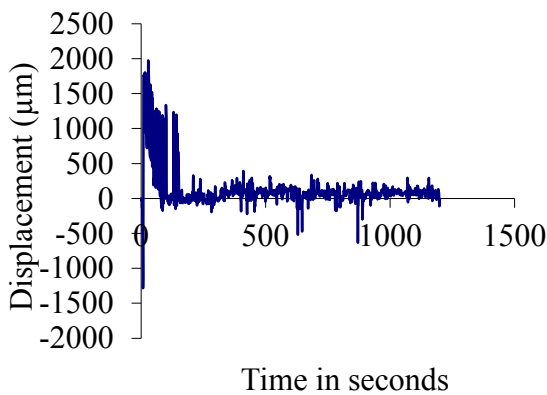
Figure 5.3 Laser spot movement (μm) on the PSD for a sample of 0.2 μl of 92.1 with a sampling rate of 1sample/sec.
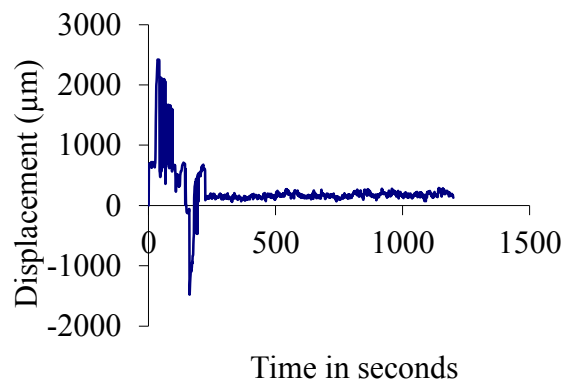
Figure 5.4 Laser spot movement (μm) on the PSD for a sample of 0.2 μl of 92.1 with Anti-Melan A with a sampling rate of 1sample/sec .
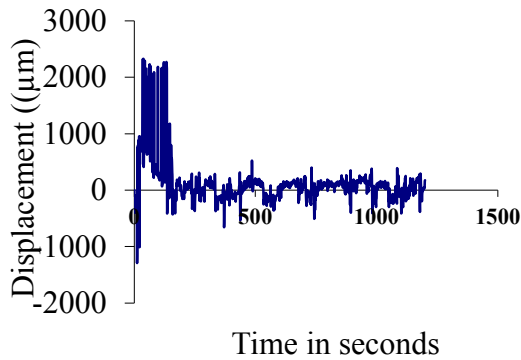
Figure 5.5 Laser spot movement (µm) on PSD for a sample of 0.2 µl of OCM-1 with a sampling rate of 1sample/sec.
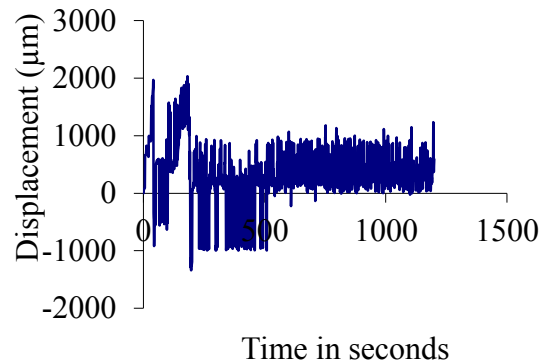
Figure 5.6 Laser spot movement (µm) on PSD for a sample of 0.2 µl of OCM-1 with Anti Melan A with a sampling rate of 1sample/sec.

The results obtained with the Uveal melanoma 92. 1 cell line, 92.1 and anti-Melan-A, OCM-1 and OCM-1 + anti-Melan-A , at 1 sample /s are shown in the Figure 5.3 to Figure 5.6.

A recording of the noise was performed with the cantilever free of loads and with 0.2 µl of distilled water placed on the sensor. In the first scenario, the recorded oscillations about the reference point were from +500 to –500 microns. For the sample of distilled water, at the beginning of the evaporating process, the recorded displacement is negative and at the of the evaporation process the position of the beam returns close to its initial position but does not reach back the reference line.
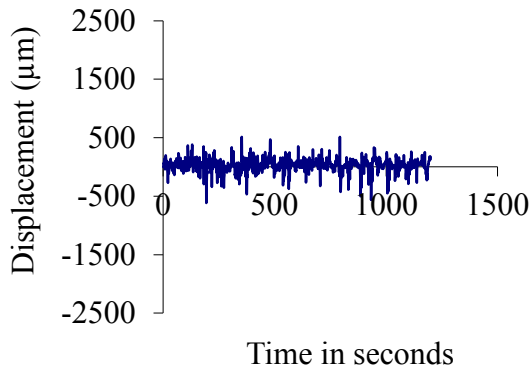
Figure 5.7 Laser spot movement in microns PSD for the cantilever without any load with a sampling rate of 1 second.
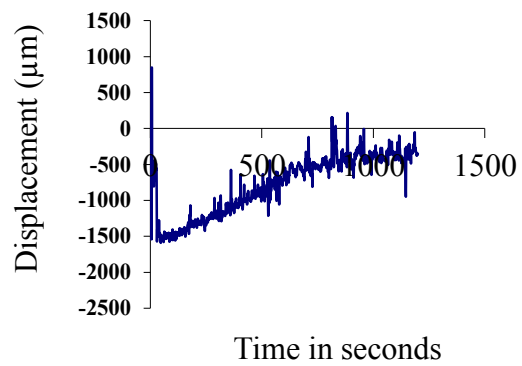
Figure 5.8 Laser spot movement in microns PSD for a sample of 0.2 μl of water with a sampling rate of 1 second.

Four types of cancer cells were used during the experiments cancer detection: Uveal melanoma, prostate cancer, breast cancer and colorectal cancer. The cancer cell lines were cultured in the laboratory at Rosalind and Morris Goodman Cancer Research Centre from McGill University and in the BioMEMS laboratory from Concordia University, Montreal. They were grown in a biological incubator in a 5% CO_2 environment, humidified with distilled water, at the constant temperature of $37C^o$. Figure 5.9 shows the matrix of the experiments performed, illustrating the malignant cell lines and their complementary antibodies. In the case of the Uveal melanoma cells, the two antibodies, CD45 and Anti MelanA were used individually on each cell line. The deflection pattern recorded through the optical lever method for the Uveal melanoma and prostate cancer will be presented in

the next subchapters, while the experiments on breast and colorectal cancer are illustrated

in the Appendix B.
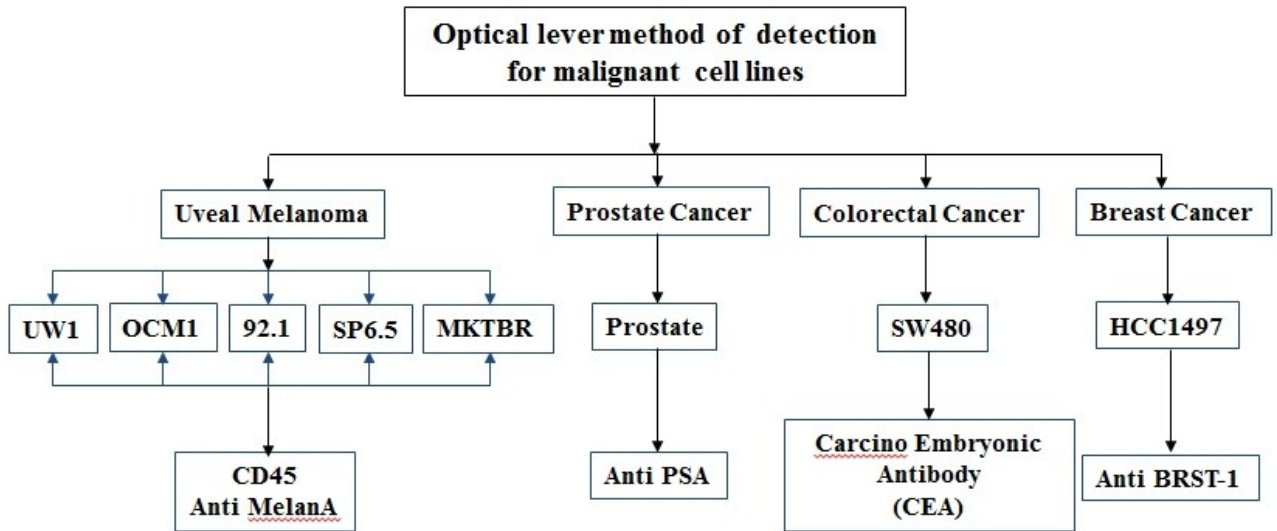
Figure 5.9 The matrix of the experiments performed on Uveal melanoma, prostate,

colorectal and breast type cancer cell lines.

5.2.1 Optical detection of Uveal melanoma cell lines

Uveal melanoma is the most common primary intraocular malignancy and is

localized in the eye in the uvea region. The incidence of the condition reaches six persons

per million per year in the United States [164] and the trend remains constant [165]. 30%-

50% from the patients having the condition develop metastasis [166] with a 5-year

survival rate of 80% [167].

For the tests performed on Uveal melanoma type of cancer, five cell lines were selected: OCM 1-1, SP 6.5, 92,.1 MKT-BR, and UW-1 (the last cell line is not in fact a Uveal melanoma but a Uveal melanocyte type of malignant cell). The medium of culture was RPMI-1640 with 5 % fetal bovine serum (FBS), 1% Penicillin-Streptomycin, and 1% fungizone in 25 ml flasks. The cultured cells attaches on the bottom on the flask as a monolayer. The medium was changed bi-weekly and prior to the experiment were detached with 2 ml of trypsin at 0.05% concentration. Following the trypsinisation, the cells were separated gravimetrically from the used medium through centrifugation at 800 RPMI for a period of 10 minutes. The resulted pellet of cells was subsequently diluted with 1 ml RPMI and the cells counted with a Coulter counter. The resulted mixture was diluted at the desired concentration (for the basic tests 1 million cells per milliliter, for the sensitivity tests at various concentrations), and mixed in a proportion of 1:50 with Anti-Melan A, their complementary antibody purchased from Nocastra Laboratories Ltd. UK. The volume of mixture used in each test was 0.6 microliters. If other volumes were employed, it will be stated in the following discussions.
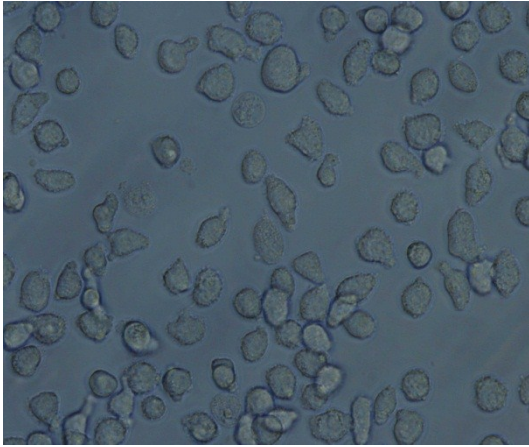
Figure 5.10 Monolayer of OCM cells in a

RPMI.
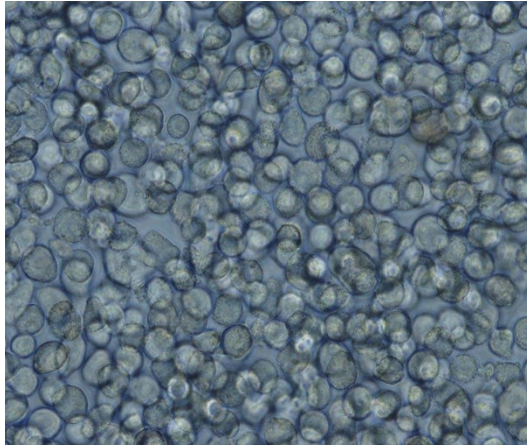
Figure 5.11 Monolayer of SP6.5 cells in a

RPMI.

In the above figures two lines of Uveal melanoma types of cells are illustrated in their living environment (RPMI solution), before their detachment with trypsine. The diameter of the cells is approximately equal, in a range between 30 and 40 microns, however each category of cells have a distinctive shape.

The reading of the displacement recorded by the PSD during the evaporation of a 0.6 microliter droplet from a sample of 1 million cells for each line of OCM, SP65, 92.1 and Anti-Melan A will be presented in the following four images. Each type of cell gives a slightly distinctive signature, all having in common an upward movement at the beginning of the evaporation but different amplitudes. The antibody Anti-Melan A shows the minimum amplitude of about 420 microns. The sample of antibody was diluted with RPMI-1640 (the main component of the medium of growth of the cells) and does not contain any cell at this moment.
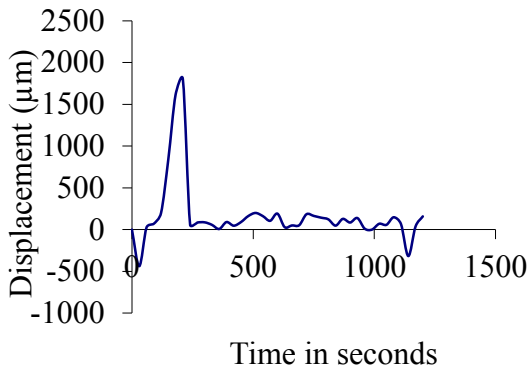
Figure 5.12 Evaporation of 0.6 μl of 92.1.
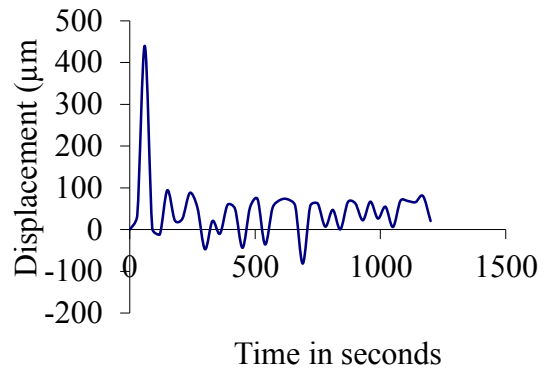
Figure 5.13 Evaporation of 0.6 μl of

antibody (Anti MelanA).
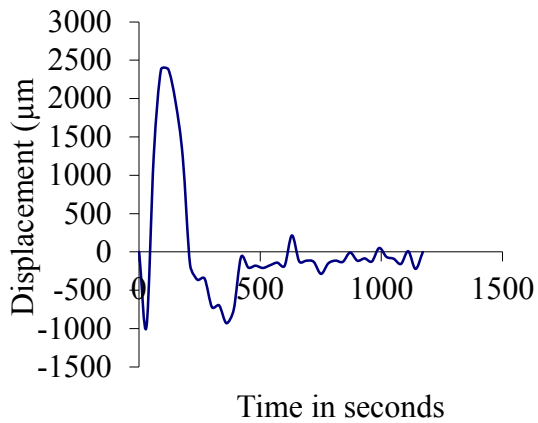
Figure 5.14 Evaporation of 0.6 μl of OCM.
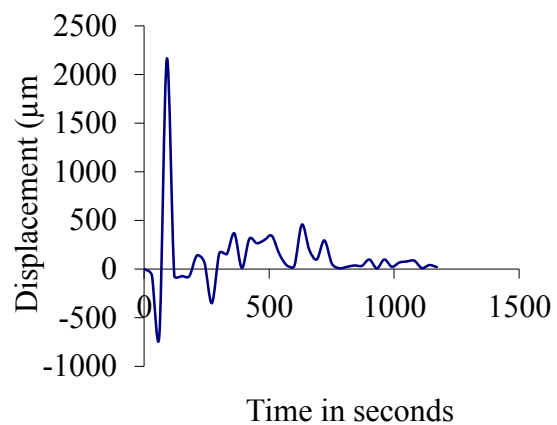
Figure 5.15 Evaporation of 0.6 μl of SP6.5.

For the reliability of the results, the above signatures were compared with the ones recorded in the same conditions, but with samples containing either a different concentration of red blood cells (RBC), or dead cells in RPMI, or RPMI alone. The four figures bellow presents these findings.
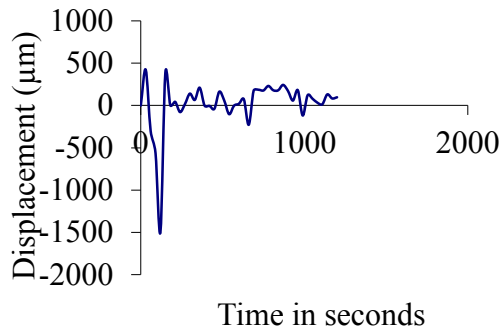
Figure 5.16 0.6 µl of RBC at a

concentration of $2.1^{\cdot}10^5$.
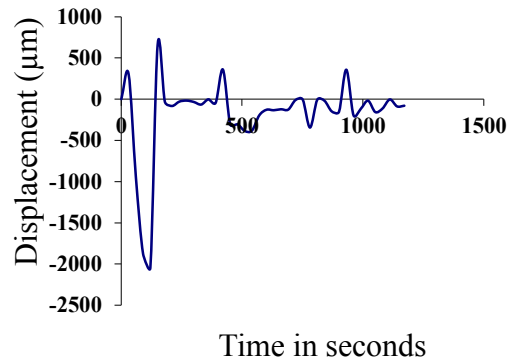
Figure 5.17 0.6 µl of RBC at a concentration

of $1.41^{\cdot}10^5$.
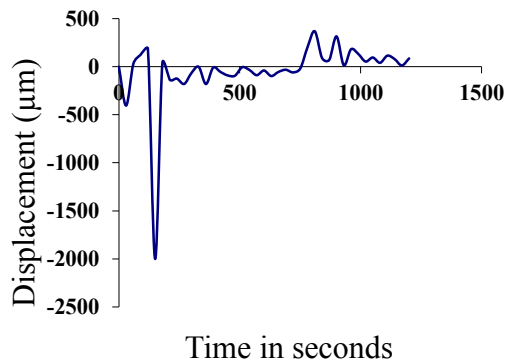
Figure 5.18 0.6 µl solution containing dead

cells.
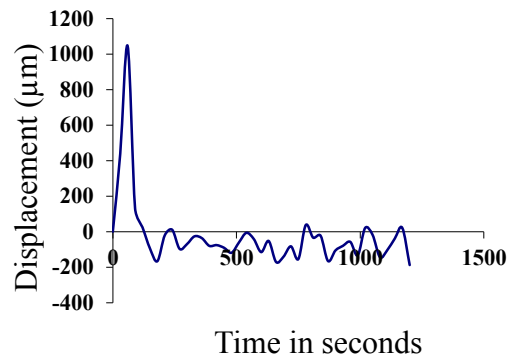
Figure 5.19 0.6 µl of RPMI-1640.

The small change in the concentration of the RBC generates a different signature, fact that comes in the defence of the hypothesis that the cantilever sensor is very sensitive for these variations. The sample containing the mixture of dead cells present the same trend of upward-downward movement giving a different amplitude to the one generated by

118

the sample of RPMI alone . The difference of amplitude may come from the surface stress created by the adherence of the dead cells on the substrate. The downward movement of the spot is presumed to be generated by the variation of surface stress or surface tension.

The five Uveal melanoma cell lines were treated with their conjugated antibody Anti-Melan A and signature generated by each of the biochemical reaction was recorded. In the two figures bellow we present the signature recorded by a 0.6 microliters of mixture of SP6.5 and OCM with Anti-Melan A.
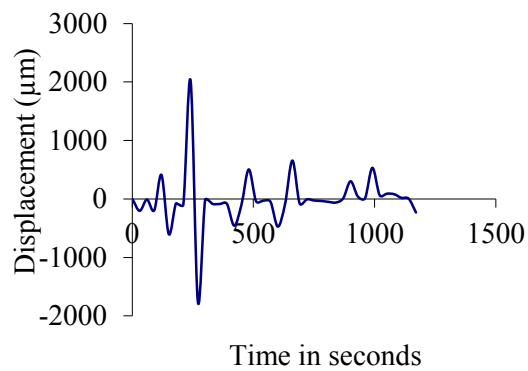
Figure 5.20 0.6 µl of mixture SP6.5 and
Anti-Melan A
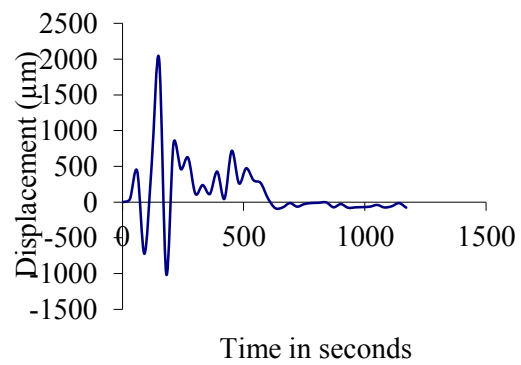
Figure 5.21 0.6 µl of mixture OCM and
Anti-Melan A

From the presence of several distinctive oscillations above the reference, it can be concluded that Anti-Melan A reacts with both SP6.5 and OCM. The antibody combines with specific proteins at the surface of the membrane, phenomenon described in the subchapter 3.3. This reaction generates the formation and the breaking of weak chemical

119

bonds, fact that affects the gradient of the surface stress in the substrate. This variation in

surface stress represents the main influence for the slope of the beam in an antibody-antigen

reaction and it is confirmed by Wu and all [168] and Amritsar and all [84] .

The remaining three cell lines give also each a distinctive signature with their

conjugate antibody.
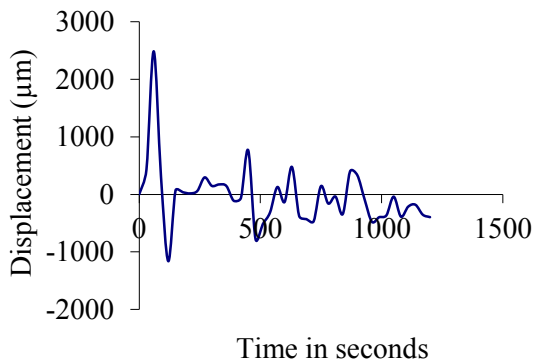
Figure 5.22 0.6 µl of mixture 92.1 and

Anti-Melan A
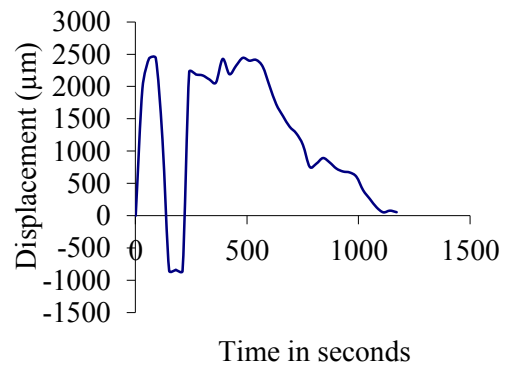
Figure 5.23 0.6 µl of mixture MKTBR and

Anti-Melan A
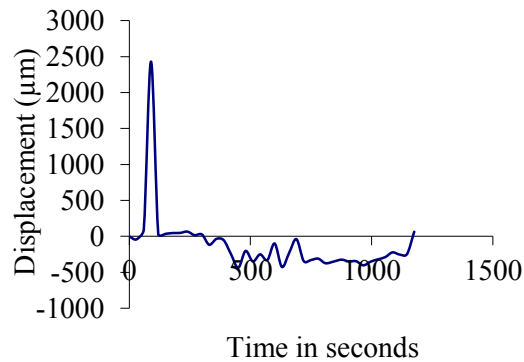
Figure 5.24 0.6 µl of mixture SP6.5 and Anti-Melan A

All five combinations of the specific antibody with the Uveal melanoma cells proved to have a unique signature. In conclusion the detection method was demonstrated to be both sensitive and specific.

In order to establish if the main reason of the signature is the specific antigen-antibody reaction and not the non-specific binding on the substrate a new set of measurements was performed combining the melanoma cells with a non-specific antibody, i.e. Anti-CD45, a leucocytes common antibody. The results are presented in the Figure 5.25 and the Figure 5.26 and they confirm indeed the specificity of the reactions between the Uveal melanoma cells and Anti-Melan A .

121
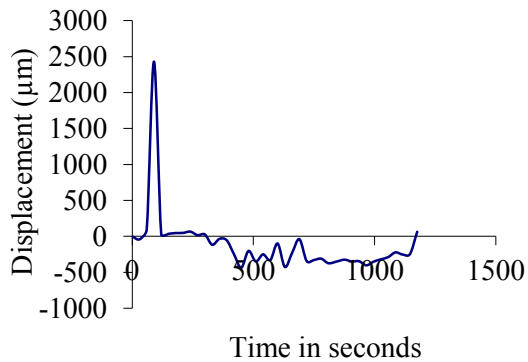
Figure 5.25 0.6 μl of mixture SP6.5 and Anti- CD45.
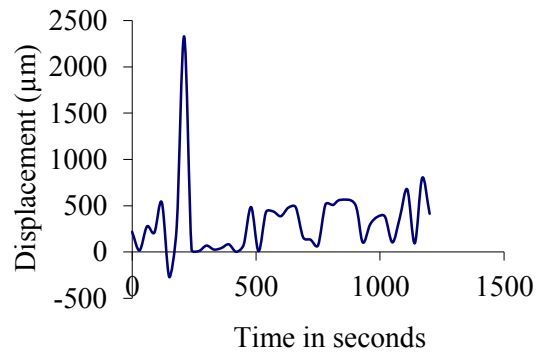
Figure 5.26 0.6 μl of mixture OCM and Anti- CD45.

5.2.2 Optical detection of prostate type cancer cell lines

An estimated number of 240 000 new cases of prostate cancer will be diagnosed in men in 2012 in United States only, and 30 000 patients are foreseen to lose their life because of this condition only [169]. Glandular cell are the main component of the seminal fluid secreted by the prostate. They are the environment in which 99% of the prostate malignant conditions occur [47]. The mechanism of proliferation for this type of condition is controlled by androgens and a high level of testosterone tends to enhance the growth of prostate malignant cells. The specific antigen secreted by the prostate type of cancers, the prostate specific antigen (PSA), is an enzyme that has its genesis in the gland ducts and ,through adsorption into blood, can spread in the entire body or attach to other prostate cells [47]. The attached form of PSA has higher values in patient with cancer, while in the healthy subject the free form of the antigen is prevalent. Almost half of the men present

122

microscopic abnormalities at the level of the prostate cells, when they reach the age of 50, condition which is called prostatic intraepithelial neoplasia (PIN) [170]. The presence of a high degree of PIN lesions gives a prognostics of 30% to 40% for the existence of malignancies at the level of prostate [171]

The prostate cancer cell line PC3 was purchased from the same supplier American Type Culture Collection as in the case of the breast cancer and colorectal cancer cell lines. They were grown in Hams F12K medium and the FBS nutrient was added in a proportion of 10%. Before the experiments the same procedures as in the previews cases regarding the dilution and detachment of the monolayer were employed.

The optical experiments with the PC3 cell line showed an early adherence on the surface of the beam. The test performed in the second day indicated that this phenomenon was encountered also in the case of the Uveal melanoma cell lines. The characteristic signature was confirmed in the second day of experiments.
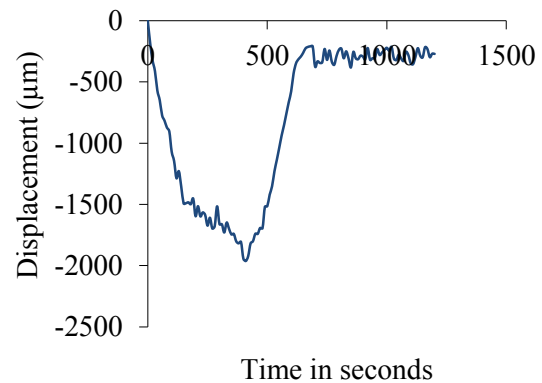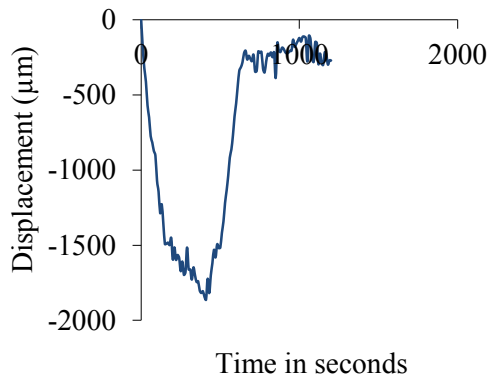
Figure 5.27 First day plots: 0.6 μl of PC3

Figure 5.28 Second day plots: 0.6 μl of PC3

The signature of the PC3 cell line change dramatically when it was combined with the specific antibody Anti-PSA. The total deflection of the beam presents a sinus like variation with an up and down displacement occurring sharply after about 650 seconds .The PSA antigen contains a large number of ions that contribute to their binding to the host cell [41] . As mentioned in the subchapter 3.3 there are various chemical bonds that break and rebind during an antibody-antigen reaction [10]. In addition to the explanation given by the biochemical reactions, the presence of numerous ions generates a bilayer like substrate on the area covered by the droplet, bilayer that creates an additional surface stress. In the following pictures, the signature of this reaction is presented for both days of experiments. The consistency of the signature highlights once again the reliability of the detection method.
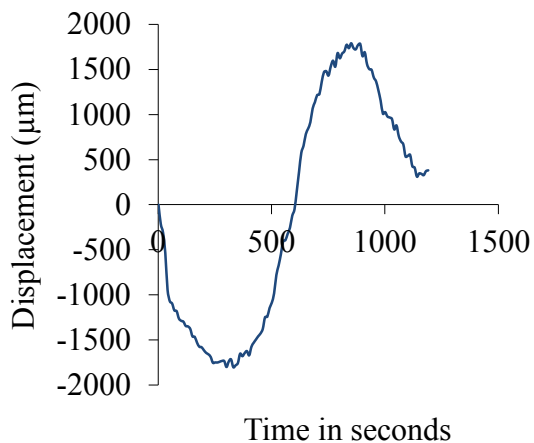
Figure 5.29 First day plots: 0.6 µl of PC3 with Anti-PSA
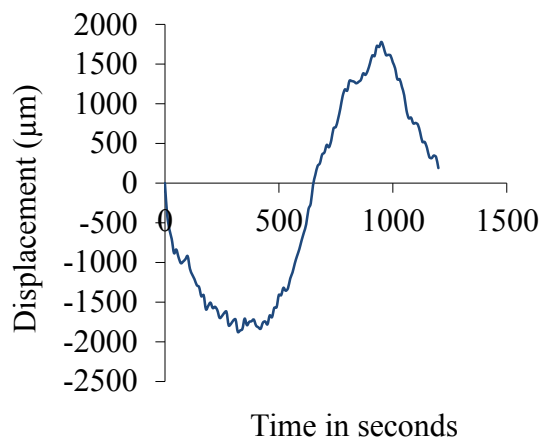
Figure 5.30 First day plots results: 0.6 µl of PC3 with Anti-PSA -second experiment
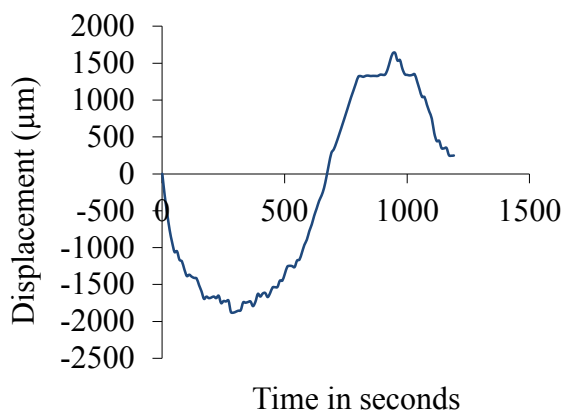
Figure 5.31 Second day plots: : 0.6 µl of PC3 with Anti-PSA
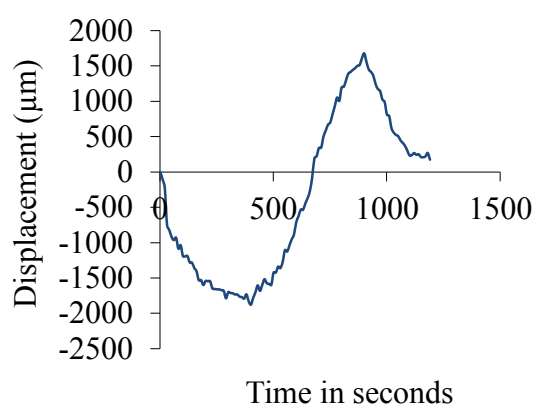
Figure 5.32 Second day plots: 0.6 µl of PC3 with Anti-PSA –second experiment.

5.2.3 Specificity and sensitivity tests

To establish the specificity of the proposed method, a blind test was performed in order to establish if it is able to identify properly the unknown component from the

125

experiment samples. A number of six samples were prepared with the following composition: four samples with cultured cancer cell lines, one sample had RPMI-1640 alone and the last one with a "healthy" cell line, fibroblast. The samples were prepared following the normal procedure at the concentration of one million cells per sample. Each type of blind specimen was prepared in triplicate.

From each blind sample a volume of 0.6 microliters was extracted and combined separately with each one of the antibodies used previously in the tests. Figure 5.33 to Figure 5.36 show the detected signature for each case and the verdict of the test. The most challenging decision was between the colorectal cancer and the breast cancer.

The results of the tests were analysed and the following conclusions were drawn:

- eleven samples containing cancer cell lines out of the total of twelve were labeled accurately.

- more tests should be performed with different concentrations of cells; it will also help in establishing a working database of signatures.
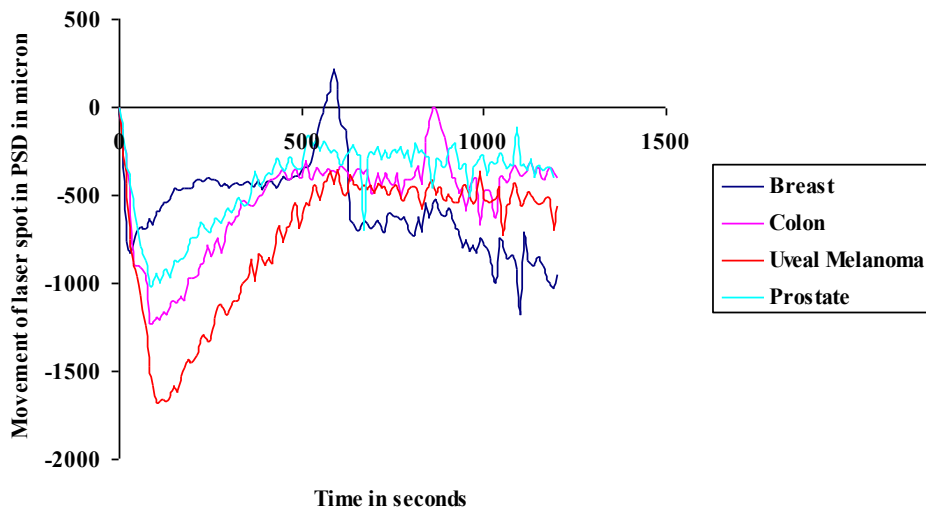
Figure 5.33 Test 1. Blind test on the unknown sample identified correctly the breast cancer
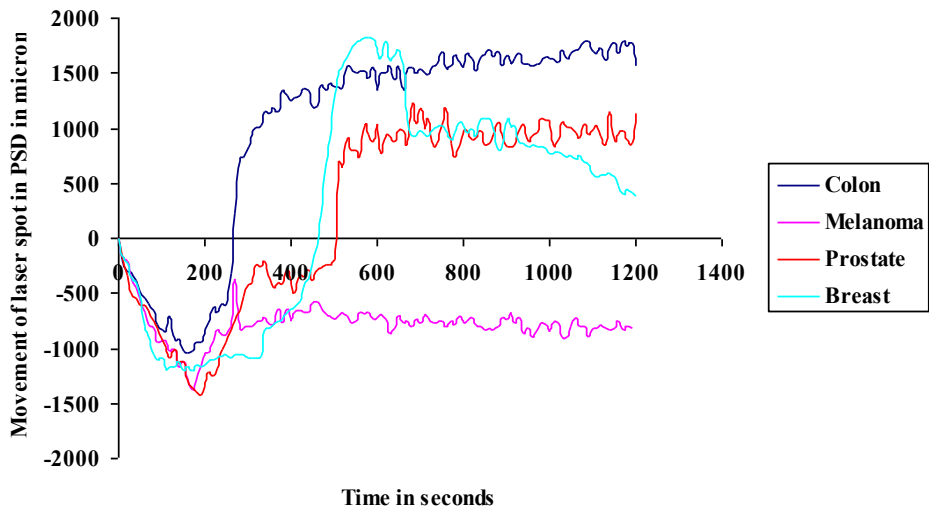
cell line.

Figure 5.34 Test 2 Blind test on the unknown sample identified correctly the breast cancer

cell line.

127
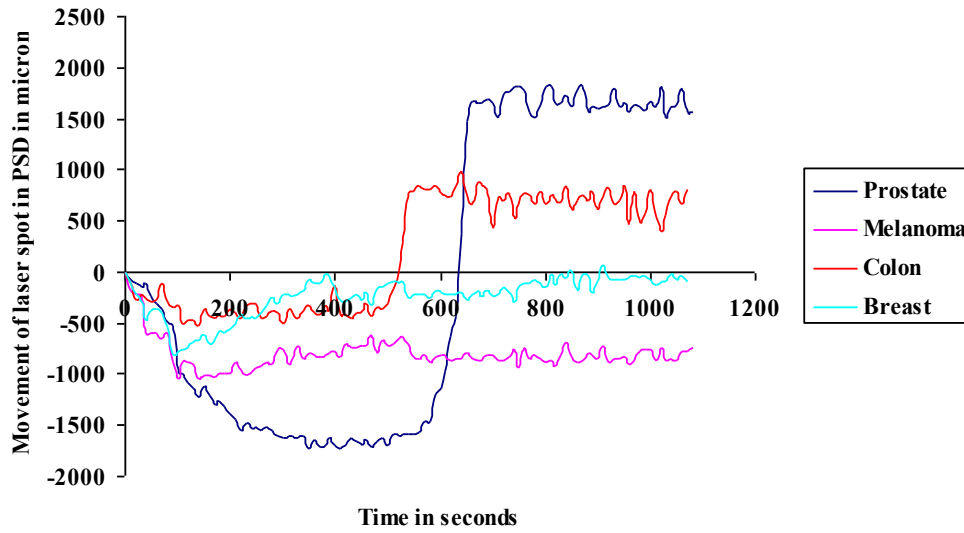
Figure 5.35 Test 3 Blind test on the unknown sample identified correctly the prostate

cancer cell line.
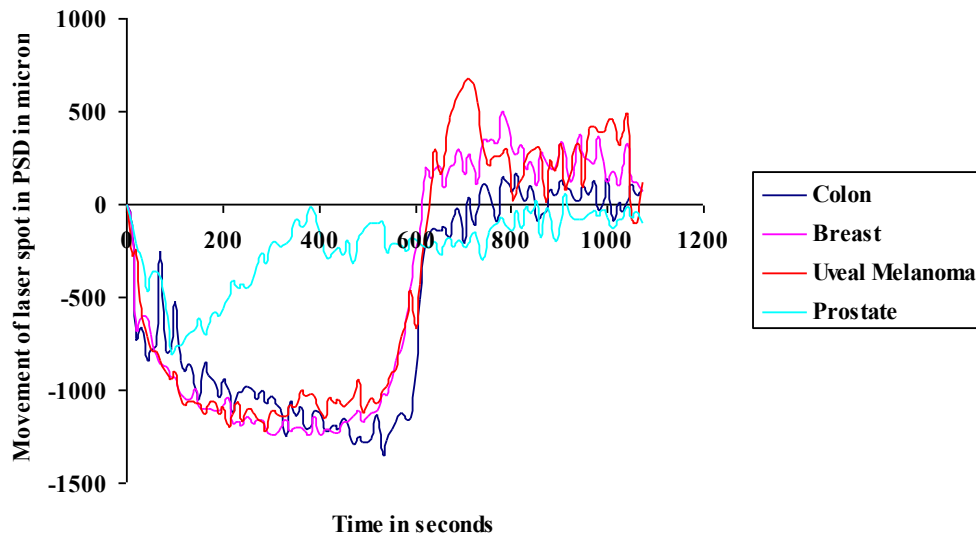
Figure 5.36 Test 4 Blind test on the unknown sample identified with difficulty the uveal

melanoma type of cancer cell line.

The sensitivity of the method was tested by varying the concentration of the cell lines from 1 cell/ml to 1 000 000 cells/ml. The selected concentrations of work were: 10 cells/ml, 100 cells/ml, 1000 cells/ml, 10 000 cells/ml, 100 000 cells/ml and 1 000 000 cells/ml. The selected cancer type for the test was the Uveal melanoma. The resulting reactions had a signature down to a concentration of 10 cells/ml. Lower than this concentration no reaction was found either because of the precision of the reading instruments, or because the cell was absent from the sample.

The following six pictures illustrate the signature of the biochemical reaction recorded during these tests.
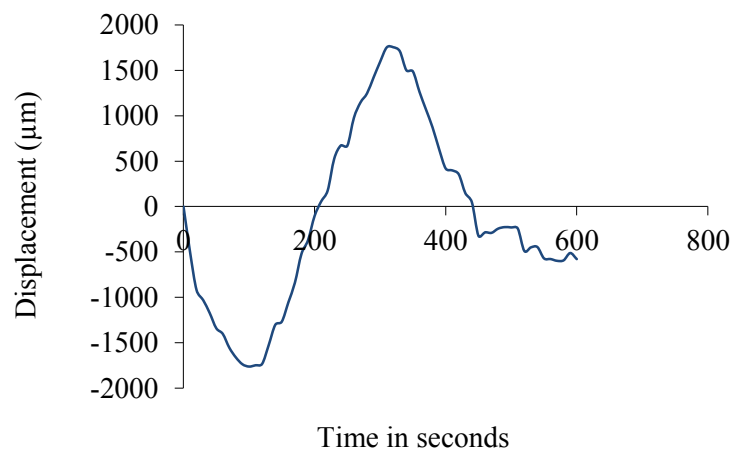
Figure 5.37 Sample with a concentration of 1 000 000 cells/ml, Uveal melanoma + Anti-Melan A.
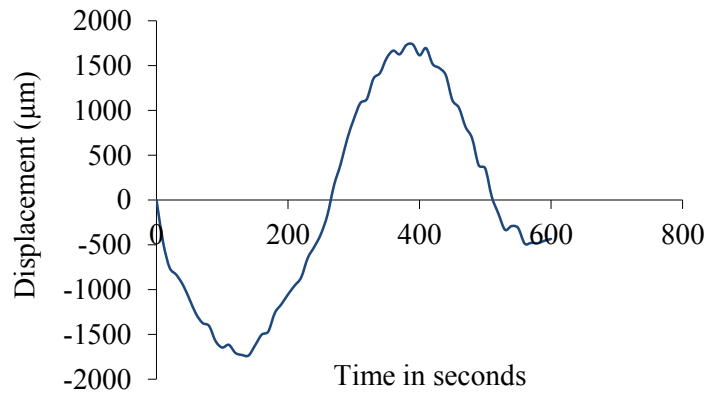
Figure 5.38 Sample with a concentration of 100 000 cells/ml, Uveal melanoma + Anti-Melan A.
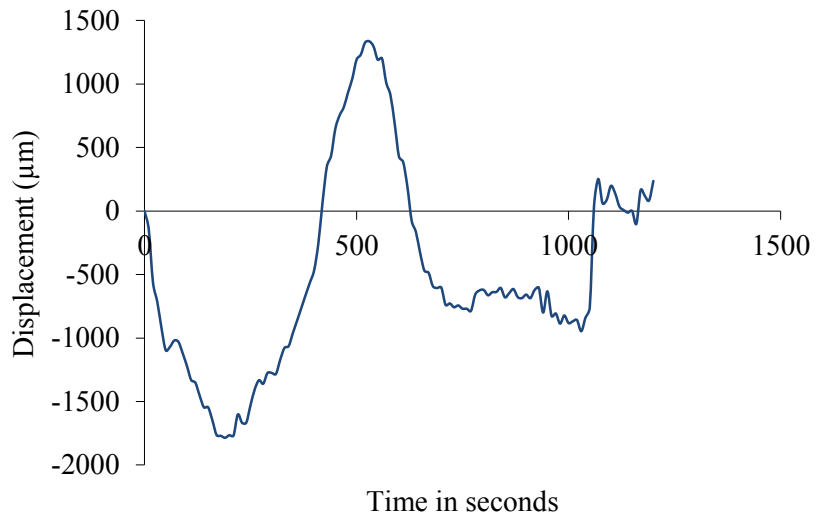
Figure 5.39 Sample with a concentration of 10 000 cells/ml, Uveal melanoma + Anti-Melan A.
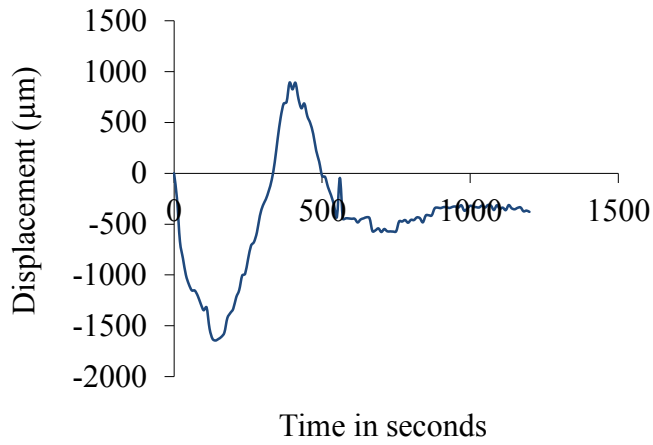
Figure 5.40 Sample with a concentration of 1000 cells/ml, Uveal melanoma+Anti-Melan A.
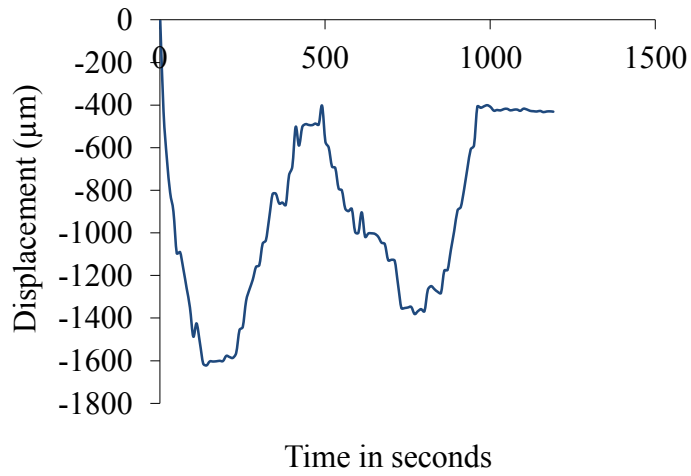
Figure 5.41 Sample with a concentration of 100 cells/ml, Uveal melanoma + Anti-Melan A.
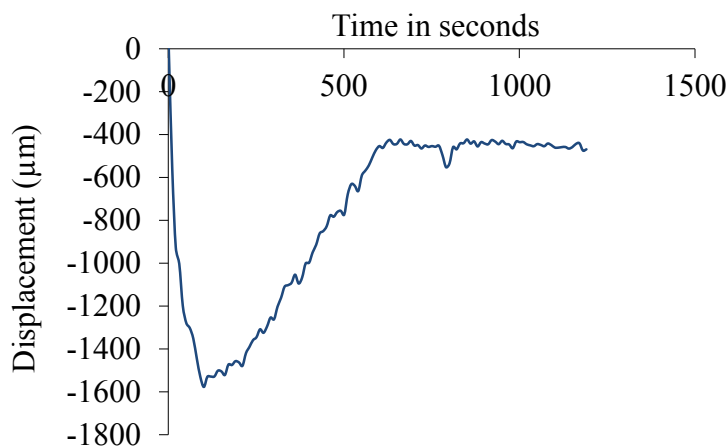
Figure 5.42 Sample with a concentration of 10 cells/ml, uveal melanoma + Anti-Melan A.

The signature of the reaction is typical up to a concentration 1000 cells/ml. Bellow this threshold, the signature becomes atypical and the time of the reaction increases. Both these remarks may be due to the fact that the covalent, ionic, and van der Waals type of bonds responsible for the chemical combination between the antigen and the antibody are more difficult to be established in a scarce environment. A difficulty in establishing the reaction may affect both the moment of initiation and the magnitude of the surface stress. More experiments should be done in order to understand the types of factors that can influence the kinetics of these biochemical combinations, namely the hydrophobicity quality of the surface and the influence of other background factors like temperature, humidity.

5.2.4 Direct measurement of the deflection due to the biochemical reaction

The images presented until now characterize the signature of the biochemical reaction recorded on the surface of the photo sensitive device and not the real deflection of the cantilever sensor. The variation of the parameters of the optical system during each calibration made the task of translating the recorded movement of the laser spot into a real deflection of the tip of the beam a very difficult and laborious task, and, in the absence of the calibration parameters (XY, and XYZ alterations), even impossible.

To establish the real displacement of the cantilever beam an experimental study was initiated. The measurement instrument, Veeco Wyko Non-contact Profilometer NT3300, is able to identify features down in the Å range (3 Å with the Phase Shifting Interferometry (PSI) method and 3 nm with the Vertical Scanning Interferometry (VSI) method.

The working principle of a profilometer is the interferometry, an optical technique in which the light is regarded as an electromagnetic wave. The intensity of the combination of two such waves reflected by the surface of the solid observed is compared to the sum of the initial individual intensities [172]. The evaluation of these two results gives a phase difference that is linearly connected the difference in optical path of the two travelling waves. Generally an individual source of monochromatic or nearly monochromatic light is involved that, through optical means (beam splitters), is divided in two. All the direct measurements of cantilever displacement were performed using the VSI method. This

133

method is a precise non-contact technique able to quantify with high accuracy the surface topography in solids and it is based on laser triangulation. In the VSI method, the white-light source is divided in two separate beams: the test beam and the reference beam [173]. The test beam scans the surface of the sample and, with the help of the same beam splitter, is recombined with the reference one. The resultant wave is analysed in the CCD detector and the characteristics of the sample identified. A schematic of the VSI principle is shown in Figure 5.43. A picture of the working station is presented in the Figure 5.44.
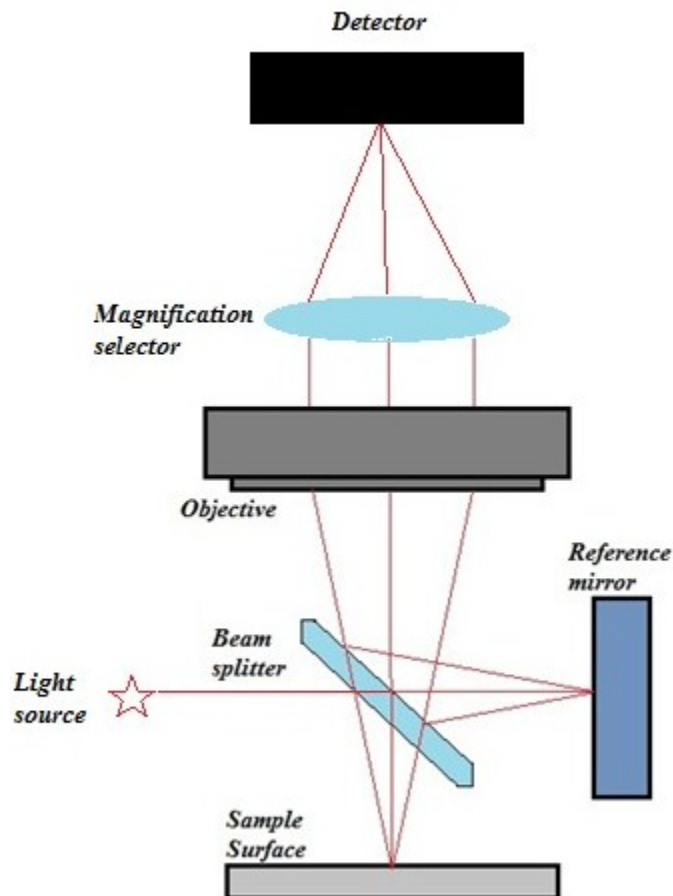
Figure 5.43 VSI principle

Figure 5.44 Profilometer with the sample fixed on the platen.

The biological tests were performed on the reactions of Uveal melanoma (92.1) and prostate antigen (PSA) with their respective conjugates: Anti-Melan A and Anti-PSA. The cantilever beams were cut at a length of 5 millimetres and a width of 0.8 millimeters manually, therefore small variations of length may occur. The material was the same: PVDF coated with 100 nanometers CrAl alloy. A volume of one microliter droplets was placed on the surface of the cantilever by using a manual pipettor and adequate tips.

The working sample was one millilitre and the concentration of one million cells/ml ,in the case of Uveal melanoma, and 100 ng/ml in the case of prostate antigen. The antibodies and the antigens were purchased from Sigma Aldrich Canada. The antibodies Anti-Melan and Anti-PSA were both diluted at a concentration of 1:50. The Uveal melanoma cells used in the experiments (92.1) were cultured in the Concordia University's

laboratory and the samples prepared according to the standard biological protocols. These procedures were described in detail in the subchapter 5.2.

The signature recorded the deflection of the beam in a point situated at a distance of about 50 microns from the tip of the beam to avoid the loss of data in the case of larger deflections occurrences. The sampling rate of one measurement per minute was maintained during the profilometer experiment. This was the duration of a full scanning of the surface of the beam in the VSI mode. The scanning depth was 250 micrometers and the back scan 50 micrometers.

The following signature was obtained for the biochemical reaction between the 92.1 cell line and Anti-Melan A:
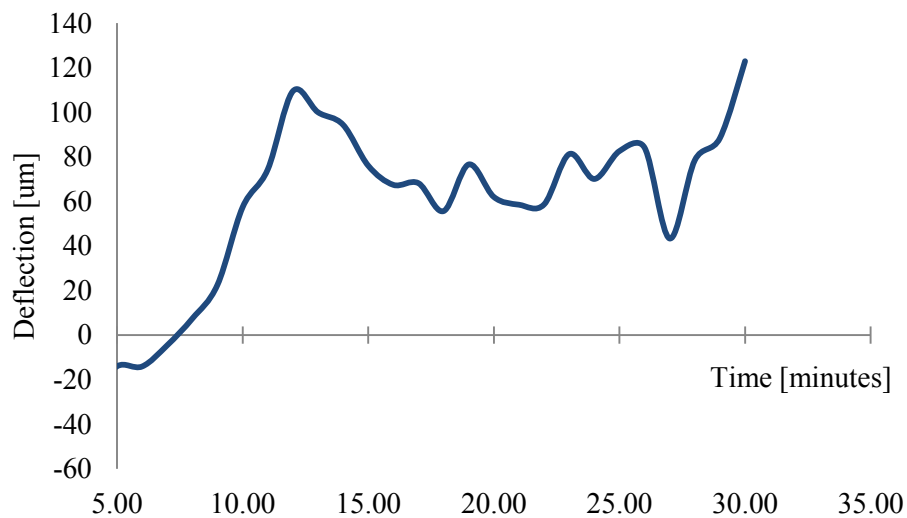
Figure 5.45 Deflection of the beam for 1 µl of 92.1 + Anti-Melan A mixture.

The recorded signature respected the pattern from Figure 5.22 with a downward deflection at the beginning of the reaction followed by an upward movement with several oscillations. However the amplitude of the deflection is different, fact that was expected due to variations in the dimensions of the beam and the volume of sample.

The deflection of the same point on the beam was recorded during the reaction of one millilitre mixture of prostate antigen PSA and its complementary antibody Anti-PSA. The recorded signature is presented in the figure below:
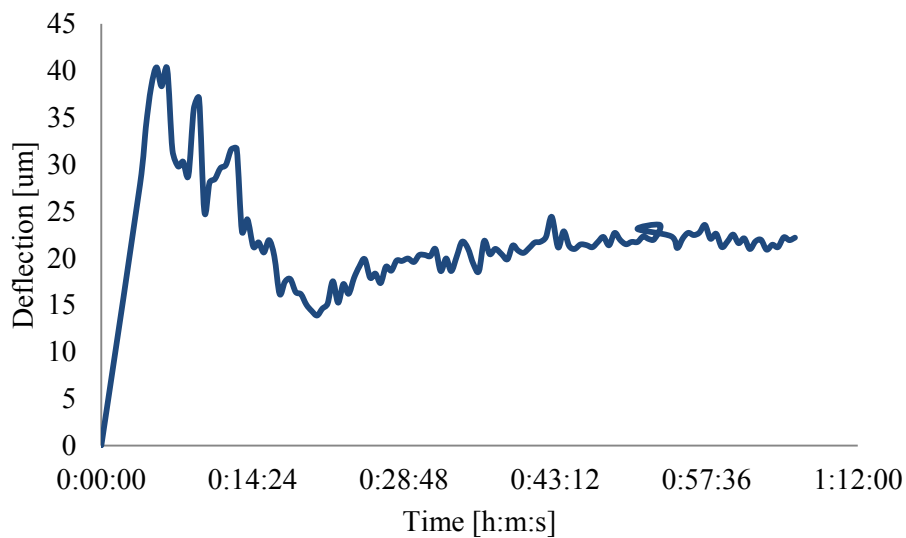
Figure 5.46 Deflection of the beam during for 1 μl of PSA + Anti-PSA mixture.

In this case the pattern recorded in the previous experiments Figure 5.27 is also confirmed. The fact that they are not perfect identical can be justified by the modification of some important parameters compared to the first experiment. A first modification come

137

from the fact that the PC3 cell line contains the PSA receptors in a much smaller concentration than in the case of the prepared solution of PSA antigen (normal level 4-9 ng/ml[174]). Another modification comes from the absence of original PC3 cell line. The presence of the cells generates a gradient of compressive surface stress of a larger magnitude than in the current situation when no cells are present to adhere at the surface of the beam.

A new reaction was generated by combining the two specific antibodies Anti-PSA and Anti- Melan A. The dilution was similar to the one used in the previous reactions, 1:50, dilution recommended by the producer. The signature of this reaction is presented below:
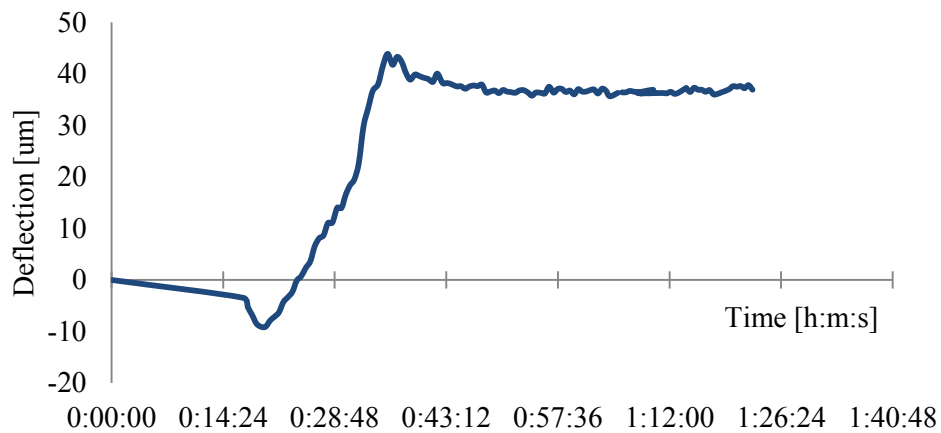
Figure 5.47 Deflection of the beam for 1 µl mixture of Anti-PSA+ Anti-Melan A.

We can conclude that a reaction occurs between the two antibodies but with a low intensity. The initial downward deflection may be initiated by the weight of the droplet, however the presence of the small oscillations indicates a variation of the contact angle and/or the surface stress. This result gives the suggestion that we cannot use a mixture of antibodies to identify an antigen because this secondary reaction may hinder the primary one. More experiments on this area are needed to fully confirm and elucidate this theory.

We verify this hypothesis by treating the Uveal melanoma cell line with the mixture of the antibodies the alteration of the reaction is evident. The deflection pattern changed.
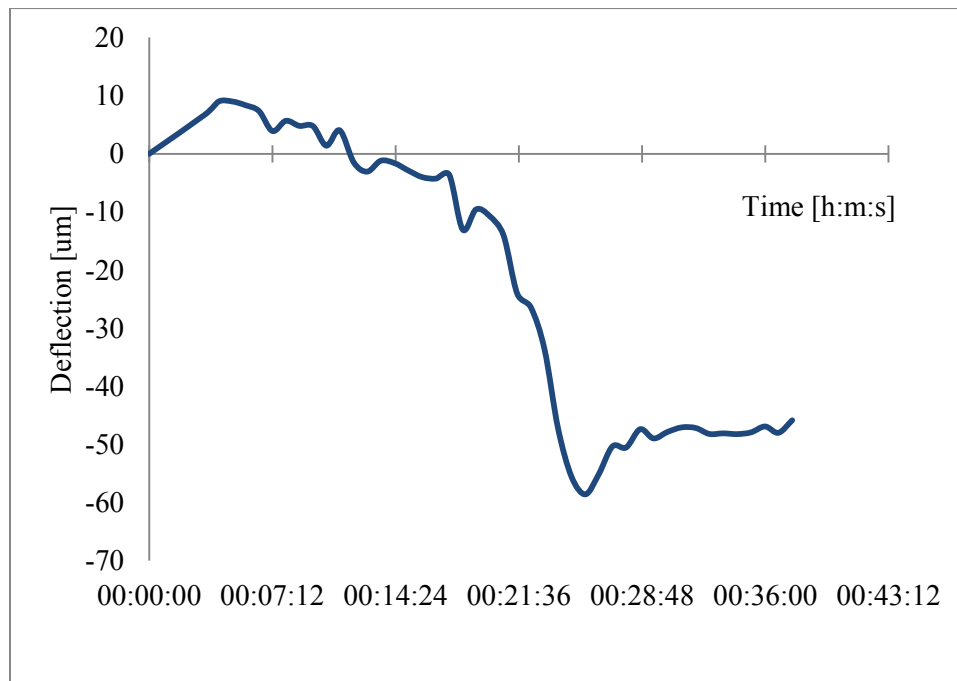
Figure 5.48 Deflection of the beam for 1 µl mixture of Anti-PSA+ Anti-Melan A.

The observation on the reaction PSA + Anti-PSA initiated a new study concerning the influence of humidity on the biochemical reaction. For this purpose a commercial Sunbeam ultrasonic humidifier was used and the resulting variation of humidity was recorded with a Fluke hygro-thermometer capable of measuring the humidity with a precision of 0.1 RH and the temperature with a precision of 0.01 C^o. The deflection of the beam was obtained by placing one millilitre of mixture 92.1+ PSA on the surface of the beam. In the first case the environmental parameters at the beginning of the reaction were 22.5 C^o and 27.4% RH. The temperature and humidity during the test oscillated between these values within a 2% range. During the second measurement the recorded temperature was the same but the humidity was increased at 32.3% RH. The same range of variation of the parameters was recorded during the second test. The recorded signatures are presented in the Figure 5.49 and the Figure 5.50.
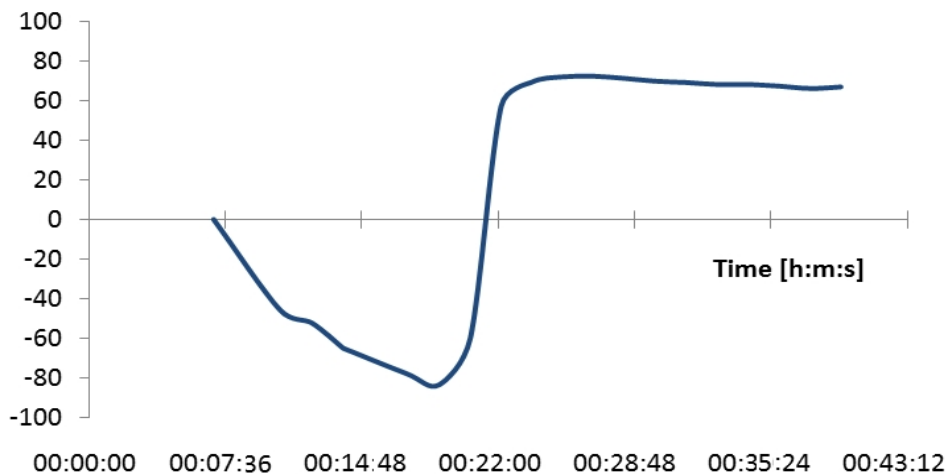
Figure 5.49 The evaporation of 1 µl of 92.1+PSA at a relative humidity of 27.4 %.

As expected the evaporation time increased from 30 minutes in the first case to 45 minutes in the second case. The shape and the amplitude of the recorded deflection changed. This may be either because of a variation in the surface stress or due to the fact that a biochemical reaction initiated. While no reaction seems to take place between the two antigens in the first case, we concluded that the culprit for the alteration of deflection amplitude is the asymmetric variation of either contact angle, surface stress or both parameters.
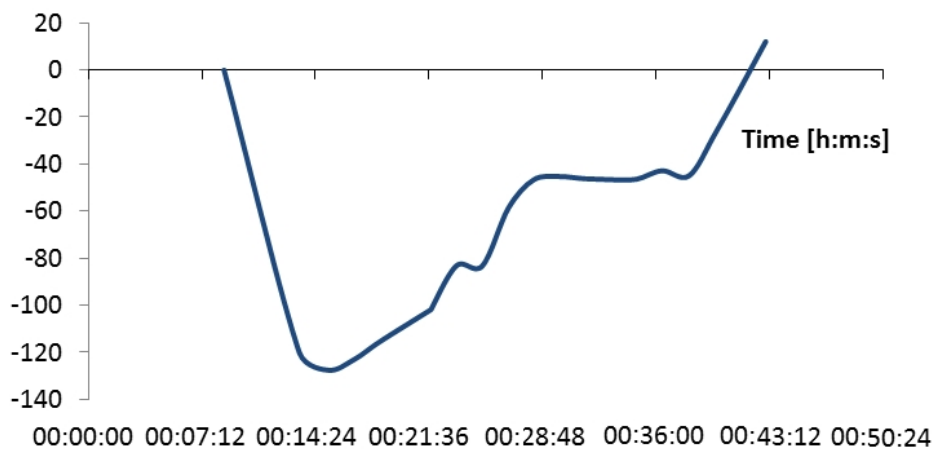
Figure 5.50 The evaporation of 1 µl of 92.1+PSA at a relative humidity of 32.3%.

5.3 Experimental investigation of the contact angle

The last observation created the need for new experiment that studies the contact angle variations during the biochemical reactions. The variation of contact angle from the

standard value is used in in many applications as a method of evaluation of the quality of the surface (its surface energy and hydrophilic or hydrophobic characteristics) [136].

The existence of the contact angle is explained through the balance between the adhesive forces at the liquid-solid interface and the cohesive forces existent in the liquid. The equilibrium of these forces is described by the Young's equation (4-20). The equation is used to define the hydrophilic and the hydrophobic characteristics of a solid surface. A solid surface is called hydrophilic if the surface tension of the liquid is smaller than the surface energy of the solid on which is place. In this case the adhesive forces liquid-solid are larger than the cohesive forces between the molecules of the liquid and consequently the spreading is larger. The contact angle in the case of hydrophilic surfaces is smaller than 90° while the hydrophobic surfaces generate an angle smaller than 90°.

A precise measurement of the contact angle implies expensive devices, optical devices of high resolution where the measurements are performed automatically (goniometric methods) [136, 175, 176] . The equipment used in this experimental study cannot perform comparable measurements. For this reason, the goal of the experiment is to assess the contact angle variation during a biochemical reaction antigen-antibody and not its precise value. In order to achieve this goal, the following equipment is employed.

5.3.1   Experimental procedure

The experiments were initiated in our facility at Concordia University and followed the directions presented by Lamour and all [175]. The experimental setup consists of the following components:

- a basic digital camera (in our case Canon PowerShot A2300 16MP);

- an Aluminum breadboard, 8" x 8" x ½" from Thorlabs;

- two post holders with spring-loaded thumbscrew from Thorlabs;

- plano-convex lens , d= 1" and confocal distance of f= 50 mm from Thorlabs;

- lens mount with a diameter of 1" with one retaining ring from Thorlabs;

- X-Y-Z (1") positioner from Thorlabs.

The optical system was protected by a cardboard box coated with aluminum in order to shield the setup from the incident light and to slow down the evaporation. A commercial lamp of 25 W is placed outside the box and opposite to the sample to provide the necessary lightning. The light passes through a diffuser made of tracing paper in order to highlight the contour of the droplet.

The setup is shown in a schematic in the Figure 5.51 and a side and interior view in the Figure 5.52 and Figure 5.53.
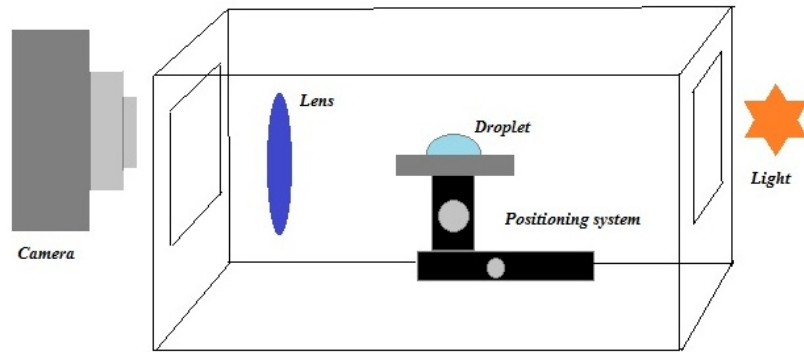
Figure 5.51 The schematic of the experimental setup.
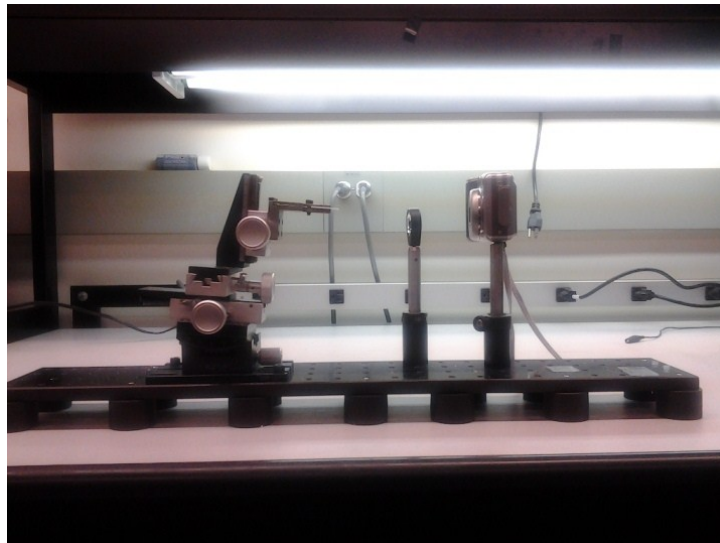
Figure 5.52 Front view of the experimental setup for the experimental study of the

capillary angle variation.

Figure 5.53 Interior view of the experimental setup for for the experimental study of the contact angle variation.

The antibody solution in a proportion of 1:50 was prepared by mixing one millilitre of the solution of RPMI-1640 containing 5 % fetal bovine serum (FBS), 1% Penicillin-Streptomycin with Anti- Melan A. The same procedure was followed for the preparation of the prostate antibody Anti –PSA. The PSA sample was diluted at a concentration of 100 ng/ml. The volume of mixture used in each test was either one or two microliters, from which half was the volume of the antigen and the other half the antibody.

The 92.1cell sample (the antigen) was prepared before each test. The monolayer of cells was detached from the wall of the flask with trypsin 0.05%, centrifuged and the resulting pellet diluted in 1 ml of RPMI-1640. After the counting of the cells the concentration of sample was adjusted at 1 million cells per milliliter.

145

The liquid sample is deposited on a PVDF foil that was prior washed three times with a mixture of ethanol and propanol and finally placed in an ultrasound cleaner for 15 minutes. Several number of picture were taken during the evaporation process. The following volumes of liquid sample were used: 1 ml of 92.1 and 2 ml of each of the following components or mixture: 92.1 +Anti-Melan A, 2 ml of Anti-Melan-A with Anti-PSA, Anti-PSA, Anti-PSA with PSA, PBS and RPMI 1640. Each experiment was repeated three times.

The acquired images were processed in order to increase the contrast of the picture of the droplet edges and the measurements were performed by the ImageJ software. The "Drop analysis" plugin was used to measure the contact angle from the acquired images by generating a B-spline active contour following the shape of the droplet. The value of the contact angle was generated automatically by the software. Each measurement was repeated three times and the average value recorded. An illustration of the procedure is shown in Figure 5.54.
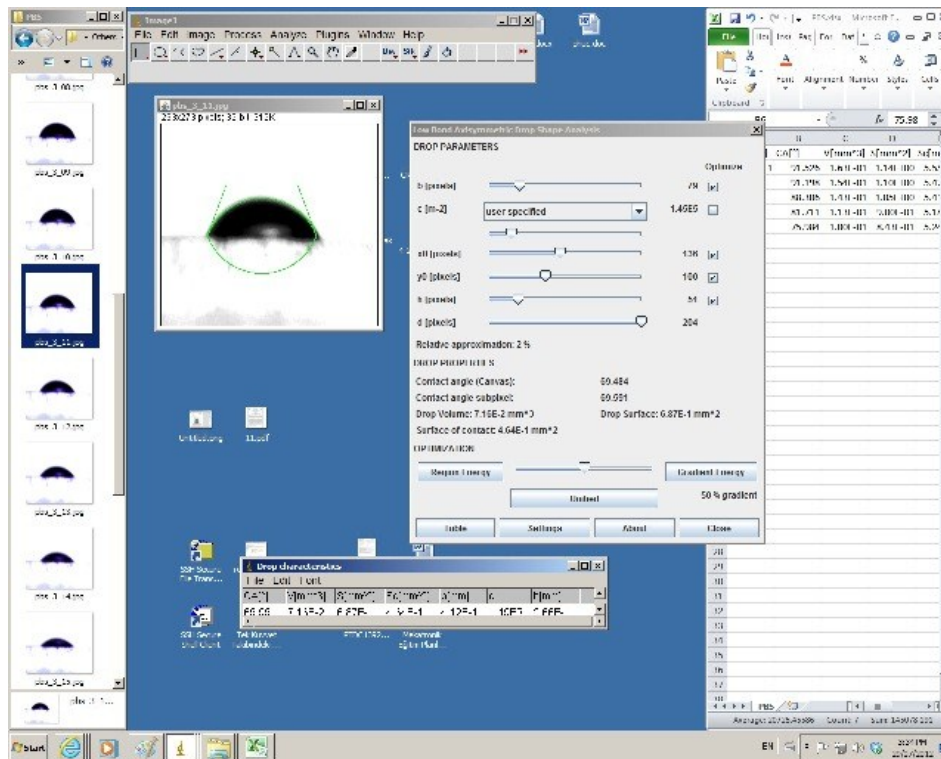
Figure 5.54 ImageJ measurement procedure of the contact angle.

An example of the evaporation process is shown in Figure 5.55. In this phase only the contact angle is variable while the contact area is pinned on the substrate.
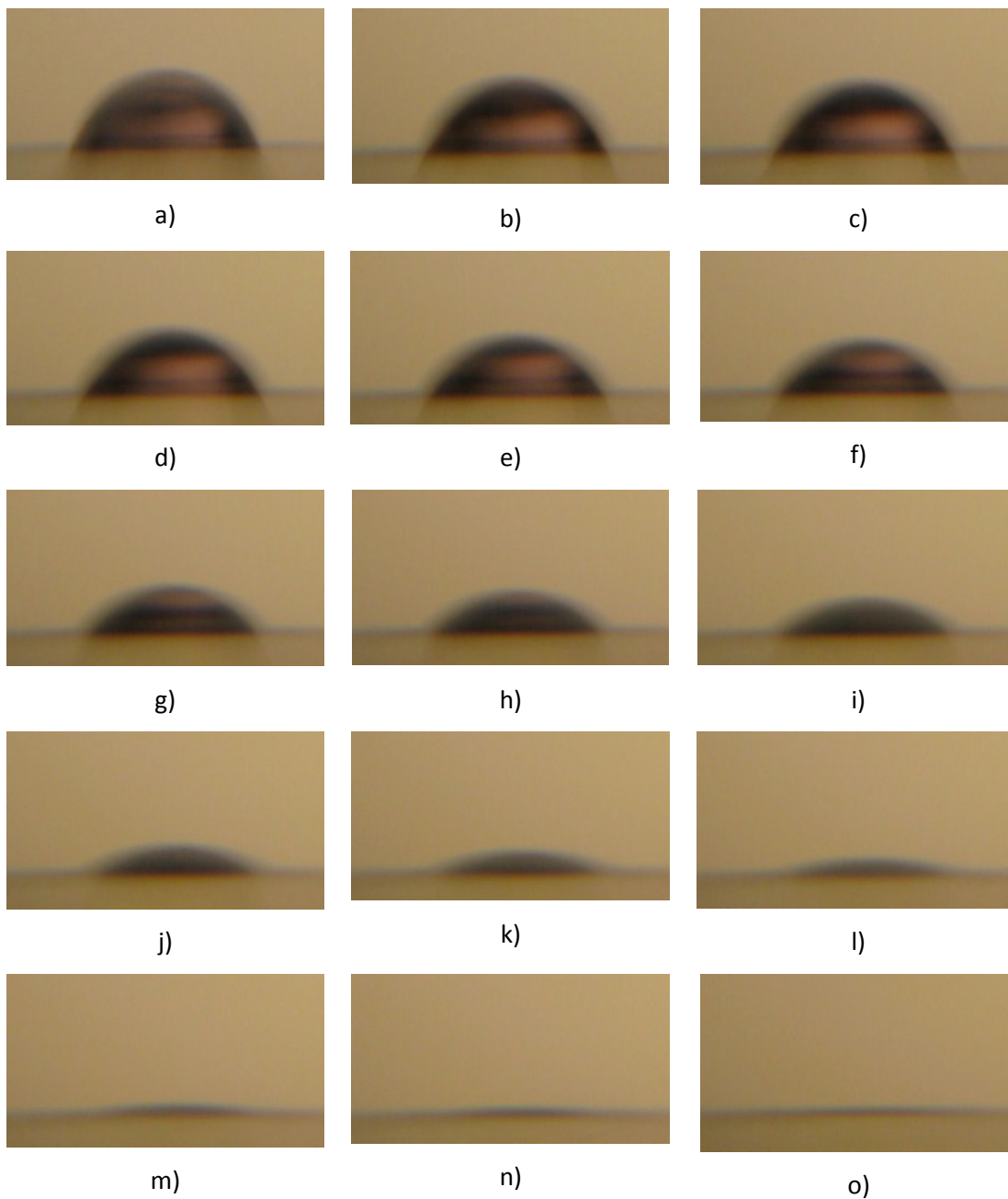
Figure 5.55 The stages of evaporation from a) to o) of a 2 ml droplet of the Anti-PSA + Anti-Melan A.

148

In the last stage of the evaporation, however, the contact area diminishes while the contact angle remains almost unchanged.
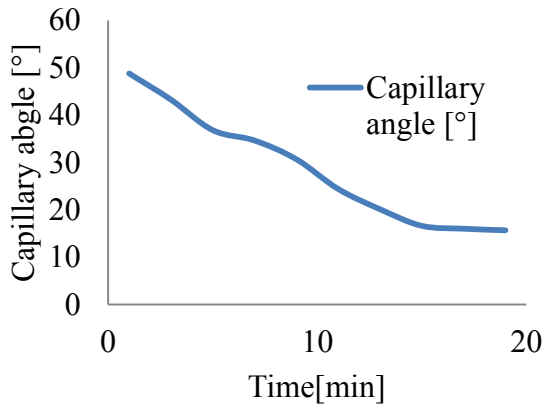
Figure 5.56 Capillary angle variation 92.1.
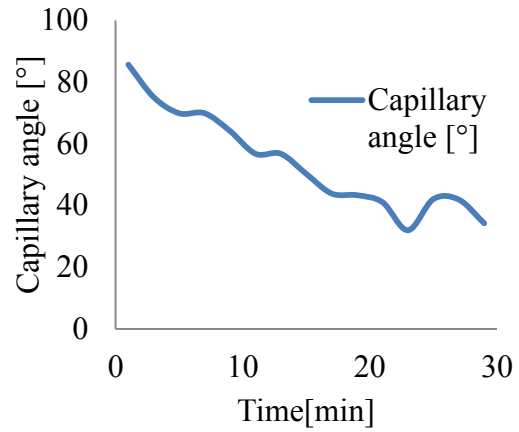
Figure 5.57 Capillary angle variation PSA.
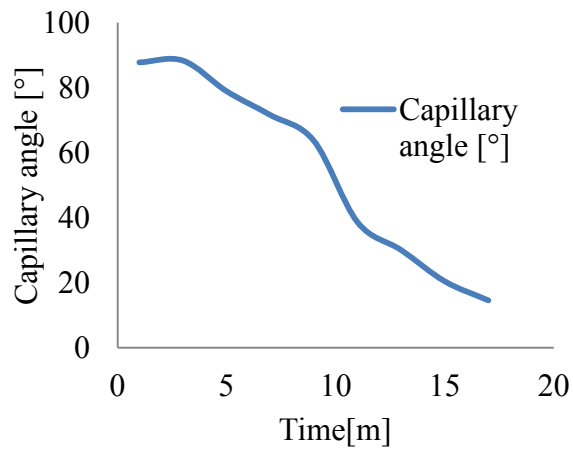
Figure 5.58 Capillary angle variation RPMI.
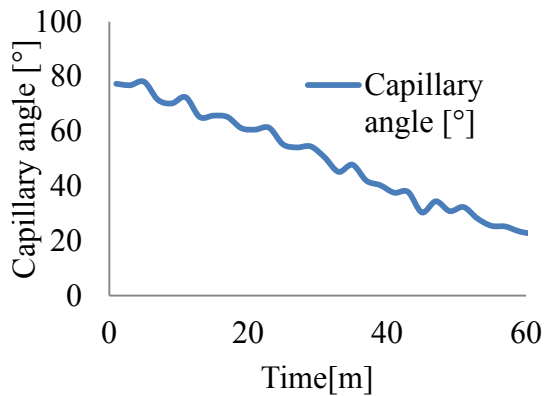
Figure 5.59 Capillary angle variation Anti-Melan A +Anti-PSA.
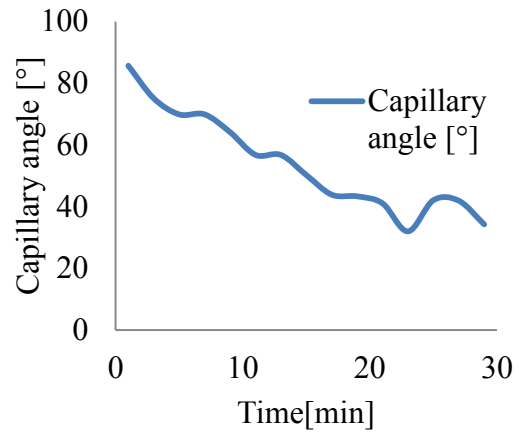
Figure 5.60 Capillary angle variation PSA+Anti-PSA.
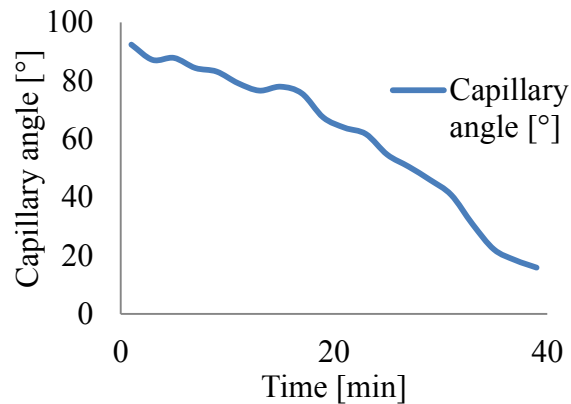
Figure 5.61 Capillary angle variation: 92.1+Anti-MelanA.

The variation of the contact angle is shown in the Figure 5.56 to Figure 5.61 . In the first three plots is illustrated the behavior of the samples containing single specimens, while in the last three, the sample consists of a mixture of antibody and antigens. Studying these plots one cannot conclude that a sample containing a mixture of specimen presents the peak

variations anticipated due to the observation of the biochemical reactions from the previous subchapters. Small peaks are visible both in in the case of the evaporation of single specimens and in the case when multiple specimen samples were evaporating and interacting biochemically in the same time.

This experiment contradicts the hypothesis that the variation of the contact angle is one important factor responsible for the particular pattern of the signature of the biochemical reactions presented earlier in this chapter found in the experiments. The magnitude of the contact angle decreases much smoother than the expect pattern.

More experiments with other pairs of analytes can contradict this finding but for the considered combinations only the variation of the surface stress seems to be responsible for the unpredictable but repeatable pattern of the rotation of the tip of the beam.

5.4   Sources of errors in the experimental work

The main sources of errors observed during the experimental phase are instrumental errors, human errors and sample preparation errors. In the following paragraphs each of them will be discussed.

The instrumental errors can appear due to the inadequate tuning of the instruments or the incorrect calibration of the optical equipment or laboratory apparatus. Another major source of instrumental error is the incorrect or the poor calibration of the measuring instruments. These types of inaccuracies can be noticed especially in the case of the

laboratory pipettors. If the profilometer is not calibrated at the beginning of each session, the readings can present large inconsistencies.

An important source of error is the insufficient cleaning of the substrate of the cantilever beam. The impurities found on the substrate can generate, in contact with the liquid sample, a series of physical and chemical phenomenon that alters the quality of the experiment. A good example of such an error is illustrated below. The droplet of RPMI in the presence of the impurities presents a strange pattern of evaporation, as seen in Figure 5.62 a)-d), most probably due to the alteration of the surface stress or to the incidence of unwanted capillarity phenomena.

a)   b)   c)   d)
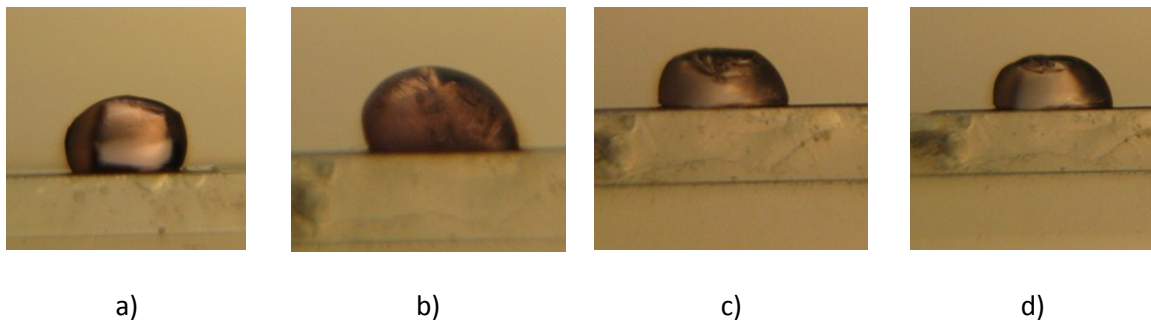
Figure 5.62 The effect of surface impurities on the evaporation of 2 ml of RPMI-1640.

Human errors can appear due to an inappropriate manipulation of the laboratory instruments, wrong readings or because of the incorrect placement of the liquid sample on the substrate. In the case of the cantilever sensor, a sample that is two large or misplaced (deposited on a position other than the center of the beam) can lead to the failure of the experiment (Figure 5.63).
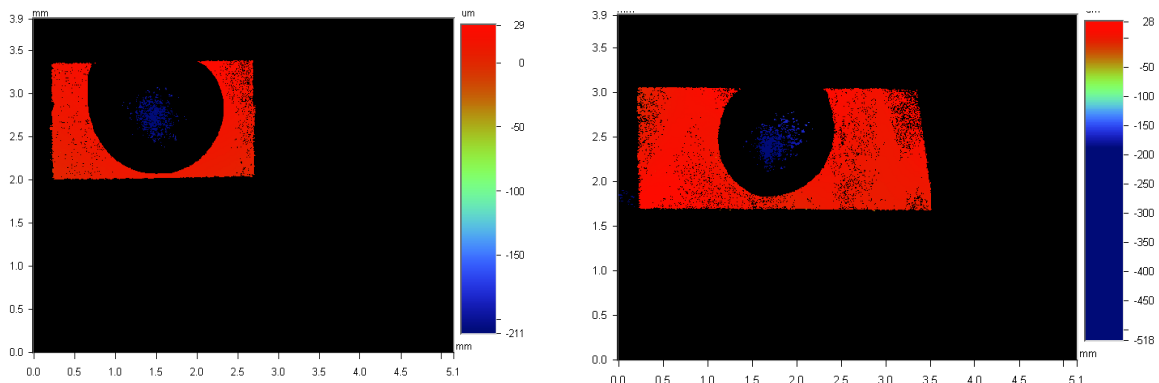
Figure 5.63 Errors of measurement with the profilometer.

The contamination of the liquid sample can also modify irreversibly the results of the experiment. From this point of view, as a precaution, most of the samples were prepared and manipulated in the clean room existent in our facilities.

5.5 Conclusion and summary

The experimental work presented in this chapter shows that the antibody-antigen reaction generates a unique signature for each pair of biochemical subspecies considered even when the concentration of the given analytes varies. A proof for this statement was given through the qualitative and quantitative tests performed with a large spectrum of complementary pairs of reactants. The pattern of the reaction was found using the indirect optical lever method and validated by direct interferometric measurement methods .

The experiments on the variation of the contact angle, owing to the complex concomitent phenomena of evaporation and chemical reaction, did not confirmed the

hypothesis that assumed the variation of this parameter to be one of the main factors influencing the abnormal deflection pattern of the cantilever beam during the biochemical reaction.

Several sources of errors were identified and analysed during the experimental work and the methods of counter their incidence suggested. Most of them are avoidable being in ceneral cause by human errors in the manipulation of the instruments or the sample.

Chapter 6:   Dielectrophoretic centering

6.1 Introduction

Before the fractioning of the liquid into droplets we need to make sure that the liquid sample includes the circulating tumor cells that are to be investigated. To solve this task, prior to the droplet generation phase, the centering stage is introduced. At the end of this step the cells can be directed to the interrogation point was the presence or the absence of the biomarker is acknowledged. An important adjacent result of the centering phase consists in the fact that the clustering of the cells is inhibited. The clogging of the cells is an unwanted phenomenon, especially if the flow takes place in narrow channels, where clogging can occur easier.

The centering of flowing particles can be acquired hydro dynamically by sheath flow[177, 178] or dielectrophoretically by applying the non-uniform electric field created between two electrodes by a sinusoidal signal at a certain frequency [179-181].

The phenomenon of dielectrophoresis (DEP) refers to the motion of particles suspended in a liquid under the action of a non-uniform electric field. The necessary condition for the suspended particles to move is to be neutral from an electric point of view but, in the same time, polarizable. They will move under the action of a force generated by the non-uniform, force, with the magnitude and direction correlated to the frequency and

155

the amplitude of the applied AC signal and to the electric properties of the particle and the surrounding fluid [182].

In a uniform electric field a suspended polarizable particle is motionless due to the fact that each half of the particle is polarized at the same value so the total resultant induced dipole force is zero [183]. In a non-uniform electric field, the generated dipole forces have different values and a displacement results due to the resultant force that points either toward the region of the channel with high electric fields (positive DEP or pDEP, when the particle is more polarized than the surrounding medium), or towards the regions with low electric field when the suspended particle is less polarized than the surrounding medium (negative DEP or nDEP) . The induction of the dielectrophoretic force is explained in Figure 6.1.
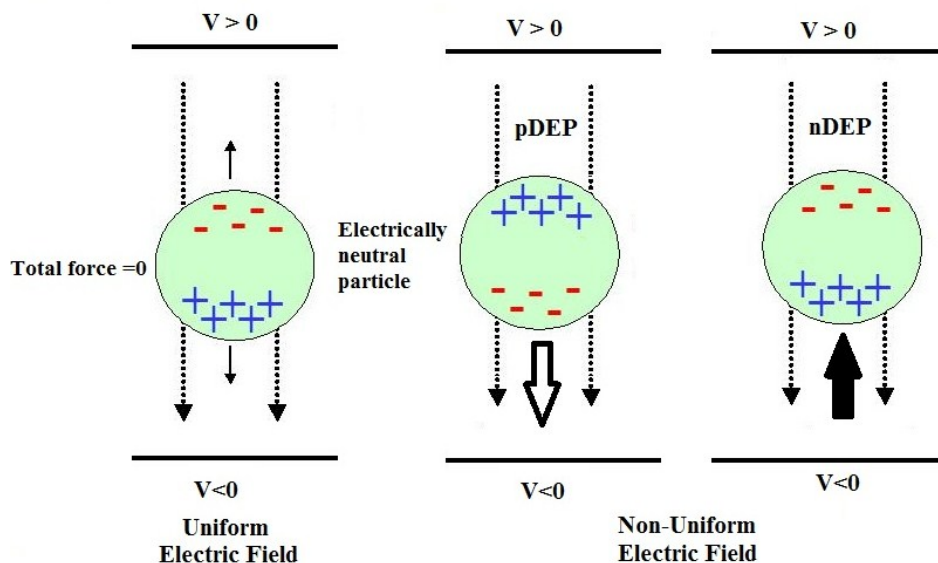
Figure 6.1 Positive and negative dielectrophoresis (adapted after [184]).

The non-uniform electric field is generated by placing the electrodes in a predetermined configuration in the microchannel and applying a difference of potential between them at a predetermined amplitude and frequency. The description of the spatial distribution of the electric field helps to understand the strength of the dielectrophoretic force acting upon the submerged particles, force that together with the buoyancy, drag and the gravitational force contribute to the characterisation of the movement of the cell.
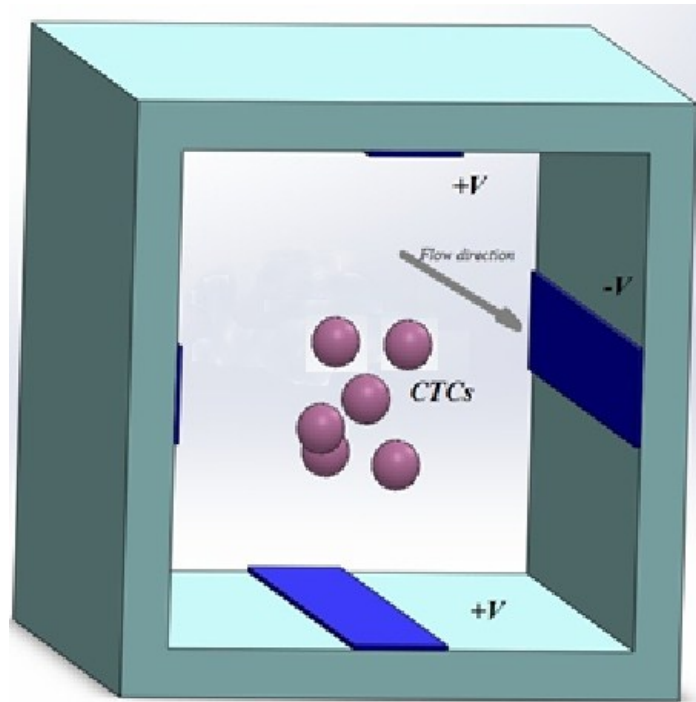
Figure 6.2 nDEP centering principle in a rectangular cross-sectioned microchannel.

In literature, the distribution of the DEP force generated by a set of electrodes in various configurations was determined analytically by several groups of researchers [185-190] by using various mathematical approaches like:

1. Green's theorem;

2. Schwarz-Cristoffel mapping;

3. Finite element method.

4. Weighted-least square differences schemes;

5. Wiener-Hopf method;

6. Fourier series.

The phenomenon of dielectrophoresis and its applications proved to be extremely useful for the purpose of our group project. It is used in the transport and the separation of the rare species from blood (nDep and pDep) [191], for centering (nDEP) and characterization of the cells (nDep and pDep) [192] especially for the fact that DEP is fully compatible with the transport and the manipulation of living cells. Owing to this interest, our research group already found analytical solutions of the spatial variation of the dielectrophoretic force for microchannels presenting different type of electrodes patterns [182, 191, 193] by using the Fourier series method.

In order to establish the parameters of DEP force, electric field and electric potential in a microchannel with squared cross section, a theoretical study is performed considering the physical characteristics of the microchannel in which the cells are submerged (dimensions and the placement of the electrodes). The distribution of the electric field was determined by semi-analytical formulations. The solution is in good agreement with the numerical one performed with commercial multiphysics software (COMSOL).

6.2 Analytical approach

The dielectrophoretic force acting on a spherical particle (cell in our case) suspended in a liquid in a non-uniform electric field has the following expression [183]:

$$F_{DEP} = 2\pi\varepsilon_m R^3 \, \text{Re}[CM](\nabla E^2)$$
(6.1)

where:

ε_m represents the absolute permittivity of the surrounding medium ($\varepsilon_m = \varepsilon_0\varepsilon_r$, $\varepsilon_0 =$ represents the permittivity of the vacuum and ε_r the dielectric constant of the medium);

R is the radius of the particle;

Re$[CM]$ is the real part of the Claussius-Mossoti factor varies from -0.5 to 1 [183] ,

$$\text{Re}[CM] \approx \varepsilon_m \left(\frac{\varepsilon_c - \varepsilon_m}{\varepsilon_c + 2\varepsilon_m}\right) \, , \, \varepsilon_c \text{ is the relative permittivity of the cell.}$$

The electric field is given by the Gauss's law:

$$\nabla.E = \frac{\rho}{\varepsilon_0}$$
(6.2)

where with ρ we denoted the electric charge density that in our case is zero (both the free and the bounded charges).

Due to the fact that the charge density in this case is zero, the equation (6.2) becomes:

$$\nabla . \boldsymbol{E} = 0 \tag{6.3}$$

In order to relate the electric field with the electric potential, the Maxwell's equation, taken in the quasi-static form, is used as follows:

$$\boldsymbol{E} = -\nabla \varphi \tag{6.4}$$

In the equation (6.4), φ represents the electric potential of the electrode.

By substituting the equation (6.3) into (6.4) the following expression is generated:

$$\frac{\partial^2 \varphi}{\partial x^2} + \frac{\partial^2 \varphi}{\partial y^2} + \frac{\partial^2 \varphi}{\partial z^2} = 0 \tag{6.5}$$

Taking only the cross-section of a rectangular micro-channel in consideration, the relation (6.5) is reduced to the 2D form as:

$$\frac{\partial^2 \varphi}{\partial x^2} + \frac{\partial^2 \varphi}{\partial y^2} = 0 \tag{6.6}$$

6.3 Boundary conditions

Figure 6.3 shows the cross-section of the entire microfluidic channel. The side of the channel is equal to *2L* and the length of the electrodes *2l*. The width and the thickness of the electrodes is negligible compared to their length. The electrodes have the electric potential $-V_0$ and $-V_0$ and the walls are considered electrically insulated.
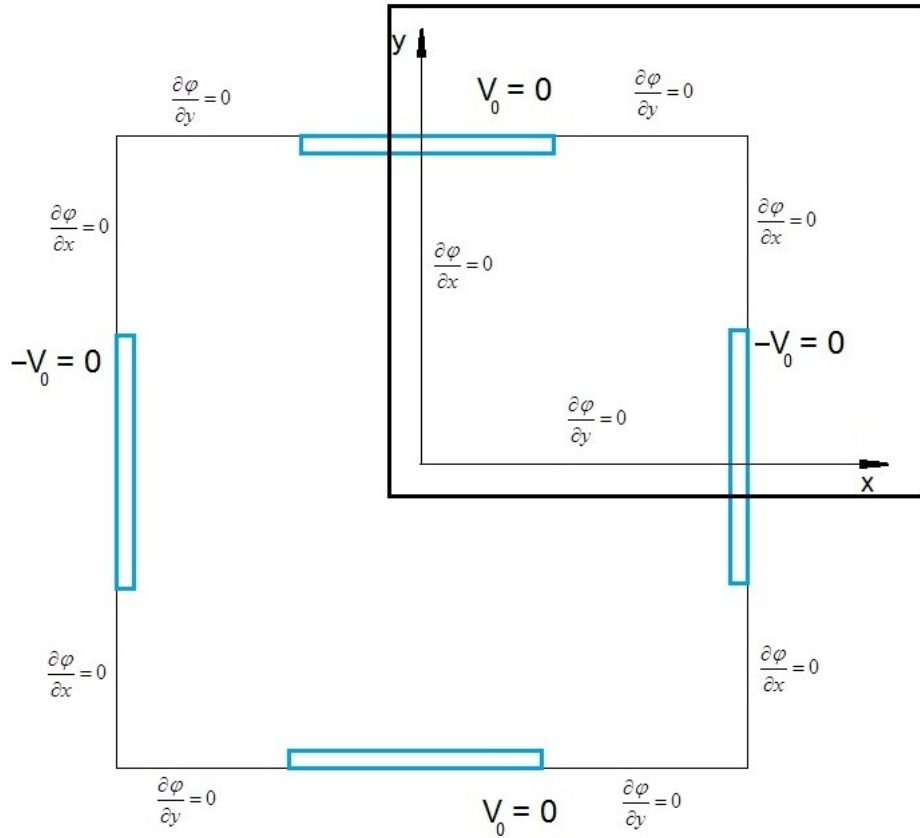
Figure 6.3 The cross-section of the rectangular microchannel.

From the above figure it is evident the existence of a symmetry of the electrical parameters above the x and y axes of the illustrated coordinate system. This observation enables a simplification of the problem by considering just the unit segment (Figure 6.3) from the first quadrant of the coordinate system when solving the equation. The height and the width of the unit segment are considered equal to L and the length of the four cross-

section electrodes is l. The length of the electrode is 50 microns, its thickness T≈100 nanometers and the side of the squared microchannel segment is 100 micrometers.

The following boundary conditions are considered:

a) The upper electrode of the squared unit segment is at the electric potential V_0.

b) The lateral electrode has the electric potential $-V_0$.

c) The upper part of the micro-channel is made of glass. Therefore, this area is considered electrically insulated. From the same reason the left, right and bottom side of the segment are also considered electrically insulated.

d) The electric potential at the right upper side is assumed to be zero because of the symmetry of the electrodes

e) The chose unit segment is symmetrical about both x and y axes.
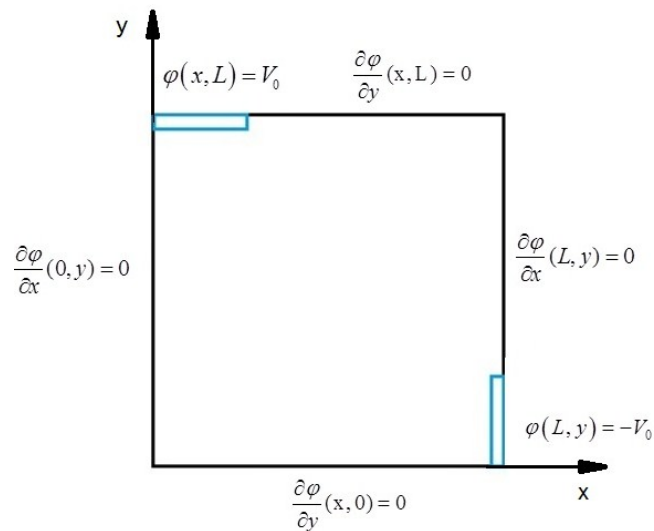
Figure 6.4 Boundary conditions for the square unit segment of the channel cross-section.

The above boundary conditions are expressed by the following expression:

$$\varphi(x,L)=V_0 \qquad\qquad 0\le x\le\frac{l}{2} \qquad\qquad (6.7)$$

$$\varphi(L,y)=-V_0 \qquad\qquad 0\le y\le\frac{l}{2} \qquad\qquad (6.8)$$

$$\frac{\partial\varphi}{\partial y}(x,L)=0 \qquad\qquad \frac{l}{2}\le x\le L \qquad\qquad (6.9)$$

$$\frac{\partial\varphi}{\partial x}(L,y)=0 \qquad\qquad \frac{l}{2}\le y\le L \qquad\qquad (6.10)$$

$$\frac{\partial\varphi}{\partial y}(x,0)=0 \qquad\qquad (6.11)$$

$$\frac{\partial\varphi}{\partial x}(0,y)=0 \qquad\qquad (6.12)$$

The following normalized dimensionless parameters will be used in order to normalize the equation with respect to the specific coordinates:

$$\bar{x}=\frac{x}{L}$$

$$\qquad\qquad (6.13)$$

$$\bar{y}=\frac{y}{L}$$

The two dimensionless parameters inserted into the equation (6.6) and the boundaries conditions (6.7) - (6.12) will generate the following relations:

163

$$\frac{\partial^2 \varphi}{\partial \bar{x}^2} + \frac{\partial^2 \varphi}{\partial \bar{y}^2} = 0 \qquad\qquad (6.14)$$

$$\varphi(\bar{x},1) = V_0 \qquad\qquad 0 \le \bar{x} \le \frac{l}{2L} \qquad\qquad (6.15)$$

$$\varphi(1,\bar{y}) = -V_0 \qquad\qquad 0 \le \bar{y} \le \frac{l}{2L} \qquad\qquad (6.16)$$

$$\frac{\partial \varphi}{\partial \bar{y}}(\bar{x},1) = 0 \qquad\qquad \frac{l}{2L} \le \bar{x} \le 1 \qquad\qquad (6.17)$$

$$\frac{\partial \varphi}{\partial \bar{x}}(1,\bar{y}) = 0 \qquad\qquad \frac{l}{2L} \le \bar{y} \le 1 \qquad\qquad (6.18)$$

$$\frac{\partial \varphi}{\partial \bar{y}}(\bar{x},0) = 0 \qquad\qquad (6.19)$$

$$\frac{\partial \varphi}{\partial \bar{x}}(0,\bar{y}) = 0 \qquad\qquad (6.20)$$

The boundary condition (6.17) and (6.18) can be represented as:

$$\varphi(\bar{x},1) = \varphi_e \qquad\qquad \frac{l}{2L} \le \bar{x} \le 1 \qquad\qquad (6.21)$$

164

and

$$\varphi(1,\bar{y})=\varphi_f \qquad\qquad \frac{l}{2L}\leq\bar{y}\leq 1 \qquad\qquad (6.22)$$

6.4 Solution of the equation

The solution of the equation will be determined using the technique of separation of variable by assuming as solution the electrical potential function φ, under this hypothesis that the function φ has two components: one linear and one another harmonic.

By applying the principle of superposition, the function consists of a sum of two constituents, φ_1 and φ_2:

$$\varphi=\varphi_1+\varphi_2 \qquad\qquad (6.23)$$

We assume the solution to be expressed by the following functions:

$$\varphi_1(\bar{x},\bar{y})=A_1+B_1\bar{x}+C_1\bar{y}+D_1\overline{xy}+F_1(\bar{x})G_1(\bar{y}) \qquad\qquad (6.24)$$

and

$$\varphi_2(\bar{x},\bar{y})=A_2+B_2\bar{x}+C_2\bar{y}+D_2\overline{xy}+F_2(\bar{x})G_2(\bar{y}) \qquad\qquad (6.25)$$

where A1, A_2, B_1, B_2, C_1, C_2, D_1 and D_2 are constants , while F_1, F_2, G_1, and G_2 are functions of one variable .

We will proceed now with the determination of the first part φ_1 of the total potential function φ.

$$
\begin{aligned}
\varphi_1(\bar{x}, \bar{y}) &= A_1 + B_1\bar{x} + C_1\bar{y} + D_1\overline{xy} + F_1(\bar{x})G_1(\bar{y}) = \\
&= A_1 + B_1\bar{x} + C_1\bar{y} + D_1\overline{xy} + \\
&+ \sum_{n=1}^{\infty}\left(a_1\sin(k_1\bar{x}) + a_2\cos(k_1\bar{x})\right)\left(b_1\sinh(k_1\bar{x}) + b_2\cosh(k_1\bar{x})\right)
\end{aligned}
\tag{6.26}
$$

The following equation will hold:

$$
\frac{\partial^2\varphi_1}{\partial\bar{x}^2} + \frac{\partial^2\varphi_1}{\partial\bar{y}^2} = 0
\tag{6.27}
$$

The boundary conditions for this function are:

$$
\varphi_1(\bar{x},1) = V_0 \qquad\qquad 0 \le \bar{x} \le \frac{l}{2L}
\tag{6.28}
$$

$$
\varphi_1(\bar{x},1) = \varphi_e \qquad\qquad \frac{l}{2L} \le \bar{x} \le 1
\tag{6.29}
$$

$$
\varphi_1(1,\bar{y}) = 0
\tag{6.30}
$$

$$
\frac{\partial\varphi_1}{\partial\bar{y}}(\bar{x},0) = 0
\tag{6.31}
$$

$$
\frac{\partial\varphi_1}{\partial\bar{x}}(0,\bar{y}) = 0
\tag{6.32}
$$

166
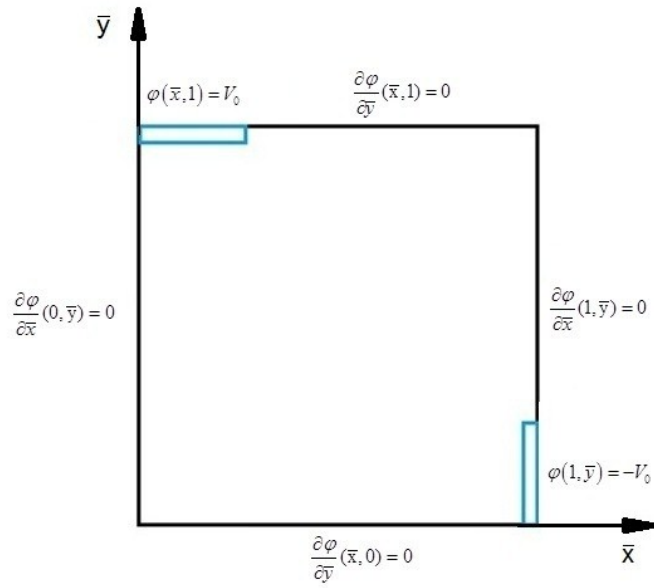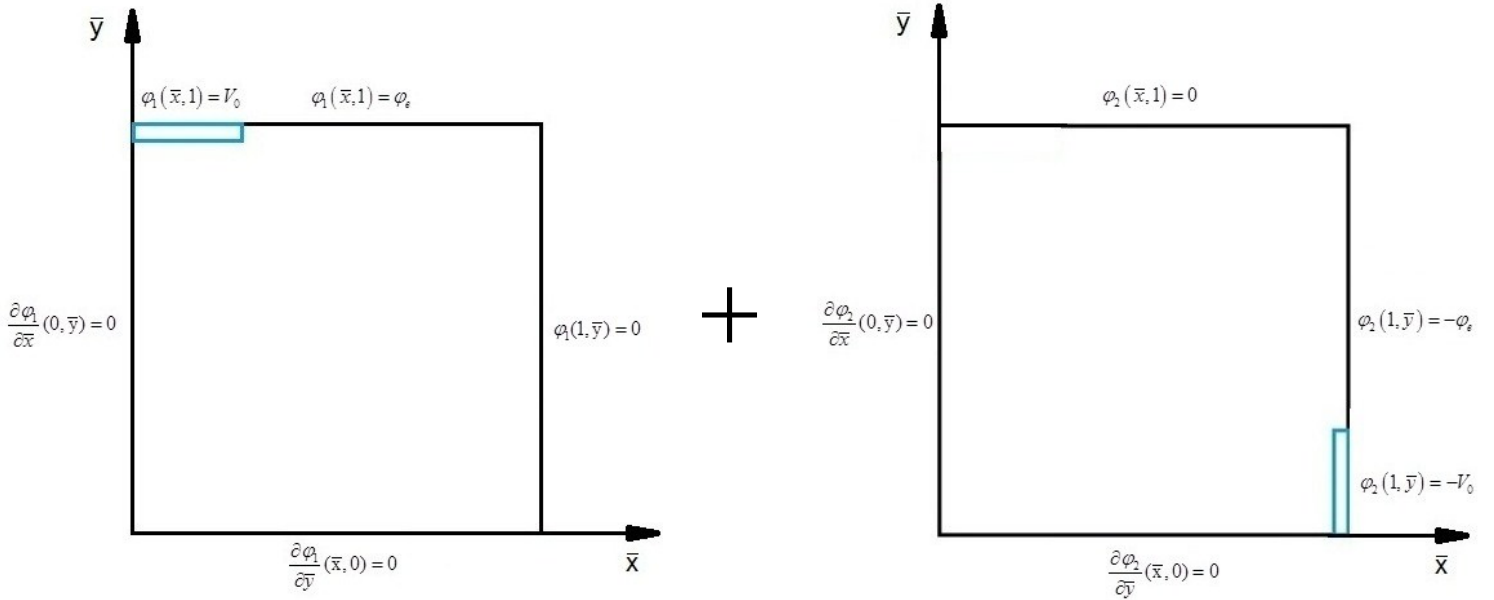
Figure 6.5 The superposition principle applied to the unit segment.

In the equation (6.24) we apply the boundary condition (6.32):

$$\frac{\partial \varphi_1}{\partial \bar{x}}(0,\bar{y}) = B_1 + D_1\bar{y} + F_{1x}(0)G_1(\bar{y}) = 0 \tag{6.33}$$

To satisfy the equation (6.33) the constants B_1 and D_1 should be zero and the differentiation with respect to $\bar{x}$ of the function F_1 takes also the value zero at $\bar{x}=0$.

$$B_1 = 0; D_1 = 0; \tag{6.34}$$

$$F_{1x}(0) = 0 \tag{6.35}$$

The boundary condition (6.31) will generate the value of the constant C_1 and the derivative with respect to $\bar{y}$ of the function G_1 when $\bar{y}$ takes the value 0:

$$\frac{\partial \varphi_1}{\partial \bar{y}}(\bar{x},0) = C_1 + D_1\bar{x} + F_1(\bar{x})G_{1y}(0) = C_1 + F_1(\bar{x})G_{1y}(0) = 0 \tag{6.36}$$

$$\begin{aligned} C_1 &= 0; \\ G_{1y}(0) &= 0 \end{aligned} \tag{6.37}$$

The boundary condition given by (6.30) yields:

$$\begin{aligned} \varphi_1(1,\bar{y}) &= A_1 + B_1\bar{x} + C_1\bar{y} + D_1\overline{xy} + F_1(\bar{x})G_1(\bar{y}) = \\ &= A_1 + F_1(1)G_1(\bar{y}) = 0 \end{aligned} \tag{6.38}$$

This condition is satisfied only if:

$$F_1(1) = 0$$
$$A_1 = 0$$

(6.39)

By substituting equation (6.24) in the Laplace equation (6.14), the following expression results:

$$F_1(\overline{x})G_{1\overline{y}\overline{y}}(\overline{y}) + F_{1\overline{x}\overline{x}}(\overline{x})G_1(\overline{y}) = 0$$

(6.40)

The expression (6.40) is equivalent to:

$$\frac{F_{1\overline{x}\overline{x}}(\overline{x})}{F_1(\overline{x})} = -\frac{G_{1\overline{y}\overline{y}}(\overline{y})}{G_1(\overline{y})} = k_1^2 \, or$$

$$\frac{F_{1\overline{x}\overline{x}}(\overline{x})}{F_1(\overline{x})} = -\frac{G_{1\overline{y}\overline{y}}(\overline{y})}{G_1(\overline{y})} = -k_1^2$$

(6.41)

If the first equality in (6.41) is chosen the following two ordinary differential equations are generated:

$$F_{1\overline{x}\overline{x}}(\overline{x}) - k_1^2 F_1(\overline{x}) = 0$$

(6.42)

$$G_{1\overline{y}\overline{y}}(\overline{y}) + k_1^2 G_1(\overline{y}) = 0$$

(6.43)

Applying the boundary condition to (6.42) only the trivial solution is obtained. Subsequently the second equality in (6.41) holds. The following differential equations will yield the solutions $F_1(\overline{x})$ and $G_1(\overline{y})$ as follows:

$$F_{1\overline{x}\overline{x}}(\overline{x}) + k_1^2 F_1(\overline{x}) = 0$$

(6.44)

$$G_{1\overline{y}\overline{y}}\left(\overline{y}\right) - k_1^2 G_1\left(\overline{y}\right) = 0 \tag{6.45}$$

$$F_1\left(\overline{x}\right) = a_1 \cos(k_1 \overline{x}) + a_2 \sin(k_1 \overline{x}) \tag{6.46}$$

The function of single variable $F_1\left(\overline{x}\right)$ is assumed to have the following expression:

$$F_1\left(\overline{x}\right) = a_1 \cos(k_1 \overline{x}) + a_2 \sin(k_1 \overline{x}) \tag{6.47}$$

Its first derivative will be:

$$F_{1\overline{x}}\left(\overline{x}\right) = -k_1 a_1 \sin(k_1 \overline{x}) + a_2 k_1 \cos(k_1 \overline{x}) \tag{6.48}$$

In order to calculate a_1 and k_1 the condition (6.35) and (6.39) will be used:

$$F_{1\overline{x}}\left(0\right) = -k_1 a_1 \sin(k_1 0) + k_1 a_2 \cos(k_1 0) = k_1 a_2 = 0$$
$$\Rightarrow a_2 = 0 \tag{6.49}$$

$$F_1\left(1\right) = a_1 \cos(k_1 1) = a_1 \cos(k_1) = 0$$
$$\Rightarrow \cos(k_1) = 0 \Rightarrow k_1 = (2n+1)\frac{\pi}{2}$$
$$n \in \mathbb{N} \tag{6.50}$$

The function of single variable $G_1\left(\overline{y}\right)$ is assumed to be expressed a relation such as the one bellow:

$$G_1\left(\overline{y}\right) = b_1 \cosh(k_1 \overline{y}) + b_2 \sinh(k_1 \overline{y}) \tag{6.51}$$

Its first derivative will be:

$$G_{1\overline{y}}\left(\overline{y}\right) = k_1 b_1 \sinh(k_1 \overline{y}) + k_1 b_2 \cosh(k_1 \overline{y}) \tag{6.52}$$

Applying the condition (6.37) the constant b_2 will be found.

$$G_{1y}(0) = k_1 b_1 \sinh(0) + k_1 b_2 \cosh(0) = k_1 b_2 = 0 \qquad (6.53)$$

$$\Rightarrow b_2 = 0 \qquad (6.54)$$

With the above results the product $F_1(\bar{x}) G_1(\bar{y})$ could be expressed as follows:

$$F_1(\bar{x}) G_1(\bar{y}) = \sum_{n=1}^{\infty} a_1 \cos\left((2n+1)\frac{\pi}{2}\bar{x}\right) b_1 \cosh\left((2n+1)\frac{\pi}{2}\bar{y}\right) \qquad (6.55)$$

Substituting the values of the found constants in the equation (6.26) the value of $\varphi_1(\bar{x}, \bar{y})$

becomes:

$$\varphi_1(\bar{x}, \bar{y}) = \sum_{n=1}^{\infty} C_n \cos\left((2n+1)\frac{\pi}{2}\bar{x}\right) \cosh\left((2n+1)\frac{\pi}{2}\bar{y}\right) \qquad (6.56)$$

To understand the characteristics of the electric potential on the top of the unit segment it is required a new computation of the Laplace's equation between the right limit of the electrode and the right-upper side of the selected region.
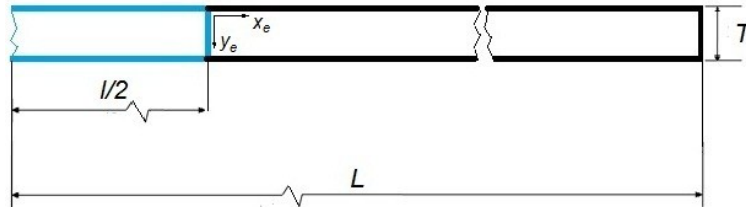
Figure 6.6 The upper part of the unit segment illustrating the top electrode and the considered local coordinate system.

171

In order to determine all the parameters involved in the equation (6.56) the potential function φ_e is defined in the coordinate system (x_e, y_e) and a new set of boundary conditions is introduced.

$$\frac{\partial^2 \varphi_e}{\partial x^2} + \frac{\partial^2 \varphi_e}{\partial y^2} = 0 \tag{6.57}$$

$$\varphi_e(0, y_e) = V_0 \tag{6.58}$$

$$\varphi_e(L - \frac{l}{2}, y_e) = 0 \tag{6.59}$$

$$\frac{\partial \varphi_e}{\partial y_e}(x_e, 0) = 0 \tag{6.60}$$

In the above boundary conditions T represents the thickness of the electrodes ($\approx$100nm).

The dimensionless parameters $\bar{x}_e$ and $\bar{y}_e$ are defined as:

$$\bar{x}_e = \frac{x_e}{L - \frac{l}{2}} \tag{6.61}$$

$$\bar{y}_e = \frac{y_e}{T}$$

The equation (6.57) and the boundary conditions (6.58) - (6.60) become:

$$\frac{1}{\left(L - \frac{l}{2}\right)^2} \frac{\partial^2 \varphi_e}{\partial \bar{x}_e^2} + \frac{1}{T^2} \frac{\partial^2 \varphi_e}{\partial \bar{y}_e^2} = 0 \tag{6.62}$$

$$\varphi_e(0, \bar{y}_e) = V_0 \tag{6.63}$$

$$\varphi_e(1, \bar{y}_e) = 0 \tag{6.64}$$

$$\frac{\partial \varphi_e}{\partial \bar{y}_e}(\bar{x}_e, 0) = 0 \tag{6.65}$$

The assumed solution for (6.62) is expressed by the function:

$$\varphi_e(\bar{x}_e, \bar{y}_e) = F_e(\bar{x}_e) G_e(\bar{y}_e) \tag{6.66}$$

where $F_e(\bar{x}_e)$ and $G_e(\bar{y}_e)$ are functions of only one variable.

Performing the substitution (6.66) into (6.62) yields

$$\frac{1}{T^2} F_e(\bar{x}_e) G_{e\bar{y}_e\bar{y}_e}(\bar{y}_e) + \frac{1}{L^{*2}} F_{e\bar{x}_e\bar{x}_e}(\bar{x}_e) G_e(\bar{y}_e) = 0 \tag{6.67}$$

with the notation $\left(L - \dfrac{l}{2} \right) = L^*$

The expression (6.67) is true only if:

$$\frac{F_{e\bar{x}_e\bar{x}_e}(\bar{x}_e)}{F_e(\bar{x}_e)} = -\frac{L^{*2}}{T^2} \frac{G_{e\bar{y}_e\bar{y}_e}(\bar{y}_e)}{G_e(\bar{y}_e)} = k_e^2 \tag{6.68}$$

This is equivalent to:

$$F_{\bar{e}\bar{x}_e\bar{x}_e}\left(\bar{x}_e\right) - k_e^2 F_e\left(\bar{x}_e\right) = 0 \tag{6.69}$$

$$G_{\bar{e}\bar{y}_e\bar{y}_e}\left(\bar{y}_e\right) + k_e^2 \frac{T^2}{L^{*2}} G_e\left(\bar{y}_e\right) = 0 \tag{6.70}$$

The assumed solutions of (6.69) and (6.70) are:

$$F_e\left(\bar{x}_e\right) = c_1 e^{k_e \bar{x}_e} + c_2 e^{-k_e \bar{x}_e} \tag{6.71}$$

$$G_e\left(\bar{y}_e\right) = c_3 \cos\left(\frac{T}{L^*}k_e\bar{y}_e\right) + c_4 \sin\left(\frac{T}{L^*}k_e\bar{y}_e\right) \tag{6.72}$$

$$\varphi_e(\bar{x}_e,\bar{y}_e) = \sum_{m=1}^{\infty}\left(c_1 e^{k_e\bar{x}_e} + c_2 e^{-k_e\bar{x}_e}\right)\left(c_3 \cos\left(\frac{T}{L^*}k_e\bar{y}_e\right) + c_4 \sin\left(\frac{T}{L^*}k_e\bar{y}_e\right)\right) \tag{6.73}$$

The boundary condition (6.65) applied to the equation (6.66) gives:

$$\frac{\partial \varphi_e}{\partial \bar{y}_e}(\bar{x}_e,0) = 0$$

$$\sum_{m=1}^{\infty}\left(c_1 e^{k_e\bar{x}_e} + c_2 e^{-k_e\bar{x}_e}\right)\left(-c_3 \frac{T}{L^*}k_e \sin\left(\frac{T}{L^*}k_e 0\right) + c_4 \frac{T}{L^*}k_e \cos\left(\frac{T}{L^*}k_e 0\right)\right) = 0$$

$$\sum_{m=1}^{\infty}\left(c_1 e^{k_e\bar{x}_e} + c_2 e^{-k_e\bar{x}_e}\right)\left(c_4 \frac{T}{L^*}k_e \cos\left(\frac{T}{L^*}k_e 0\right)\right) = 0 \tag{6.74}$$

$$\sum_{m=1}^{\infty}\left(c_1 e^{k_e\bar{x}_e} + c_2 e^{-k_e\bar{x}_e}\right)\left(c_4 \frac{T}{L^*}k_e\right) = 0$$

$$\Rightarrow c_4 = 0$$

The boundary condition (6.64) in (6.66) yields:

$$\varphi_e(1, \bar{y}_e) = 0$$

$$\sum_{m=1}^{\infty} \left(c_1 e^{k_e} + c_2 e^{-k_e} \right) \left(c_3 \cos\left(\frac{T}{L^*} k_e \bar{y}_e \right) \right) = 0$$

$$\Rightarrow \sum_{m=1}^{\infty} \left(c_1 e^{k_e} + c_2 e^{-k_e} \right) = 0 \qquad (6.75)$$

$$c_1 e^{k_e} + c_2 e^{-k_e} = 0$$

$$c_2 = -c_1 e^{2k_e}$$

The boundary condition (6.63) applied to (6.66)gives:

$$\varphi_e(0, \bar{y}_e) = \sum_{m=1}^{\infty} \left(c_1 e^{k_e 0} - c_1 e^{2k_e} e^{-k_e 0} \right) c_3 \cos\left(\frac{T}{L^*} k_e \bar{y}_e \right) = V_0 \qquad (6.76)$$

The new constants will be $c_1 c_3 = c_5$. The following expression holds:

$$\sum_{m=1}^{\infty} c_5 \left(1 - e^{2k_e} \right) \cos\left(\frac{T}{L^*} k_e \bar{y}_e \right) = V_0 \qquad (6.77)$$

Knowing that $\sum_{m=1}^{\infty} \dfrac{1}{2^m} = 1$ we can express V_0 as:

$$\sum_{m=1}^{\infty} \frac{V_0}{2^m} = V_0 \qquad (6.78)$$

Inserting (6.78) into (6.77)gives the value of c_5:

$$\sum_{m=1}^{\infty} \frac{V_0}{2^m} = \sum_{m=1}^{\infty} c_5 \left(1-e^{2k_e}\right)\cos\left(\frac{T}{L^*}k_e \bar{y}_e\right)$$

$$\Rightarrow c_5 = \frac{V_0}{2^m\left(1-e^{2k_e}\right)}$$

(6.79)

The cosine term from the equation (6.79) approaches 1 because the term $\frac{T}{L^*}$ is very small due to the size of T ($\approx$ 100 nm) compared to L^* (10-30 µm) .

Now we can represent the electric potential in the upper part of the unit segment as:

$$\varphi_1(\bar{x},1) = V_0 \qquad\qquad 0 \le \bar{x} \le \frac{l}{2L}$$

(6.80)

$$\varphi_e(\bar{x}_e,1) = \sum_{m=1}^{\infty} c_5 \left(e^{(k_e \bar{x}_e)} - e^{k_e(2-\bar{x}_e)}\right)\cos\left(\frac{T}{L^*}k_e\right) =$$

$$= \sum_{m=1}^{\infty} \frac{V_0}{2^m\left(1-e^{2m\beta}\right)}\left(e^{(m\beta \bar{x}_e)} - e^{m\beta(2-\bar{x}_e)}\right)$$

$$0 \le \bar{x}_e \le 1$$

(6.81)

In the condition (6.81) $\cos\left(\frac{T}{L^*}k_e\right)$ can be approximated to 1.

Over the entire upper part of the unit channel, the potential function is assumed to be:

$$\varphi_1(\bar{x},1) = \sum_{n=0}^{\infty} C_n \cos\left((2n+1)\frac{\pi}{2}\bar{x}\right)\cosh\left((2n+1)\frac{\pi}{2}\right)$$

(6.82)

176

In order to identify the values of the constants C_n of the function, a numerical approach is adopted. In a first step, the values of the boundary conditions $\varphi_1(\bar{x},1)$ are calculated numerically. The equation (6.7) is used for $\left(0 < \bar{x} < \dfrac{l}{L}\right)$, while the equation (6.81) is used for $\left(\dfrac{l}{L} < \bar{x} < 1\right)$. In a second step, least-mean squared method (LMS) is employed to calculate the first 100 terms of the solution. The MATLAB toolbox CFTOOL is used with the equation (6.82) as custom equation. As a result, the values of C_n and implicitly of the function $\varphi_1(\bar{x}, \bar{y})$ are identified over the entire domain.

To find how the number of terms included in the solution affect results, a study is performed. For each number of terms considered in the equation (6.85) in other words the value of n, the following value is calculated:

$$N(n) = norm\left(\frac{\varphi(n) - \varphi(n-1)}{\varphi_{max}}\right) \tag{6.83}$$

where $\varphi(n)$ is the value of the potential function (6.85) calculated with n terms and $\varphi_{max} = V$ is the maximum value of the electric potential of the upper electrode.

The graphical representation of N(n) is shown below:
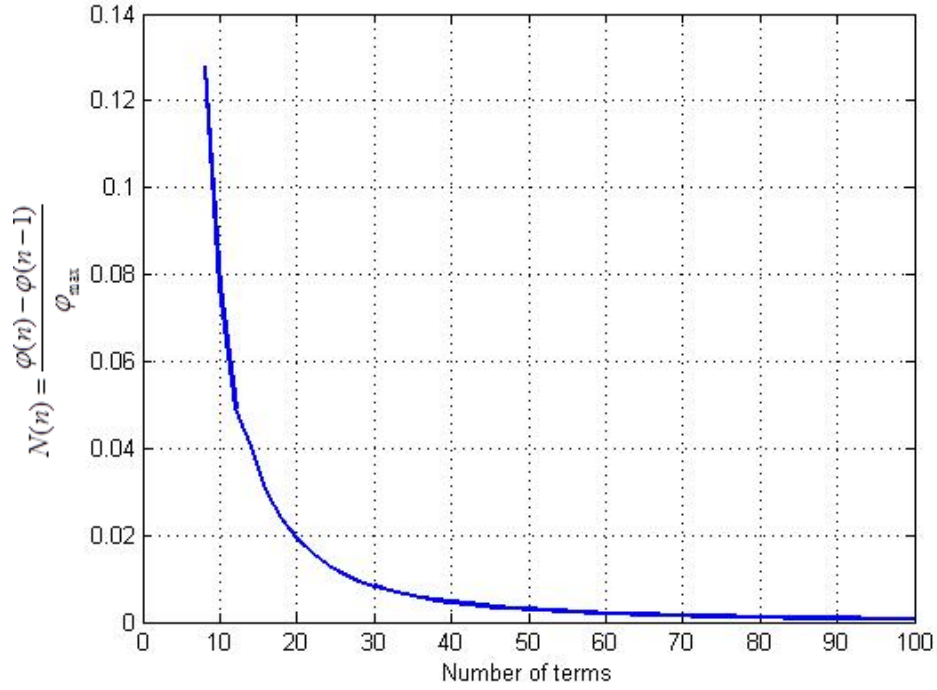
Figure 6.7 The influence of the number of terms on the accuracy of the solution.

According to the present calculation, considering only 25 terms of the equation (6.85) the magnitude of the potential function will be affected by only 0.01 %. Adding more than 60 terms will increase the solution accuracy to 0.003%. Therefore, in this work only the first 60 terms of the solution are included.

Owing to symmetry, the function $\varphi_2(1, \bar{y})$ that characterises the potential over the right side of the unit channel (Figure 6.5) can be expressed as:

$$\varphi_2(1, \bar{y}) = \sum_{n=0}^{\infty} C_n \cos\left((2n+1)\frac{\pi}{2} \right) \cosh\left((2n+1)\frac{\pi}{2}\bar{y} \right) \qquad (6.84)$$

By superposition, the expression of the total potential function in the unit channel is:

$$\varphi(\overline{x},\overline{y}) = \sum_{n=0}^{\infty} C_n \cos\left((2n+1)\frac{\pi}{2}\overline{x} \right)\cosh\left((2n+1)\frac{\pi}{2} \right) + \\ + \sum_{n=0}^{\infty} C_n \cos\left((2n+1)\frac{\pi}{2} \right)\cosh\left((2n+1)\frac{\pi}{2}\overline{y} \right)$$

(6.85)

For n=60, the value of N(n) becomes 99.997 . According to the present calculation, considering only 25 terms of the equation (6.85) will modify the magnitude of the potential function only by 0.01 %.

The potential function identified as shown semi-analytically allows determining the expressions of electric field and also the gradient of the intensity of the electric field. Knowing these expressions and the dielectric characteristics of the suspended particles and liquid, the distribution of the dielectrophoretic force over the entire channel can be determined with the relation (6.1).

6.5 Electric Field

To find the distribution of the electric field, the quasi-electrostatic form of the Maxwell's equation that relates the values of $\overline{E}$ and φ as written in the equation (6.4):

$$\overline{E}(\overline{x},\overline{y}) = E_x\overline{i} + E_y\overline{j} = -\nabla\varphi$$

(6.86)

where $\overline{i}$ and $\overline{j}$ are the unit vector in the x and y directions.

$$E_x(\overline{x},\overline{y}) = -\frac{\partial \varphi}{\partial \overline{x}}$$

$$E_y(\overline{x},\overline{y}) = -\frac{\partial \varphi}{\partial \overline{y}}$$

(6.87)

E_x and E_y after the differentiation of the potential function become:

$$E_x(\overline{x},\overline{y}) = \frac{1}{2}\frac{C(m)(2m-1)\pi\left(\begin{array}{l}\sin\left(\frac{1}{2}(2m-1)\pi\overline{x}\right)\cosh\left(\frac{1}{2}(2m-1)\pi\overline{x}\right)+\\ +\cos\left(\frac{1}{2}(2m-1)\pi\overline{x}\right)\sinh\left(\frac{1}{2}(2m-1)\pi\overline{x}\right)\end{array}\right)}{L\cosh\left(\pi m - \frac{1}{2}\pi\right)}$$

(6.88)

$$E_y(\overline{x},\overline{y}) = -\frac{1}{2}\frac{C(m)(2m-1)\pi\left(\begin{array}{l}\cos\left(\frac{1}{2}(2m-1)\pi\overline{x}\right)\sinh\left(\frac{1}{2}(2m-1)\pi\overline{y}\right)+\\ +\sin\left(\frac{1}{2}(2m-1)\pi\overline{y}\right)\cosh\left(\frac{1}{2}(2m-1)\pi\overline{x}\right)\end{array}\right)}{L\cosh\left(\frac{1}{2}(2m-1)\pi\right)}$$

(6.89)

1.1 Dielectrophoretic force

The dielectrophoretic force acting on a polarized cell suspended in a liquid and exposed to a non-uniform electric field $\overline{E}$ is given by (6.1). Its formulation implies its linear proportionality with the factor $\nabla|\overline{E}|^2$ that represents the gradient of the intensity of

the electric field. If the dielectric properties of the liquid and of the suspended particle are known the expression of the dielectrophoretic force can be found.

The gradient of the electric field intensity can be expressed as [191] :

$$\bar{E}(\bar{x},\bar{y}) = \mathrm{E}_x \bar{i} + \mathrm{E}_y \bar{j}$$
$$\Rightarrow |\bar{E}|^2 = \left(\sqrt{\mathrm{E}_x^2(\bar{x},\bar{y}) + \mathrm{E}_y^2(\bar{x},\bar{y})} \right)^2 \tag{6.90}$$

$$\nabla |\bar{E}|^2 = \frac{\partial \left(\mathrm{E}_x^2(\bar{x},\bar{y}) + \mathrm{E}_y^2(\bar{x},\bar{y}) \right)}{\partial \bar{x}} \bar{i} + \frac{\partial \left(\mathrm{E}_x^2(\bar{x},\bar{y}) + \mathrm{E}_y^2(\bar{x},\bar{y}) \right)}{\partial \bar{y}} \bar{j} \tag{6.91}$$

$$\nabla |\bar{E}|^2 = \left(2E_x \frac{\partial E_x}{\partial x} + 2E_y \frac{\partial E_y}{\partial x} \right) \bar{i} + \left(2E_x \frac{\partial E_x}{\partial y} + 2E_y \frac{\partial E_y}{\partial y} \right) \bar{j} \tag{6.92}$$

The relation describing the dielectrophoretic force is:

$$F_{DEP} = 2\pi\varepsilon_m R^3 \operatorname{Re}[CM] \left[\left(2E_x \frac{\partial E_x}{\partial x} + 2E_y \frac{\partial E_y}{\partial x} \right) \bar{i} + \left(2E_x \frac{\partial E_x}{\partial y} + 2E_y \frac{\partial E_y}{\partial y} \right) \bar{j} \right] \tag{6.93}$$

The expressions of $\dfrac{\partial E_x}{\partial x}$, $\dfrac{\partial E_x}{\partial y}$, $\dfrac{\partial E_y}{\partial x}$ and are:

$$\frac{\partial E_x}{\partial \bar{x}} = \frac{1}{4} \frac{C(m)(2m-1)^2 \pi^2 \begin{pmatrix} \cos\left(\frac{1}{2}(2m-1)\pi\bar{x}\right)\cosh\left(\frac{1}{2}(2m-1)\pi\bar{y}\right) + \\ +\cos\left(\frac{1}{2}(2m-1)\pi\bar{y}\right)\cosh\left(\frac{1}{2}(2m-1)\pi\bar{x}\right) \end{pmatrix}}{L^2 \cosh\left(\frac{1}{2}(2m-1)\pi\right)} \tag{6.94}$$

$$\frac{\partial E_x}{\partial \overline{y}} = \frac{1}{4} \frac{C(m)(2m-1)^2 \pi^2 \left(\begin{array}{l} \sin\left(\frac{1}{2}(2m-1)\pi\overline{x}\right)\sinh\left(\frac{1}{2}(2m-1)\pi\overline{y}\right) - \\ -\sin\left(\frac{1}{2}(2m-1)\pi\overline{y}\right)\sinh\left(\frac{1}{2}(2m-1)\pi\overline{x}\right) \end{array} \right)}{L^2 \cosh\left(\frac{1}{2}(2m-1)\pi\right)} \tag{6.95}$$

$$\frac{\partial E_y}{\partial x} = \frac{1}{4} \frac{C(m)(2m-1)^2 \pi^2 \left(\begin{array}{l} \sin\left(\frac{1}{2}(2m-1)\pi\overline{x}\right)\sinh\left(\frac{1}{2}(2m-1)\pi\overline{y}\right) - \\ -\sin\left(\frac{1}{2}(2m-1)\pi\overline{y}\right)\sinh\left(\frac{1}{2}(2m-1)\pi\overline{x}\right) \end{array} \right)}{L^2 \cosh\left(\frac{1}{2}(2m-1)\pi\right)} \tag{6.96}$$

$$\frac{\partial E_y}{\partial \overline{y}} = -\frac{1}{4} \frac{C(m)(2m-1)^2 \pi^2 \left(\begin{array}{l} \cos\left(\frac{1}{2}(2m-1)\pi\overline{x}\right)\cosh\left(\frac{1}{2}(2m-1)\pi\overline{y}\right) + \\ +\cos\left(\frac{1}{2}(2m-1)\pi\overline{y}\right)\cosh\left(\frac{1}{2}(2m-1)\pi\overline{x}\right) \end{array} \right)}{L^2 \cosh\left(\frac{1}{2}(2m-1)\pi\right)} \tag{6.97}$$

The results found for the electric potential, electric field and the gradient $\nabla\left|\overline{E}\right|^2$ are plotted with in Matlab$^{\text{TM}}$. They are validated with the numerical results from COMSOL. For the numerical simulation the cross-section of a squared microchannel with the length of the side L= 100 micrometer, the length of the electrode l=50 micrometers is considered. The mesh considered is triangular and it is set to be 0.25 micrometers. The liquid chosen to fill the channel is water. There is a good agreement between the semi-analytical and the numerical solution and the results are presented in Figure 6.8 to Figure 6.13 .
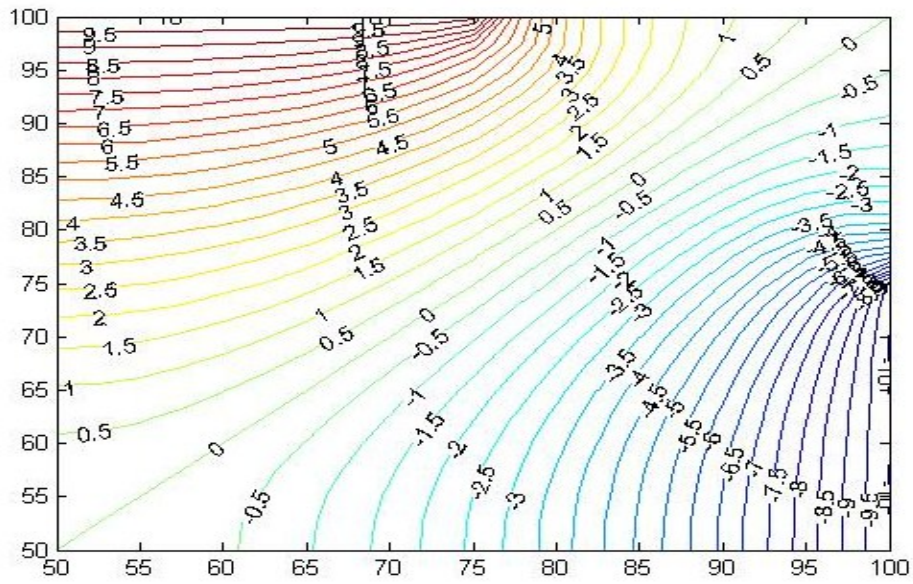
Figure 6.8 The semi-analytical result of the potential distribution over the unit channel.
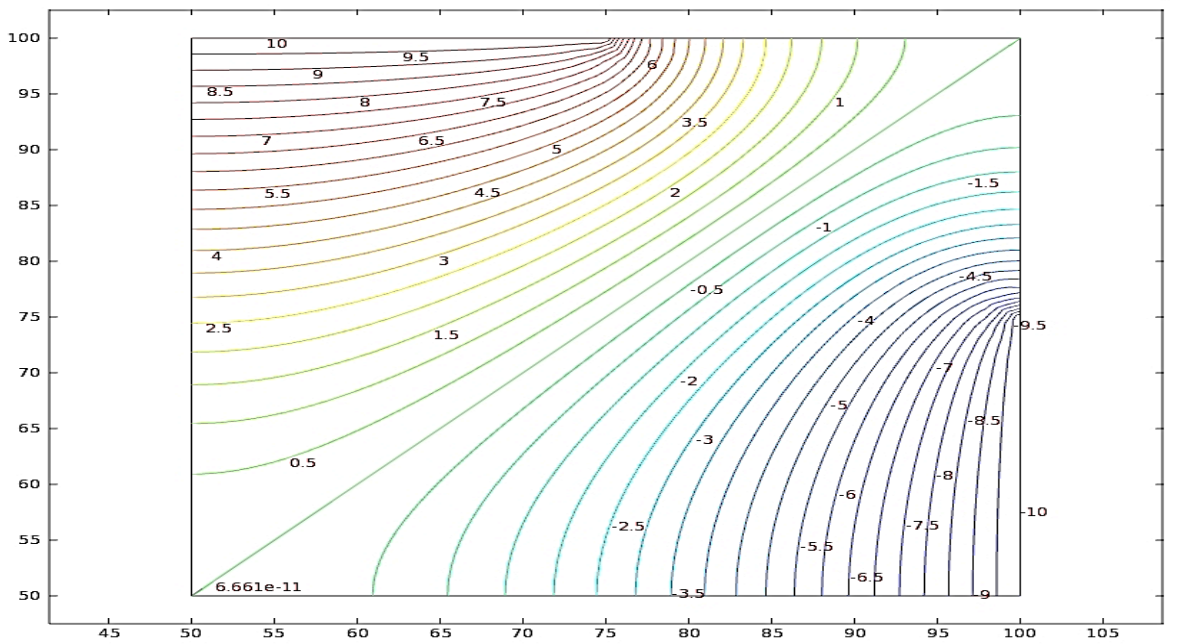
Figure 6.9 The numerical solution of the potential distribution over the unit channel
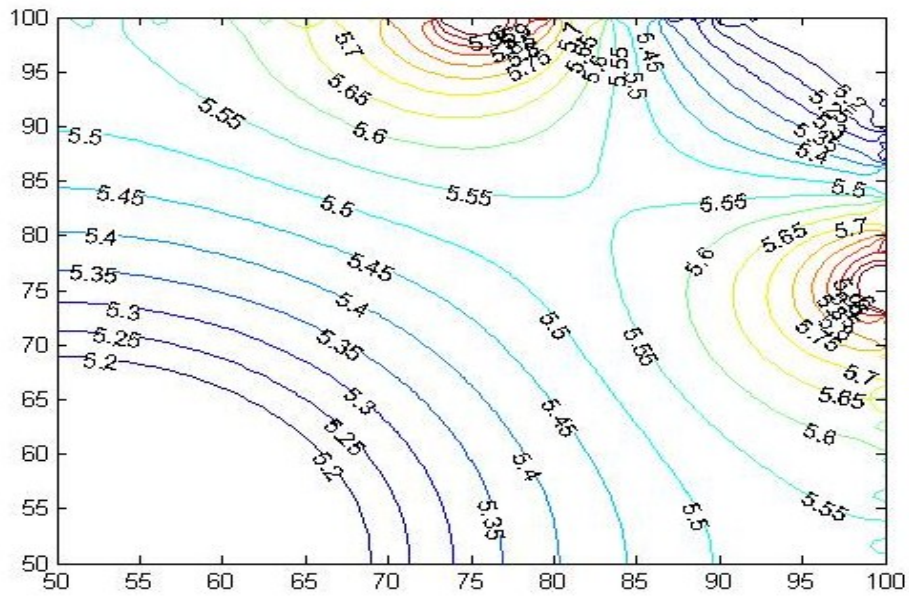
Figure 6.10The semi-analytical result of the electric field distribution over the unit channel.
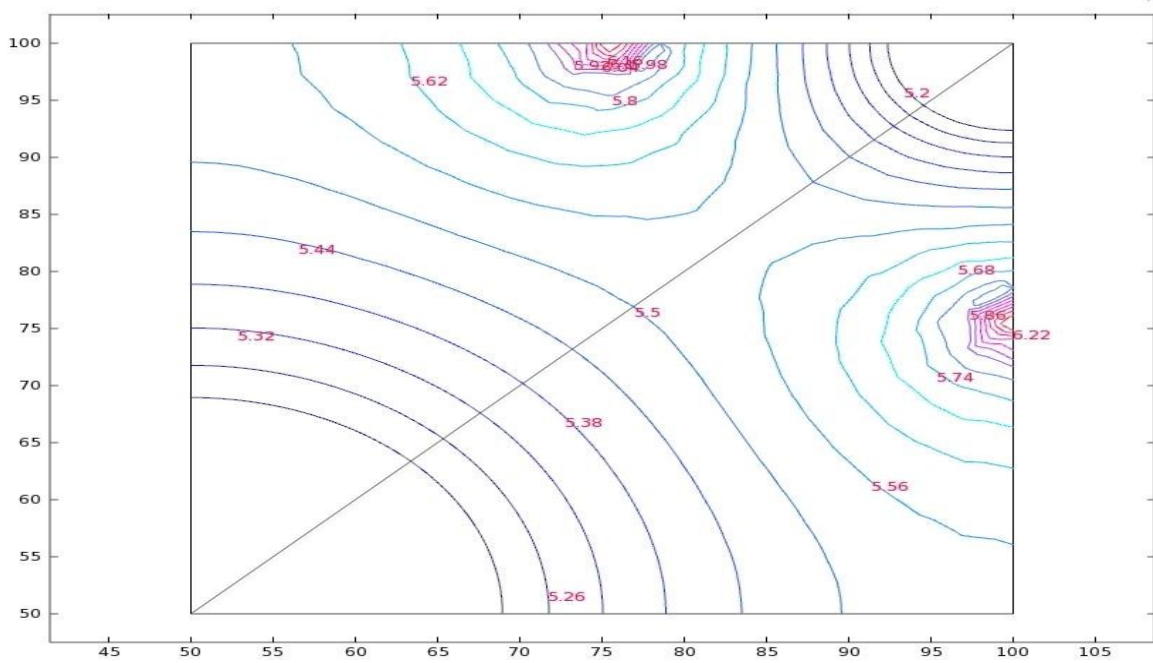
Figure 6.11 The numerical solution of the electric field distribution over the unit channel.
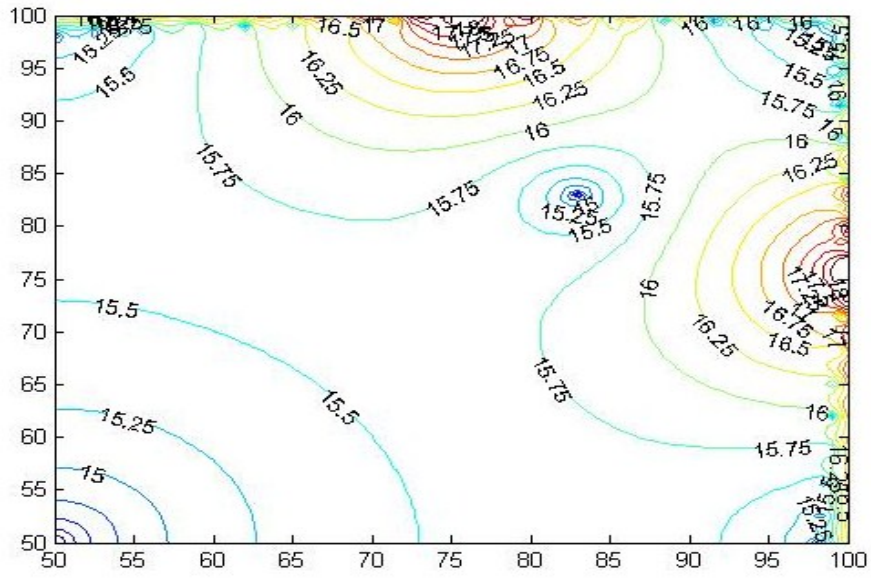
Figure 6.12 The semi-analytical result of the $\nabla\left|\bar{E}\right|^2$ distribution over the unit channel.
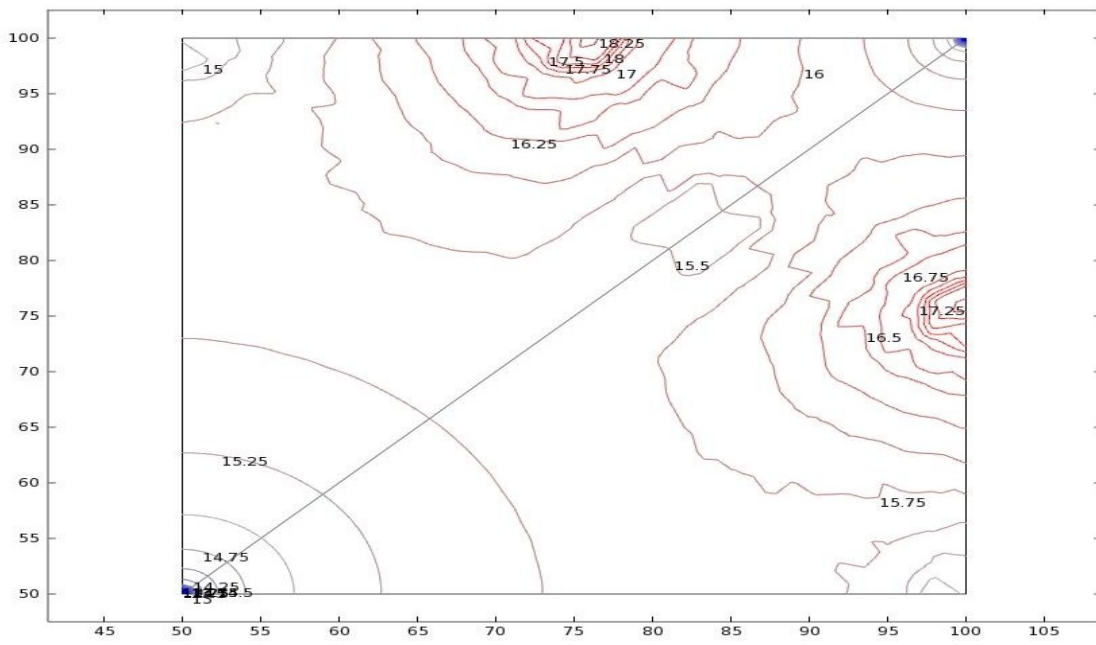
Figure 6.13 The numerical solution of the $\nabla\left|\bar{E}\right|^2$ distribution over the unit channel.

Examining the distribution of the electric field (Figure 6.10and Figure 6.11) one can notice that the maximum values are at the edge of the electrodes and the minimum ones are in the center of the channel. The rounded-edged distribution of $\nabla\left|\bar{E}\right|^{2}$ noticed in the semi-analytical solution (Figure 6.12) is attributed to the round-off errors due to the calculation of hyperbolic functions dealing with large terms and was noticed before [192].

6.6 Experimental validation

DEP is a phenomenon that is fully compatible with transport and manipulation of living cells. Negative DEP was successfully used to group, cluster and focus cells in a test device that simulates 3D microfluidic channels with 3D electrode configuration

An experimental study was performed in order to observe the effect of the dielectrophoretic force on suspended particle. The solution with the conductivity of 10 mS/m was prepared by adding 8.5% volumetric sucrose and 0.3% volumetric dextrose in 10 ml RPMI cell culture medium. RPMI culture medium consists of RPMI 1640 in which was added 10% fetal bovine serum (2% FBS) and 1% Penicillin/ Streptomycin. The conductivity of solution was adjusted to 10 mS/m by adding 700 microliters Trypsin in 0.53 mM Ethylene Diamino Tetraacetic Acid (EDTA). The value of the conductivity was tested using a PH-Conductivity-TDS meters, model Oyster 341350 from Extech. In the final solution five droplets of monodisperse polystyrene microspheres of 15 μm diameter

(Megabead NIST Traceable Particle Size Standard) with 1% solids suspensions were added.

Two microliters of diluted beads were deposited on the centering device manufactured by FineLine Imaging with Chrome electrodes platted on glass in the desired configuration. The AC signals from 100 kHz to 12 MHz were generated with a Tektronix CFG280 function generator that allows a range of voltages from 0 to 20 Volts peak to peak. This volume covers completely the area of the electrodes. The centering of the particles due to the presence of the negative dielectrophoresis phenomenon was observed starting from a frequency of 100 kHz and up to 3 MHz, with a voltage varying from 5 to 20 V peak to peak. The experimental results are presented in the action of the dielectrophoretic force on the polystyrene microbeads suspended in the RPMI solution.
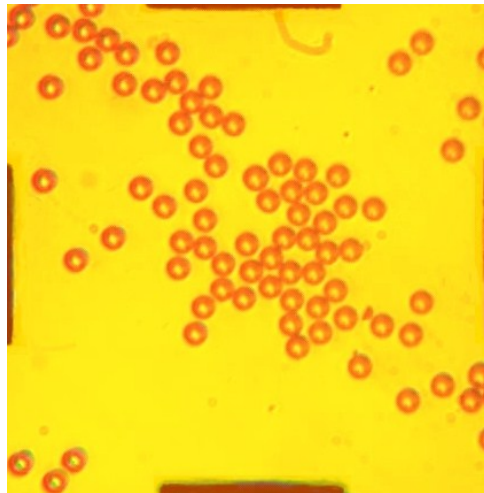
Figure 6.14 The polystyrene beads move freely in the absence of the non-uniform electric field.
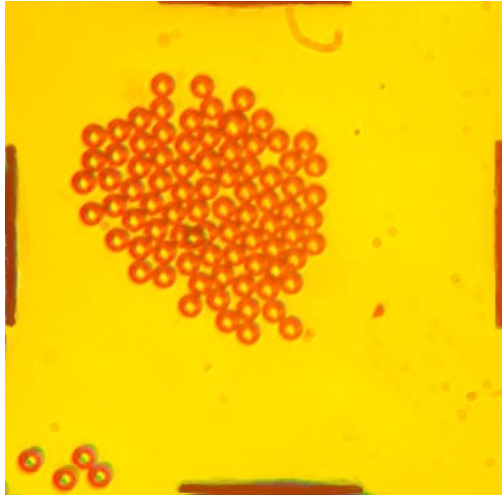
Figure 6.15 The centering of the beads due to the phenomenon of negative

dielectrophoresis.

The range of frequency and the difference of potential responsible for the positive and the negative dielectrophoresis of the following cell lines: 92.1, OCM and MDA 231 were determined previously in our laboratories [192]. However, for centering purposes, only the range of frequencies and potentials responsible for the negative dielectrophoretic behavior of the cells are needed for a given value of the conductivity of the liquid environment (Table 6.1).

Table 6-1 The cross frequency of different living cells with different media conductivities. (adapted with permission after [192])

92.1 (UM)	pDEP all frequencies	From nDEP to pDEP f = 28 KHz ± 5 %	From nDEP to pDEP f = 48 KHz ± 5 %	From nDEP to pDEP f = 90 KHz ± 5 % From pDEP to nDEP f = 42 MHz ± 5 %	No DEP effect
OCM (UM)	From nDEP to pDEP f = 8 KHz ± 5 %	From nDEP to pDEP f = 12 KHz ± 5 %	From nDEP to pDEP f = 38 KHz ± 5 %	From nDEP to pDEP f = 78 KHz ± 5 %	From nDEP to pDEP f = 90 KHz ± 5 %
MDA 231	From nDEP to pDEP f = 7 KHz ± 5 %	From nDEP to pDEP f = 17 KHz ± 5 %	From nDEP to pDEP f = 21 KHz ± 5 %	From nDEP to pDEP f = 33 KHz ± 5 %	From nDEP to pDEP f = 36 KHz ± 5 %

The chosen two-dimensional device represents only the cross-section of the microchannel so the drag and gravitational forces do not have the same behavior as in the case of a three-dimensional microfluidic structure. This design was chosen due the fact that the present methods of micro fabrication do not allow the manufacturing of a microfluidic channel having all four sides plated with the electrodes [146].

6.7   Conclusions and summary

In this chapter the planar distribution of the potential, electric field and DEP force was determined. The solution of the Laplace partial differential equation was found through semi-analytical means. A numerical curve fitting approach was employed in order to determine the values of the constants of the potential function. The semi-analytical and the numerical solutions were compared and a good agreement was observed.

The presence of DEP force in a channel with a design similar to the one used in the theoretical calculations was experimentally validated by using polystyrene spherical particles suspended in a solution with a known conductivity. The range of frequencies and the voltage responsible to generate the centering were determined. The two-dimensional chip used in the presented experiments can be successfully applied for the gathering or the centering of several cancer cell lines (92.1, OCM and MDA 231) that have known dielectrophoretic parameters.

Chapter 7:   Conclusions and future work

The effort of this thesis is concentrated mainly on reasoning of the method of characterization of the malignant cells through the bio-chemical reaction between an antigen and its complementary antibody that generates a recognizable and unique signature of the cantilever mini-structure due to the variation of the loads produced during the process. The experimental data shown that the signature of the antibody-antigen reaction of the investigated cells is unique for each complementary pair [2]. The success of the blind test gives hope for the developments of a microsensor that can be succesfully implemented in a POC device.

The theoretical and numerical analysis of the the complex loading combined with the experimental work identified the surface stress as the main load responsible for the pattern of angular displacement of the tip of the beam, while the Laplace pressure, the vertical surface tension and the weight as loads causing the vertical displacement.

The magnitude of the surface stress is variable during the chemical reaction, depending on the mechanism through which the bonds are broken and recreated, the adsorption and the desorption pattern of the new formed chemical components on the surface, the variation in the concentration of ions and the surface alteration.

The caloric aspects of the reaction were found to not generate noticeable deflections. The environmental temperature however can influence the signature of a certain reaction by affecting its duration.

A parametric study on the geometrical features of the cantilever enables to improve the sensitivity of the sensor for a given volume of specimen. The in-plane optimized structure can be successfully implemented in a micro application and presents advantages over an out of plane sensor due to the fact that solves the main concerns regarding the droplet deposition while reducing the evaporation.

The dielectrophoretic formulation was used to determine the theoretical distribution of the potential, electric field and dielectrophoretic force in microchannel with a square cross-section. The semi-analytical solution was validated both numerically and experimentally. The pattern of electrodes analysed allows both centering in a microchannel and gathering of the cell in a fixed region prior to their manipulation towards the lysing, test or droplet generation section.

Future developments regarding the cantilever sensor point in the direction of miniaturization. The scaling down of the experiments will be a step forward in the development of a POC device. Other methods of sensing can be investigated especially a piezoresistive based one where the variation of the surface stress can be detected. The influence of the material of the cantilever and its layers can be studied in order to observe their influence on the signature pattern.

192

In the perspective of miniaturization the integration of the sensor with a microfluidic chip is essential. The chip should include both the preparation of the liquid sample, droplet generation, transportation and deposition. Through electro wetting techniques all the above steps can be performed.

In the area of bio detection other pairs of analytes could be studied through the same method presented in this work. Extensive experiments can be performed also and sensed with direct detection methods to validate the uniqueness signature of specific reactions. The influence of the temperature on the kinetics of the reaction can be studied. More accurate methods could be used to investigate further the evolution of the contact angle during the chemical reaction. Meanwhile, mico-callorimetry methods could be employed to estimate the heat produced by a bio-chemical reaction.

The semi-analytical model of the electric potential, electric field and dielectrophoretic force distribution inside the channel can be improved by taking other types of functions in consideration that can open the perspective of an exact analytical result. Different electrode patterns could be considered and theoretically and experimentally analysed in the perspective of the miniaturization of the entire application.

7.1 Summary of Contributions

The understanding and the segregation of the loads responsible for the deflection pattern generated by the bio-chemical reactions between an antigen and its complementary antibody on the cantilever sensor for several types of cancer cell lines represents the most

193

important contribution of this work. The originality of the studied method comes from the fact that the antibody-antigen pair is mixed before its deposition on the surface of the sensor: without a prior coating with a biological species.

The study on the contact angle variation during a biochemical reaction confirmed that the surface stress has the main responsibility for the pattern of variation in slope of the tip of the beam.

The parametrical study on the geometry of the sensor and the positioning of the sample allow an improvement in its sensing capabilities. The numerical simulations and optimisation are important in the understanding of the phenomenon and the design of the sensing structure.

A major influence in the deflection/rotation of the tip of the cantilever is played by the evaporation. During the evaporation process the contact angle changes. Both evaporation and contact angle were investigated and it was found that the dominant effect on the process is played by the mass variation of the droplet due to evaporation process that generates changes both in the horizontal component of the surface tension and the surface stress. This finding excludes the need of measurement of the contact angle in further investigations of the studied cell lines.

The negative dielectrophoresis was used to cluster and center cells for future automatic handling of the test in a POC device. The model of the electric field was formulated and solved using a semi-analytical method. The results are accurate and they are

validated experimentally and numerically, using a finite element method (Comsol) model.

The method enables fast tracking of the cells with no interaction with the microchannel.

Chapter 8: Appendixes

Appendix A. Hyperworks topology optimization

Contour Plot
Element Densities(Density)
9.000E-01
8.333E-01
7.667E-01
7.000E-01
6.333E-01
5.667E-01
5.000E-01
4.333E-01
3.667E-01
3.000E-01
No result
Max = 9.000E-01
2D 3625085
Min = 3.000E-01
2D 3613741
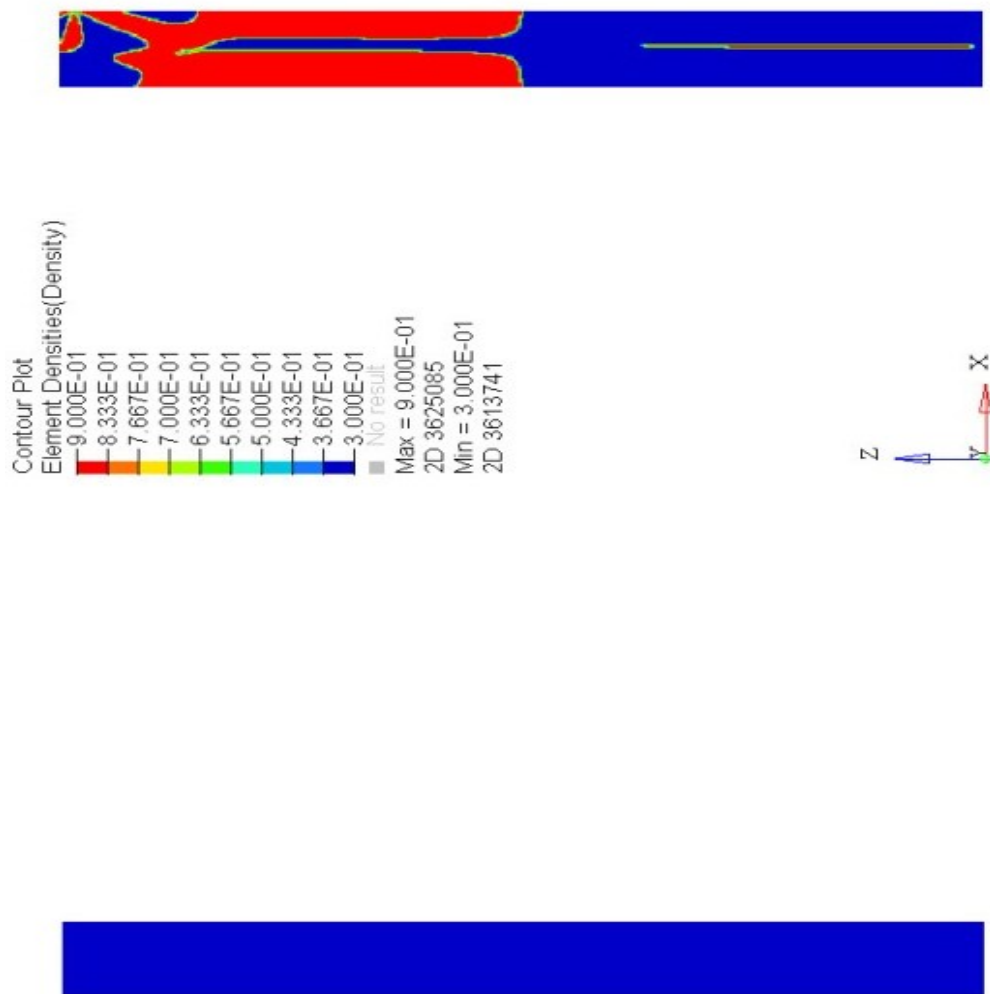
Figure 8.1 Steps 1 and 2.

Figure 8.2 Steps 3 and 4.

197

Contour Plot
Element Densities(Density)
1.000E+00
8.910E-01
7.819E-01
6.729E-01
5.639E-01
4.549E-01
3.458E-01
2.368E-01
1.278E-01
1.875E-02
No result
Max = 1.000E+00
2D 3621385
Min = 1.875E-02
2D 3613741

Contour Plot
Element Densities(Density)
1.000E+00
8.931E-01
7.861E-01
6.792E-01
5.722E-01
4.653E-01
3.583E-01
2.514E-01
1.444E-01
3.750E-02
No result
Max = 1.000E+00
2D 3625085
Min = 3.750E-02
2D 3613741

Figure 8.3 Steps 5 and 6.

198
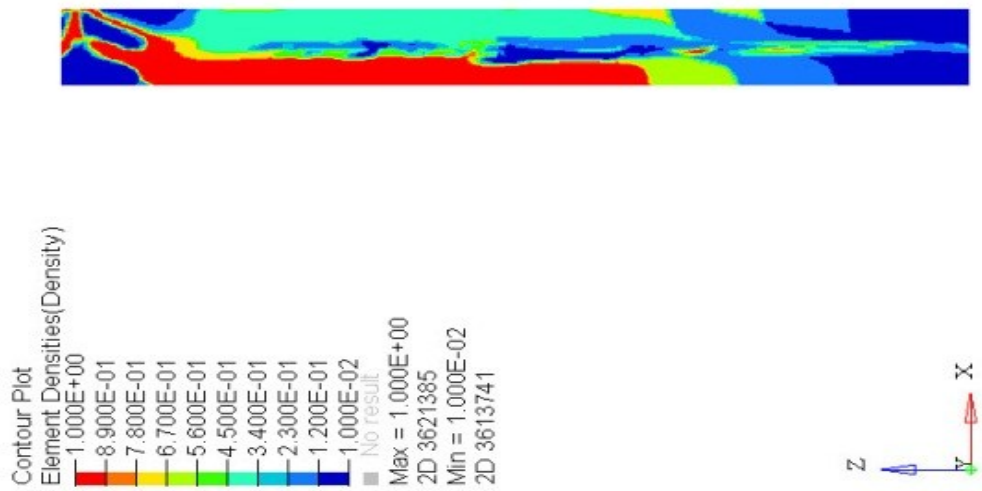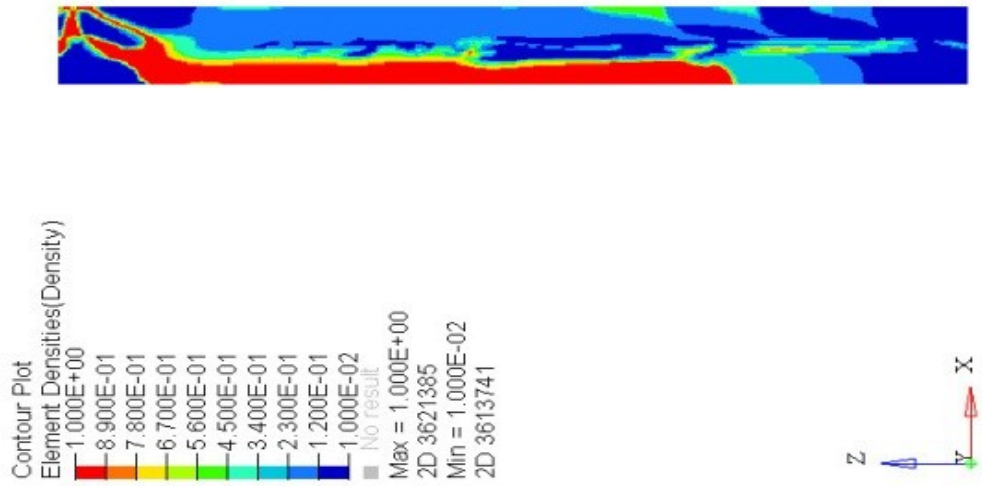
Figure 8.4 Steps 7 and 8.

199
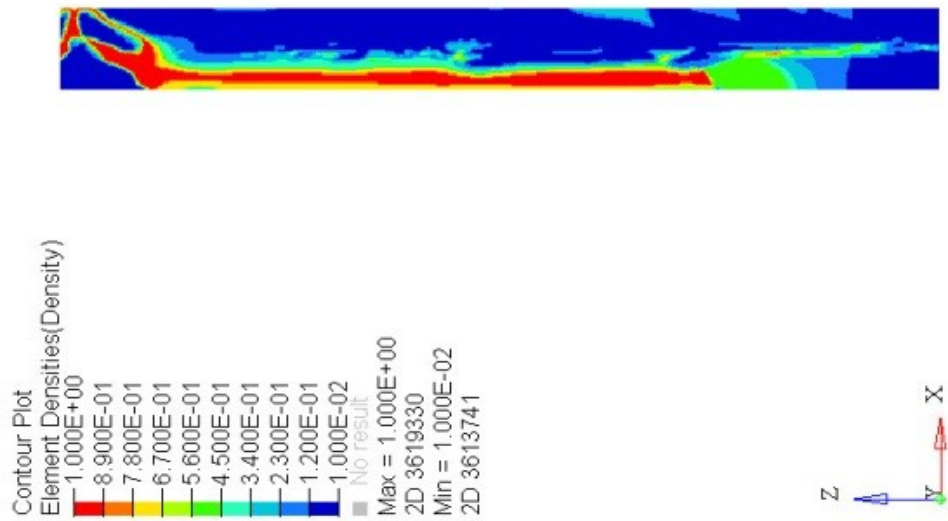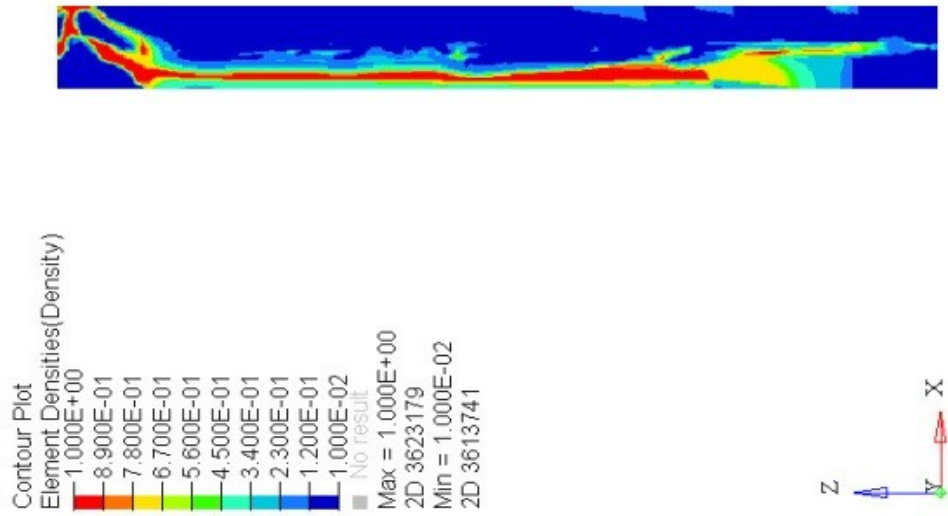
Figure 8.5 Steps 9 and 10.
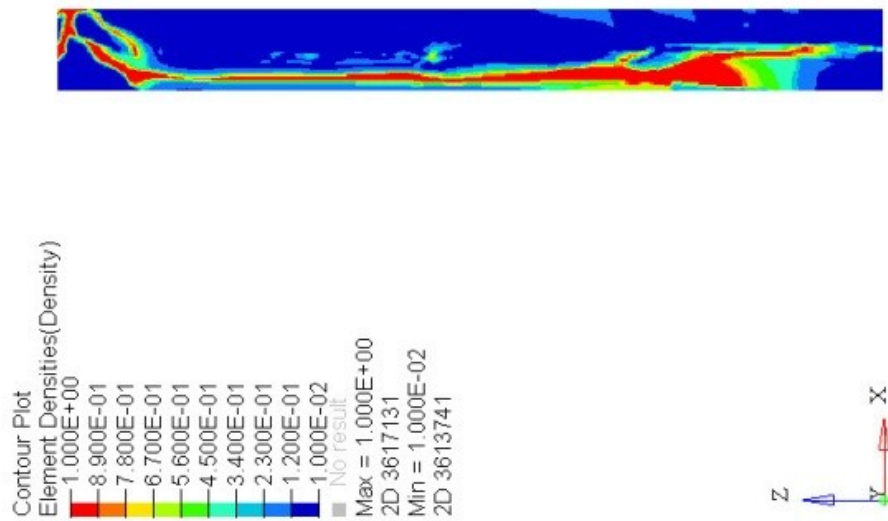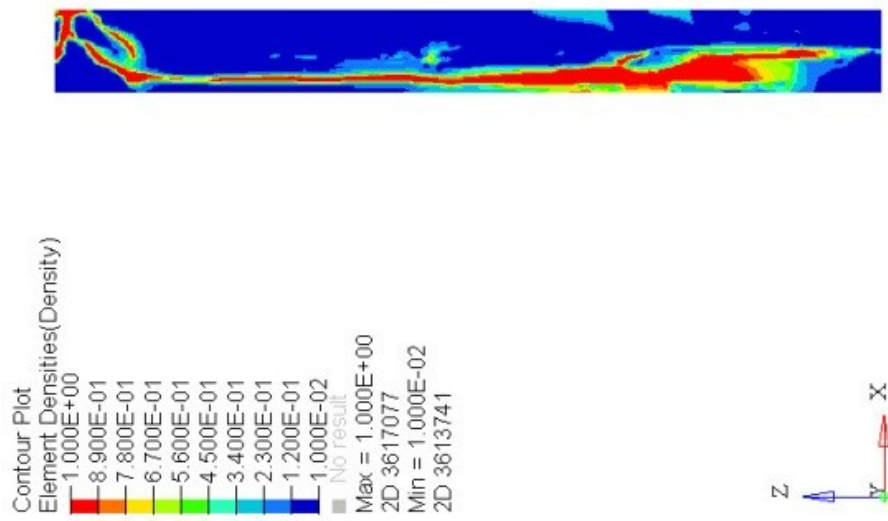
Figure 8.6 Steps 11 and 12.

Figure 8.7 Steps 13 and 14.

202

Contour Plot
Element Densities(Density)
1.000E+00
8.900E-01
7.800E-01
6.700E-01
5.600E-01
4.500E-01
3.400E-01
2.300E-01
1.200E-01
1.000E-02
No result
Max = 1.000E+00
2D 3618823
Min = 1.000E-02
2D 3616735

Contour Plot
Element Densities(Density)
1.000E+00
8.900E-01
7.800E-01
6.700E-01
5.600E-01
4.500E-01
3.400E-01
2.300E-01
1.200E-01
1.000E-02
No result
Max = 1.000E+00
2D 3619318
Min = 1.000E-02
2D 3635185
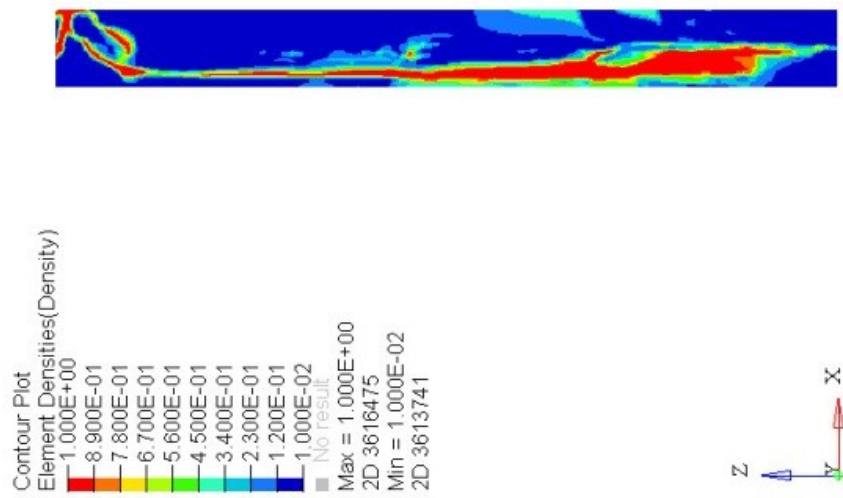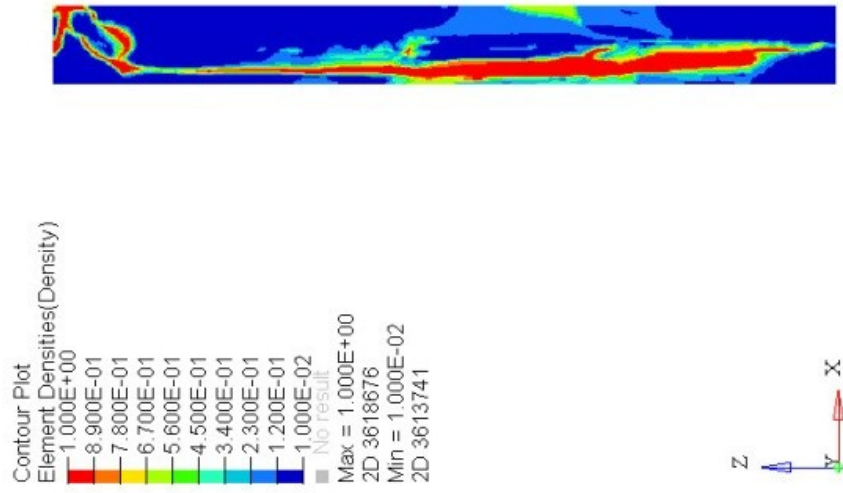
Figure 8.8 Steps 15 and 16.

203

Appendix B.   Detection of breast and colorectal cancer using optical level method

8.1   Optical detection of breast cancer HCC1419 cell line

Breast cancer ranks as the most common form of cancer for women and it affects 12 % of all the American women. A number of 226 870 new cases are foreseen to appear in US only [49]. A first step in the prevention of this condition is with specific vaccines like liposome vaccines can provide a certain degree of immunisation [194]. The micro detection also is believed to be a turning point for the treatment and the diagnosis of all the oncological conditions. The detection method presented in this study can help in the identification of the disease in an early stage.

The same method of detection was used for the breast cancer cell line HCC1419. The breast cancer cell line is cultured in 25 ml flasks containing a solution of RPMI-1640, 10% FBS and 1% Penicillin-Streptomycin in the same type of incubators as in the case of Uveal melanoma cell lines. The supplementation in the quantity of FBS, that constitutes the nutrient of the cultured cells, is justified by their difficulty of expansion in *in vitro* conditions. Before each test the monolayer of cells was detached from the wall of the flask with trypsin 0.05%, centrifuged and the resulting pellet diluted in 1 ml of RPMI-1640. After the counting of the cells the concentration of sample was adjusted at 1 million cells per milliliter. The antibody used in this step is Anti Breast-1. It targets the receptor from

the surface of the cells, the complementary antigen, namely BRST-2 [195]. The antibody is known to have a low sensitivity of only 50% [196]. The monoclonal antibodies HMFG-1 and HMFG-2 have a better specificity[197] but unfortunately they were unavailable for this study.

The tests were performed over a period of three days on the same type of beams as in the previous experiments on the uveal melanoma cell lines. The optical detection results are presented below:
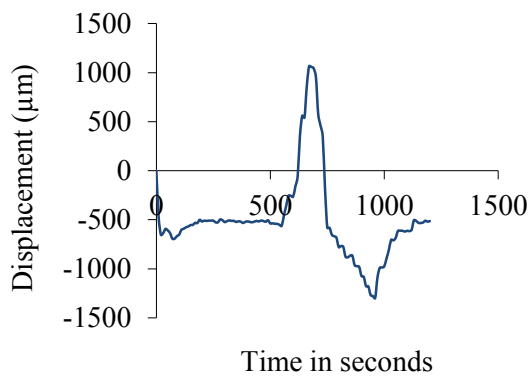
Figure 8.9 First day plots: 0.6 μl of HCC1419 with Anti-BRST-1.
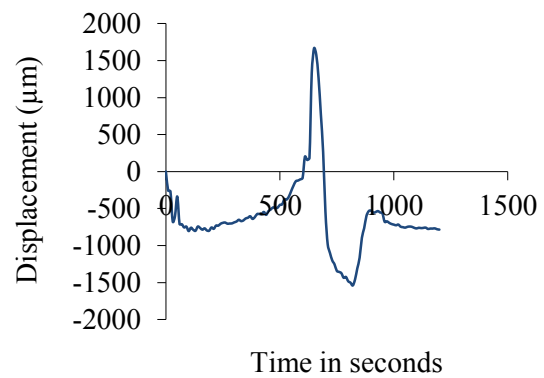
Figure 8.10 First day plots: 0.6 μl of HCC1419 with Anti-BRST-1.
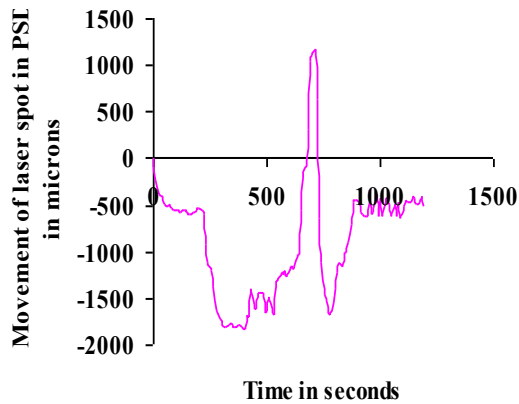
Figure 8.11 Second day plots: 0.6 µl of

HCC1419 with Anti-BRST-1 .
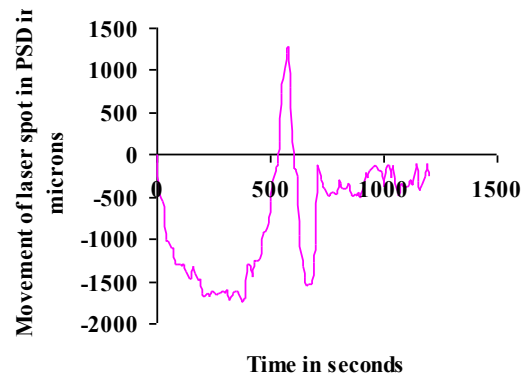
Figure 8.12 Second day plots: 0.6 µl of

HCC1419 with Anti-BRST-1.
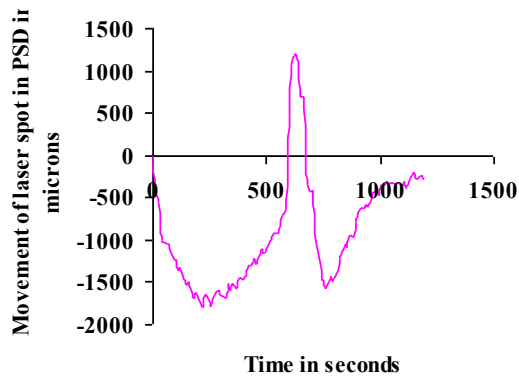
Figure 8.13 Third day plots 0.6 µl of

HCC1419 with Anti-BRST-1.
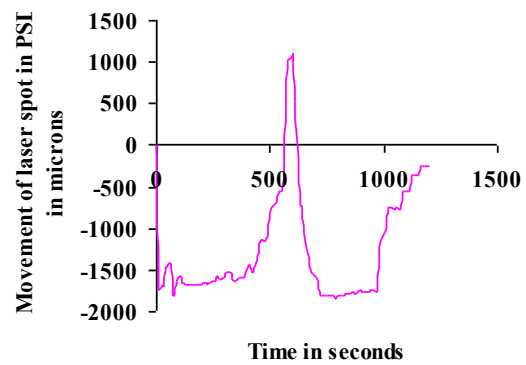
Figure 8.14 Third day plots: 0.6 µl of

HCC1419 with Anti-BRST-1.

The interaction between Anti-Brst-1 and HCC1419 is very strong and the staining

indicates with clarity the presence of the antigens within the HCC1419. The sensitivity of

the cantilever is proved once more by the presence of the high amplitude upward movement (upward on the PSD, downward deflection in the cantilever) that appears after approximately 500 seconds from the beginning of the reaction. After 1000 seconds the cantilever tends to move back towards the reference line but the initial position is not reached. The explanation behind this fact is the presence of complex antibody-antigen deposited on the substrate that creates during this reaction, a precipitate that generates a residual stress. This deposition is common for all the biochemical reactions scrutinized in this study and was examined with a scanning electronic microscope (SEM) in more detail.

It is clear that all the reaction Anti-BRST-1 with HCC1419 cell line follow the same pattern but it is also noticeable a slight shift in time and a small modification in amplitude from one day to the other. A possible explanation for this fact is the minute deterioration of the antibody during refrigeration, manipulation errors and small modification of the temperature and humidity in the environment. For an optimum reaction, the temperature should be maintained at the optimum of each antibody-antigen pair so this is a parameter that should be measured during a future study. The influence of humidity on the evaporation is also a factor to be determined.

One day after their initial deposition, when the sediment was in a dry state, the images were taken on the SEM. They represent the Uveal melanoma and breast cancer cells adherent on the cantilever beam substrate. The pictures clearly present the morphological differences between the cell lines and also their unique adherence pattern, pattern that can be decisive for the gradient of the surface stress at the surface of the beam. It also can alter

the surface tension through the modification in the characteristics of the surface, i.e. making it more hydrophilic or hydrophobic. This is an area of investigation that will bring a good contribution in the understanding of the phenomena that takes place at the substrate level.
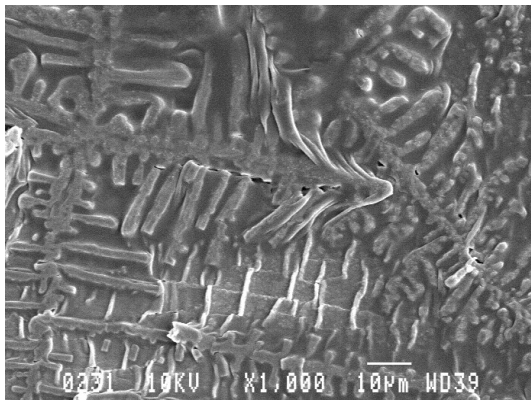
Figure 8.15 SEM image of 92.1 cell line.
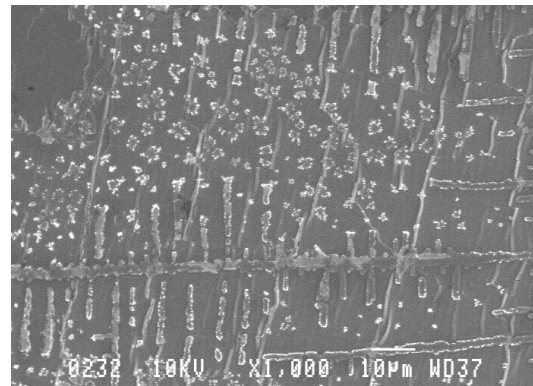
Figure 8.16 SEM image of OCM cell line.
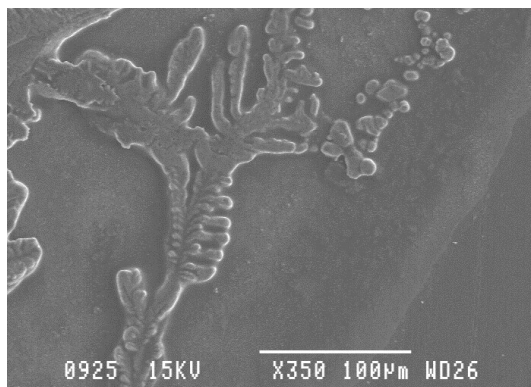
Figure 8.17 SEM image of MKTBR.
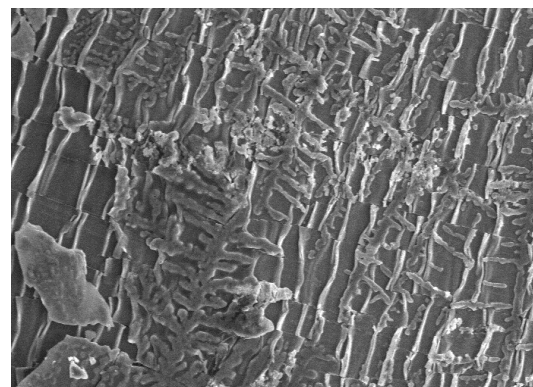
Figure 8.18 SEM image of SP6.5.
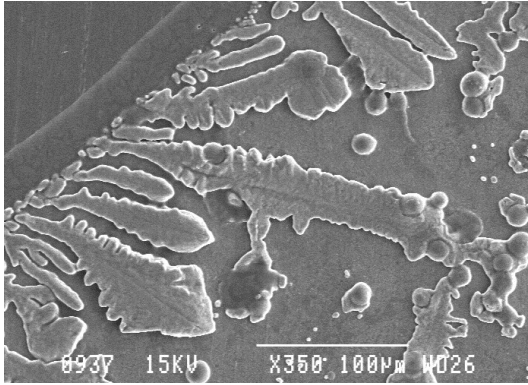
Figure 8.19 Lower magnification of SP6.5.
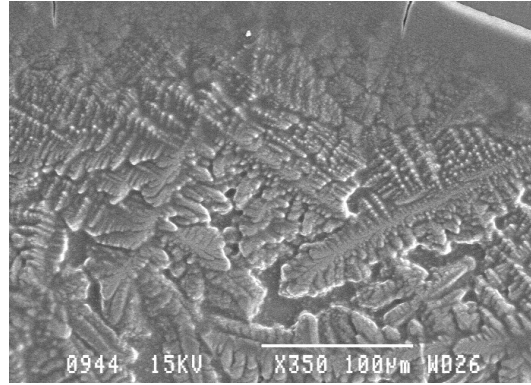
Figure 8.20 SEM image of UW-1 cell line.
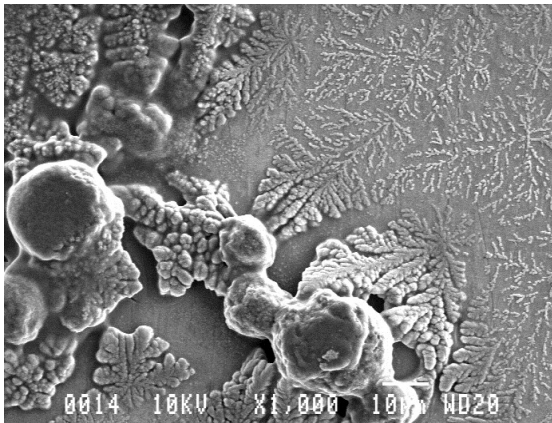
Figure 8.21 SEM image of HCC1419 cell line.
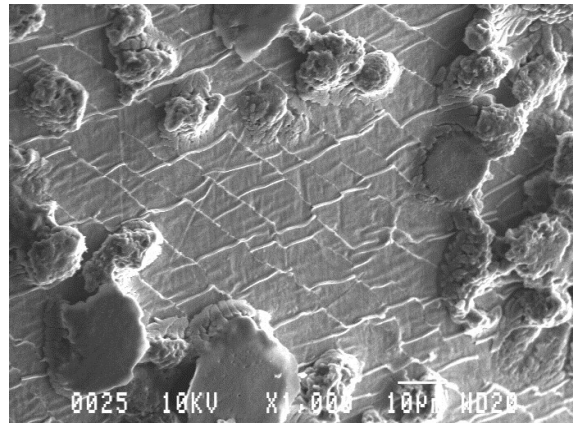
Figure 8.22 Higher magnification of the substrate pattern for HCC1419 cells.

8.2   Optical detection of the colorectal cancer SW480 cell line

The name of colorectal cancer denominates in fact two types of cancer: the cancer of the colon and the cancer of the rectum. The many common characteristics were the decisive factor of grouping them together in the oncological nomenclature. The cancer of

colon has its origin, as the name suggests, in the colon, while the cancer of rectum takes its name from rectum which, anatomically is situated next to the colon.

Colorectal type of cancer starts with the development of polyps at the level of the colon epithelium where, in time, malignant cells can develop. If the condition is not treated in an incipient phase, the malignant cells can escape the site, spread and metastasize in other regions of the body. [198] .Classified as the third both in incidence and leading cause of dead from an oncological condition, in 2011 was diagnosed in about a number of 140 000 of people while 50 000 persons lost their life because of it [199] .

The SW480 cell line designates two groups of cells: the major subpopulation consists of epithelial cells, while the second one contains round types of cells. These components bring forth a special pattern of development with a longer growth time and a reduced adherence to the wall of the culture flask. The SW480 cells were cultured in the same type of biological incubator; however the medium of growth is no longer the RPMI-1640, but Leibovitz L-15, in which the FBS nutrient was added at 10% concentration. Before each experiment the monolayer of cells is separated with trypsin, centrifuged, countered and brought at a concentration of 1 million cells per millilitre.

When treated with their specific antibody (Anti-CEA) the SW480 cells can combine with only a small quantity of it most, most probably due to their spherical and bipolar morphology. The carcinoenbryonic antibody Anti-CEA is the complementary of the antigen CEA. CEA is a powerful immunogen and is overexpressed when some types of

adenocarcinoma are present in colon, lung or breast. The visual inspection of the evaporation of 0.6 microliters of SW480 mixture on the cantilever substrate confirms the low adherence properties of this cell line.

The images presented below show a unique signature characterized by a longer transition time, in comparison with the other types of cells, and the presence of two peaks close to the end of evaporation (1000 s) that can be created by a different pattern of adhesion that generates a particular gradient of surface stress and hydrophobicity.
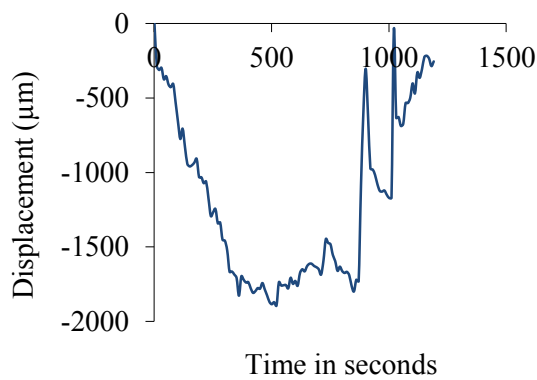
Figure 8.23 First day results for 0.6 μl of SW480 alone.
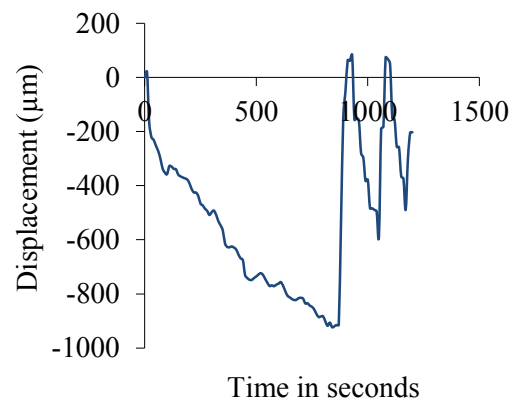
Figure 8.24 First day results for 0.6 μl of SW480 alone – second experiment.
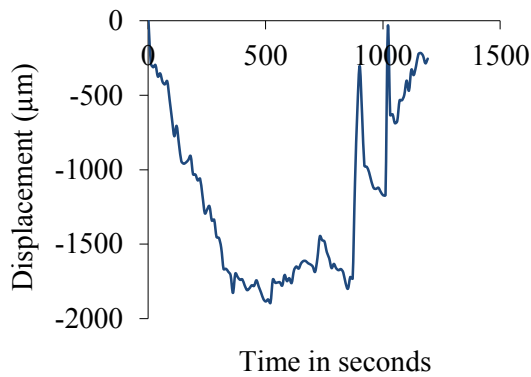
Figure 8.25 Second day results for 0.6 µl of SW480 alone.
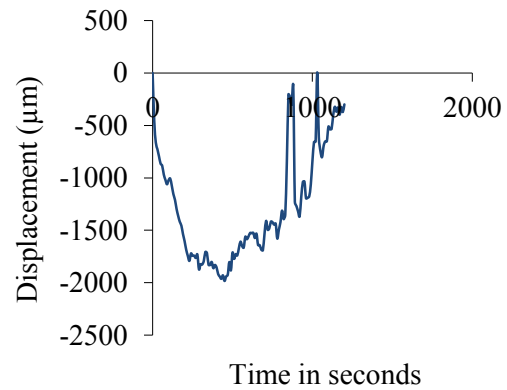
Figure 8.26 Second day results for 0.6 µl of SW480 alone – second experiment.

The pattern of adhesion of the SW480 cells is shown in the SEM images taken for the dried specimens, after 24 hours from the cantilever experiments. Figure 8.27 highlights cells with an exploded nucleus while Figure 8.28 indicates the presence of sites where clusters of cells where formed before their death.

The existence of a unique signature for this cell line when combined with the Anti-CEA antibody is proved in the plots form Figure 8.29 to Figure 8.34. During the third day experiments a supplementary peak occurs towards the end of the evaporation ($\approx$1200 s). A tentative hypothesis for this occurrence is either a difference in the life stage of the cells, a boosted response to the antibody or small variations in temperature and humidity.
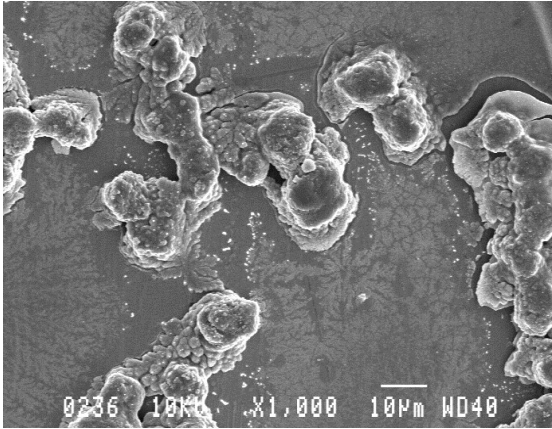
Figure 8.27 Epithelial round type of SW480 cells with disrupted nucleus
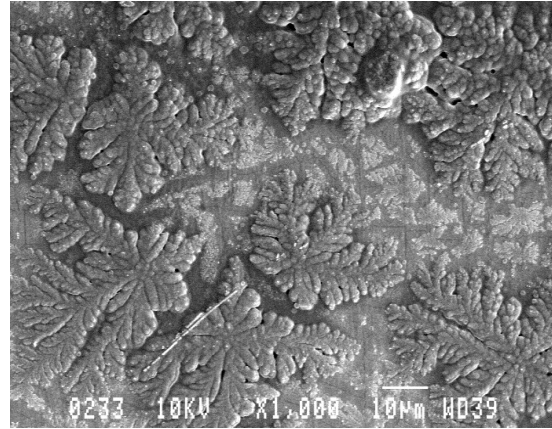
Figure 8.28 SW480 clustered cells.
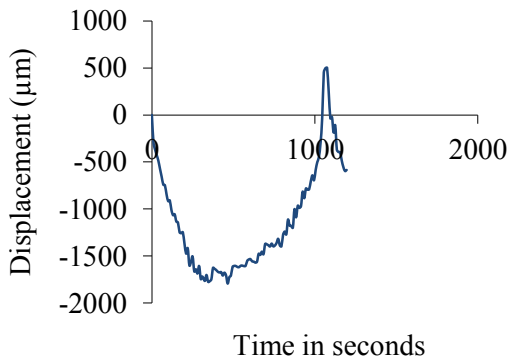
Figure 8.29 First day plots: 0.6 μl of SW480 with Anti-CEA.
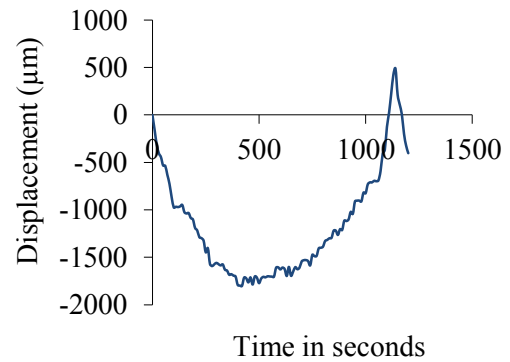
Figure 8.30 First day plots: 0.6 μl of SW480 with Anti-CEA –second experiment.

213
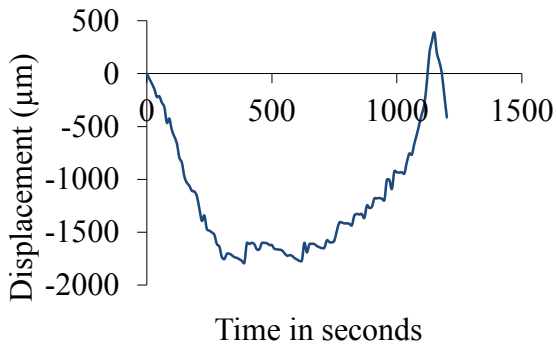
Figure 8.31 Second day plots: 0.6 µl of
SW480 with Anti-CEA.
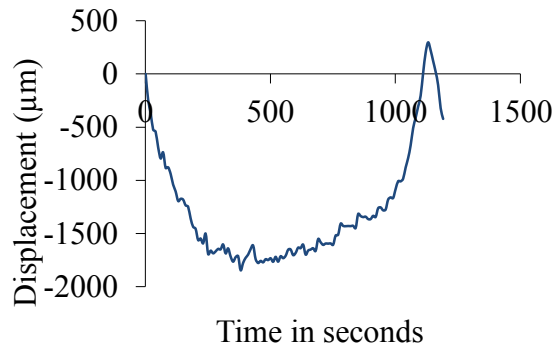
Figure 8.32 Second day plots: 0.6 µl of
SW480 with Anti-CEA – second experiment
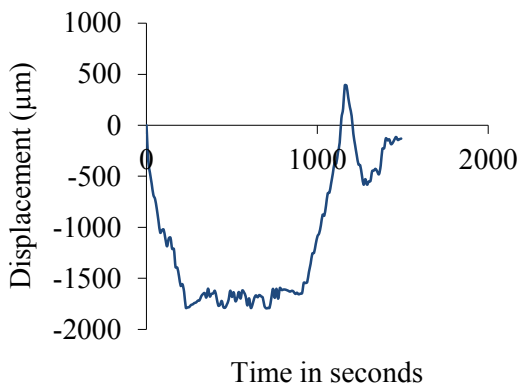
Figure 8.33 Third day plots: 0.6 µl of
SW480 with Anti-CEA.
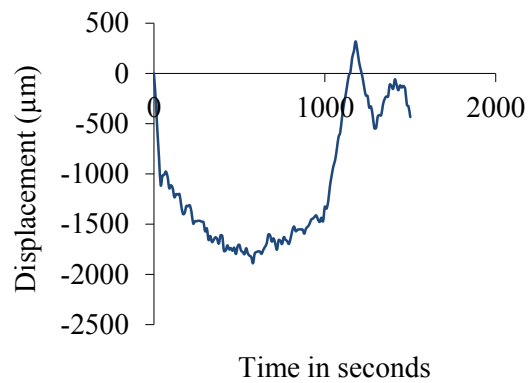
Figure 8.34 Third day plots: 0.6 µl of
SW480 with Anti-CEA.

Appendix C.   Publications

As follows will be listed the conference and the journal papers having the author of this work as a contributor.

Conference papers

Roman, D., Nerguizian, V., Stiharu, I. (2008) *Droplet evaporation in capillary bridges*, Proceedings of the ASME 2008 Summer Bioengineering Conference (SBC2008), Marco Island, USA, pages.

Roman, D., Dulipovici, A., Allazam, A., Stiharu, I., Nerguizian, V., Constantin, N. G., *Analysis of On-Chip Heat Distribution in the Design of RF Power Detectors and RF Transistor Arrays for MMIC Power Amplifiers*, COMSOL Conference Digest, October 2009.

Dulipovici, A., **Roman, D**., Stiharu, I., Nerguizian, V., and Constantin, N. G**.**, *An Efficient Finite Element Analysis on an RF Structure Used to Evaluate the Effect of Microwave Radiation on Uveal Melanoma Cells,* COMSOL Conference Digest, October 2009.

Alazzam, A., **Roman, D.,** Nerguizian, V. Stiharu, I, Bhat, R., Yasmeen, A., Al Moustafa, A. E., *Real-time continuous dielectrophoretic separation of malignant cells*, 1st Microsystems and Nanoelectronics Research Conference, MNRC 2008, October 14-15, 2008, Ottawa, Canada.

Journal papers:

Nerguizian, V., Alazzam, A., **Roman, D**., Stiharu, I., Burnier, M., *Analytical Solutions and Validation of Electric Field and Dielectrophoretic Force in a Bio-microfluidic Channel*, Journal of Electrophoresis, 2012, Volume 33, Issue 3, p 426-435.

Alazzam, A., **Roman, D.**, Nerguizian, V., Stiharu, I., Bhat, R. *Analytical formulation of electric field and dielectrophoretic force for moving dielectrophoresis using Fourier series*, Journal of Microfluidics and Nano fluidics, 2010, Volume 9, Issue 6, p 1115-1124.

Nerguizian, V., Alazzam, A., **Roman, D**., Brisebois, S., Stiharu, I., Burnier M, *Dielectric Characterization of Biological Cells at Microwave Frequencies*, (on hold for confidentiality purposes).

Changizi, M.,**Roman D**., Stiharu, I., *Detection of bio-chemical reactions through micro structural interactions. Journal of Optoelectronics and Advanced Materials*, 2011. 13(7): p. 1020.

Roman, D., Yasmeen, A., Mireuta M., Stiharu, I, Al Moustafa, A. E., *Significant toxic role for single-walled carbon nanotubes during normal embryogenesis, Journal of Nanomedicine,* (submitted second review December 2012).

Roman, D. Alazzam, A.,, Nerguizian, V. Stiharu, I, *Integrated micro-system for real time cell bio-chemical assessment,* Recent Patents on Nanomedicine, 2013 (to be submitted).

References

1. Veridex, V. *Prospective monitoring of circulating tumor cells in breast cancer patients treated with primary systemic therapy—A translational project of the German Breast Group study GeparQuattro*. 2007.

2. Stiharu, I., et al., *Methods and devices for early detection of cancer cells and types through micromechanical interactions*, 2008, Google Patents.

3. Wu, J., et al., *Biomedical and clinical applications of immunoassays and immunosensors for tumor markers*. TrAC Trends in Analytical Chemistry. **26**(7): p. 679-688.

4. Petersen, K. and S. Cepheid. *Biomedical applications of MEMS*. 1996.

5. Chatterjee, S. and B. Zetter, *Cancer biomarkers: knowing the present and predicting the future.* Future Oncology, 2005. **1**(1): p. 37-50.

6. Chin, C.D., V. Linder, and S.K. Sia, *Lab-on-a-chip devices for global health: past studies and future opportunities.* Lab on a Chip, 2007. **7**(1): p. 41-57.

7. Alvarez, M. and L. Lechuga, *Microcantilever-based platforms as biosensing tools.* Analyst, 2010. **135**: p. 827-836.

8. Savran, C.A., et al., *Micromechanical detection of proteins using aptamer-based receptor molecules.* Analytical chemistry, 2004. **76**(11): p. 3194-3198.

9. Krivacic, R., et al., *A rare-cell detector for cancer*. Proceedings of the National Academy of Sciences, 2004. **101**(29): p. 10501.

10. Fritz, J., et al., *Translating biomolecular recognition into nanomechanics.* Science, 2000. **288**(5464): p. 316-318.

11. McKendry, R., et al., *Multiple label-free biodetection and quantitative DNA-binding assays on a nanomechanical cantilever array.* Proceedings of the National Academy of Sciences, 2002. **99**(15): p. 9783.

12. Fritz, J., *Cantilever biosensors.* Analyst, 2008. **133**(7): p. 855-863.

13. Hwang, K.S., et al., *Micro- and Nanocantilever Devices and Systems for Biomolecule Detection.* Annual Review of Analytical Chemistry, 2009. **2**(1): p. 77-98.

14. Liu, M. and Y. Tai, *A 3-D MICROFLUIDIC COMBINATORIAL CELL CULTURE ARRAY.* 2009.

15. Freeman, D.W. *Johnson & Johnson "Liquid Biopsy" Cancer Blood Test: What It Would Mean for Patients*. 2011.

16. Ahn, C.H., et al., *Disposable smart lab on a chip for point-of-care clinical diagnostics.* Proceedings of the IEEE, 2004. **92**(1): p. 154-173.

17. Lee, B., et al., *A fully automated immunoassay from whole blood on a disc.* Lab on a Chip, 2009. **9**(11): p. 1548-1555.

18. Weigl, B.H., R.L. Bardell, and C.R. Cabrera, *Lab-on-a-chip for drug development.* Advanced drug delivery reviews, 2003. **55**(3): p. 349-377.

19. Dittrich, P. and A. Manz, *Lab-on-a-chip: microfluidics in drug discovery.* Nature Reviews Drug Discovery, 2006. **5**(3): p. 210-218.

20. Li, P., *Implantable bioMEMS drug delivery systems*, in *DOCTOR OF PHILOSOPHY*2009, UNIVERSITY OF SOUTHERN CALIFORNIA.

21. Rao, R., *A rapid multiplexed diagnostic system for breast cancer*, 2006, UNIVERSITY OF CALIFORNIA, DAVIS.

22. Kai, J., S. Thati, and C. Ahn. *An ultra-high sensitive protein lab-on-a-chip on polymer for prostate cancer diagnostics*. 2005.

23. Yager, P., et al., *Microfluidic diagnostic technologies for global public health.* NATURE-LONDON-, 2006. **442**(7101): p. 412.

24. Figeys, D. and D. Pinto, *Lab-on-a-Chip: A Revolution in Biological and Medical Sciences.* Analytical Chemistry, 2000. **72**(9): p. 330-335.

25. Manz, A., N. Graber, and H. Widmer, *Miniaturized total chemical analysis systems: a novel concept for chemical sensing.* TRANSPORT, 1990. **1**: p. 1.

26. Manz, A., et al., *Micro total analysis systems. 1. Introduction, theory, and technology.* ANALYTICAL CHEMISTRY-WASHINGTON DC-, 2002. **74**(12): p. 2623-2636.

27. Manz, A., T. Vilkner, and D. Janasek, *Micro total analysis systems. Recent developments.* Anal. Chem, 2004. **76**(12): p. 3373-3386.

28. Raiteri, R., et al., *Micromechanical cantilever-based biosensors.* Sensors and Actuators B: Chemical, 2001. **79**(2-3): p. 115-126.

29. Men, Y., et al., *Digital Polymerase Chain Reaction in an Array of Femtoliter Polydimethylsiloxane Microreactors.* Analytical Chemistry-Columbus, 2012. **84**(10): p. 4262.

30.   Kricka, L., *Miniaturization of analytical systems.* Clinical Chemistry, 1998. **44**(9): p. 2008-2014.

31.   Zuker, C.S. and Y. Zhang, *Assays for taste receptor cell specific ion channel*, 2001, Google Patents.

32.   Ferrari, M., *Cancer nanotechnology: opportunities and challenges.* Nature Reviews Cancer, 2005. **5**(3): p. 161-171.

33.   Manz, A., et al., *Micro total analysis systems: latest achievements.* Analytical Chemistry, 2008. **80**(12): p. 4403-4419.

34.   Waggoner, P.S. and H.G. Craighead, *Micro- and nanomechanical sensors for environmental, chemical, and biological detection.* Lab on a Chip, 2007. **7**(10): p. 1238-1255.

35.   Manz, A., et al., *Micro total analysis systems. 2. Analytical standard operations and applications.* ANALYTICAL CHEMISTRY-WASHINGTON DC-, 2002. **74**(12): p. 2637-2652.

36.   Larsen, R., *Microblood analyzers for the sensitive and portable detection of clinically relevant cardiac markers*, 2007, University Microfilms International, P. O. Box 1764, Ann Arbor, MI, 48106, USA.

37.   Henderson, E., *BioForce Nanosciences, Inc.* Nanomedicine, 2007. **2**(3): p. 391-396.

38.   Legge, C., *Chemistry under the Microscope--Lab-on-a-Chip Technologies.* Journal of Chemical Education, 2002. **79**: p. 173.

39.   Yi, C., et al., *Microfluidics technology for manipulation and analysis of biological cells.* Analytica Chimica Acta, 2006. **560**(1-2): p. 1-23.

40. Chakraborty, S., *Microfluidics and Microfabrication*2009: Springer.

41. Hwang, K.S., et al., *In-situ quantitative analysis of a prostate-specific antigen (PSA) using a nanomechanical PZT cantilever.* Lab on a Chip, 2004. **4**(6): p. 547-552.

42. Leclipteux, T., et al., *Double-sided device for multiplex dipstick immunodiagnostic*, 2006, EP Patent 1,657,550.

43. Gervais, L., N. De Rooij, and E. Delamarche, *Microfluidic Chips for Point-of-Care Immunodiagnostics.* Advanced Materials, 2011. **23**(24): p. H151-H176.

44. Nagrath, S., et al., *Isolation of rare circulating tumour cells in cancer patients by microchip technology.* Nature, 2007. **450**(7173): p. 1235-1239.

45. Hessel, V., H. Löwe, and F. Schönfeld, *Micromixers—a review on passive and active mixing principles.* Chemical Engineering Science, 2005. **60**(8): p. 2479-2501.

46. Xue-Feng, Z., et al., *Actuation and control of droplets by using electrowetting-on-dielectric.* Chinese Physics Letters, 2004. **21**: p. 1851.

47. Ruddon, R., *Cancer biology*2007: Oxford University Press, USA.

48. LIVESTRONG, T.A.C.S.a., *The Global Economic Cost Of Cancer*, 2010.

49. Society, A.C., *Cancer facts & figures*2012: The Society.

50. Toner, M. and D. Irimia, *Blood-on-a-chip.* 2005.

51. Gabriel, J., *The biology of cancer*2007: Wiley.

52. Kastan, M., *Checkpoint controls and cancer*1997: Cold Spring Harbor Laboratory Press.

53.   Pantel, K. and C. Alix-Panabières, *Circulating tumour cells in cancer patients: challenges and perspectives.* Trends in Molecular Medicine, 2010.

54.   Koop, R., *Combinatorial biomarkers: from early toxicology assays to patient population profiling.* Drug discovery today, 2005. **10**(11): p. 781-788.

55.   Armakolas, A., et al., *Detection of the circulating tumor cells in cancer patients.* Future Oncology, 2010. **6**(12): p. 1849-1856.

56.   Kops, G.J.P.L., B.A.A. Weaver, and D.W. Cleveland, *On the road to cancer: aneuploidy and the mitotic checkpoint.* Nature Reviews Cancer, 2005. **5**(10): p. 773-785.

57.   Allard, W., et al., *Tumor cells circulate in the peripheral blood of all major carcinomas but not in healthy subjects or patients with nonmalignant diseases.* 2004. **10**(20): p. 6897-6904.

58.   Münger, K., et al., *Complex formation of human papillomavirus E7 proteins with the retinoblastoma tumor suppressor gene product.* The EMBO journal, 1989. **8**(13): p. 4099.

59.   Yarden, R.I. and L.C. Brody, *BRCA1 interacts with components of the histone deacetylase complex.* Proceedings of the National Academy of Sciences, 1999. **96**(9): p. 4983-4988.

60.   van de Stolpe, A., et al., *Circulating tumor cell isolation and diagnostics: toward routine clinical use.* Cancer Research, 2011. **71**(18): p. 5955-5960.

61. Riethdorf, S., et al., *Detection of circulating tumor cells in peripheral blood of patients with metastatic breast cancer: a validation study of the CellSearch system.* Clinical Cancer Research, 2007. **13**(3): p. 920-928.

62. Gasent Blesa, J., et al., *Circulating tumor cells in breast cancer: methodology and clinical repercussions.* Clinical and Translational Oncology, 2008. **10**(7): p. 399-406.

63. Virella, G., *Medical immunology*2001: Informa Healthcare.

64. Kumagai, I. and K. Tsumoto, *Antigen–Antibody Binding.*

65. Law, B., *Immunoassay: A practical guide*1996: CRC.

66. Chatterjee, S. and B. Zetter, *Cancer biomarkers: knowing the present and predicting the future.* Future Oncol., 2005. **1**(1): p. 37-50.

67. Browning-Kelley, M., et al., *Atomic force microscopic study of specific antigen/antibody binding.* Langmuir, 1997. **13**(2): p. 343-350.

68. Wu, G., et al., *Bioassay of prostate-specific antigen (PSA) using microcantilevers.* Nature Biotechnology, 2001. **19**(9): p. 856-860.

69. Kaufman, H.L. and J.D. Wolchok, *General principles of tumor immunotherapy: basic and clinical applications of tumor immunology*2007: Springer Verlag.

70. Wilson, K., *Cancer Biomarkers: Analytical Techniques for Discovery.* The Yale Journal of Biology and Medicine, 2007. **80**(3): p. 137.

71. Meyer, G. *Immunology - Chapter Seven Immunoglobulins- Antigen-Antibody Reactions And Selected Tests*. Microbiology and Immunology 2010; Available from: http://pathmicro.med.sc.edu/mayer/ab-ag-rx.htm.

72.   Hu, G., Y. Gao, and D. Li, *Modeling micropatterned antigen-antibody binding kinetics in a microfluidic chip.* Biosensors and Bioelectronics, 2007. **22**(7): p. 1403-1409.

73.   Sadana, A. and D. Sii, *Binding kinetics of antigen by immobilized antibody: influence of reaction order and external diffusional limitations.* Biosensors and Bioelectronics, 1992. **7**(8): p. 559-568.

74.   Sadana, A. and Z. Chen, *Influence of non-specific binding on antigen-antibody binding kinetics for biosensor applications.* Biosensors and Bioelectronics, 1996. **11**(1-2): p. 17-33.

75.   Wu, G., et al., *Origin of nanomechanical cantilever motion generated from biomolecular interactions.* Proceedings of the National Academy of Sciences of the United States of America, 2001. **98**(4): p. 1560.

76.   Yue, M., et al., *Label-free protein recognition two-dimensional array using nanomechanical sensors.* Nano letters, 2008. **8**(2): p. 520-524.

77.   Lang, H., M. Hegner, and C. Gerber, *Cantilever array sensors.* Materials today, 2005. **8**(4): p. 30-36.

78.   Watari, M., et al., *Investigating the molecular mechanisms of in-plane mechanochemistry on cantilever arrays.* Journal of the American Chemical Society, 2007. **129**(3): p. 601-609.

79.   Sushko, M.L., et al., *Physics of nanomechanical biosensing on cantilever arrays.* Advanced Materials, 2008. **20**(20): p. 3848-3853.

80.   Kwon, T., et al., *Micromechanical observation of the kinetics of biomolecular interactions.* Applied Physics Letters, 2008. **93**: p. 173901.

81.   Stachowiak, J.C., et al., *Chemomechanics of surface stresses induced by DNA hybridization.* Langmuir, 2006. **22**(1): p. 263-268.

82.   Ziegler, C., *Cantilever-based biosensors.* Analytical and bioanalytical chemistry, 2004. **379**(7): p. 946-959.

83.   Jeetender, A., et al., *MEMS-based sensor and method for optical detection of peptides bio-reaction time (Proceedings Paper).* 2006.

84.   Jeetender, A., I. Stiharu, and M. Packirisamy. *Micro-opto mechanical biosensors for enzymatic detection.* 2005.

85.   Chandrasekaran, A. and M. Packirisamy, *Experimental investigation of evanescence-based infrared biodetection technique for micro-total-analysis systems.* Journal of Biomedical Optics, 2009. **14**: p. 054050.

86.   Chandrasekaran, A., G. Rinaldi, and M. Packirisamy, *Label-free detection of enzymatic interaction through dynamic behaviour of microstructures.* International Journal of Advances in Engineering Sciences and Applied Mathematics, 2009: p. 1-7.

87.   Pierstorff, E. and D. Ho, *Monitoring, diagnostic, and therapeutic technologies for nanoscale medicine.* Journal of Nanoscience and Nanotechnology, 2007. **7**(9): p. 2949-2968.

88.   Zougagh, M. and Á. Ríos, *Micro-electromechanical sensors in the analytical field.* The Analyst, 2009. **134**(7): p. 1274-1290.

89. Shih, W. and W.Y. Shih, *SPECIFICITY AND SENSITIVITY ENHANCEMENT IN CANTILEVER SENSING*, 2010, US Patent App. 20,100/210,032.

90. Yang, M., et al., *Piezoelectric biosensor and biosensor array for parallel detection of multiple biomarkers*, 2009, EP Patent 2,017,613.

91. Mutharasan, R., et al., *Enhanced sensitivity of a cantilever sensor via specific bindings*, 2011, Google Patents.

92. Hempen, C. and U. Karst, *Labeling strategies for bioassays.* Analytical and bioanalytical chemistry, 2006. **384**(3): p. 572-583.

93. Waggoner, P.S. and H.G. Craighead, *Micro-and nanomechanical sensors for environmental, chemical, and biological detection.* Lab Chip, 2007. **7**(10): p. 1238-1255.

94. Pease, A.C., et al., *Light-generated oligonucleotide arrays for rapid DNA sequence analysis.* Proceedings of the National Academy of Sciences, 1994. **91**(11): p. 5022.

95. Dubois, L.H. and R.G. Nuzzo, *Synthesis, structure, and properties of model organic surfaces.* Annual Review of Physical Chemistry, 1992. **43**(1): p. 437-463.

96. Weetall, H.H., *Trypsin and papain covalently coupled to porous glass: preparation and characterization.* Science, 1969. **166**(3905): p. 615-617.

97. Betts, T.A., et al., *Selectivity of chemical sensors based on micro-cantilevers coated with thin polymer films.* Analytica Chimica Acta, 2000. **422**(1): p. 89-99.

98. Brinker, C.J. and G.W. Scherer, *Sol-gel science: the physics and chemistry of sol-gel processing*1990: Academic Pr.

99. Loui, A., et al., *The effect of piezoresistive microcantilever geometry on cantilever sensitivity during surface stress chemical sensing.* Sensors and Actuators A: Physical, 2008. **147**(2): p. 516-521.

100. Rugar, D., H. Mamin, and P. Guethner, *Improved fiber‑optic interferometer for atomic force microscopy.* Applied Physics Letters, 1989. **55**(25): p. 2588-2590.

101. Boisen, A., et al., *Environmental sensors based on micromachined cantilevers with integrated read-out.* Ultramicroscopy, 2000. **82**(1): p. 11-16.

102. Johnson, B.N. and R. Mutharasan, *Biosensing using dynamic-mode cantilever sensors: A review.* Biosensors and Bioelectronics, 2011.

103. Burg, T.P., et al., *Weighing of biomolecules, single cells and single nanoparticles in fluid.* Nature, 2007. **446**(7139): p. 1066-1069.

104. Oden, P., *Gravimetric sensing of metallic deposits using an end-loaded microfabricated beam structure.* Sensors and Actuators B: Chemical, 1998. **53**(3): p. 191-196.

105. Godin, M., et al., *Measuring the mass, density, and size of particles and cells using a suspended microchannel resonator.* Applied Physics Letters, 2007. **91**(12): p. 123121-123121-3.

106. Van De Vijver, M.J., et al., *A gene-expression signature as a predictor of survival in breast cancer.* New England Journal of Medicine, 2002. **347**(25): p. 1999-2009.

107. Zheng, S., et al., *Analysis of DNA hybridization regarding the conformation of molecular layer with piezoelectric microcantilevers.* Lab Chip, 2010. **11**(1): p. 63-69.

108.   Tabard-Cossa, V., et al., *Microcantilever-based sensors: Effect of morphology, adhesion, and cleanliness of the sensing surface on surface stress.* Anal. Chem, 2007. **79**(21): p. 8136-8143.

109.   Arntz, Y., et al., *Label-free protein assay based on a nanomechanical cantilever array.* Nanotechnology, 2003. **14**: p. 86.

110.   Raiteri, R., M. Grattarola, and H.J. Butt, *Measuring electrostatic double-layer forces at high surface potentials with the atomic force microscope.* The Journal of Physical Chemistry, 1996. **100**(41): p. 16700-16705.

111.   Shu, W., et al., *DNA molecular motor driven micromechanical cantilever arrays.* Journal of the American Chemical Society, 2005. **127**(48): p. 17054-17060.

112.   Timoshenko, S., *Analysis of bi-metal thermostats.* J. Opt. Soc. Am, 1925. **11**(3): p. 233-255.

113.   Chu, W.H., M. Mehregany, and R.L. Mullen, *Analysis of tip deflection and force of a bimetallic cantilever microactuator.* Journal of Micromechanics and Microengineering, 1993. **3**: p. 4.

114.   Gere, J., S. P. Timoshenko, *Mechanics of Materials.* Mechanics of Materials. Third edition, PWS-Kent, 1990.

115.   Gimzewski, J., et al., *Observation of a chemical reaction using a micromechanical sensor.* Chemical Physics Letters, 1994. **217**(5): p. 589-594.

116.   Bonaccurso, E. and H. Butt, *Microdrops on atomic force microscope cantilevers: Evaporation of water and spring constant calibration.* J. Phys. Chem. B, 2005. **109**(1): p. 253-263.

228

117.   Cappella, B. and G. Dietler, *Force-distance curves by atomic force microscopy.* Surface Science Reports, 1999. **34**(1-3): p. 1-104.

118.   Sumali, H. and T.G. Carne, *Air-Drag Damping on Micro-Cantilever Beams.*

119.   Baker, W.E., W.E. Woolam, and D. Young, *Air and internal damping of thin cantilever beams.* International Journal of Mechanical Sciences, 1967. **9**(11): p. 743-766.

120.   Chandra, S., et al., *Effect of liquid-solid contact angle on droplet evaporation.* Fire safety journal, 1996. **27**(2): p. 141-158.

121.   Bryan, J.L., *Fire suppression and detection systems*1974: Glencoe Press.

122.   Allegrini, M., et al., *Laser thermal effects on atomic force microscope cantilevers.* Ultramicroscopy, 1992. **42**: p. 371-378.

123.   Kipp, S., R. Lacmann, and M. Schneeweiss, *Problems in temperature control performing in situ investigations with the scanning force microscope.* Ultramicroscopy, 1995. **57**(4): p. 333-335.

124.   Golovko, D., et al., *Evaporative cooling of sessile water microdrops measured with atomic force microscope cantilevers.* Journal of Micromechanics and Microengineering, 2008. **18**: p. 095026.

125.   Hu, H. and R.G. Larson, *Marangoni effect reverses coffee-ring depositions.* The Journal of Physical Chemistry B, 2006. **110**(14): p. 7090-7094.

126.   Bareisis, J., *Stiffness and strength of multilayer beams.* Journal of composite materials, 2006. **40**(6): p. 515-531.

127. Bareisis, J.P., V. . *Design of Multilayer Composite Structural Elements*, in *Mokomoji knyga,*, Technologija, Editor 1995: Kaunas.

128. Gere, J. and S. Timoshenko, *Mechanics of materials, PWS Pub.* Co., Boston, 1997.

129. Haschke, T., et al., *Sessile-drop-induced bending of atomic force microscope cantilevers: a model system for monitoring microdrop evaporation.* Journal of Micromechanics and Microengineering, 2006. **16**: p. 2273.

130. Yu, Y. and Y. Zhao, *Deformation of PDMS membrane and microcantilever by a water droplet: Comparison between Mooney-Rivlin and linear elastic constitutive models.* Journal of colloid and interface science, 2009. **332**(2): p. 467-476.

131. Sang, M.E.S., *An approach to the design of surface stress-based PDMS micro-membrane biosensors—.*

132. Zhang, Y., Q. Ren, and Y. Zhao, *Modelling analysis of surface stress on a rectangular cantilever beam.* Journal of Physics D: Applied Physics, 2004. **37**: p. 2140.

133. Bonaccurso, E., *Microdrops Evaporating on AFM Cantilevers.* Surface and Interfacial Forces–From Fundamentals to Applications, 2008: p. 57-65.

134. Johnson Jr, R.E., *Conflicts between Gibbsian Thermodynamics and Recent Treatments of Interfacial Energies in Solid-Liquid-Vapor.* The Journal of Physical Chemistry, 1959. **63**(10): p. 1655-1658.

135. Pericet-Ca mara, R., et al., *Effect of capillary pressure and surface tension on the deformation of elastic surfaces by sessile liquid microdrops: An experimental investigation.* Langmuir, 2008. **24**(19): p. 10565-10568.

136.   De Gennes, P.G., F. Brochard-Wyart, and D. Quéré, *Capillarity and wetting phenomena: drops, bubbles, pearls, waves*2004: Springer Verlag.

137.   Shuttleworth, R., *The surface tension of solids.* Proceedings of the Physical Society. Section A, 2002. **63**(5): p. 444.

138.   Liu, J., et al., *Abnormal bending of micro-cantilever plate inducecd by a droplet.* Acta Mechanica Solida Sinica, 2010. **23**(5): p. 428-436.

139.   Li, F., et al., *Effects of Static Magnetic Fields on the Physical and Chemical Properties of Cell Culture Medium RPM1 1640.* Electromagnetic Biology & Medicine, 2007. **26**(1): p. 25-32.

140.   Haschke, T., et al. *Simulation of evaporating droplets on AFM-cantilevers.* 2005.

141.   Young, W.C. and R.G. Budynas, *Roark's formulas for stress and strain.* 2002.

142.   Meacham, J., et al., *Micromachined ultrasonic droplet generator based on a liquid horn structure.* Review of Scientific Instruments, 2004. **75**: p. 1347.

143.   Abbott, C.E. and T.W. Cannon, *A droplet generator with electronic control of size, production rate, and charge.* Review of Scientific Instruments, 1972. **43**(9): p. 1313-1317.

144.   Lin, H.B., J. Eversole, and A. Campillo, *Vibrating orifice droplet generator for precision optical studies.* Review of Scientific Instruments, 1990. **61**(3): p. 1018-1023.

145.   Fair, R., *Digital microfluidics: is a true lab-on-a-chip possible?* Microfluidics and Nanofluidics, 2007. **3**(3): p. 245-281.

146.   Madou, M.J., *MEMS Handbook*, 2002, CRC PRESS.

147. Akashi, T., Y. Yoshimura, and S. Higashiyama. *Deep reactive ion etching of pyrex glass using a bonded silicon wafer as an etching mask*. 2005. IEEE.

148. Van Den Berg, A. and T. Lammerink, *Micro total analysis systems: microfluidic aspects, integration concept and applications*. Topics in Current Chemistry, 1998. **194**: p. 21-50.

149. Hong, J. and S. Quake, *Integrated nanoliter systems*. Nature biotechnology, 2003. **21**(10): p. 1179-1183.

150. Bikerman, J., *Capillarity before Laplace: Clairaut, Segner, Monge, Young.* Archive for History of Exact Sciences, 1978. **18**(2): p. 103-122.

151. Hotta, K., K. Takeda, and K. Iinoya, *The capillary binding force of a liquid bridge.* Powder Technology, 1974. **10**(4-5): p. 231-242.

152. Rabinovich, Y.I., M.S. Esayanur, and B.M. Moudgil, *Capillary forces between two spheres with a fixed volume liquid bridge: theory and experiment.* Langmuir, 2005. **21**(24): p. 10992-10997.

153. Lowry, B.J. and P.H. Steen, *Capillary surfaces: stability from families of equilibria with application to the liquid bridge.* Proceedings of the Royal Society of London. Series A: Mathematical and Physical Sciences, 1995. **449**(1937): p. 411-439.

154. Gad-el-Hak, M., *The MEMS handbook*. Vol. 17. 2002: CRC Pr I Llc.

155. Wang, M.Y., X. Wang, and D. Guo, *A level set method for structural topology optimization.* Computer methods in applied mechanics and engineering, 2003. **192**(1): p. 227-246.

156. Olason, A. and D. Tidman, *Methodology for topology and shpe optimization in the design process.* 2010.

157. Nishiwaki, S., et al., *Topology optimization of compliant mechanisms using the homogenization method.* 1998.

158. Suzuki, K. and N. Kikuchi, *A homogenization method for shape and topology optimization.* Computer methods in applied mechanics and engineering, 1991. **93**(3): p. 291-318.

159. Bendsøe, M.P. and N. Kikuchi, *Generating optimal topologies in structural design using a homogenization method.* Computer methods in applied mechanics and engineering, 1988. **71**(2): p. 197-224.

160. Bendsøe, M.P. and O. Sigmund, *Material interpolation schemes in topology optimization.* Archive of Applied Mechanics, 1999. **69**(9): p. 635-654.

161. Bendsøe, M.P., *Optimal shape design as a material distribution problem.* Structural and Multidisciplinary Optimization, 1989. **1**(4): p. 193-202.

162. Xie, Y. and G.P. Steven, *A simple evolutionary procedure for structural optimization.* Computers & structures, 1993. **49**(5): p. 885-896.

163. Bendsøe, M.P. and O. Sigmund, *Topology optimization: theory, methods, and applications*2003: Springer Verlag.

164. Kincaid, M.C., *Uveal melanoma.* Cancer Control, 1998. **5**: p. 299-309.

165. Inskip, P.D., S.S. Devesa, and J.F. Fraumeni, *Trends in the incidence of ocular melanoma in the United States, 1974–1998.* Cancer causes and control, 2003. **14**(3): p. 251-257.

166.   Diener-West, M., et al., *A review of mortality from choroidal melanoma: II. A meta-analysis of 5-year mortality rates following enucleation, 1966 through 1988.* Archives of ophthalmology, 1992. **110**(2): p. 245.

167.   Singh, A.D. and A. Topham, *Survival rates with uveal melanoma in the United States: 1973–1997.* Ophthalmology, 2003. **110**(5): p. 962-965.

168.   Wu, G., et al., *Origin of nanomechanical cantilever motion generated from biomolecular interactions.* Proceedings of the National Academy of Sciences, 2001. **98**(4): p. 1560.

169.   Siegel, R. and A. Jemal, *Cancer Facts and Figures 2012.* Atlanta, GA: American Cancer Society, 2012. **10**.

170.   Bostwick, D.G. and J. Qian, *High-grade prostatic intraepithelial neoplasia.* Modern pathology, 2004. **17**(3): p. 360-379.

171.   Bostwick, D.G., *High grade prostatic intraepithelial neoplasia. The most likely precursor of prostate cancer.* Cancer, 1995. **75**(S7): p. 1823-1836.

172.   Quan, C., et al., *Study on the use of white light interferometry for multifiber-end surface profile measurement.* Optical Engineering, 2006. **45**(5): p. 055603-055603-9.

173.   Wyant, J.C. *White light interferometry.* in *AeroSense 2002.* 2002. International Society for Optics and Photonics.

174.   Keetch, D., W. Catalona, and D. Smith, *Serial prostatic biopsies in men with persistently elevated serum prostate specific antigen values.* The Journal of urology, 1994. **151**(6): p. 1571.

175. Lamour, G., et al., *Contact angle measurements using a simplified experimental setup.* Journal of Chemical Education, 2010.

176. Kwok, D. and A. Neumann, *Contact angle measurement and contact angle interpretation.* Advances in Colloid and Interface Science, 1999. **81**(3): p. 167-249.

177. Lee, G.B., et al., *Hydrodynamic focusing for a micromachined flow cytometer.* Journal of fluids engineering, 2001. **123**(3): p. 672-679.

178. Howell Jr, P.B., et al., *Two simple and rugged designs for creating microfluidic sheath flow.* Lab Chip, 2008. **8**(7): p. 1097-1103.

179. Holmes, D., H. Morgan, and N.G. Green, *High throughput particle analysis: Combining dielectrophoretic particle focussing with confocal optical detection.* Biosensors and Bioelectronics, 2006. **21**(8): p. 1621-1630.

180. Chou, C.F. and F. Zenhausern, *Electrodeless dielectrophoresis for micro total analysis systems.* Engineering in Medicine and Biology Magazine, IEEE, 2003. **22**(6): p. 62-67.

181. Holmes, D., N.G. Green, and H. Morgan, *Microdevices for dielectrophoretic flow-through cell separation.* Engineering in Medicine and Biology Magazine, IEEE, 2003. **22**(6): p. 85-90.

182. Alazzam, A., et al., *Analytical formulation of electric field and dielectrophoretic force for moving dielectrophoresis using Fourier series.* Microfluidics and Nanofluidics, 2010. **9**(6): p. 1115-1124.

183. Pethig, R., *Review Article—Dielectrophoresis: Status of the theory, technology, and applications.* Biomicrofluidics, 2010. **4**: p. 022811.

184. Sung, J.M., *Dielectrophoresis and Optoelectronic Tweezers for Nanomanipulation.*

185. Morgan, H., et al., *The dielectrophoretic and travelling wave forces generated by interdigitated electrode arrays: analytical solution using Fourier series.* Journal of Physics D: Applied Physics, 2001. **34**: p. 1553.

186. Wang, X., et al., *A theoretical method of electrical field analysis for dielectrophoretic electrode arrays using Green's theorem.* Journal of Physics D: Applied Physics, 1996. **29**: p. 1649.

187. Sun, T., et al., *Analytical electric field and sensitivity analysis for two microfluidic impedance cytometer designs.* IET nanobiotechnology, 2007. **1**: p. 69.

188. Kua, C.H., et al., *Cell motion model for moving dielectrophoresis.* Analytical Chemistry, 2008. **80**(14): p. 5454-5461.

189. Kua, C.H., et al., *Dynamic cell fractionation and transportation using moving dielectrophoresis.* Analytical Chemistry, 2007. **79**(18): p. 6975-6987.

190. Green, N.G., A. Ramos, and H. Morgan, *Numerical solution of the dielectrophoretic and travelling wave forces for interdigitated electrode arrays using the finite element method.* Journal of Electrostatics, 2002. **56**(2): p. 235-254.

191. Alazzam, A., et al. *Real-time continuous dielectrophoretic separation of malignant cells*. 2008. IEEE.

192. Nerguizian, V., *Non-Destructive Bio-Assay of Single Living Cell*, 2012, Concordia University.

193. Nerguizian, V., et al., *Analytical solutions and validation of electric field and dielectrophoretic force in a bio‑microfluidic channel.* Electrophoresis, 2012. **33**(3): p. 426-435.

194. Wright, S.E., *Immunotherapy of breast cancer.* Expert Opinion on Biological Therapy, 2012. **12**(4): p. 479-490.

195. Ansai, S., Y. Hozumi, and S. Kondo, *An immunohistochemical study of BCA-225 in various skin cancers.* The Journal of dermatology, 1994. **21**(1): p. 20.

196. Parham, D., G. Coghill, and A. Robertson, *Critical evaluation of monoclonal antibody staining in breast carcinoma.* Journal of clinical pathology, 1989. **42**(8): p. 810-813.

197. Burchell, J., et al., *Development and characterization of breast cancer reactive monoclonal antibodies directed to the core protein of the human milk mucin.* Cancer Research, 1987. **47**(20): p. 5476-5482.

198. Morson, B.C., *Evolution of cancer of the colon and rectum.* Cancer, 1974. **34**(S3): p. 845-849.

199. CO, C. and I. IN, *Colorectal Cancer Facts & Figures 2011–2013.* Facts & Figures 2011-2013 .